



Structure Design and Degradation Mechanisms in Coastal Environments

Edited by
Abdelkarim Aït-Mokhtar
Olivier Millet

@Seismicisolation

Structure Design and Degradation Mechanisms
in Coastal Environments

@Seismicisolation

Series Editor
François Nicot

Structure Design and Degradation Mechanisms in Coastal Environments

Edited by
Abdelkarim Aït-Mokhtar
Olivier Millet

iSTE

WILEY

 @Seismicisolation

First published 2015 in Great Britain and the United States by ISTE Ltd and John Wiley & Sons, Inc.

Apart from any fair dealing for the purposes of research or private study, or criticism or review, as permitted under the Copyright, Designs and Patents Act 1988, this publication may only be reproduced, stored or transmitted, in any form or by any means, with the prior permission in writing of the publishers, or in the case of reprographic reproduction in accordance with the terms and licenses issued by the CLA. Enquiries concerning reproduction outside these terms should be sent to the publishers at the undermentioned address:

ISTE Ltd
27-37 St George's Road
London SW19 4EU
UK

www.iste.co.uk

John Wiley & Sons, Inc.
111 River Street
Hoboken, NJ 07030
USA

www.wiley.com

© ISTE Ltd 2015

The rights of Abdelkarim Ait-Mokhtar and Olivier Millet to be identified as the authors of this work have been asserted by them in accordance with the Copyright, Designs and Patents Act 1988.

Library of Congress Control Number: 2015931948

British Library Cataloguing-in-Publication Data
A CIP record for this book is available from the British Library
ISBN 978-1-84821-732-4

Contents

GENERAL INTRODUCTION	xi
CHAPTER 1. POROUS CONSTRUCTION MATERIALS: CHARACTERIZATIONS AND MODELING	1
Abdelkarim AÏT-MOKHTAR, Ameur HAMAMI, Philippe TURCRY and Ouali AMIRI	
1.1. Definition of porous media.	1
1.2. Different experimental tools for the characterization of porous materials	3
1.2.1. Measurements of porosity.	3
1.2.2. Pore size distribution by sorption/desorption isotherms	6
1.2.3. Characterization of pore structure by NMR	7
1.2.4. Imaging techniques.	10
1.3. Some constructed models for porous microstructures	14
1.3.1. Models based on pore size distribution	14
1.3.2. Tridimensional-constructed microstructures	24
1.4. Some approaches for linking microstructure data to permeability	27
1.4.1. Permeability from MIP tests	29
1.4.2. Permeability from constructed microstructures	32
1.5. Bibliography	34
CHAPTER 2. MOISTURE TRANSFERS IN POROUS CONSTRUCTION MATERIALS: MECHANISMS AND APPLICATIONS	41
Rafik BELARBI, Kamilia ABAHRI and Abdelkarim TRABELSI	
2.1. Introduction.	41
2.2. Quantitative characteristics describing moisture in porous media	42

2.3. Phenomenon of transfer and moisture storage	43
2.3.1. Moisture diffusion	43
2.3.2. Capillarity	45
2.3.3. Infiltration	48
2.3.4. Physical and chemical adsorption	49
2.4. Moisture transfer modeling: macroscopic approach	49
2.4.1. Driving potentials.	51
2.4.2. Conservation equations	52
2.4.3. Moisture transfer	54
2.4.4. Heat transfer	57
2.4.5. Case study	58
2.5. Transfer and storage properties	66
2.5.1. Vapor permeability	66
2.5.2. Moisture diffusion coefficient	77
2.5.3. Infiltration coefficient	86
2.5.4. Water vapor sorption–desorption isotherms	93
2.6. Effect of statistical variability of water vapor desorption used as input data	101
2.6.1. Variability of water vapor desorption	102
2.6.2. Effect of statistical variability	105
2.7. Conclusion	108
2.8. Bibliography	109
CHAPTER 3. HOMOGENIZATION METHODS FOR IONIC TRANSFERS IN SATURATED HETEROGENEOUS MATERIALS.	117
Olivier MILLET, Khaled BOURBATACHE, Abdelkarim AÏT-MOKHTAR	
3.1. General introduction	117
3.2. Different techniques of homogenization	119
3.2.1. Homogenization <i>via</i> volume averaging	119
3.2.2. Periodic homogenization method	122
3.3. Periodic homogenization of ionic transfers accounting for electrical double layer	124
3.3.1. Dimensional analysis of equations	128
3.3.2. Reduction to a one scale problem	129
3.3.3. Homogenized microscopic diffusion-migration model with EDL	132
3.4. Particular case of ionic transfer without EDL	134
3.4.1. Dimensional analysis and scale problem.	134
3.4.2. Homogenized macroscopic diffusion-migration model	135
3.5. Simulations and parametric study of the EDL effects.	137
3.5.1. Implementation in COMSOL Multiphysics software and validation	138

3.5.2. Bidimensional elementary cells	140
3.5.3. Three-dimensional elementary cells	149
3.6. Calculations of effective chlorides diffusion coefficients using a multiscale homogenization procedure	153
3.7. Bibliography	156
CHAPTER 4. CHLORIDE TRANSPORT IN UNSATURATED CONCRETE	161
Ouali AMIRI, Abdelkarim AÏT-MOKHTAR, Hassan SLEIMAN and Phu-Tho NGUYEN	
4.1. Introduction	161
4.2. Chloride diffusion in unsaturated case	162
4.2.1. Definition of the problem	162
4.2.2. Theoretical aspects	163
4.2.3. Ionic transport model	164
4.2.4. Moisture transport model	171
4.3. Summary of the model	174
4.3.1. Output model	175
4.3.2. Constant parameters	176
4.4. Difficulties in determining some parameters of the model	176
4.5. Numerical method description	179
4.5.1. Finite volume method	179
4.5.2. Numerical simulations of chloride profiles: parametrical study	183
4.6. Conclusions	193
4.7. Bibliography	194
CHAPTER 5. CONSTRUCTION DEGRADATION BY EXTERNAL SULFATE ATTACKS	197
Emmanuel ROZIÈRE, Rana EL-HACHEM and Ahmed LOUKILI	
5.1. Introduction	197
5.2. Mechanisms of degradation	198
5.2.1. Chemical reactions and crystallization pressure	198
5.2.2. Ingress of sulfate ions and scenario of sulfate attack	202
5.2.3. Influence of exposure conditions	207
5.3. Influence of concrete composition and standards requirements	219
5.3.1. Influence of binder composition	219
5.3.2. Influence of concrete composition	223
5.3.3. Standards requirements	228
5.4. Testing for sulfate resistance	229
5.4.1. Material and scale of the tests	229
5.4.2. Acceleration of the degradation process	230

5.4.3. Recommendations for testing	235
5.5. Conclusion	237
5.6. Bibliography	238

**CHAPTER 6. PERFORMANCE-BASED DESIGN OF STRUCTURES AND
METHODOLOGY FOR PERFORMANCE RELIABILITY EVALUATION** 247

Vikram PAKRASHI and Ciarán HANLEY

6.1. Introduction	247
6.2. Code treatment of structural reliability	249
6.2.1. Formulation of structural reliability analysis	249
6.2.2. Incorporation of reliability analysis into normative documents	251
6.2.3. Reliability targets	252
6.2.4. Consistency with deterministic and semi-deterministic methods	253
6.3. Second moment transformation and simulation methods	254
6.3.1. Problem formulation	255
6.3.2. First-order reliability method	256
6.3.3. Second-order reliability method	256
6.3.4. Monte Carlo simulation for reliability analysis	258
6.3.5. Computational aspects and related software	259
6.3.6. Practical implementation aspects	261
6.4. Load and resistance modeling considering uncertainty	261
6.4.1. Uncertainty modeling	262
6.4.2. Need for resistance modeling	264
6.4.3. Measurement of resistance variables	265
6.4.4. Typical loading scenarios	265
6.5. Probabilistic assessment of limit-state violation	265
6.5.1. Reliability index and probability of failure	266
6.5.2. The concept of the design point	267
6.5.3. Sensitivity studies	269
6.5.4. Parameter importance measures	270
6.6. Component versus system reliability	271
6.6.1. Network requirements	271
6.6.2. Illustration of component and system reliability	272
6.6.3. Methods of estimating system reliability from component reliability	273
6.6.4. Practical implementation aspects	275
6.7. Time-dependent reliability	276
6.7.1. Concept of time dependence	276
6.7.2. Handling time dependency in reliability analysis	277
6.7.3. Time-dependent deterioration modeling	279

6.8. Conclusion	280
6.9. Bibliography	281
CHAPTER 7. COASTAL PROTECTION DEGRADATION SCENARIOS	285
Daniel POULAIN and Rémy TOURNENT	
7.1. Functions and types of coastal dikes	285
7.1.1. Main types of dikes.	286
7.1.2. Functional analysis of the protection system	295
7.2. Stress of coastal dikes.	309
7.2.1. Hydraulic stresses.	310
7.2.2. Marine geomorphology	318
7.2.3. Mechanical stresses.	321
7.3. Dysfunction and failure of coastal dikes	322
7.3.1. Definitions	322
7.3.2. Classic process to damage and failure of embankment dikes (elementary mechanisms)	325
7.3.3. Case studies of the damage and failure of coastal dikes	337
7.4. Bibliography	345
LIST OF AUTHORS	347
INDEX	349

@Seismicisolation

General Introduction

Any type of construction must ensure, from its inception, certain safety conditions for its users. This primarily occurs due to the mechanical performance of the structure which must be designed to account for cost optimization. Therefore, man has, over time, built structural codes based on the advancement of knowledge in the mechanical behavior of component materials of structures. These codes were designed to ensure safe behavior of the structure under mechanical stresses of its environment: supporting its own weight, excessive misuse and extreme climates (mainly snow and wind), while optimizing the cost of the structure. These codes have evolved to incorporate, in a modulated way, the hazards of accidental mechanical stresses such as seismic activity. Thus, we have seen established in these codes criteria dealing with the geophysical knowledge determining the geographical zoning of seismic activity.

The evolution of the landscape sector in construction over the past few decades can be schematically described in the following way:

- The advancement of knowledge in the mechanical behavior of materials coupled with the design of increasingly reliable building materials has allowed us to initiate more important construction projects with more gigantic structures, requiring increasingly important production costs.
- The continual aging of building heritage generates increasingly important maintenance and repair requirements.

Introduction written by Abdelkarim AIT-MOKHTAR.

- The extension of entropic areas leads inexorably to saturation and to the occupation of other areas which are climatically less secure: flooding and/or submersible zones, for example. Added to this is climate change which currently tends to emphasize the hazards and make extreme conditions more frequent (rainfall, storms, hurricanes, cyclones, etc.).
- The increase in the globalized competition in economic and financial management continually tends to improve the optimization of project costs.

All these elements lead to a main requirement in the construction sector: the resistance over time, i.e. the durability of structures, including environmental stresses. This requirement is gradually being integrated into the specifications of international design codes.

Coastline buildings are among the most exposed to these environmental burdens and hazards. They simultaneously bring together two types of continuous attacks: (1) physical and chemical attacks such as chlorides and sulfates present in the seawater and (2) mechanical attacks of waves in coastal zones, particularly on protection structures such as dikes. Recent events (2010) that took place on the French Atlantic coast (Cyclone Xynthia) have testified to their violence, which, though temporary, generated substantial damage and casualties.

Thus, issues of material and structure durability and that of environmental hazards were echoed from the research community worldwide, with academic research prevalent in different national, European and international programs. The literature is becoming more abundant on the various aspects involved in these phenomena: from fundamental approaches in fluid mechanics and transport in porous media at microscopic scales up to applications in structural calculations on degraded structures, with monitoring concepts of residual performances and performance thresholds according to repair actions.

Far from being exhaustive, this book aims to provide a summary through the presentation of examples of scientific approaches on research topics related to the physical, chemical and mechanical processes involved in the mechanisms of degradation or destruction of structures located in coastal zones. This book is organized into six chapters:

Chapter 1 is devoted to the description of microstructure materials widely used in built structures and the techniques of its investigation at the laboratory scale. For this purpose, a presentation of the different tools used is addressed. Then, different methodologies of the literature are given. They allow us to numerically build the microstructure of a porous medium and determine its associated transfer properties.

Chapter 2 focuses on heat and moisture transport since water is the vehicle of the transfer of aggressive agents from the atmosphere to porous materials by diffusion and advection. In unsaturated cases, wetting/drying cycles of the material also induce heat transfers. All these aspects are presented with some applications on concrete materials.

Chapter 3 deals with chloride transfer, mainly in saturated media. Given the well-known heterogeneity of porous building materials, the homogenization techniques used in the literature on porous media are discussed first. Then, the periodic homogenization technique has been chosen for its application to the case of chloride ion transfers in saturated materials. The electro-capillary phenomena involved in this kind of ionic transfer are integrated and parametric studies are supplied.

Chapter 4 studies chloride transfer through unsaturated materials by integrating advection phenomena in addition to electro-capillary phenomena mentioned above. In this chapter, the volume averaging technique is used to establish the macroscopic equations governing ionic transport coupled to liquid water transport leading to the obtainment of water and chloride profiles through the material submitted to a marine environment.

Chapter 5 focuses on the action of the second aggressive agent, i.e. sulfates present in seawater. The degradation mechanism is different from that of chlorides since sulfates act by modification of the hydrates formed in concrete. They induce some crystallized phases that are expansive. Also, they induce strengths that give rise to cracks in the materials. These cracks weaken the material and make it more permeable to any other agents, such as chlorides themselves. This leads to the facilitation of corrosion processes in reinforced concrete.

Chapter 6 deals with monitoring of structures. It expands the scale of the study to encompass the structure or the building and focus on the monitoring of the structure's performances according to its degradation state. According

to safety conditions, it also aims to define a critical state of degradation depending on loading conditions and stresses coupled with a probabilistic approach, including the uncertainties on these parameters.

In order to be complete regarding structures in marine environment, Chapter 7 deals with a different kind of structures. This concerns protection systems against marine floods such as dikes or earth-fills. This chapter describes mechanism and mode degradation of these kinds of structures.

Porous Construction Materials: Characterizations and Modeling

This chapter presents experimental methods and some modeling of microstructural properties of porous media, mainly applied to construction materials. The methods shown are generally recommended by some specialized users or by standards. Some models shown are based on the microstructural properties of the medium, while others describe simulated microstructures built numerically based on experimental data, such as porosity, tortuosity and connectivity, and on the hydration process in the particular case of cementitious materials.

In the final section of the chapter, the microstructural properties of a porous medium are linked to a transfer property, namely intrinsic permeability. For this purpose, several approaches are presented: calculation of the permeability from data on the pore structure (e.g. distribution of pore radii) and calculation from 3D constructed microstructures.

1.1. Definition of porous media

A porous medium is composed of a rigid solid matrix, or with low deformation, and of a void network. The porosity, denoted as ε_p in the

Chapter written by Abdelkarim AÏT-MOKHTAR, Ameur HAMAMI, Philippe TURCRY and Ouali AMIRI.

following, is expressed by the ratio of the void phase volume and the total volume of the medium (equation [1.1]):

$$\epsilon_p = \frac{V_{voids}}{V_{total}} \quad [1.1]$$

The pores (Figure 1.1) can be connected and cross the medium from side to side. In this case, the pore structure is known as “percolating”. Trapped gaps or blind pores can also be found within the medium.

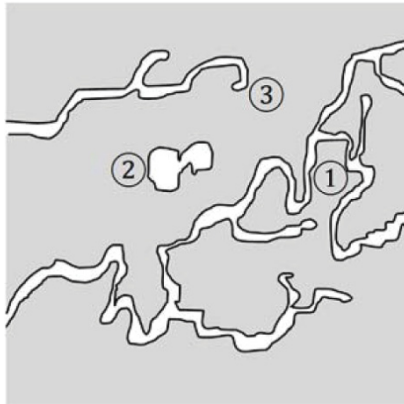


Figure 1.1. Porosity: ① Percolation/connected porosity,
② Trapped gap, ③ Blind pore

A lot of construction materials are porous. The pore structure, i.e. porosity and pore size and shape, depends, of course, on the type of the material. The porosity of construction materials is the place where transfer phenomena occur. These phenomena are affected by microstructural parameters, such as pore size distribution or connectivity. Generally speaking, it is necessary to consider all these parameters in order to study the transfer properties. For instance, the most porous material is not necessarily the most permeable material: pore size also affects the transfer by permeation.

From this point of view, two relevant microstructural parameters are usually used to characterize the pore structure: tortuosity and constrictivity. The tortuosity (τ) quantifies the elongation of the transfer path due to pore geometry, as shown in Figure 1.2(a).

Usually, tortuosity (equation [1.2]) is calculated as the ratio of the average pore length and the sample thickness. The tortuosity models the average transfer path through the material:

$$\tau = \frac{l}{l_0} \quad [1.2]$$

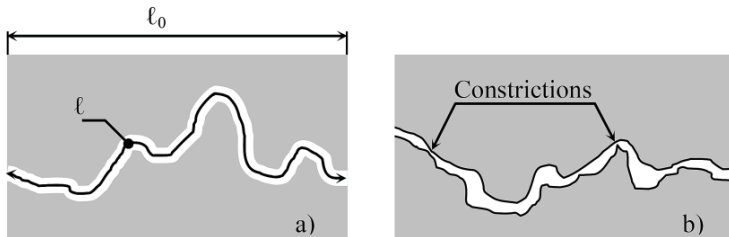


Figure 1.2. Microstructural parameters: a) tortuosity and b) constrictivity

The constrictivity (δ) (Figure 1.2(b)) consists of a reduction of the pore size along the pore. It reflects the fact that the pore section is not uniform but undergoes several constrictions that affect the transfer phenomena.

1.2. Different experimental tools for the characterization of porous materials

The transfer of chemical species in a porous medium is closely related to the porous microstructure [OLL 92]. Thus, its characterization is required to study the structure's durability. The knowledge of parameters such as porosity or pore-specific areas is necessary for the investigation of the physicochemical phenomena involved during mass exchanges between the wall of the pore and the pore solution interface inside the medium, which governs boundary conditions in the study of mass transfer.

1.2.1. Measurements of porosity

The main direct methods of porosity measurements in construction materials are water porosimetry and mercury intrusion porosimetry (MIP). These two methods are described hereafter. In the case of cementitious

materials, recommended protocols exist, particularly in France [AFP 97, ARL 07].

1.2.1.1. Water porosimetry

Generally, the water porosimetry test is carried out according to the procedure recommended by the French association AFREM (*Association Française de Recherche et d'Essais sur les Matériaux et les Constructions*, French Association for the Research and Testing of Materials and Structures) [AFP 97] and the standard NF P18-459 [AFN 10]. The samples are first water-saturated with distilled water under vacuum at a saturation vapor pressure of 18 mmHg in order to obtain the saturated mass m_{sat} . The sample volumes V_{tot} are then determined from buoyancy weighing. Finally, samples are dried at a temperature between 60 and 105°C until mass stabilization to obtain the dried mass m_{dry} . The mass stabilization is obtained when the relative mass loss in 24 h is less than 0.05%. The porosity ε_p is calculated using equation [1.3]:

$$\varepsilon_p = \frac{m_{sat} - m_{dry}}{\rho_w \cdot V_{total}} \times 100 \text{ (%)} \quad [1.3]$$

where ρ_w is the density of water.

1.2.1.2. Mercury intrusion porosimetry

The MIP test is carried out by injecting mercury through a porous medium sample of 1–2 cm³ placed under vacuum in a penetrometer. This injection is performed by varying the injection pressure P , which can reach more than 400 MPa, so that the mercury penetrates pores whose diameters D are between 0.003 and 360 µm. Each pressure increment permits the calculation of the diameter of the pores filled with a volume of mercury V_{Hg} according to the Laplace's law (equation [1.4]). The principle of measurement is schematized in Figure 1.3:

$$D = \frac{4\gamma \cos \theta}{P} \quad [1.4]$$

where γ is the surface tension between the pore surface and the mercury (N/m). This parameter varies with the purity of mercury. The value usually used is 0.485 N/m. θ is the contact angle in degree between the mercury meniscus and the pore wall. The usual value for this parameter is 130°.

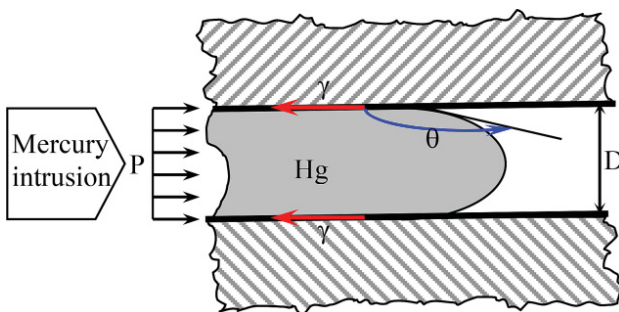


Figure 1.3. Schematic view of the MIP principle. For a color version of the figure, see www.iste.co.uk/ait-mokhtar/coastal.zip

At the end of the test, a pore size distribution of the porous network is obtained. The latter is given by a plot of the differential log of the mercury volume intrusion versus the pore diameter. Figure 1.4 gives an example of a result obtained by this method. The specific area of the material can also be calculated from the collected data.

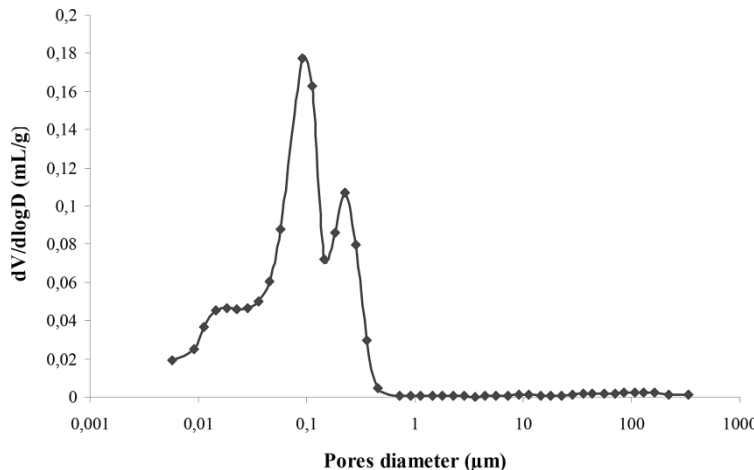


Figure 1.4. Example of pore size distribution obtained by MIP on a mortar with $W/C = 0.6$ [HAM 09]

The MIP is a measurement technique widely used to characterize a porous material. It gives a simplified representation of the microstructure of

the material because the pores are assumed to be cylindrical. Moreover, this method facilitates only the determination of the pore entrance diameter. As shown in Figure 1.5, large pores located after smaller ones cannot be detected by the MIP method, because the required pressure to fill the larger pores is the same than that necessary for penetrating the smallest ones (this phenomenon is commonly called “ink-bottle” effect) [DIA 00].

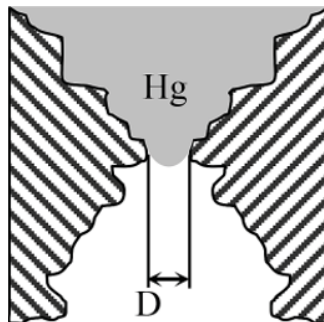


Figure 1.5. Pore diameter measured by MIP

Despite these assumptions and approximation, the MIP technique remains one of the main tools used for the characterization of porous materials.

1.2.2. Pore size distribution by sorption/desorption isotherms

The water vapor sorption/desorption isotherm gives the evolution of the water content of a porous material as a function of the ambience relative humidity (RH) at constant temperature. For each RH, it is possible to determine a pore diameter D that is filled with water. A pore size distribution is obtained for a range of RH. For this purpose, the Kelvin–Laplace law, given in equation [1.5], is used to calculate the pore diameter:

$$D = -\frac{4M_v \gamma_{aw}}{\rho_{aw} RT \ln(RH)} \quad [1.5]$$

where M_v is the molar mass of the water vapor (18 g/mol), γ_{aw} is the surface tension of the liquid water (equal to 0.07275 N.m⁻¹ at 20°C), ρ_w is the mass density of liquid water and R is the ideal gas constant (8.314 J.K⁻¹.mol⁻¹).

The pore diameters obtained by this technique are located between 0.6 and 35 nm for an RH range between 3 and 94%.

The measurement of sorption/desorption isotherms can also be carried out by using a gas such as nitrogen. This method consists in measuring the amount of nitrogen molecules adsorbed by the material under a constant temperature of 77 K. This technique is based on the works of Brunauer *et al.* [BRU 38], which is commonly known as the Brunauer–Emmett–Teller (BET) technique. The latter makes the determination of the specific area of a solid possible, the pore size distribution that can reach pore with a diameter smaller than 200 nm. This pore size distribution is based on the step-by-step analysis of the sorption/desorption isotherms following the Barrett–Joyner–Halenda (BJH) method [BAR 51].

1.2.3. Characterization of pore structure by NMR

The application of nuclear magnetic resonance (NMR) for the characterization of pore structure is an attractive method [PLA 01]. Contrary to intrusion methods, it is fully non-destructive and does not require sample preparation such as drying, liquid saturation or polishing.

In a material, any nucleus with a spin (i.e. nucleus with an odd number of protons) shows an intrinsic magnetic moment. When the material is immersed in an intense magnetic field, classically denoted as \vec{B}_0 , it becomes magnetized due to the interactions between this external magnetic field and the magnetic moments of the nuclei. The overall magnetization is characterized by a magnetic moment \vec{M}_0 which rotates around the direction of \vec{B}_0 . This motion, called precession, occurs at a given frequency (called Larmor frequency) specific to each nucleus. NMR consists of perturbing this equilibrium state by applying a second magnetic field \vec{B}_1 , perpendicular to \vec{B}_0 and pulsed during a short time. Due to electromagnetic radiation from \vec{B}_1 , the overall magnetization temporarily changes from \vec{M}_0 to \vec{M} . When \vec{B}_1 is stopped, the system returns progressively to its equilibrium state ($\vec{M} \rightarrow \vec{M}_0$). This phenomenon is called relaxation. During NMR experiments, the time evolution of M is recorded and two characteristic times are

determined. The first time (T_1) characterizes the relaxation time of the component of the vector \overrightarrow{M} parallel to \overrightarrow{B}_0 (spin–lattice relaxation), while the second time (T_2) is the relaxation time of its components in the plane perpendicular to \overrightarrow{B}_0 (spin–spin relaxation).

In the case of porous materials, NMR experiments often concern the relaxation phenomenon of the proton ^1H . The characterization of pore structure is based on the existing dependence of the relaxation times, T_1 and T_2 , on the pore size. In fact, the overall recorded relaxation time is the mean of the contribution of two terms: the relaxation of “bulk protons” (i.e. inside the porosity) and “surface protons” (i.e. at the pore surface).

For instance, Figure 1.6 gives relaxation rates ($1/T_1$) measured in the case of a cement paste, i.e. a material with a multiscale pores structure [KOR 07]. Four classes of relaxation rates can be observed, which reveals the dependency of the relaxation process on pore size. The two higher classes correspond to the smaller pore sizes (i.e. pores in Calcium-Silicate-Hydrate (CSH) gel), while the two lower classes can be associated with capillary pores.

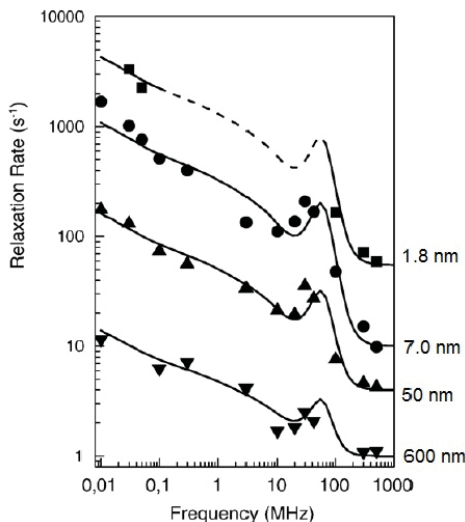


Figure 1.6. Relaxation rates ($1/T_1$) versus Larmor frequency measured for a cement paste (cement = C_3S , $\text{W}/\text{C} = 0.4$, age = 1 year). The four curves correspond to the material responses due to four average pore sizes (given on the right). The latter are calculated values by the authors [KOR 07]

The use of NMR relaxometry for porous material characterization has some limits. Especially, the so-obtained relaxation times are usually given in milliseconds and cannot be easily converted in a size scale, for instance in nanometers. Such a conversion depends on experimental conditions and calculation methods [FAU 12]. Thus, results from relaxometry are mainly used to compare the evolution of relaxation times as a function of studied parameters. For instance, Figure 1.7 shows the time evolution of T_1 distribution measured for a cement paste at the early age. This evolution reveals the structuration of the material and the refining of the pore structure due to cement hydration. Another example is given in Figure 1.8, which shows the influence of cellulose ether on the time evolution of the relaxation rate ($1/T_1$) of cement pastes.

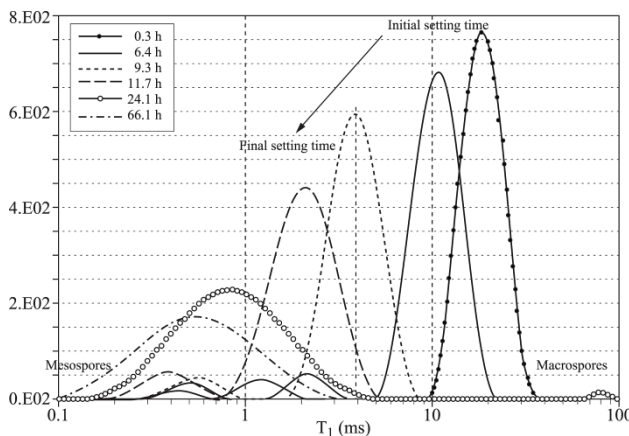


Figure 1.7. Time evolution of the relaxation time T_1 distribution due to hydration of a cement paste at very early age (cement = OPC, W/C = 0.35) [WAN 13]

In addition to the characterization of pore structure, NMR can also be used as an imaging technique (magnetic resonance imaging (MRI)). In this case, magnetic field gradients are applied in three directions (three-dimensional (3D) imaging). Consequently, the precession frequency of the protons immersed in the magnetic field depends on the location. This technique is used, for instance, to image water contents of porous materials [FAU 12]. Resolution of MRI (~1 mm) is, however, too low for this technique to be able to serve image pore structure.

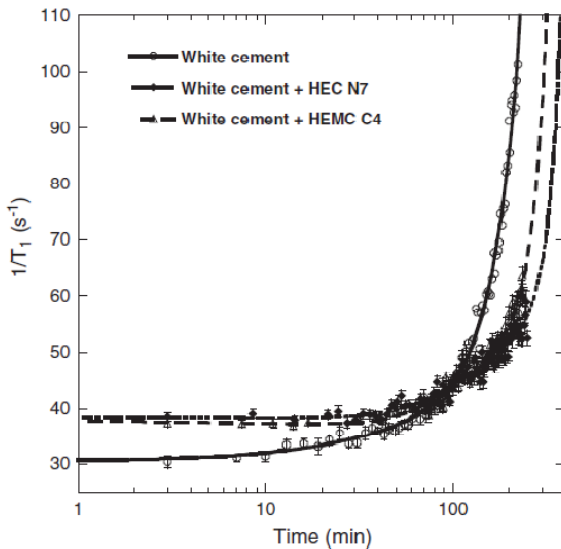


Figure 1.8. Time evolution of the relaxation rate ($1/T_1$) measured at a Larmor frequency of 10 kHz for cement pastes (white cement, W/C = 0.4) – effect of the presence of two cellulose ether (HEC and HEMC) [PAT 12]

1.2.4. Imaging techniques

Characterization methods shown previously, for instance MIP, give a first level of information on the pore structure, i.e. open porosity, pore size distribution or surface area. Of course, this is not enough to describe completely the voids network, since other characteristics, such as connectivity or pore shape, are not provided [SIN 04]. These characteristics are, however, very relevant for the modeling of transfer properties of materials with disordered pore structure, such as cementitious materials.

In this scope, imaging techniques are powerful tools [LEV 07]. Indeed, they permit a mapping of the pore structure in 3D which offers, among others, direct assessments of the connectivity.

Two families of imaging methods can be distinguished. The first family is based on the acquisition of 2D images of cut-sections of the material followed by a reconstruction of the pore structure in 3D. The second family consists of mapping the pore structure in 3D more directly, without any

sample preparation such as slicing or polishing, e.g. computed X-ray microtomography or electron tomography.

1.2.4.1. *From 2D to 3D images of the pore structure*

Images in two dimensions can be obtained by many techniques. Scanning electron microscopy (SEM) and transmission electron microscopy (TEM) are undoubtedly the most popular techniques. In brief, SEM uses a focused beam of electrons, which interacts at the surface of solid specimens. In the case of TEM, the beam is transmitted through the specimen. The various signals generated by the electrons–specimen interactions give information about chemical composition and densities of the different phases in the material. For instance, from polished sections of cement-based materials, the detection of backscattered electrons (BSEs) in SEM facilitates the construction of high-resolution 2D images of the anhydrous and hydrated phases. In electron microscopy, the resolution can be less than the nanometer scale.

Before SEM imaging, the material porosity can also be injected by a metal, such as wood's metal or gallium [WIL 98, KUR 06]. The X-rays emitted by the specimen due to the electron beam can be observed using an electron probe microanalysis (EPMA). The so-measured repartition of the intruded metal provides a 2D map of the pore structure.

To obtain 3D images from 2D images, a serial cross-sectioning has to be performed. This consists of repeatedly polishing the observed specimen. After each polishing, a scanning of the obtained surface is performed by SEM, for instance. The reconstruction of the 3D image is done by stacking the 2D images, as shown in Figure 1.9.

In the polishing operation, the serial cross-sections should be as close as possible. Otherwise, the resolution of the 3D image reconstructed by stacking would not be the same in the direction perpendicular to polishing compared to the scanned section. To avoid this obvious shortcoming, the polishing operation can be performed directly in the SEM microscope by using a focus ion beam [MUN 09, LUR 11]. In a microscope equipped with Focused Ion Beam (FIB), a beam of ions such as gallium ions hits the specimen surface, resulting in an ablation of a few nanometers. Figure 1.10 gives a schematic representation of the FIB technique [KEL 11]. By coupling FIB and SEM, the serial sectioning and 3D reconstruction become much more accurate. Although this technique is promising, it has not been

widely used for imaging the pore structure of cement-based materials. However, this latter is used more for applications regarding soil studies [HOL 10, NAD 13].

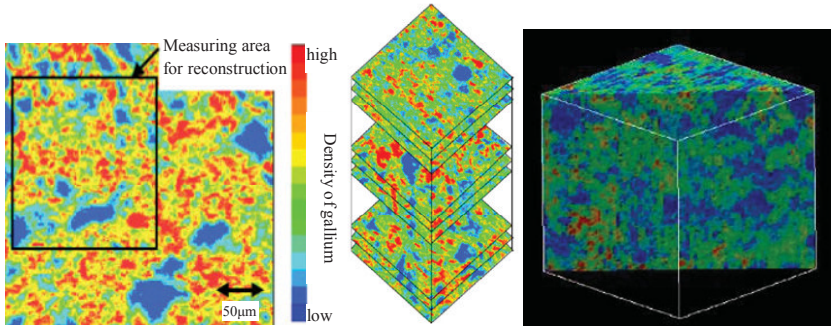


Figure 1.9. 3D reconstruction of the pore structure from 2D images stacking. The 2D images were obtained by EPMA on a cement paste sample intruded by gallium [KUR 06]. For a color version of the figure, see www.iste.co.uk/ait-mokhtar/coastal.zip

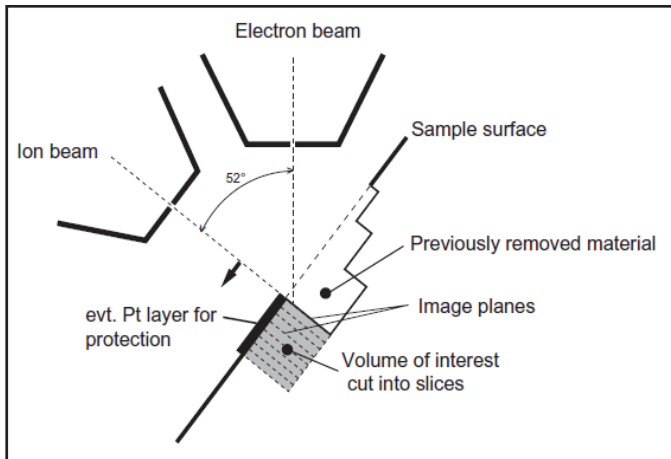


Figure 1.10. Schematic representation of SEM coupled with FIB device [KEL 11]

1.2.4.2. Non-destructive 3D mapping by X-ray microtomography

Computed X-ray microtomography (μ CT) consists of subjecting a material sample to an X-ray source [LAN 10]. X-ray beam passing through the sample is more or less absorbed depending on the absorptivity of the

various phases in the material. A plane detector is used to acquire a 2D image of the intensity spatial variations of the absorbed beam (projection image). The X-ray source is then rotated around the sample. A series of 2D projections are so-recorded. Based on the mathematical methods of inversion, such as Fourier transforms, it is possible to reconstruct a 3D image usually given with gray levels corresponding to the different absorption levels of the material phases. In the case of a porous material, since X-rays are mainly absorbed by the solid phase, μ CT can provide a 3D map of the pore structure. When differences in absorption levels are less significant than in the case of solid/voids segmentation, image analysis methods, such as edge detection, can be necessary to extract spatial distribution of phases.

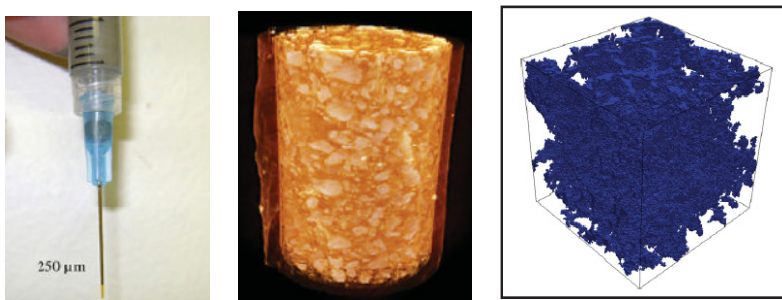


Figure 1.11. Investigation of cement paste microstructure by X-ray microtomography. Sample of a plastic tube (left), reconstructed 3D image at 1 day age (middle), pore structure of a volume of interest (VOI) after image segmentation (right) [ZHA 12]. For a color version of the figure, see www.iste.co.uk/ait-mokhtar/coastal.zip

X-ray microtomography is a completely non-destructive method. This is one of its main interests, as compared to 3D reconstruction based on 2D microscopy which needs polishing operations (see the previous section). One of the drawbacks of μ CT can be its resolution which is currently of approximately 1 μm for a desktop apparatus, which is not enough to investigate the pore structure of materials such as cementitious materials. The latter contain many pores lower than 100 μm in diameter. For instance, μ CT has been applied by Gallucci *et al.* for the study of the microstructure formation of cement paste between 1 and 60 days [GAL 07]. Beyond a few days, the resolution is not high enough to distinguish the pores of the cementitious matrix.

In the near future, μ CT resolution is likely to be improved. Especially, in the case of synchrotron X-ray, resolution of lower than 500 μm per voxel is already obtained and porosity of cement-based materials can be investigated in more detail [PRO 09]. Investigations with high resolution are, however, limited to small-size specimens of cement pastes, as shown in Figure 1.11 [ZHA 12]. At lower resolution, μ CT is an interesting tool increasingly used for the investigation of materials degradation phenomena, e.g. [LAN 00, ROU 09] (Figure 1.12).

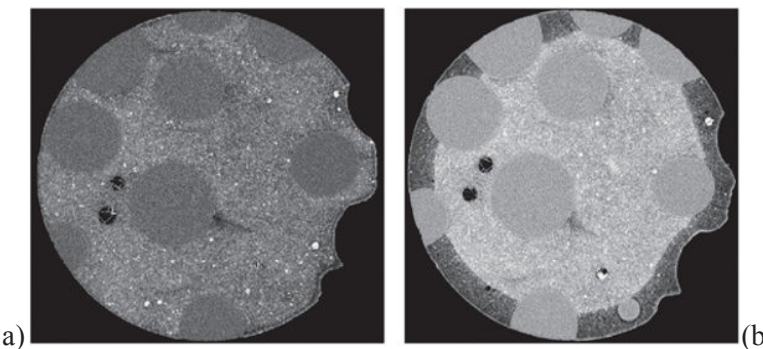


Figure 1.12. A concrete leaching investigated by X-ray microtomography. Cross-section of a sound specimen before leaching a) and cross-section after 11 h of leaching b) [ROU 09]

1.3. Some constructed models for porous microstructures

Experimental tests, such as MIP tests or moisture sorption/desorption tests, provide a pore size distribution using some assumptions dealing mainly with the geometrical shape of the pores within the material. From data provided by these techniques, the objective is to build models describing microstructures aiming linking them to mass transfer modeling for the prediction of degradation of structures, particularly in the case of chloride in coastal zones [AIT 04].

1.3.1. Models based on pore size distribution

While providing results sometimes discussed [FAU 80, VAN 81, WAR 81, COO 93], MIP remains a powerful tool for characterizing the pore size distribution of a porous medium. However, let us recall that the physical properties of mercury as a liquid measurement are different from those of

water, while water is the main, if not only, fluid carrying aggressive species within porous materials and dissolving certain fractions of hydrated compounds in the case of cementitious materials. Furthermore, mercury does not penetrate the smallest pores such as CSH¹ [HAL 95]. In addition, devices available actually limit the penetration to pores with 3 nm in diameter.

Despite these considerations, the technique is widely used for the characterization of porous media. Therefore, results provided by this technique are used for the construction of models describing the porous network properties.

1.3.1.1. Statistical functions of pore size distribution

In addition to the overall porosity ε_p , MIP test provides the logarithmic differential intrusion as a function of pore radius penetrated at a pressure i by unit volume of sample, which is nothing but the pore size distribution:

$$f(R_p) = -\frac{1}{L} \frac{V_{pi} - V_{p(i-1)}}{\ln R_{pi} - \ln R_{p(i-1)}} \quad [1.6]$$

where R_{pi} and $R_{p(i-1)}$ are the radii penetrated, respectively, at stages i and $(i-1)$; V_{pi} and $V_{p(i-1)}$ are the corresponding porous volumes and L is the samples length.

The plot of equation [1.6] can be modeled by a statistical distribution with a random variable, R_p , set by the results of MIP test.

The aim of the modeling that we propose is then a parametric characterization of the experimental pore size distribution for the calculation of other material properties such as specific area and permeability.

According to Diaz *et al.* [DIA 87], based on the assumption of cylindrical pores, some researchers have established simplified relationships between the pore volume and their entry diameters. Some other authors (e.g. [AÏT 99]) have presented models, called parallel channels, based on a

¹ Cement industry notations of the hydrated calcium silicates whose classical chemical formula is: 3CaO.2SiO₂.3H₂O. We can also define them in a “generic” manner in the form CaO.SiO₂.nH₂O [DUN 89].

probability calculation. This probabilistic aspect makes the use of these models difficult. As a first approach, we assume that the porous network is represented by cylindrical pores of different radii R_p with the same length L within the material with a unit representative surface (Figure 1.13).

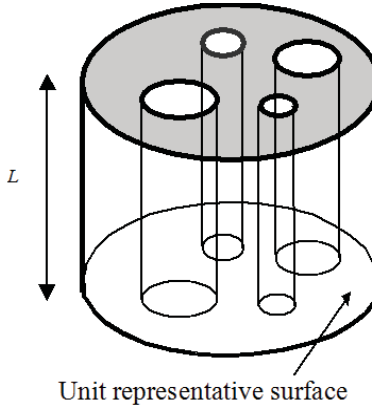


Figure 1.13. Simplification of the porous structure referred to a unit representative surface

Two main categories of pore size distribution may be found (Figure 1.14). First, we have the case where the distribution has only one “mode” pore radius around a single average, which is called “porosity peak”. The pore structure is then a single porous mode, which is called a “single-mode structure”. On the other hand, if the distribution has more than one group of radii around two or more “porosity peaks”, the pore structure has then more porous modes and is qualified as “polymodal”.

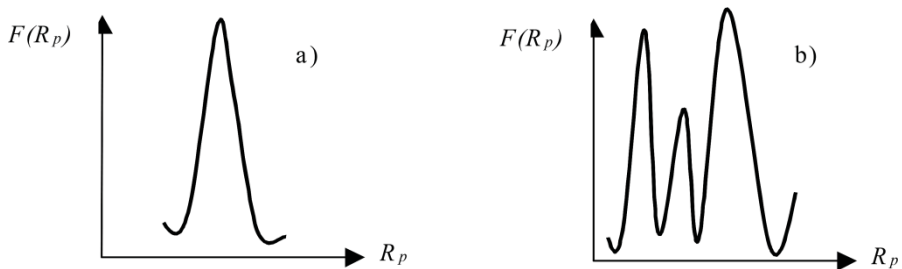


Figure 1.14. Examples of pore size distributions: a) monomodal distribution and b) polymodal distribution

1.3.1.1.1. Case of monomodal porous structures

We first discuss the case where the pore structure has only one mode, i.e. the distribution has a single “peak”.

In this case and according to Shi *et al.* [SHI 89], we can express the number of pores per unit surface representative dn_p whose radii are between R_p and (R_p+dR_p) by a statistical distribution of log-normal type, but use here the total number of pores per unit surface representative n_p :

$$dn_p = \frac{n_p}{\xi\sqrt{2\pi}} \exp\left(-\frac{\ln^2(R_p/R_{pm})}{2\xi^2}\right) d(\ln R_p) \quad [1.7]$$

where ξ is a location parameter which is dimensionless and ensures that dn_p is the probability density function for the area $[0; \infty[$, R_{pm} is the statistical average pore radius and n_p is the number of pores per unit surface.

To the variation dn_p corresponds the following elementary variation of volume between R_p and (R_p+dR_p) :

$$dV_p = \pi R_p^2 L dn_p \quad [1.8]$$

From equations [1.6]–[1.8], we obtain:

$$f(R_p) = \frac{\pi R_p^2 n_p}{\xi\sqrt{2\pi}} \exp\left(-\frac{\ln^2(R_p/R_{pm})}{2\xi^2}\right) \quad [1.9]$$

which allows a maximum α such that:

$$\left. \begin{cases} R_{p\max} = R_{pm} e^{2\xi^2} \\ \alpha = f(R_{p\max}) = \frac{\pi R_{pm}^2 n_p}{\xi\sqrt{2\pi}} e^{2\xi^2} \end{cases} \right\} \quad [1.10]$$

The porosity per surface unit is obtained from [1.1], [1.7] and [1.8]:

$$\varepsilon_p = \frac{1}{\sqrt{2\pi}} \int_0^{\infty} \frac{\pi R_p^2 n_p}{\xi} \exp\left(-\frac{\ln^2(R_p/R_{pm})}{2\xi^2}\right) d(\ln R_p) \quad [1.11]$$

whose solution is:

$$\varepsilon_p = \pi R_{pm}^2 n_p e^{2\xi^2} \quad [1.12]$$

From [1.10] and [1.12], we obtain:

$$\begin{aligned} \xi &= \frac{\varepsilon_p}{\alpha \sqrt{2\pi}} \\ R_{pm} &= \frac{R_{p\max}}{e^{2\xi^2}} \\ n_p &= \frac{\varepsilon_p}{\pi R_{pm}^2 e^{2\xi^2}} \end{aligned} \quad [1.13]$$

The MIP test provides the porosity ε_p and the pore size distribution of the material. From the latter, $R_{p\max}$ and α are obtained. Using these two experimental data, parameters [1.13] are calculated. Thus, we obtain the probability law of pore size distribution (equation [1.9]). This law can be used for the determination of other transport properties of the medium and for the upscaling in behavior modeling of heterogeneous media [AMI 01a, AMI 01b].

1.3.1.1.2. Case of polymodal porous structures

In the event that there is N porous mode, i.e. N peaks, the pore size distribution is divided up into N elementary classes according to the number of peaks. Then, the expression of the pore number will be the sum of elementary functions of distribution with the same random variable R_p :

$$dn_p = \frac{1}{\sqrt{2\pi}} \sum_{j=1}^N \frac{n_{pj}}{\xi_j} \exp\left(-\frac{\ln^2(R_p/R_{pmj})}{2\xi_j^2}\right) d(\ln R_p) \quad [1.14]$$

With each porous mode is associated an elementary porosity ε_{pj} and an elementary pore size distribution law with the following parameters:

$$\begin{aligned}\xi_j &= \frac{\varepsilon_{pj}}{\alpha_j \sqrt{2\pi}} \\ R_{pmj} &= \frac{R_{p\max j}}{e^{2\xi_j^2}} \\ n_{pj} &= \frac{\varepsilon_{pj}}{\pi R_{pmj}^2 e^{2\xi_j^2}}\end{aligned}\quad [1.15]$$

1.3.1.1.3. Determination of the pore-specific area

Based on the assumption that the pore-specific area is only linked to the arithmetic average of pore radii penetrated by the mercury during the test, MIP acquisition devices generally provide a value of this parameter. To ensure consistency in the use of MIP results, a relationship can be built by integrating the statistical pore size distribution.

Given the assumption of cylindrical pores, to the elementary pore volume dV_p (equation [1.8]) corresponds an elementary surface dA_p developed by pores having radii between R_p and $(R_p + dR_p)$, whose expression is:

$$dA_p = 2\pi R_p L dn_p \quad [1.16]$$

Reduced to a unit volume of material, the elementary-specific area is obtained:

$$da_p = 2\pi R_p dn_p \quad [1.17]$$

The pore surface area of the material can be obtained by the integration of equation [1.17], in which d_{np} is substituted by its expression (equation [1.7]):

$$a_p = 2\pi R_{pm} n_p e^{\frac{1}{2}\xi^2} \quad [1.18]$$

1.3.1.2. Models including geometrical parameters

The approach described above is based on the main assumption that the pores are cylindrical, i.e. neither tortuosity nor constrictivity is considered. It

means that construction materials are known to have microstructures with complex geometries, where parameters such as tortuosity, constrictivity or connectivity of the pores play a significant role in the transfer of aggressive agents, and then in the structures durability. Hereafter, an approach describing these parameters is presented.

Based on the isotropic porous network model in a cubic representative elementary volume (REV) proposed by Aït-Mokhtar *et al.* [AÏT 02], let us consider a wider scheme (Figure 1.15), with pores having different lengths l_1, l_2, \dots, l_n and different sections S_1, S_2, \dots, S_n . These sections are classified such as $S_1 > S_2 > \dots > S_n$ (Figure 1.16). Then, we can define the tortuosity as [AMI 05]:

$$\tau = \left(\frac{l_1 + l_2 + \dots + l_n}{l} \right) = \left(\frac{1}{l} \sum_{i=1}^n l_i \right) \quad [1.19]$$

The contraction effect and the pores length ratio are introduced, respectively, by m_{ij} and q_{ij} :

$$m_{ij} = \frac{S_j}{S_i}; \quad q_{ij} = \frac{l_j}{l_i} \quad [1.20]$$

where $S_i > S_j$ if $i < j$.

Then, tortuosity becomes:

$$\tau = \frac{l_n}{l} \sum_{i=1}^n \frac{1}{q_{in}} \quad [1.21]$$

Given the configuration of Figures 1.15 and 1.16, N^3 is the number of elementary cubes per representative sample of material with cubic shape. Then, the total pore section S_p and the total section S of the material cube are, respectively:

$$S_p = \frac{(n!+1)^2}{n} N^2 \sum_{i=1}^n S_i \text{ and } S = (n!+1)^2 l^2 N^2 \quad [1.22]$$

Given the pore entry section on an elementary cube surface, the porous volume and the global volume of the representative material are, respectively:

$$V_p = 3(n!+1)^3 N^3 \sum_{i=1}^n S_i l_i \text{ and } V = (n!+1)^3 l^3 N^3 \quad [1.23]$$

We deduce from [1.25], [1.22] and [1.23] the porosity of the material:

$$\varepsilon_p = \frac{V_p}{V} = \frac{3(n!+1)^3 N^3 \sum_{i=1}^n S_i l_i}{(n!+1)^3 l^3 N^3} = \frac{3}{l^3} \sum_{i=1}^n S_i l_i = 3\tau \frac{\sum_{i=1}^n \frac{1}{m_{in} q_{in}}}{\sum_{i=1}^n \frac{1}{q_{in}}} \quad [1.24]$$

where:

$$l = \sqrt[3]{\frac{3}{\varepsilon_p} \sum_{i=1}^n S_i l_i} \text{ and } \tau = \left(\frac{\varepsilon_p}{3\pi \sum_{i=1}^n R_i^2 l_i} \right)^{1/3} \left(\sum_{i=1}^n l_i \right) \quad [1.25]$$

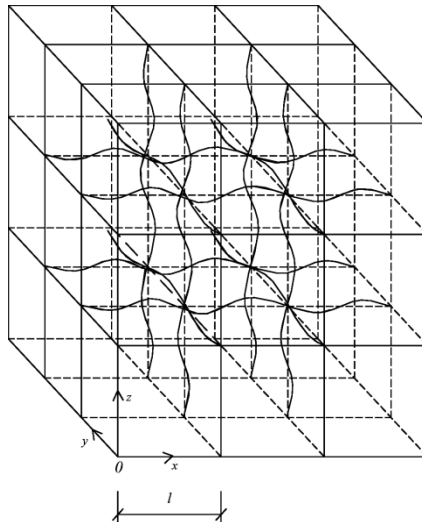


Figure 1.15. Schematic view of the porous network in a cubic representative elementary volume (REV)

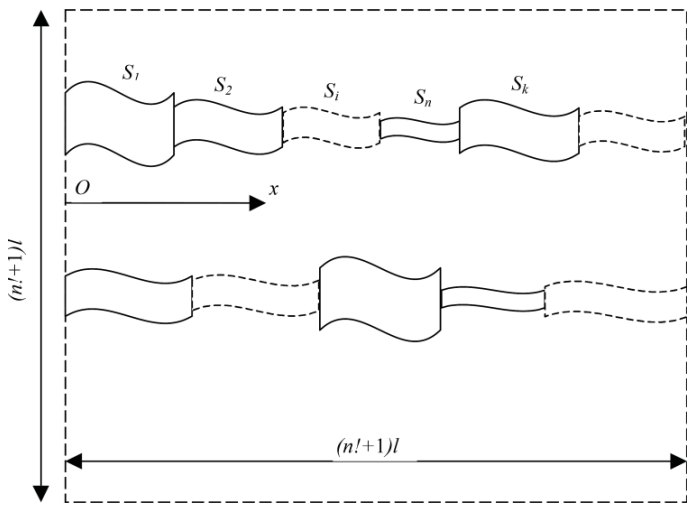


Figure 1.16. A cross-section of the material

A more recent work presented by Khaddour *et al.* [KHA 13, KHA 15] gives a simplified method for microstructure representation based on MIP data. This microstructure consists of parallel, cylindrical and tortuous pores of different diameters crossing the sample as shown in Figure 1.17. The total length of a pore of diameter d_i and volume V_{pi} is calculated using equation [1.26]:

$$L_i = \frac{4V_{pi}}{\pi d_i^2} \quad [1.26]$$

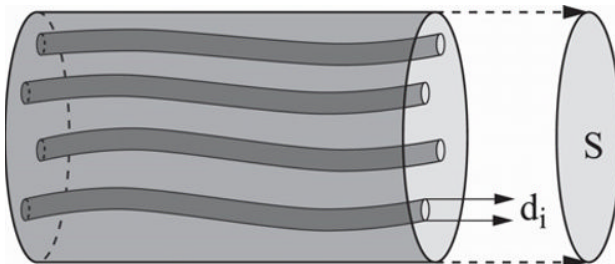


Figure 1.17. Microstructure obtained from parallel pores assembly [KHA 15]

A pore crosses the porous media sample if its length L_i reaches a critical length L_c (equation [1.27]) which depends on the sample thickness L_e and the pores tortuosity τ :

$$L_c = \tau \cdot L_e \quad [1.27]$$

$$L_e = \sqrt[3]{V_t} \quad [1.28]$$

where V_t is the total volume of the porous media containing x_i pores of diameter d_i . The quantity x_i is the characteristic quantity of the pore size distribution.

A pore that does not cross the sample, i.e. one whose length L_i does not reach the value of the critical length L_c , is connected to the pore with the next smallest diameter in order to obtain a serial assembly of pores with decreasing diameters as shown in Figure 1.18 [KHA 09].

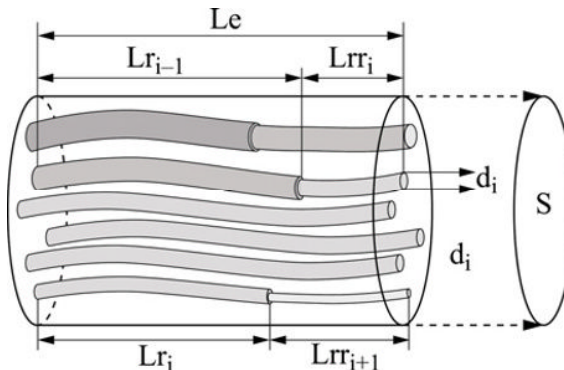


Figure 1.18. Microstructure obtained from parallel and serial pores assembly [KHA 09]

According to Figure 1.18, the total length of the pores of a diameter d_i is given by equation [1.29] as follows:

$$L_i = Lrr_i + x_i L_c + Lr_i \quad [1.29]$$

1.3.2. Tridimensional-constructed microstructures

Microstructures of porous materials can be modeled from input data, such as pore size distribution, provided by various experimental techniques. Another approach consists of modeling the different phenomena involved in the formation of the pore structure. Such approaches were developed especially in the field of cementitious materials. Hydration of Portland cement has extensively been studied during the last century (and is still ongoing), resulting in accurate models of hydration kinetics. From such models, the formation of the microstructure of a cement paste can be computed from stacks of anhydrous cement grains whose volume progressively increases due to the hydration. This facilitates obtaining pore structures in 3D and information on percolation of the pore network. Of course, the realism of the computed microstructure greatly depends on the initial stacks of cement (grains shape, size distribution) and on the hydration model [SCR 04].

In the following, some approaches are described for the construction of evolving microstructures of cementitious materials. For most of the models described, the materials do not exceed the scale of cement pastes. For this microstructure construction, two kinds of approaches are commonly used: vectorial expansion approach of the cement grains and a 3D voxel-segmented image approach. Finally, an ideal way for the cement paste microstructure construction is presented on the basis of regular spherical grains stacks.

1.3.2.1. Vectorial approach

The first approach is based on a vector expansion of the anhydrous cement grains composing the stack. Two examples are given here:

– The first example, named hydration, morphology and structural development (HYMOSTRUC), was developed by van Breugel [VAN 91, VAN 95] and based on the work of Berlage [BER 87]. This model considers all the chemical phases of the cement and assumes that the cement grains are spherical. The hydration products are formed around these grains in dissolution. The density of reaction products is supposed to be constant during the hydration. The development of the microstructure depends on the interaction between the particles of different sizes. Thus, it is important that such a model considers the particle size distribution of cement grains as well as their spatial distribution.

A schematic view of the particle hydration is given in Figure 1.19.

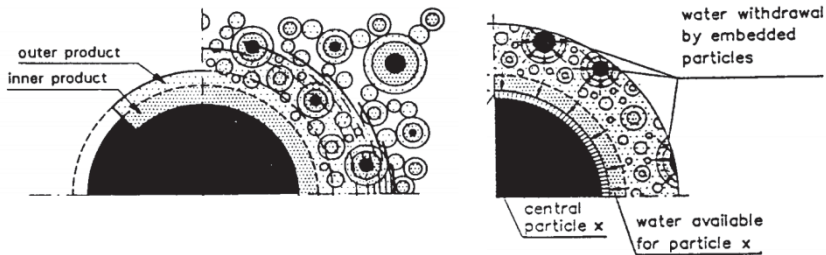


Figure 1.19. Schematic representation of expansion mechanism during cement hydration [VAN 95]

– The second example, called “μic” model, was developed by Bishnoi and Scrivener [BIS 09] to succeed the “IPKM” model developed by Pignat and Navi [PIG 05]. The “μic” model is based on the same approach like theHYMOSTRUC. The main difference lies in the segmentation of the volume into smaller cubes to make the calculation of the interaction between particles faster. In addition, the “μic” model facilitates the simulation of cement hydration in the presence of other materials such as fillers and mineral additives. The proportion of various materials is defined by volumes calculated using the stoichiometry of the reactions and the density of each individual phase.

At the output of these two models, we can obtain a 3D microstructure shown in Figure 1.20.

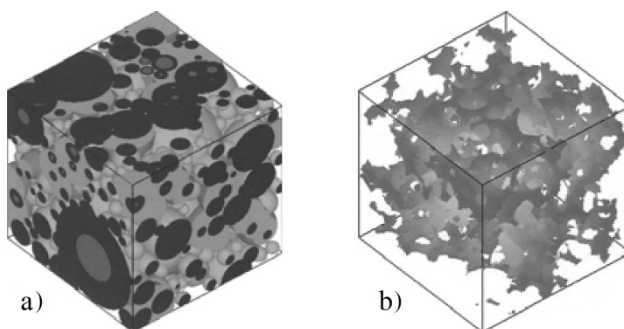


Figure 1.20. 3D representation of the microstructure obtained:
a) solid phase and b) pore network [PIG 05]

1.3.2.2. Voxel-based method

A second approach for microstructure construction is based on randomly stacked cement grains in a cubic volume. For this method, the model named CEMHYD3D, which was developed by Bentz at the NIST² in 1997 [BEN 97], is the most efficient model. This model was improved by Bullard [BUL 14] and is now named as VCCTL.

Such a model makes the simulation of the cement hydration possible, the use of mineral additions and aggregates and the microstructure development of a 3D stacking of cement grains. The considered cement grains may be spherical or may take a realistic shape of cement particles. Typically, the built 3D microstructure consists of a cube of sides 200 µm composed of 200 × 200 × 200 microcubes of side 1 µm. These microcubes (voxels) are the smallest and indivisible element of the microstructure and contain only one chemical phase of the cement.

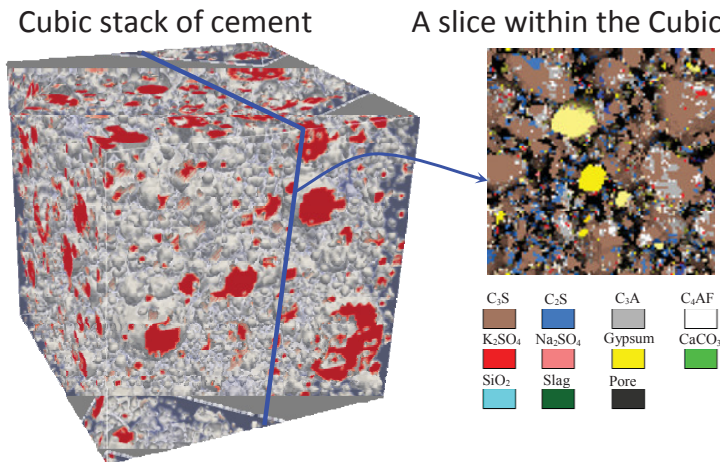


Figure 1.21. Schematic representation of the obtained anhydrous microstructure.
For a color version of the figure, see www.iste.co.uk/ait-mokhtar/coastal.zip

The input data of this model correspond to the real properties of the considered materials. Cement hydration is performed through several cycles of dissolution–precipitation–chemical reaction. The hydration products are formed in the space between the cement grains and around the latter in

² National Institute of Standard and Technology, USA.

dissolution. The output data are the porosity, the degree of hydration, the fractions of percolated porosity and solid, the heat released by the reaction, the fractions of hydration products, the chemical shrinkage and several other properties [BUL 14]. Figures 1.21 and 1.22 give a schematic view of the microstructure before and after hydration.

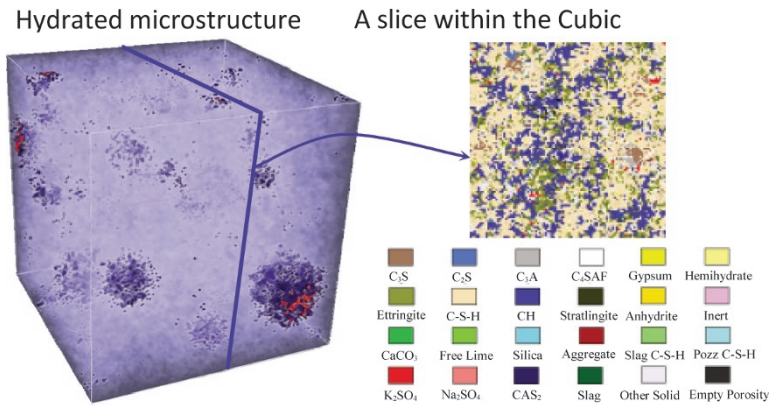


Figure 1.22. Schematic representation of the hydrated microstructure.
For a color version of the figure, see www.iste.co.uk/ait-mokhtar/coastal.zip

1.4. Some approaches for linking microstructure data to permeability

Transfer of aggressive agents is closely related to the permeability of the porous medium, since these transfers are made possible by water during its circulation in the medium. Predicting the permeability as a function of the microstructure data is then important. In the following, after a brief definition of the permeability, some models of permeability based on the investigation or modeling of microstructures of materials are presented.

The permeability of a porous medium represents its ability to be crossed by a fluid under a total pressure gradient. This permeability can be obtained by using Darcy's law for laminar flow of a Newtonian fluid. This law, given by equation [1.30], expresses the relationship between the flow velocity v and the total pressure gradient ∇P . This relationship also depends on the dynamic viscosity η and the permeability K :

$$v = -\frac{K}{\eta} \nabla P \quad [1.30]$$

The permeability K can only be assessed based on intrinsic parameters such as porosity ε_p and the critical pore diameter D_c as shown in Figure 1.23 [HAM 12]. The critical diameter D_c corresponds to the smallest section pore crossed by the fluid.

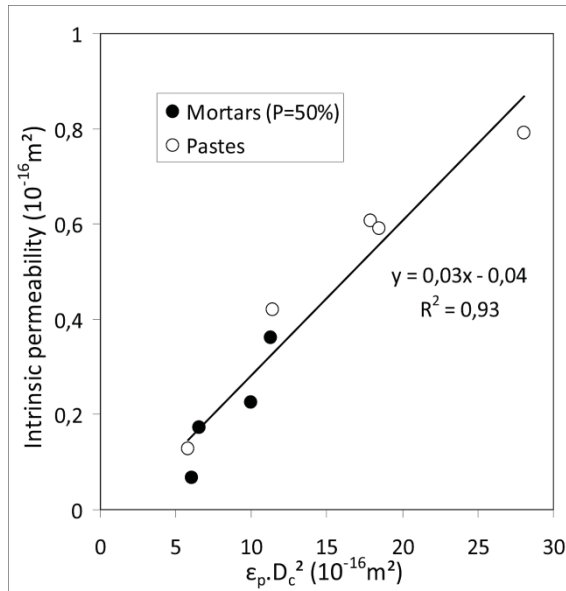


Figure 1.23. Correlation between the intrinsic gas permeability of cementitious materials (pastes and mortars made with various water to cement ratios) and the pore structure parameter $\varepsilon_p \cdot D_c^2$ [HAM 12]

1.4.1. Permeability from MIP tests

1.4.1.1. Case of cylindrical pores

The approach described above is based on the assumption that the pores are cylindrical, i.e. neither tortuosity nor constrictivity is considered. It means that construction materials are known to have microstructures with complex geometries, where parameters such as tortuosity, constrictivity or connectivity of the pores play a significant role in the transfer of aggressive agents, and then in the structures durability. In the following, an approach describing these parameters is presented.

In the case of a viscous and laminar flow, the permeability of a porous medium K is expressed according to Darcy and Hagen's law as follows:

$$K = \frac{\epsilon_p}{8} \frac{\sum_{i=1}^{\infty} V_{pi} R_{pi}^2}{\sum_{i=1}^{\infty} V_{pi}} \quad [1.31]$$

Many works have been conducted on the relationship between permeability and pore structure. Researchers such as Holly *et al.* [HOL 93] based their approach on other works [AIT 57, SHI 89] to build numerical relationship in order to link these two parameters. Other researchers [BRO 92, OLL 92, REI 92] have solved equation [1.31] with the assumption of equal pore radii, i.e. with neglecting the random variable R_p and the statistical distribution. Then an analytical relationship of permeability is suggested according to some microstructure parameters.

Taking into account equations [1.7] and [1.8], resolution of [1.31] leads to:

$$K = \frac{\epsilon_p}{8} R_{pm}^2 e^{6\xi^2} \quad [1.32]$$

If the microstructure is polymodal with a pore size distribution with N peaks, the expression of the permeability becomes:

$$K = \sum_{j=1}^N \frac{\epsilon_{pj}}{8} R_{pmj}^2 e^{6\xi_j^2} \quad [1.33]$$

1.4.1.2. Case of more complex geometrical shape of pores

Let us consider a laminar and unidirectional fluid flow, with dynamic viscosity μ , along the Ox axis in the porous medium of Figure 1.15 and dP_i be the pressure difference between the entry and the exit of each pore with section S_i . Given the Poiseuille law, the volumic flow rate dq_i of fluid in capillary with radius R_i and length l_i is:

$$dq_i = -\frac{\pi R_i^4}{8\mu} \frac{dP_i}{l_i} = -\frac{S_i^2}{l_i} \frac{dP_i}{8\mu\pi} \quad [1.34]$$

The flow conservation in successive pores with sections S_i and S_j leads to $dq_i = dq_j = dq$. The global volumic flow rate Q through the pore structure is:

$$Q = \frac{(n!+1)^2}{n} N^2 \sum_{i=1}^n dq_i = (n!+1)^2 N^2 dq \quad [1.35]$$

and the total pressure difference along the length l is $dP = \sum_{i=1}^n dP_i$. Given equations [1.34] and [1.35], we obtain:

$$dP = dP_n \sum_{i=1}^n \left(\frac{m_{in}^2}{q_{in}} \right) \quad [1.36]$$

We note that ΔP is the total pressure difference between the parallel sides of the cubic porous medium with distance L ($L = 1$ is the unit porous medium thickness) such that:

$$\Delta P = (n! + 1)NdP \text{ and } L = (n! + 1)lN \quad [1.37]$$

Given the average flow velocity $u = Q/S$ and according to Darcy's law $K = -\frac{\mu L}{\Delta P} u$, the combination of equations [1.21], [1.22], [1.24], [1.35] and [1.36] leads to the intrinsic permeability:

$$K = \frac{\delta \epsilon_p}{24 \tau^2} R_n^2 \quad [1.38]$$

where δ is the constrictivity factor such that:

$$\delta = \frac{\left(\sum_{i=1}^n \frac{1}{q_{in}} \right)^2}{\left(\sum_{i=1}^n \frac{1}{q_{in} m_{in}} \right) \left(\sum_{i=1}^n \frac{m_{in}^2}{q_{in}} \right)} \quad [1.39]$$

The permeability of a multimodal material represented by the serial/parallel pores assembly proposed by Khaddour *et al.* [KHA 13, KHA 09] (see section 1.3.2.1.2) is estimated by a combination of

Poiseuille's law (at the microscale) and Darcy's law (at the macroscale). At the microscale, the volume flow Q through the pore of a diameter d_i generated by a pressure gradient at the sample borders ($\Delta P = P_1 - P_2$) is decomposed into: (i) the flow Q_p through the pores in parallel (equation [1.40]) and (ii) the flow Q^a through the pores in series (equation [1.41]):

$$Q^p = \sum_{i=1}^N x_i Q_i^p = \frac{\pi}{256\mu} \frac{P_1^2 - P_2^2}{L_c P_2} \sum_{i=1}^N x_i d_i^4 \quad [1.40]$$

$$Q^a = \sum_{i=1}^N Q_i^a = \frac{\pi}{256\mu} \frac{P_1^2 - P_2^2}{P_2} \sum_{i=1}^N \frac{1}{\left(\sum_{k=i}^{j-1} \frac{Lr_k}{d_k^4} \right) + \frac{Lrr_j}{d_j^4}} \quad [1.41]$$

$$Q = Q^p + Q^a = \frac{\pi}{256\mu} \sum_{i=1}^N \left(\frac{x_i d_i^4}{L_c} + \frac{1}{\left(\sum_{k=i}^{j-1} \frac{Lr_k}{d_k^4} \right) + \frac{Lrr_j}{d_j^4}} \right) \quad [1.42]$$

Figure 1.24 gives a schematic representation of a serial assembly with the parameters needed for Q^a calculation.

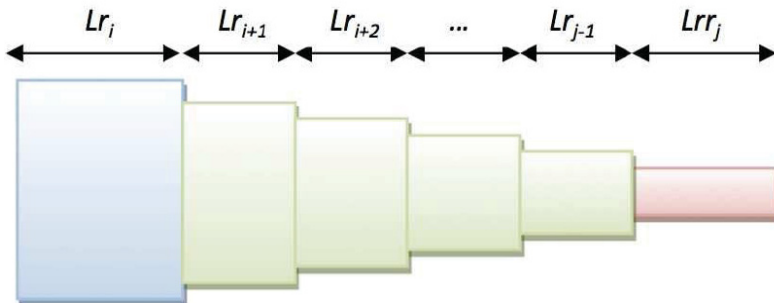


Figure 1.24. Serial pores assembly from diameter d_i to d_j [KHA 13]. For a color version of the figure, see www.iste.co.uk/ait-mokhtar/coastal.zip

The permeability is obtained at the macroscale by using the Darcy's law, without considering the sliding effect at the pore wall, following equation [1.43]:

$$K = \frac{\pi L_c}{128S\tau} \sum_{i=1}^N \left(\frac{x_i d_i^4}{L_c} + \frac{1}{\left(\sum_{k=i}^{j-1} \frac{Lr_k}{d_k^4} \right) + \frac{Lrr_j}{d_j^4}} \right) \quad [1.43]$$

1.4.2. Permeability from constructed microstructures

1.4.2.1. Permeability determination from network of capillaries

From 3D representations of the pore structure, obtained by imaging techniques (see section 1.2.4) or by modeling (see section 1.3.2), permeability can be calculated from a network of capillaries which is placed inside the porosity [PIG 05, BIS 09, YE 06]. From this simplification of the pore structure, it is relatively easy to calculate the permeability of the network using Hagen–Poiseuille law (as shown in the previous section). In order to illustrate this approach, let us consider the determination of the permeability made by Ye *et al.* for their simulated microstructure of cement paste as shown in Figure 1.25 [YE 06].

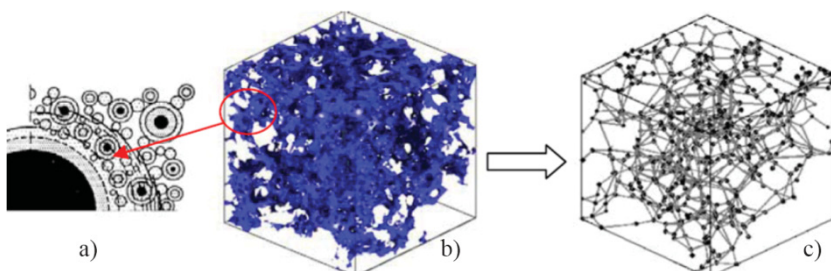


Figure 1.25. Porous network obtained microstructure from HYMOSTRUC model:
 a) at the scale of grains,
 b) real obtained microstructure and
 c) simulated microstructure by connected cylindrical tubes [YE 06].
 For a color version of the figure, see www.iste.co.uk/ait-mokhtar/coastal.zip

The hydraulic conductivity g_{ij} (equation [1.44]) is calculated for each capillary and placed between peaks i and j of the network:

$$g_{ij} = \frac{\pi R_{\min}^4}{64 \Delta d} \quad [1.44]$$

where Δd is the distance between peaks i and j , and R_{\min} is the minimum hydraulic radius of the branch, i.e. the minimum of R_i at peak i and R_j at peak j .

The flux q_{ij} in each capillary is then calculated according to Hagen–Poiseuille law following equation [1.45]:

$$q_{ij} = g_{ij} \frac{\Delta P_{ij}}{\eta} \quad [1.45]$$

where ΔP_{ij} is the pressure difference between peaks i and j , and η is the dynamic viscosity of the fluid crossing the microstructure.

The intrinsic permeability K of the obtained microstructure is directly calculated by Darcy's law following equation [1.46] [YE 06] by requiring a pressure difference ΔP across the pore network (Figure 1.26):

$$K = \frac{LQ}{A\Delta P} \eta \quad [1.46]$$

where Q is the average total flux at the outlet of the microstructure sample, A is the cross-sectional area of the sample and L is the length of the sample in the direction of the flow.

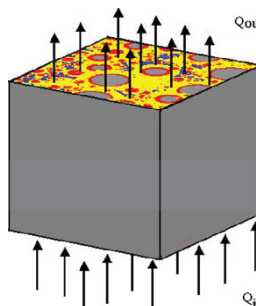


Figure 1.26. One-dimensional flow representation through the simulated microstructure [YE 06]. For a color version of the figure, see www.iste.co.uk/ait-mokhtar/coastal.zip

1.4.2.2. Permeability determination by Stokes equation resolution

Another approach consists of solving the equation modeling transfer by permeation, for instance the Stokes equation [1.47], directly in the constructed or measured 3D pore structure. This can be done by meshing the porosity, and using computation method such as FEM or the finite volume method.

For instance, this method was proposed by Bentz for the microstructure of cement paste computed by CEMHYD3D [BEN 07].

$$\begin{cases} \mu \nabla^2 v = \nabla p \\ \nabla \cdot v = 0 \\ v = 0 \quad \text{at solid/fluid interface} \end{cases} \quad [1.47]$$

The resolution of Stokes equations needs the pressure gradient as input data and gives an average outlet velocity of the fluid flow. The permeability is then calculated from this velocity according to Darcy's law, as done in [1.46].

1.5. Bibliography

- [AFN 10] AFNOR, Standard NF P18-459: Béton – Essais pour béton durci – Essai de porosité et de masse volumique, 2010.
- [AFP 97] AFPC-AFREM (Association Française de Recherches et Essais sur les Matériaux) (sous la direction de Ollivier J.P.), Durabilité des bétons: Méthodes recommandées pour la mesure des grandeurs associées à la durabilité, Comptes rendus des Journées Techniques, Toulouse, France, 11–12 December 1997.
- [AIT 57] AITCHISON J., BROWN J.A.C., *The Log-Normal Distribution*, Chapter 10, Cambridge University Press, 1957.
- [AÏT 99] AÏT-MOKHTAR A., AMIRI O., SAMMARTINO S., “Analytic modeling and experimental study of the porosity and the permeability of porous media, application to cement mortars and granitic rocks”, *Magazine of Concrete Research*, vol. 51, no. 6, pp. 391–396, 1999.
- [AÏT 02] AÏT-MOKHTAR A., AMIRI O., DUMARGUE P. *et al.*, “A new model to calculate water permeability of cement based materials from MIP results”, *Advances in Cement Research*, vol. 14, no. 2, pp. 43–49, 2002.

- [AÏT 04] AÏT-MOKHTAR A., AMIRI O., POUPARD O. *et al.*, “A new method for determination of chloride flux in cement-based materials from chronoamperometry”, *Cement and Concrete Composites*, vol. 26, pp. 339–345, 2004.
- [AMI 01a] AMIRI O., AÏT-MOKHTAR A., DUMARGUE P. *et al.*, “Electrochemical modeling of chlorides migration in cement-based materials, Part 1. Theoretical basis at microscopic scale”, *Electrochimica Acta*, vol. 46, pp. 1267–1275, 2001.
- [AMI 01b] AMIRI O., AÏT-MOKHTAR A., DUMARGUE P. *et al.*, “Electrochemical modeling of chlorides migration in cement-based materials, Part 2. Experimental study – calculation of chlorides flux”, *Electrochimica Acta*, vol. 46, pp. 3589–3597, 2001.
- [AMI 05] AMIRI O., AÏT-MOKHTAR A., SARHANI M., “Three-dimensional modeling of cementitious materials permeability from polymodal pore-size distribution obtained by MIP tests”, *Advances in Cement Research*, vol. 17, pp. 39–45, 2005.
- [ARL 07] ARIGUIE G., HORNAIN H., *GranDuBé: Grandeurs associées à la durabilité des bétons*, Presses de l’Ecole Nationale des Ponts et Chaussées, 2007.
- [BAR 51] BARRETT P., JOYNER G., HALEND P., “The determination of pore volume and area distributions in porous substances. Computations from nitrogen isotherms”, *American Chemical Society*, vol. 73, pp. 373–380, 1951.
- [BAR 98] BAROGHEL-BOUNY V., “Texture and moisture properties of ordinary and high-performance cementitious materials”, *Proceedings of the International Rilem Conference, Concrete from Material to Structure*, Arles, 1998.
- [BEN 97] BENTZD P., “Three-dimensional computer simulation of Portland cement hydration and microstructure development”, *Journal of the American Ceramic Society*, vol. 80, no. 1, pp. 3–21, 1997.
- [BEN 07] BENTZ D.P., MARTYS N.S., A Stokes permeability solver for three-dimensional porous media, NIST internal Report 7416, 2007.
- [BER 87] BERLAGE A.J.C., Strength development of hardening concrete, PhD Thesis, Delft University of Technology, Delft, The Netherlands, 1987.
- [BIS 09] BISHNOI S., SCRIVENER K.L., “μic: a new platform for modeling the hydration of cements”, *Cement and Concrete Research*, vol. 39, no. 4, pp. 266–274, 2009.
- [BRO 92] BROWN P.W., SHI D., SKALNY J.P., “Porosity – permeability relationships”, in SKALNY J. (ed.), *Materials Science of Concrete*, American Ceramic Society, pp. 83–109, 1992.

- [BRU 38] BRUNAUER S., EMMETT P.H., TELLE E., "Adsorption of gases in multimolecular layers", *American Chemical Society*, vol. 60, no. 2, pp. 309–319, 1938.
- [BUL 14] BULLARD J.W., *Virtual Cement and Concrete Testing Laboratory. Version 9.5 User Guide*, NIST Special Publication 1173, 2014.
- [CHO 06] CHOINSKA M., Effet de la température, du chargement mécanique et de leurs interactions sur la perméabilité du béton de structure, PhD Thesis, Central School of Nantes – University of Nantes, France, 2006.
- [COO 93] COOK R.A., HOVER K.C., "Mercury porosimetry of cement-based materials and associated correction factors", *ACI Materials Journal*, vol. 90, pp. 152–161, 1993.
- [DIA 87] DIAZ C.E., CHATZIS I., DULLIEN F.A.L., "Simulation of capillary pressure curves using Bond correlated site percolation on a cubic network", *Transport in Porous Media*, vol. 2, pp. 215–240, 1987.
- [DIA 00] DIAMOND S., "Mercury porosimetry: an inappropriate method for the measurement of pore size distribution in cementitious materials", *Cement and Concrete Research*, vol. 30, no. 10, pp. 1517–1525, 2000.
- [DUN 89] DUNSTER A.M., "An interpretation of the carbonation of the cement paste using trimethylsilation", *Advances in Cement Research*, vol. 2, pp. 99–106, 1989.
- [FAU 80] FAUDOT D., "Etude structurale d'un corps poreux", *Pétrole et techniques*, vol. 273, pp. 19–29, 1980.
- [FAU 12] FAURE P.F., CARE S., MAGAT J. *et al.*, "Drying effect on cement paste porosity at early age observed by NMR methods", *Construction and Building Materials*, vol. 29, pp. 496–503, 2012.
- [GAL 07] GALLUCCI E., SCRIVENER K.L., GROSO A. *et al.*, "3D experimental investigation of the microstructure of cement pastes using synchrotron X-ray microtomography (μ CT)", *Cement and Concrete Research*, vol. 37, no. 3, pp. 360–368, 2007.
- [HAL 95] HALAMICKOVA P., DETWILER R.J., BENTZ D.P., *et al.*, "Water permeability and chloride ion diffusion in Portland cement mortars: relationship to sand content and critical pore diameter", *Cement and Concrete Research*, vol. 25, pp. 790–802, 1995.
- [HAM 09] HAMAMI A.A., Vers une prédition de la perméabilité au gaz à partir de la composition des matériaux cimentaires, PhD Thesis, University of La Rochelle, 2009.

- [HAM 12] HAMAMI A.A., TURCRY P., AÏT-MOKHTAR A., “Influence of mix proportions on microstructure and gas permeability of cementpastes and mortars”, *Cement and Concrete Research*, vol. 42, no. 2, pp. 490–498, 2012.
- [HOL 93] HOLLY J., HAMPTON D., THOMAS A., “Modeling relationships between permeability and cement paste pore microstructures”, *Cement and Concrete Research*, vol. 23, pp. 1317–1330, 1993.
- [HOL 10] HOLZER L., MÜNCH B., RIZZI M. *et al.*, “3D-microstructure analysis of hydrated bentonite with cryo-stabilized pore water”, *Applied Clay Science*, vol. 47, nos. 3–4, pp. 330–342, 2010.
- [KEL 11] KELLER L.M., HOLZER L., WEPF R. *et al.*, “On the application of focused ion beam nanotomography in characterizing the 3D pore space geometry of Opalinus clay”, *Physics and Chemistry of the Earth*, vol. 36, no. 17–18, pp. 1539–1544, 2011.
- [KHA 09] KHADDOUR F., Amélioration de la production de gaz des Tight Gas Reservoirs , PhD Thesis, University of Pau and Pays de l'Adour, 2009.
- [KHA 13] KHADDOUR F., GREGOIRE D., PIJAUDIER-CABOT G., “Upscaling permeation properties in porous materials from pore size distributions”, in PIJAUDIER-CABOT G., PEREIRA J.-M. (eds), *Geomechanics in CO₂ Storage Facilities*, ISTE Ltd., London and John Wiley & Sons, pp. 43–56, 2013.
- [KHA 15] KHADDOUR F., GREGOIRE D., PIJAUDIER-CABOT G., “Capillary bundle model for the computation of the apparent permeability from pore size distributions”, *European Journal of Environmental and Civil Engineering*, vol. 19, no. 2, pp. 168–183, 2015.
- [KOR 07] KORB J.-P., “Microstructure and texture of cementitious porous materials”, *Magnetic Resonance Imaging*, vol. 25, no. 4, pp. 466–469, 2007.
- [KUR 06] KURUMISAWA K., TANAKA K., “Three-dimensional visualization of pore structure in hardened cement paste by the gallium intrusion technique”, *Cement and Concrete Research*, vol. 36, no. 2, pp. 330–336, 2006.
- [LAN 00] LANDIS E.N., NAGY E.N., “Three-dimensional work of fracture for mortar in compression”, *Engineering Fracture Mechanics*, vol. 65, no. 2, pp. 223–234, 2000.
- [LAN 10] LANDIS E.N., KEANEB D.T., “X-ray microtomography”, *Materials Characterization*, vol. 61, no. 12, pp. 1305–1316, 2010.
- [LEV 07] LEVITZ P., “Toolbox for 3D imaging and modeling of porous media: relationship with transport properties”, *Cement and Concrete Research*, vol. 37, no. 3, pp. 351–359, 2007.

- [LUR 11] LURA P., TRTIK P., MÜNCH B., “Validity of recent approaches for statistical nanoindentation of cement pastes”, *Cement and Concrete Composites*, vol. 33, no. 4, pp. 457–465, 2011.
- [MUN 09] MUNROE P.R., “The application of focused ion beam microscopy in the material sciences”, *Materials Characterization*, vol. 60, no. 1, pp. 2–13, 2009.
- [NAD 13] NADAH J., BIGNONNET F., DAVY C. *et al.*, “Microstructure and poromechanical performance of Haubourdin chalk”, *International Journal of Rock Mechanics and Mining Sciences*, vol. 58, pp. 149–165, 2013.
- [OLL 92] OLLIVIER J.P., MASSAT M., “Permeability and microstructure of concrete: a review of modeling”, *Cement and Concrete Research*, vol. 22, pp. 503–514, 1992.
- [PAT 12] PATURAL L., KORB J-P., GOVIN A. *et al.*, “Nuclear magnetic relaxation dispersion investigations of water retention mechanism by cellulose ethers in mortars”, *Cement and Concrete Research*, vol. 42, no. 10, pp. 1371–1378, 2012.
- [PIC 01] PICANDET V., Influence d'un endommagement mécanique sur la perméabilité et sur la diffusivité hydrique des bétons, PhD Thesis, University of Nantes, 2001.
- [PIG 05] PIGNAT C., NAVI P., SCRIVENER K., “Simulation of cement paste microstructure hydration, pore space characterization and permeability determination”, *Materials and Structures*, vol. 38, no. 4, pp. 459–466, 2005.
- [PLA 01] PLASSAIS A., POMIÈS M-P., LEQUEUX N. *et al.*, “Micropore size analysis in hydrated cement paste by NMR”, *Magnetic Resonance Imaging*, vol. 19, nos. 3–4, pp. 493–495, 2001.
- [PRO 09] PROMENTILLA M.A.B., SUGIYAMA T., HITOMI T. *et al.*, “Quantification of tortuosity in hardened cement pastes using synchrotron-based X-ray computed microtomography”, *Cement and Concrete Research*, vol. 39, no. 6, pp. 548–557, 2009.
- [REI 92] REINHARDT H.W., GABER K., “From pore size distribution to an equivalent pore size of cement mortar”, *Materials and Structures*, vol. 25, pp. 3–15, 1992.
- [ROU 09] ROUGELOT T., SKOYLAS F., BURLION N., “Water desorption and shrinkage in mortar and cement pastes: experimental study and poromechanical model”, *Cement and Concrete Research*, vol. 39, no. 1, pp. 36–44, 2009.
- [SCR 04] SCRIVENER K., “Backscattered electron imaging of cementitious microstructures: understanding and quantification”, *Cement and Concrete Composites*, vol. 26, no. 8, pp. 935–945, 2004.

- [SHI 89] SHI D., BROWN P.W., KURTZ S., *In Pore Structure and Permeability of Cementitious Materials*, Materials Research Society, Pittsburgh, pp. 23–34, 1989.
- [SIN 04] SING K.S.W., “Characterization of porous materials: past, present and future”, *Colloids and Surfaces A: Physicochemical and Engineering Aspects*, vol. 241, nos. 1–3, pp. 3–7, 14 July 2004.
- [TOR 99] TORRENTI J-M., DIDRY O., OLLIVIER J-P. et al., *La dégradation des bétons. Couplage fissuration – dégradation chimique*, Hermès, 1999.
- [VAN 81] VAN BRAKEL J., MODRY S., SVATA M., “Mercury porosimetry: the state of the art”, *Powder Technology*, vol. 29, pp. 1–12, 1981.
- [VAN 91] VAN BREUGEL K., Simulation of hydration and formation of structure in hardening cement-based materials, PhD Thesis, Delft University of Technology, Delft, The Netherlands, 1991.
- [VAN 95] VAN BREUGEL K., “Numerical simulation of hydration and microstructural development in hardening cement-based materials (I) theory”, *Cement and Concrete Research*, vol. 25, no. 2, pp. 319–331, 2009.
- [WAN 13] WANG B., FAURE P., THIÉRY M. et al., “¹H NMR relaxometry as an indicator of setting and water depletion during cement hydration”, *Cement and Concrete Research*, vol. 45, pp. 1–14, 2013.
- [WAR 81] WARDLAW N.C., MCKELLAR M., “Mercury porosimetry and the interpretation of pore geometry in sedimentary rocks and artificial models”, *Powder Technology*, vol. 29, pp. 127–143, 1981.
- [WIL 98] WILLIS K.L., ABELL A.B., LANGE D.A., “Image-based characterization of cement pore structure using wood’s metal intrusion”, *Cement and Concrete Research*, vol. 28, no. 12, pp. 1695–1705, 1998.
- [YE 06] YE G., LURA P., VAN BREUGEL K., “Modeling of water permeability in cementitious materials”, *Materials and Structures*, vol. 39, no. 9, pp. 877–885, 2006.
- [ZHA 12] ZHANG M., HE Y., YE G. et al. “Computational investigation on mass diffusivity in Portland cement paste based on X-ray computed microtomography (μ CT) image”, *Construction and Building Materials*, vol. 27, no. 1, pp. 472–481, 2012.

@Seismicisolation

Moisture Transfers in Porous Construction Materials: Mechanisms and Applications

This chapter provides an overview of the current state of knowledge of the physical phenomena involved in the coupled heat, air and moisture (HAM) transfer in porous building materials. The main parameters characterizing the porous medium are explained first. Then, the mechanisms involved in the hygrothermal transfers are addressed. Finally, a brief overview of the driving potential in porous media and their sensitivity on the transfer are discussed.

2.1. Introduction

Building envelopes are constantly exposed to multiple changes in indoor and outdoor climates. The variations in temperature, relative humidity (RH) and air pressure have a major impact on the physical state of the building elements. Indeed, their thermal comfort evaluation is strongly affected by the combined HAM transfer history within the materials. This means that the preliminary selection of materials used for the construction plays an important role in the success of a high environmental quality project.

In this context, the problem of predicting HAM behavior inside the porous building material is placed acutely, as the porous portions of the building structure may contain a very variable proportion of free water. These proportions of water are derived either from the effects of rain and

moisture in the air or from those initially used in the manufacture or the implementation of the materials used.

Additionally, these proportions of moisture are subjected to external solicitations such as moisture sources (occupants and vegetation), ventilation, etc.

Unfortunately, moisture accumulation within the material can lead to poor thermal performance of the envelope, degradation of organic materials, metal corrosion and structure deterioration.

In addition to the building's construction damage, moisture migrating through building envelopes can also lead to poor interior air quality as high ambient moisture levels result in microbial growth, which may seriously affect human health and be a cause of allergy and respiratory symptoms.

In fact, the occurrence of these transfer phenomena can be directly reflected on the overall energy performance of a building, which has significant effect on the air-conditioning loads, especially the latent cooling load. To ensure optimal conditions in the indoor space, international research projects and researchers of the civil engineering community focused on a better comprehension and prediction of the hygrothermal behavior of these envelope components.

It is, therefore, important to predict and explain HAM transfer in porous building materials not only for the characterization of behavior in connection with durability, waterproofing and thermal performance, but also for building energy efficiency and avoiding health risk due to the growth of microorganisms.

2.2. Quantitative characteristics describing moisture in porous media

Mass transfer phenomena in porous media are closely related to its water content that involves complex interactions of different heat and moisture transport mechanisms. Before looking at these phenomena, it is important to understand the environment in which they occur. Porous media may be regarded as macroscopically heterogeneous and anisotropic. These properties give this environment all its complexity.

The porous material is presented as a medium consisting of three distinct phases: solid, liquid and gas. The solid phase or the matrix of material consists of a porous network called “capillary pores”. The liquid phase itself is composed of water contained in the pore space. Finally, the gas phase, also contained in the pore space, is composed of water vapor and dry air.

A porous medium may be described in many ways. We can look at its metrics and physical aspects; thus, several quantities can be extracted to characterize it. Table 2.1 summarizes the main quantities describing the state of a porous medium.

Quantity	Expression	Notes
Porosity	$\varepsilon_0 = V_p/V_0$	
Specific surface	$s = S/V_0$	$V: Volume$ $S: Surface$
Density	$\rho_s = m_s/V_0$	$m: mass$
Water content	$u = m_l/V_0$	$p_v: vapor pressure$ $p_{v,sat}: Saturated vapor pressure$
Mass water content	$\omega = m_l/V_s$	<u>Index:</u> $p: pores$
Volumetric water content	$\theta_l = V_l/V_0$	$0: apparent$ $s: solid$
Water vapor content	$u_v = m_v/V_a$	$m: moisture$ $l: liquid$
Relative humidity	$RH = p_v/p_{v,sat}$	

Table 2.1. Quantities describing the state of a porous medium

2.3. Phenomenon of transfer and moisture storage

2.3.1. Moisture diffusion

In isothermal conditions, theory on vapor transport in porous building materials is originally based on Fick's diffusion. It is a microscopic scale transfer mode that reflects the erratic movement of the elements on a smaller scale than the scale of particles driven by the difference in water vapor concentration across the material. This phenomenon is commonly dominated in pores with a radius larger than 10^{-6} m [GER 91], where the water vapor

transport is governed by the collision between particles or molecules without interaction with the material matrix. For this type of diffusion, there is no interaction with the solid matrix. In free air, the diffusion coefficient proposed by DeVeries [DEV 66] follows equation [2.1].

$$D_v = c \left(\frac{P_0}{P} \right) \left(\frac{T}{T_0} \right)^n \quad [2.1]$$

where the reference pressure $P_0 = 1.01325 \cdot 10^{-5} [\text{Pa}]$, the reference temperature is $T_0 = 273.15 [\text{K}]$, $c = 2.17 \cdot 10^{-5} [\text{m}^2/\text{s}]$ and $n = 1.88$.

In other types of diffusion, such as Knüden diffusion, there is an interaction with the solid matrix. In a capillary, if the diameter is much less than the mean free path, then there are no more collisions between particles but particle-wall collisions. The parameter which defines the conditions for this mode of motion is the Knüden number Kn . It is the ratio between the mean free path λ and the diameter of the capillary d according to equation [2.2].

$$Kn = \frac{\lambda}{d} \quad [2.2]$$

For a cylindrical capillary of radius r [cm], the Knüden diffusion coefficient D_k [m^2/s] [DEL 69] is given by equation [2.3].

$$D_k = 9.7 \cdot 10^3 \cdot r \cdot \sqrt{T/M} \quad [2.3]$$

where T [K] is the absolute temperature and M is the molar mass of water.

Another important diffusional phenomenon, named surface diffusion, is worth mentioning. It is the movement of the adsorbed phase. This movement takes place if a certain activation energy that allows the jump of the adsorbed molecules is provided [DUO 98]. In this case, the water vapor flux density can be expressed according to the concentration of the phase adsorbed C_μ (see equation [2.4]).

$$\vec{J}_{vs} = -D_s \nabla C_\mu \quad [2.4]$$

where $D_s [\text{m}^2/\text{s}]$ is the diffusion coefficient at the surface.

Equation [2.4] can be expressed in terms of vapor content of the gas phase by assuming the existence of a local equilibrium between the adsorbed and the free phases. This hypothesis is acceptable as adsorption rate is much more important than the kinetics of diffusion in two phases.

Figure 2.1 gives a schematic view of the three types of diffusion:

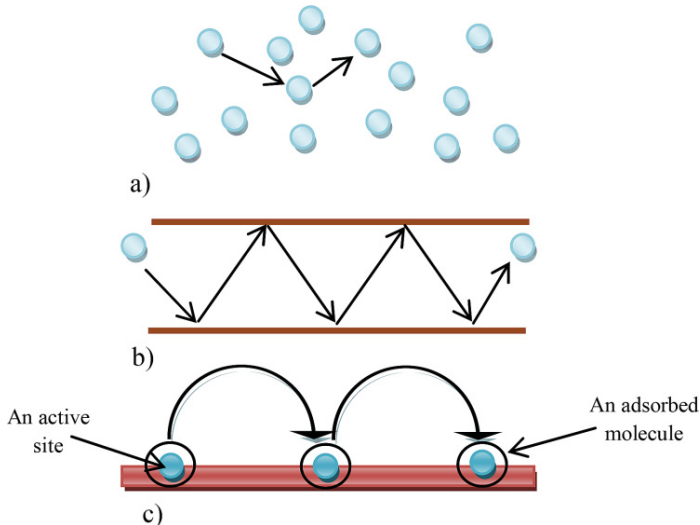


Figure 2.1. Illustration of a) diffusion in a continuum, b) Knudsen diffusion and c) surface diffusion. For a color version of the figure, see www.iste.co.uk/ait-mokhtar/coastal.zip

However, in non-isothermal conditions, another type of moisture transfer mechanism can be presented in the porous structure; it concerns the thermal diffusion. It is based on the density difference between dry air and vapor molecules, which makes the water vapor move from cold to warm, and results in transport against the temperature gradient. In building physics, the transport of water vapor occurs primarily by molecular diffusion [HEN 06].

2.3.2. Capillarity

When wetting a porous material, at water content u [kg/m^3] greater than the maximum water content u_c [kg/m^3], liquid menisci can be formed between pores space. These phenomena result from the particular water

properties of wettability on the solids constituting the porous matrix. This leads to the creation of interfaces curves between the wetting fluid (water) and the non-wetting fluid (humid air). Analysis of the equilibrium conditions of such an interface shows the existence of a positive pressure difference between the moist air and the water, called capillary pressure P_c :

$$P_c = P_a - P_l \quad [2.5]$$

where:

- p_a : [Pa] is the air pressure;

- p_l : [Pa] is the liquid pressure.

The capillary pressure difference is given by Laplace's law. This property can be experimentally quantified. It is function of the surface tension of the air–water interfaces $\sigma(T)$, of the interface principal radii of curvatures $R_1[m]$ and $R_2[m]$ and function of the contact angle θ defined by the slope of the liquid phase at the fluid–solid contact point:

$$P_c = \sigma \cdot \cos \theta \cdot \left(\frac{1}{R_1} + \frac{1}{R_2} \right) \quad [2.6]$$

For a capillary of circular cross-section of radius r , the previous expression becomes:

$$P_c = \frac{\sigma \cdot \cos \theta}{r} \quad [2.7]$$

σ [kg/m] is the water vapor surface tension.

The capillary pressure can be expressed in water level; it is called suction ψ [m]:

$$\psi = -\frac{P_c}{\rho_l g} = \psi(T, u) \quad [2.8]$$

- ρ_l [kg/m³] is the water density;

- g [m/s²] is the gravity acceleration.

The suction varies depending on the water content u [kg/m³]. It is canceled for water content equal to the water content at saturation u_{\max} in which all the pores are filled, and increases significantly near the hygroscopic domain. However, it should be noted that there are hysteresis phenomena where the drainage equilibrium profile is different from the wetting equilibrium profile.

The total suction in the hygroscopic domain is often expressed by the suction pressure obtained by Kelvin's law whose expression is as follows:

$$P_c = \frac{RT\rho_l}{M} \ln(\varphi) \quad [2.9]$$

The relationship between the ambient humidity and the corresponding suction is defined by one of the fundamental relationships of thermodynamics, i.e. Kelvin's law whose expression is as follows:

$$\psi = -\frac{RT}{gM} \ln(\varphi) \quad [2.10]$$

- R [J/mol.K] is the molar gas constant ($R = 8.31443$ J/mol.K);
- g [m/s²] is the acceleration due to gravity ($g = 9.81$ m/s²);
- ρ_l [kg/m³] is the water density;
- M [kg/mol] is the water molar mass;
- φ [%] is the relative humidity;
- T [K] is the thermodynamic temperature.

This expression revealed a correspondence between ψ and φ . This will determine the suction in the hygroscopic range for humidity less than 95%.

However, there is a part of interstitial water (free water) which can move between the solid particles due to the pressure differences caused by various actions (gravity, dessication or transforming water into ice assimilated to the drying process).

2.3.3. Infiltration

The existence of sources, such as ventilation, wind and air density variation, creates low total pressure gradients between wall's facades. The presence of these pressure gradients inside the material creates a new driving potential of molar moisture transfer given by Darcy's law that can be added to the mass diffusion process.

In the literature, only few existing heat and moisture transfer models include this total pressure (air flow) effect as coupled components. They are usually expressed by the combination of phenomenological laws of Darcy and Fick [FUN 07].

In fact, migration of water molecules caused by total pressure gradient (called infiltration) applied on building facades may create a large increase in moisture relatively to that induced by vapor diffusion phenomena. This effect contrary to vapor diffusion has been underestimated for a long time [PHI 57]. It can be explained by the high level of vapor pressure difference through an outside wall, which is approximately 1,500 Pa, compared to those of total pressure gradient that do not exceed 200 Pa. In reality, the mass flow caused by the low total pressure difference is often the efficient driving potential of water vapor transfer through building components [PAD 98].

As flows are relatively at low velocity, steady state can be assumed and pressure gradient is proportional to the flow velocity inside the pores. This proportional relationship is preserved if we make the average of flow and total pressure gradients on a large volume compared to the pore size.

For a sample of section S of length L , the volume flow Q_v verifies the following relationship of Darcy:
$$\frac{Q_v}{S} = \frac{K}{\mu} \frac{\Delta P}{L}$$

The ratio of the total volume flow rate per unit surface of the material Q_v/S represents the filtration of the fluid, corresponding to the average of fluid velocity taken by a representative volume element.

Here, μ [Pa.s] represents the dynamic viscosity of the fluid (water in our case) and the constant of proportionality K [kg/m.s.Pa] represents the permeability (infiltration in our case). It is homogeneous to a surface and

depends only on the geometry and the porosity of the solid matrix. The obtained permeability at a given pressure gradient depends on this gradient and the water status of the material (it is an apparent permeability).

2.3.4. Physical and chemical adsorption

The adsorption of a gas by a solid is a phenomenon that occurs when the molecular concentration of a gas in contact with a solid is larger in the surface area than it is in the gas phase [MIC 90]. We can distinguish two types of adsorption: physical and chemical.

Physical adsorption consists of the condensation of molecules on the surface of the solid material. Adsorbed molecules are weakly linked to the solid by intermolecular forces of attraction (mainly Van Der Waal's forces) [CAR 04]. The energy involved is less than 20 kJ/mol. Adsorption is multimolecular and multilayers without privileged site for adsorption. It is a reversible phenomenon since the adsorption is little influenced by the nature of the surface.

Chemical adsorption is due to ionic or covalent chemical bonds between gas and solid surfaces. This implies a change in its structure or reactivity. The energies involved are more important. They vary from 80 to 400 kJ/mol. Chemical adsorption can be monolayer. It is an irreversible phenomenon that is specific because it depends on the nature of the chemical bonds that the atoms in contact may contract.

2.4. Moisture transfer modeling: macroscopic approach

Coupled heat and moisture transfers in porous media are explored in many scientific areas such as wood drying [YOU 06], hygroscopic textile materials [FEN 04], food [FUR 07] and building envelopes [BEL 08], among others. Therefore, these porous media are in the most cases exposed to external excitations (solar radiation, rain, etc.), which must be taken into consideration. In building material, the pressurization by ventilation, buoyancy and the wind on height building create generally differential pressure variation which ranges between 5 and 10 Pa in houses and between 50 and 150 Pa in tall buildings. This pressure can modify considerably the

kinetics and the properties of transfers within the material [GRU 06]. It becomes a significant driving force above the boiling point of water as in the case for some drying problems [DEG 87].

The most available works did not consider the pressure gradient parameter: [CRA 96, YOU 06, QIN 09]. Their effect appears in other formulation such as the velocity which is considered as a boundary condition. However, few works that took pressure gradient into account are found in the literature; the authors of [LEW 93] confirmed the possibility of incorporating the pressure term introduced in [LUI 66]. They assumed that during an excessive period of drying, a total pressure gradient appears within the material. This pressure gradient generates an additional transfer of heat and moisture resulting from the filtration motion of the liquid and vapor within the porous material [LEW 90]. In terms of modeling, Lewis and W. Ferguson studied a one-dimensional cross-section through a container wall with air inside subjected to 2 atm. They presented their numerical investigation by clarifying the sensitivity between the fully nonlinear formulation (where all material properties are allowed to vary) and the partially nonlinear formulation (where some material properties are held constant). The authors of [SAN 09] have elaborated a mathematical model to describe the transfer through hollow porous blocks and demonstrated the necessity of taking into account the gas phase at the internal brick boundary. They used the multi-tridiagonal matrix algorithm (MTDMA) to solve their algebraic equations for the three driving potentials which describe the transfer in the porous material. They conducted their analysis in terms of water vapor flow and heat flux applied on three types of bricks: hollow, massive and insulating.

On the other hand, the effect of atmospheric pressure on the heat and moisture transfers in hygroscopic textile was investigated by the authors of [FEN 04]. By comparing two cases (1 and 2 atm) of the same treated model, these authors confirmed that the pressure gradient has a significant effect on the transfer. In addition, other modeling works concerning wood derived from either classical approach [YOU 06, DIE 06] are discussed. In the literature, the evaluation of pressure incidence on the hygrothermal behavior of the porous building material was not considered. For this purpose, a coupled HAM model based on three driving potentials, temperature, moisture and total pressure, is developed.

2.4.1. Driving potentials

The question of the appropriate driving potentials in the coupled heat and moisture transfer problems remains a point of discussion for several researchers in the civil engineering community. All equations of moisture transfer using the main driving potential (e.g. moisture content, vapor pressure and chemical potential) and an independent secondary potential (e.g. temperature and liquid pressure) are equivalent [FUN 07]. However, in terms of experiment, this multiple choice is not always so obvious as the case of the RH that is not considered as a thermodynamic state variable. In particular, it is not continuous at the boundary between two different material layers, and has a random spatial distribution in a heterogeneous medium. The suitable driving potential in walls agreed by experts of construction field is the vapor pressure difference, which is generally caused by wind, pressurization by ventilation or by buoyancy and the stack effects.

In reality, the vapor pressure driving potential dominates partially the whole of moisture transfer within porous components. In addition to the driving potential, the suction pressure related to the liquid transfer was taken into consideration by the authors of [PED, 90]. Furthermore, the authors of [PAD 98] declared that there is evidence that it is the RH difference that drives diffusion through the material. Specifically, water vapor and the RH flux have often opposite gradients which cause opposite flows of water. In this context, the author of [PEU 03] confirmed that the capillary pressure, similarly for temperature gradient, contributes to the moisture transfer. She indicated that the orientation of this different driving potential applied on the specimen has an important role in the moisture behavior inside the material: the RH potential operates as the lowest driving potential when temperature and vapor pressure gradient are in parallel position. This remark is not valid for all hygroscopic insulations such as cellulose insulation. Also, the author of [BEL 08] quantified the thermodiffusion phenomenon in building materials through a new experimental parameter called thermogravitational coefficient. It has been shown that it is sensitive in the case of low vapor content gradients. Unfortunately, the [JAN 11] study contradicts this experimental finding that the temperature gradients contribute to the moisture transfer. Hence, in order to check this, it seems necessary to resort to other fields outside the civil engineering, where porous media are exposed to temperature gradients. Regarding the published data on porous media [DAV 10, MOJ 08], the temperature effect on the moisture transfer in these

porous structures is well presented and has a significant role as shown in Figure 2.2.

In this regard, several points concerning the reality of moisture transfer (vapor + liquid phase) in porous material are questioned and they need to be examined in more detail. Transfers of mass of all phases and the transfer of heat must be considered simultaneously and not separately.

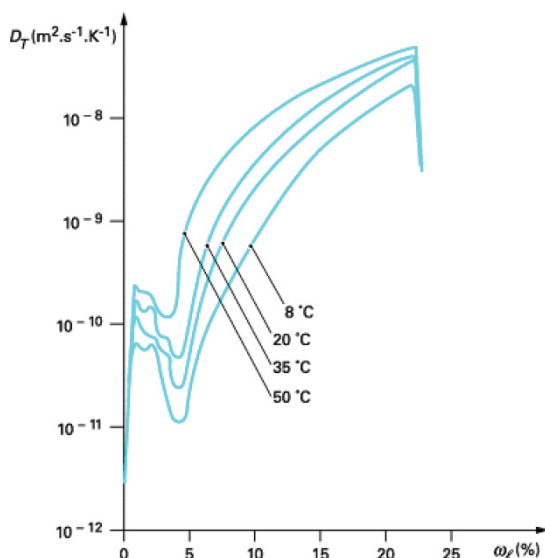


Figure 2.2. Non-isothermal moisture diffusion coefficient function of the water content of porous media at four different temperatures, in the case of sand [MOJ 08]

2.4.2. Conservation equations

Building materials can be considered as open porous media containing variable proportion of water and a mixture of vapor and air. These proportions move due to the capillary forces – generally for liquid transfer – vapor diffusion, vapor convection and liquid infiltration. The developing model should describe HAM transfer inside hygroscopic materials. Therefore, the choice was made to take into account the interaction between all phases and their contribution to the transfer.

First, the balance and energy equations are written for all considered phases. Then, the equations are defined according to the driving forces of transfer. Then, the phenomenological description consists of writing the equations according to the driving forces of transfer described by the total pressure, the temperature and the humidity:

- the temperature of all considered phases is being equal at any point of unsaturated porous continuum;
- only masses of liquid and vapor are considered;
- the solid medium is homogeneous with no chemical reaction between the material and moisture;
- the gas phase respects the ideal gas law;
- the heat transfer by radiation is negligible.

The four balance equations, moisture mass balance divided into liquid (equation [2.11]) and vapor (equation [2.12]), the dry air mass balance (equation [2.13]) and the energy balance (equation [2.14]), can be written locally as following:

$$\frac{\partial u_l}{\partial t} = -\operatorname{div}(j_l) + \dot{m} \quad [2.11]$$

$$\frac{\partial u_v}{\partial t} = -\operatorname{div}(j_v) - \dot{m} \quad [2.12]$$

$$\frac{\partial u_a}{\partial t} = -\operatorname{div}(j_a) \quad [2.13]$$

$$c\rho_s \frac{\partial T}{\partial t} = -\operatorname{div}(j_q) - h_v \dot{m} \quad [2.14]$$

where:

– u [kg/m^3] is the moisture content of the considered phase (liquid, vapor and air);

– j_l [$\text{kg/m}^2 \text{ s}$] is the density of liquid flow rate;

- j_v [kg/m² s] is the density of vapor flow rate;
- j_a [kg/m² s] is the density of dry air flow rate;
- j_q [W/m²] is the heat flow;
- \dot{m} [kg/m³ s] is the rate of phase change;
- c [J/kg] is the heat capacity;
- ρ_s [kg/m³] is the dry density;
- T [K] is the absolute temperature.

Heat transfer has been attributed to three forms [CRA 96]: conductive transfer calculated by the Fourier's law, convective transport of sensible heat by the liquid and vapor flows and transfer of latent heat carried by the vapor. Thus, the density of heat transport can be written as:

$$j_q = -\lambda \nabla T + h_l j_l + h_v j_v \quad [2.15]$$

where:

- λ [w/m K] is the thermal conductivity;
- h_l [J/kg] is the liquid specific enthalpy;
- h_v [J/kg] is the vapor specific enthalpy.

2.4.3. Moisture transfer

2.4.3.1. Vapor transfer

In the hygroscopic zone, liquid–vapor interface is assumed in thermodynamic equilibrium. The vapor moves inside the porous material by diffusion as expressed by the first term of equation [2.16]. Furthermore, the second term represents the effect of the vapor filtration due to the total gas pressure gradient:

$$j_v = -D_v \nabla \rho_v - k_{fv} \nabla P \quad [2.16]$$

where the vapor density is a function of moisture content and temperature. It can be written as:

$$\nabla \rho_v = \left(\frac{\partial \rho_v}{\partial \omega} \right)_T \nabla \omega + \left(\frac{\partial \rho_v}{\partial T} \right)_\omega \nabla T$$

This explains the first term indicated by equation [2.17]:

$$j_v = -D_v \rho_s [\nabla \omega + \delta_v \nabla T] - k_{fv} \nabla p \quad [2.17]$$

The vapor thermogradient coefficient is $\delta_v = \left(\frac{\partial \rho_v}{\partial T} \right)_\omega / \left(\frac{\partial \rho_v}{\partial \omega} \right)_T$. The vapor filtration coefficient k_{fv} is the result of two components: capillary surface area and capillary hydraulic conductance. The vapor diffusion coefficient is given by $D_v = D'_v \frac{\partial \rho_v}{\rho_s \partial \omega}$.

Here :

$-\delta_v [kg_{moisture} / kg.K]$ is the thermal gradient coefficient;

$-k_{fv} [Kg/m s Pa]$ is the vapor infiltration coefficient;

$-D_v [m^2/s]$ is the vapor diffusion coefficient.

2.4.3.2. Liquid transfer

Non-isothermal liquid flow in unsaturated porous materials is induced by the gradient of capillary potential where migration of moisture under the effect of the gravity is neglected. Using the mathematical formulation of the capillary suction pressure which is a function of moisture content and temperature, the density of liquid flow can be written as:

$$j_l = -D_l \rho_s [\nabla \omega + \delta_l \nabla T] \quad [2.18]$$

The expansion of air bubbles by forcing the liquid toward the direction of heat flow creates an additional movement of liquid filtration under the total gas pressure gradient which can be added to equation [2.18] as follows:

$$j_l = -D_l \rho_s [\nabla \omega + \delta_l \nabla T] - k_f \nabla P \quad [2.19]$$

By adding equations [2.17] and [2.18] and by injecting the total moisture flow $j_m = j_l + j_v$ which is the sum of the calculated liquid and vapor flows, the following mass balance equation is obtained:

$$\frac{\partial \omega}{\partial T} = \operatorname{div}[D_m (\nabla \omega + \delta \nabla T + \alpha \nabla P)] \quad [2.20]$$

with $D_m = D_v + D_l$, $\delta = \frac{D_v \delta_v + D_l \delta_l}{D_v + D_l}$, $k_f = k_{fl} + k_{fv}$ and $\alpha = \frac{k_f}{D_m \rho}$.

$-k_f$ [Kg/m s Pa] is the liquid infiltration coefficient;

$-D_v$ [m²/s] is the vapor diffusion coefficient;

$-D_l$ [m²/s] is the vapor diffusion coefficient.

2.4.3.3. Gas transfer (dry air and vapor)

The presence of a gradient of the total pressure ∇P within the hygroscopic material causes transfer of vapor and dry air according to the type of filtration. This transfer of water vapor is described by the author of [LUI 66] as follows:

$$j_a + j_v = -\lambda_f \nabla P \quad [2.21]$$

Equation [2.21] is injected into the total pressure balance equation, which is summarized by the addition of differential equation [2.12] and equation [2.13] as follows:

$$\frac{\partial(u_a + u_v)}{\partial t} = \frac{\partial(\omega_g)}{\partial t} = -\operatorname{div}(j_a + j_v) - \dot{m} \quad [2.22]$$

where $\omega_g = \omega_a + \omega_v = \varepsilon \frac{\rho_g}{\rho_s} (1 - s_l)$ and $\varepsilon \cdot s_l = \frac{\rho_s}{\rho_l} \omega_l$.

Hence, the differential equation [2.22] assumes the form:

$$\frac{\partial(\varepsilon\rho_g(1-s_l))}{\partial t} = \operatorname{div}(\lambda_f \nabla P) - \dot{m} \quad [2.23]$$

Therefore, the dry air transport can be described as a function of pressure, temperature and liquid water saturation:

$$\varepsilon\rho_g(1-s_l) = \frac{PM}{RT} \varepsilon(1-s_l) \quad [2.24]$$

In order to close this system, after differentiating of equation [2.24] where the contribution of dT and dS_l factors is neglected (assuming that $T^2 \gg \frac{M}{RT} \varepsilon(1-s_l)$ and $T > s_l$), the equation of the phase gas is determined:

$$h_a \frac{\partial P}{\partial t} = \operatorname{div}(\lambda_f \nabla P) - \dot{m} \quad [2.25]$$

where $((1-S_l)M\varepsilon)/RT$ is denoted by h_a ;

$-s_l[-]$ is the liquid water saturation;

$-\varepsilon[-]$ is the material porosity;

$-\lambda_f [\text{kg/m s Pa}]$ is the moist air permeability coefficient.

2.4.4. Heat transfer

Based on the previous steps and by replacing the heat flow formulation, the liquid and vapor flows in the energy balance equation, we obtain:

$$c\rho_s \frac{\partial T}{\partial t} = \operatorname{div}(a_t \nabla T + \delta_t \nabla u + \alpha_t \nabla P) - h_v \dot{m} \quad [2.26]$$

where $a_t = (\lambda + D_l \rho_s \delta_l h_l + D_v \rho_s \delta_v h_v)$, $\delta_t = \rho_s (D_l h_l + D_v h_v)$, $\alpha_t = (h_l k_{fl} + h_v k_{fv})$

The phase change rate can be developed as follows:

$$\dot{m} = -\rho_s \chi \frac{\partial \omega}{\partial t} \quad [2.27]$$

with, $\chi = \frac{D'_v}{D_m \rho_s} \frac{\partial \rho_v}{\partial \omega} = \frac{D'_v}{\delta D_m \rho_s} \frac{\partial \rho_v}{\partial T} = \frac{k_{fv}}{k_f}$

Based on the above assumptions, the following mathematical equations for the coupled HAM transfer in porous building materials can be established:

$$\begin{aligned} \frac{\partial \omega}{\partial T} &= \operatorname{div}[D_m (\nabla \omega + \delta \nabla T + \alpha \nabla P)] \\ c \rho_s \frac{\partial T}{\partial t} &= \operatorname{div}(a_t \nabla T + \delta_t \nabla u + \alpha_t \nabla P) + h_v \rho_s \chi \frac{\partial \omega}{\partial t} \quad [2.28] \\ h_a \frac{\partial P}{\partial t} &= \operatorname{div}(\lambda_f \nabla P) + \rho_s \chi \frac{\partial \omega}{\partial t} \end{aligned}$$

where ω [kg/kg] is the moisture content and is related to u [kg/m³] through the material density $u = \omega \cdot \rho$.

2.4.5. Case study

In the application of the theoretical study, a numerical investigation is considered for the developed coupled heat and moisture model. It is undertaken using COMSOL Multiphysics code [FEM 07].

To assess the hygrothermal behavior, this solution is compared with the analytical model applied on wood drying presented by the author of [CHA 00]. They used similar driving potentials without the total pressure gradient. As a consequence, the pressure sensitivity will be evaluated. These authors employed the concept of moisture potential introduced on the basis of thermodynamic similarity between the heat and moisture transfer. It is a

linear function of the moisture content ω ; it is expressed as $\omega = C_m \cdot m$. The dimension of specific mass capacity is $\text{kg} \cdot \text{kg}^{-1} \cdot {}^{\circ}\text{M}$, where ${}^{\circ}\text{M}$ denotes a mass transfer degree. In this way, the moisture potential parameter is introduced in equation [2.28] for one-dimensional case. The application concerns a wood slab of a thickness l subjected to symmetrical boundary conditions of Fourier type as shown in Figure 2.3. Initial conditions of $T_b = 10^{\circ}\text{C}$, $m_b = 86^{\circ}\text{M}$ and $P_b = 101325 \text{ Pa}$ have been used for all simulations.

2.4.5.1. Boundary conditions

The boundary conditions are the same as those reported by the authors of [CHA 00] and [LIU 91]. The condensation of vapor on the border of the specimen is produced by convective transfer. It takes place through a convective mass transfer coefficient β , modeled by a law of this type:

$$D_m (\nabla m + \delta \nabla T + \alpha \nabla P) = \beta(m_\infty - m) \quad [2.29]$$

At the same time, the heat transfer at the boundary is convective. The law describing the thermal convective exchanges is similar to the previous law. A convective heat transfer coefficient σ is introduced:

$$D_m (\nabla m + \delta \nabla T + \alpha \nabla P) = \beta(m_\infty - m) \quad [2.30]$$

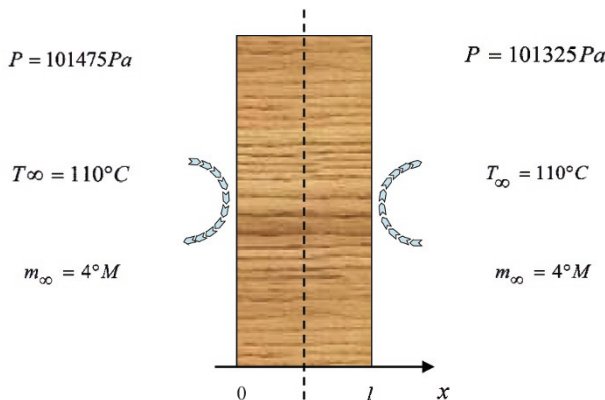


Figure 2.3. Schematic representation of the porous slab and the external boundary conditions

The other hygrothermal properties are removed from the reference [TRE 01] and are used to calculate the values of a_t , δ_t , α_t and α (see Table 2.2). In reality, the hygrothermal properties of building materials depend on the moisture content and the temperature [QIN 08, BEL 08].

Parameter	Value	Parameter	Value
$D_m = (d_m / \rho_s C_m)(m^2 / s)$	5.94×10^{-9}	$\lambda_f (kg / m.s.Pa)$	8×10^{-10}
$\sigma(W / m^2 k)$	22.5	$a_t (W / m.k)$	7.02×10^{-7}
$d_m (kg / m.s.^{\circ}M)$	2.2×10^{-8}	$h_a (m.s^2 / kg)$	1.77×10^{-8}
$\alpha_t (J / m.s.Pa)$	7.96×10^{-12}	$\alpha (m.s^2 / kg)$	36.2×10^{-15}

Table 2.2. Input parameters of the studied case

2.4.5.2. Results and discussions

To realize the study of the atmospheric pressure sensitivity on the porous material, a pressure gradient of 150 Pa is imposed on the vertical faces during all the numerical simulations.

In the first part, moisture content and temperature profiles resulting from our numerical simulations are directly compared to the analytical results given by Chang *et al.* [CHA 00] Figure 2.4 shows the one-dimensional moisture content variation with time at the center of the slab ($l = 24$ mm) for both models. It shows a similar reproducibility of the Chang and Weng's approach. The effect of pressure filtration appears only after 40 min to reach the center of the material. It is estimated to be approximately 0.1 kg/kg. This difference is explained by the fact that ∇P impedes the motion of moisture and heat. Moreover, the evolution of moisture and air phase's distributions within the porous medium depends on the competition between capillary forces and viscosity.

Figure 2.5 shows the temperature profiles versus time where the difference appears quickly. This variation is explained by the fact that the mass diffusion is slow than the heat diffusion. It is noteworthy that the temperature in the case of the presence of pressure gradient is lower than that obtained by Chang and Weng.

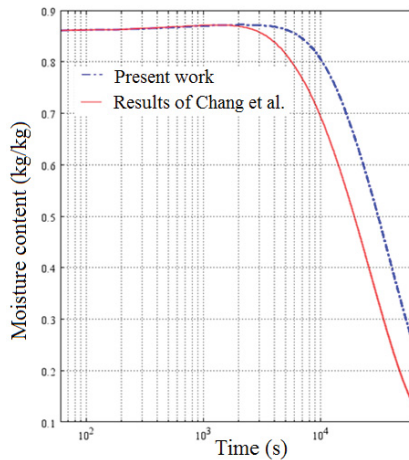


Figure 2.4. Moisture content at the center of wood specimen ($x=0.012\text{ m}$)

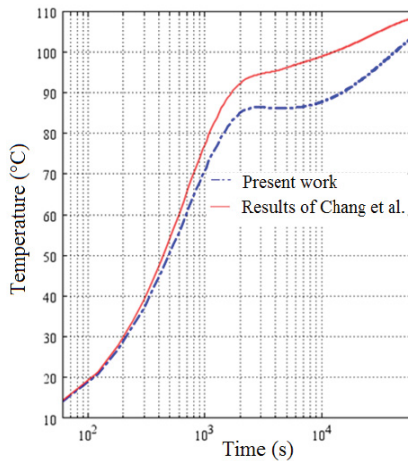


Figure 2.5. Temperature at the center of wood specimen ($x=0.012\text{ m}$)

The distribution of moisture content obtained by both models at the surface $x=0\text{ m}$ is shown in Figure 2.6. The results show the same shape obtained by the authors of [CHA 00] with a mean difference of about 0.04 kg/kg. This variation under the presence of total pressure indicates a decrease in the moisture content which takes place immediately on the surface. The pressure here is considered as a source of convection that dries

water at the surface. This completes the explication of moisture content behavior at the center of the component where the vapor desorption impeded in the time.

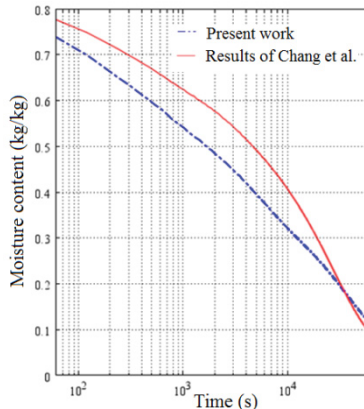


Figure 2.6. Moisture content at the surface of wood specimen at ($x = 0 \text{ m}$)

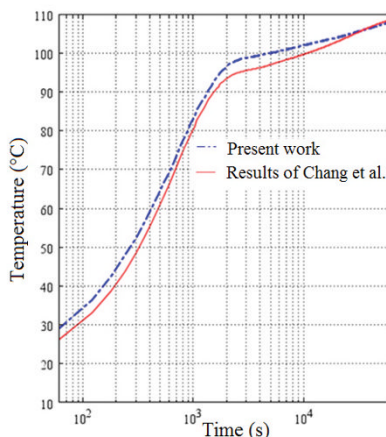


Figure 2.7. Temperature at the surface of wood specimen at ($x = 0 \text{ m}$)

We can notice in Figure 2.7 that the temperature on the surface under the presence of the pressure gradient is slightly higher (about 2°C) than in the other case. This difference is due to the vapor excess brought by the

moisture desorption toward the wall surfaces. The equilibration process of drying of the present simulations corresponds to 59 h compared to 55 h given by Chang *et al.* [CHA 00].

To test the validity of numerical simulations to physical reality, the total pressure profiles in the porous specimen are performed for the same boundary conditions mentioned above. It concerns:

- the pressure evolution over time at different positions of the slab $x = 0.008 \text{ m}$, $x = 0.012 \text{ m}$, and $x = 0.02 \text{ m}$, as can be seen in Figure 2.8;
- the total pressure distribution inside the material for $t = 30000 \text{ s}$, $t = 40000 \text{ s}$, and $x = 0.02 \text{ m}$, as can be observed in Figure 2.9.

These two figures permit us to conclude that during the first phase of drying, the material undergoes a transient pressurization corresponding to the fields of pressure subjected at the boundary conditions. This drop is caused by the pressure difference applied by external forces, which is slightly higher than the initial pressure of the material. After this short phase, the total pressure decreases gradually versus time as shown in Figure 2.8.

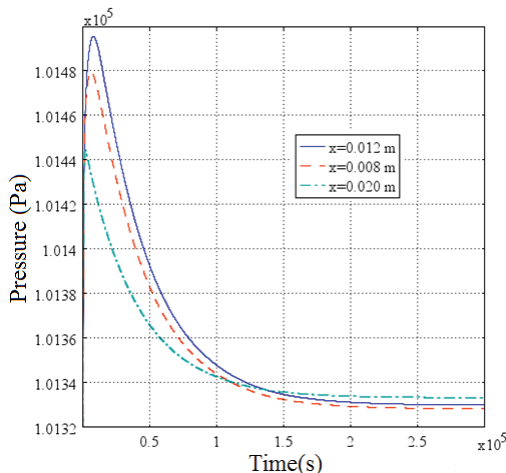


Figure 2.8. Total pressure variation for different positions of the wood specimen

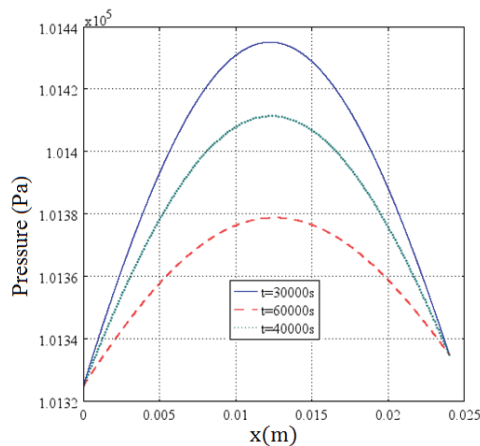


Figure 2.9. Total pressure profiles at different times

On the other hand, another series of tests is performed by using the same previous simulations with lower temperature conditions (30 and 60°C). The initial conditions are the same as the previous simulations. The results are shown in Figure 2.10. A small difference of the moisture content variation can be observed in Figures 2.10(a) and (c) due to the similarity between the initial state ($m_b = 86^\circ M$) and the external environment conditions of the material ($m_\infty = 50^\circ M$). This variation is also observed in the case of a large difference of RH between the material and the exterior ambiance at 30°C as indicated in Figure 2.10(b).

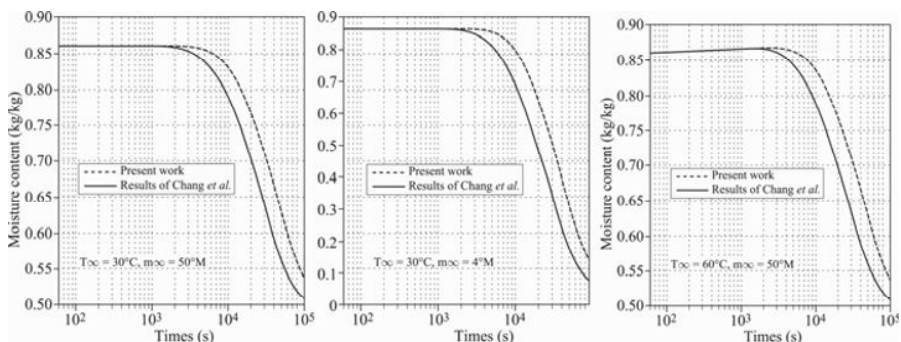


Figure 2.10. Moisture content distributions at the center of the wood specimen corresponding to different temperatures under the same initial condition ($T_b = 10^\circ C$, $m_b = 86^\circ M$)

To confirm the low sensitivity of the moisture content behavior to the total pressure in the low temperature range, other confirmation tests are realized for summer and winter conditions in the same material (wood). It concerns the physical application presented in [ABA 11] where the testing conditions have been indicated. The results are shown in Figures 2.11 and 2.12.

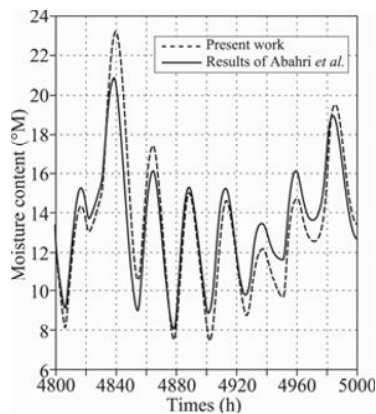


Figure 2.11. Moisture content profile within the wood specimen in summer conditions ($x = 0.025\text{ m}$)

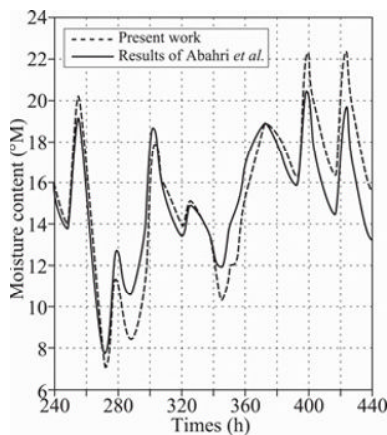


Figure 2.12. Moisture content profile within the wood specimen in winter conditions ($x = 0.025\text{ m}$)

From these figures, a small change can be seen in moisture content distribution compared to the wood drying process: the moisture content average variation in the first simulations is about 10%; however, in the second case, it is about 3%. As the total pressure is directly related to temperature through the ideal gas law, these two parameters vary proportionally. Therefore, the trapped gas inside the porous media will be expanded under the elevation of temperature pushing the liquid to areas of low moisture content which create another additional movement. Indeed, when the moisture content inside the porous media is very important, it takes more time to reach the vapor pressure in the material. This is explained by the fact that in winter conditions, the initial moisture content is sufficient to accelerate the transfer within the material.

From this section, it can be concluded that the total pressure gradient has an important effect on the moisture content transport phenomena, especially with high temperature (drying process). The spatiotemporal evolutions of water content show qualitatively the influence of climatic conditions on the hygrothermal behavior of the building component. More precisely, this variation is about 15% in the high temperature and about 3% in the normal conditions of the envelope of building. The non-consideration of the total pressure can extend the drying time and subsequently prevent undesirable microbiological reaction due to the increase in the moisture level inside the material compared to the classical cases.

2.5. Transfer and storage properties

2.5.1. Vapor permeability

In terms of moisture analysis, the water vapor permeability is the property often used in the building field to get the hydrothermal behavior inside materials. This behavior is relatively simple when the gaseous diffusion is the vapor driving mechanism. Hence, the diffusion process can be complicated by other forms of transport which can affect the permeability measurement of the material.

The water vapor permeability is not only dependent on the material and its thickness, but also on the vapor pressure applied on the material [TRE 01]. In fact, the diffusion process is also sensitive to the kind of materials used, i.e. hygroscopic or non-hygroscopic materials, as shown in Figure 2.13.

Water vapor permeability of non-hygroscopic material is slightly affected by the RH range. Therefore, in hygroscopic materials, two distinct regions can be observed. The first region is the low RH region where gaseous diffusion dominates and the water vapor permeability behavior is quasi-stable. The second region takes place from 60% of RH where the permeability increases with RH. This phenomenon was discussed in [CLA 09]. These authors present the water vapor permeability data for hygroscopic components at a separate range in order to distinguish such materials from other non-hygroscopic. This transmits some idea about the amplitude of changes to expect in RH zone greater than 60%. Furthermore, it allows more information about the condensation risk assessment. Consequently, an essential distinction has to be made between hygroscopic and non-hygroscopic materials.

The water vapor permeability varies with the temperature and RH. Furthermore, the surrounding RH is usually 50% such that the vapor pressure difference is nominally the same for each set of the so-called “service condition”. Thus, the test method provides only an average value of two separate ranges (for dry cup condition, it is represented by the area under the curve between 0 and 50% of RH and for the wet cup the area is between 50 and 100%). This treatment of two ranges of RH is reasonable for non-hygroscopic material but not for hygroscopic material. It must be noticed that these methods are steady state and they are never representative of the transient conditions experienced in a building [TRE 94].

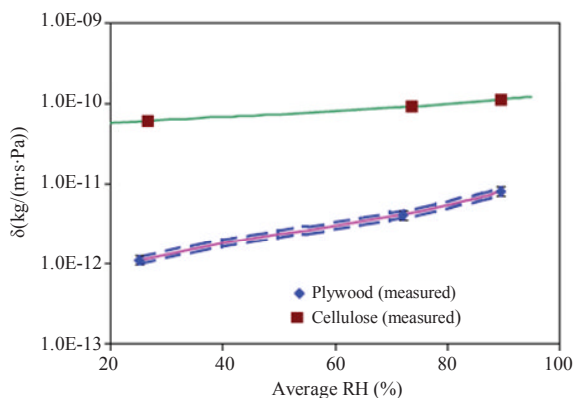


Figure 2.13. Water vapor permeability of spruce plywood and cellulose insulation [TAL 07]. For a color version of the figure, see www.iste.co.uk/ait-mokhtar/coastal.zip

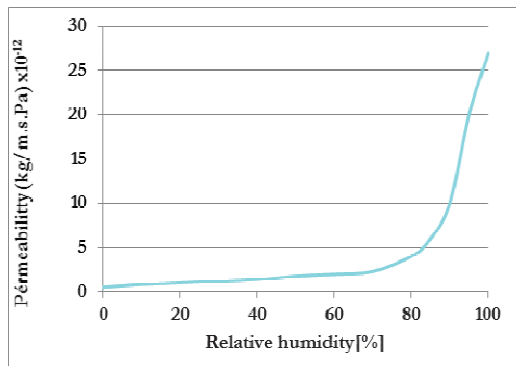


Figure 2.14. Differential permeability of a 5-ply, 12 mm thick sample of exterior quality plywood at 20°C [MAC 88]

As expected above, the water vapor permeability varies with the temperature and RH. This sensitivity was discussed in many works available in the literature. Talukdar *et al.* [TAL 07] give an empirical formulation for cellulose insulation and plywood. Changing the thickness of plywood, other experimental interest – water vapor permeability of plywood – was discussed by the author of [MAC 88] as shown in Figure 2.14.

2.5.1.1. Experimental methods and references

The cup method is a well-accepted method for the determination of water vapor permeability coefficient for building materials. The test specimen is sealed to the open side of a test cup containing either a desiccant (dry cup) or an aqueous saturated solution (wet cup). The method is used for both non-hygroscopic and hygroscopic materials, and in both cases it is necessary to wait for a steady state flow. Equilibrium depends on the initial moisture state [DEL 89]. In cup measurements, there are isothermal conditions, i.e. the temperature is uniform and constant.

Different considerable protocols of cup method are found in the literature. ASTM Standard E96 [AST 05] widely used in North America is one of the most widely used test methods which is adopted for materials that allow the passage of large steam flow. Among these materials are the fiberboards, gypsum and plaster products, and wood products. The thickness does not exceed 32 mm. Desiccant and the Water protocols are reported in this

standard. These current test methods of water vapor permeability are based on the principles of Fick's law, but in reality other factors influence the vapor transport. The question is: is this norm "correct" for insulation material and opened porous component as well as for cementitious material? This question concerns especially insulation materials that have more probability to form an air layer resistance inside the cup which wrong the vapor permeability calculation. To take this into consideration, some revisions have been made to the method, i.e the ASTM E96 [AST 05], recently. This concerns the bouncy effect, masked edge and resistance of still air layer. In addition, there is another available standard method: ASTM E398 [AST 09]. It covers dynamic evaluation of the rate of transfer of water vapor through a flexible barrier material. Mainly, it is adapted for thin films and sheet materials.

The adopted protocol is conformant to the European standard method EN-ISO, [EN ISO 01]. Similar works based on the same method can be found in the literature (e.g. [TAL 07] and [DES 10]).

All the corrections made in the ASTM E96 (2005) [AST 05] standard are taken into consideration in the present method as necessary. The process starts with an initial uniform moisture content in the material, which is placed as a cover over a cup containing a saturated salt-water solution keeping the RH of the air inside the cup at a constant level (called cup climate). According to the dimensions of the sample, a minimum of three specimens will be tested. The cup with cover is placed in a climatic chamber, where the air has a higher or lower RH (called ambient climate) than that inside the cup. The edges of fibrous insulation in the cup are sealed with silicone to avoid leakage between the cup and the insulation material (see Figure 2.15).

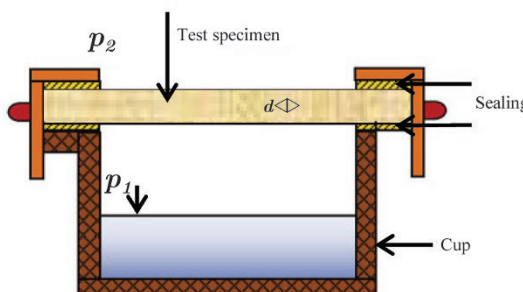


Figure 2.15. Schematic presentation of the cup method

If the ambient climate has a higher RH than the cup climate, then it is possible to define a starting point for the time and the moisture is transported by diffusion into the cup. By weighing the cups regularly, the moisture flux transferred through materials can be determined. A small fan is placed in the chamber to gently mix the air in the chamber with a velocity of 0.06 m/s.

The mass change rate for each set of successive weighing of the specimens can be calculated by the following formula:

$$\Delta \dot{m} = \frac{m_{i+1} - m_i}{t_{i+1} - t_i} \quad [2.31]$$

where:

- $\Delta \dot{m}$ [kg/s] is the change of mass per time for a simple determination;
- m_i [kg] is the mass of the test assembly at time t_i ;
- m_{i+1} [kg] is the mass of the test assembly at time t_{i+1} ;
- t_i and t_{i+1} are the successive times of weighing.

The access to the water vapor flow rate G [kg/s] through the specimen is defined by the slope of the line between mass and time. Then the water vapor flow density j_v is calculated as follows:

$$j_v = \frac{G}{A} \quad [2.32]$$

A [m^2] is the exposed surface of the specimen.

The water vapor permeability is defined by using Fick's diffusion law:

$$\delta_p = \frac{j_v}{\Delta p_v} \quad [2.33]$$

Δp_v [Pa] is the pressure difference.

Most results obtained in the literature on the measurement of water vapor permeability show a wide variation of this value which is the mean RH.

Z_a is the air gap diffusion, Z_1 and Z_2 are the film surface resistances, Z_p is the specimen resistance and p_1 and p_2 are the water vapor pressures in the two sides of the specimen.

Other parameters need to be mentioned here: the water vapor resistance. It takes into account the ability of materials to let water vapor pass through. It is a source of uncertainty and errors in the cup method and can be caused by the surface diffusion resistances and air layer thickness inside the cup.

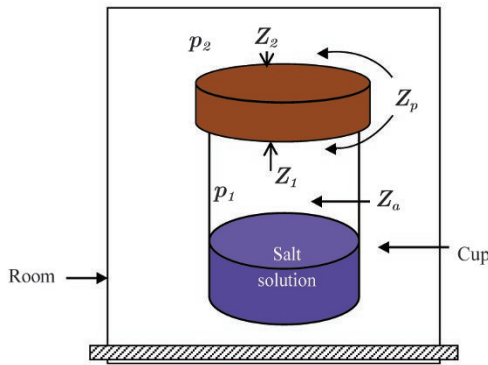


Figure 2.16. Resistance to water vapor flow in permeation cup experiment

The cup experiment consists of a number of resistances in series. They are the resistance inside the material Z_p , the surface resistances at the specimen surfaces Z_1 and Z_2 , and the resistance in the air layer inside the cup Z_a which is taken into consideration (Figure 2.16). The total water vapor resistance [$\text{m}^2 \cdot \text{s.Pa/kg}$] is given by:

$$Z = \frac{1}{\delta_p} \quad [2.34]$$

Using Lewis's law [PED 90], the surface diffusion resistances can be determined as follows:

$$\delta_{p,sur} = \frac{1}{\beta_p} \quad [2.35]$$

There is a link between the surface moisture transfer coefficient and the convective surface heat transfer coefficient c . The relationship is expressed by the Lewis formula for turbulent flows:

$$\beta_p = \frac{h_c}{r_v T (\rho C_p)_{air}} \quad [2.36]$$

- h_c [W/m²K] is the convective surface heat transfer coefficient;

- ρ [kg/m³] is the density;

- C_p [J/kg K] is the heat capacity of air.

For buildings and air, some simplified correlations for average values of convection coefficient for typical surfaces can be found in the literature. It is a common fact to consider that indoor heat transfer is mainly due to natural convection and therefore is temperature dependent, and outdoor heat transfer is mainly due to forced convection and therefore is wind velocity dependent [ANN 07]:

$$h_c = 5.7 + 3.8 V \quad [2.37]$$

V [m/s] is the air velocity.

For highly permeable materials, the air layer thickness in the test cup between the base of the specimen and the saturated salt solution contributes to the evaluation of the diffusion resistance Z_a . It increases nonlinearly with an increase in the thickness of air layer and the permeance of the material. For an air layer thickness of d [m] is:

$$Z_a = \frac{d}{\delta_a} \quad [2.38]$$

where δ_a [$\frac{m^2}{s}$] is the water vapor permeability in air, defined in the European standard EN ISO 12572 [EN ISO 01] as:

$$\delta_a = \frac{2.306}{r_v \cdot T \cdot P} 10^{-5} \left(\frac{T}{273} \right)^{1.81} \quad [2.39]$$

More details of calculation related to the resistance terms can be found in the Nordtest method of 1984.

For practical purposes, a parameter called water vapor resistance factor is introduced here. Regarding water vapor diffusion through a porous material, the water vapor flux density j_v can be given by using:

$$j_v = -\frac{\delta_a}{\mu} \nabla u_v \quad [2.40]$$

where the water vapor diffusion resistance factor μ represents the ratio of the diffusion coefficients of water vapor in the air and in the building material. It expresses that how many times better the material resists to water vapor passage than the air. As a matter of application, it is often considered that an insulating material should have a μ value of at least several thousands to be satisfactory for most applications or that special means should be used to protect it from moisture penetration and transfer.

The flux of water vapor given by this method can be written as follows:

$$\delta_{p,corr} = \frac{\Delta p_v}{d / (Z - Z_1 + Z_2 + Z_a)} \quad [2.41]$$

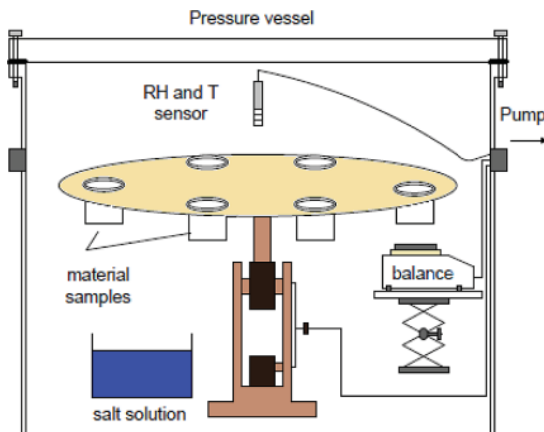


Figure 2.17. Schematic presentation of the water vapor permeability measurement

The building materials used in the experimental tests are fibrous insulation, Oriented Strand Board (OSB) and other non-hygroscopic materials. Twelve cups are used for conditioning the specimens. They are stored in a room at constant temperature of 23°C and constant relative humidity 50% (Figure 2.17).

To be coherent with the discussion mentioned above and to cover a full range of RH, we adopted the chosen RH to the material (fibrous insulation) which is hygroscopic. It means that we focus more on the value of RH above 50%. The saturated salt solutions used for obtaining different RHs in the cups are silica gel (0%), NaCl (75.7%), KCl (86%) and KNO₃ (94.5%). The specimens were weighted regularly until the steady state is reached.

2.5.1.2. Wood fibrous insulation measurements

The relative variation of weight function of time for the 12 cups is given in Figures 2.18–2.21. The evolutions of the weight for each three cups at the same hygric range are proportional. A constant vapor flow rate was obtained for each test.

The average vapor permeability obtained after resistance correction using equation [2.36] are shown in Figure 2.22. Cups 1, 2 and 3 are called dry cups as they absorb the RH of the ambient air which corresponds to an increase in their mass as a function of time. The other cups are called wet cups: their inner vapor pressures are higher than that of the chamber.

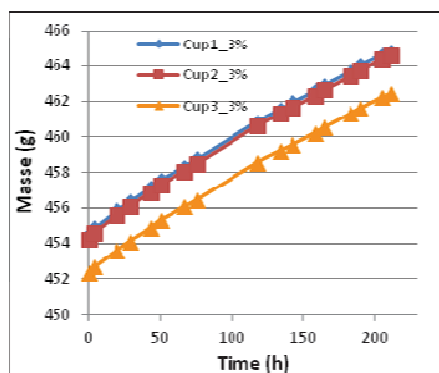


Figure 2.18. Relative variation of weight versus time for three cups of 3% RH inside each one

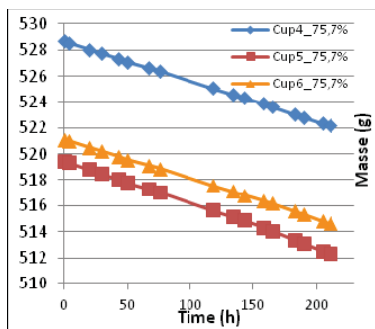


Figure 2.19. Relative variation of weight versus time for three cups of 75.5% RH inside each one

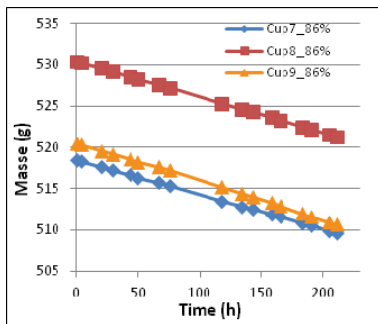


Figure 2.20. Relative variation of weight versus time for the three cups of 86% RH inside each one

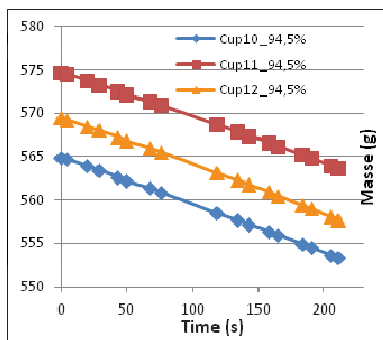


Figure 2.21. Relative variation of weight versus time for the three cups of 94.5% RH inside each one

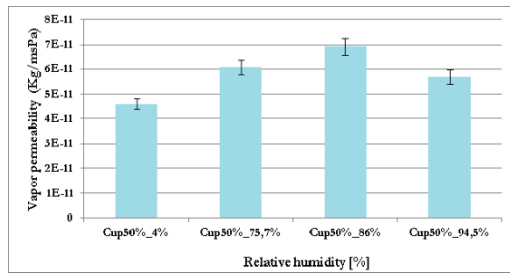


Figure 2.22. Average water vapor permeability of wood fibrous insulation resulting from different stages of relative humidity

The average permeabilities corresponding for each RH difference are shown in Figure 2.22. It can be seen that these values increase with the increase in the average RH belonging to the hygroscopic range. A similar behavior is found in the literature by Talukdar *et al.* [TAL 07]. However, beyond this regime (50–94% cup), the vapor permeability decreases. This behavior is explained by the fact that the wood fiber insulation is highly hygroscopic, which gives it a nonlinear property to water vapor permeability. Also, the diffusion process may be affected by other forms of liquid transport phase, since this range of RH (50–94%) promotes condensation. This result (Figure 2.22) provided average values of vapor permeability of the wood fiber insulation for several separated hygric water ranges.

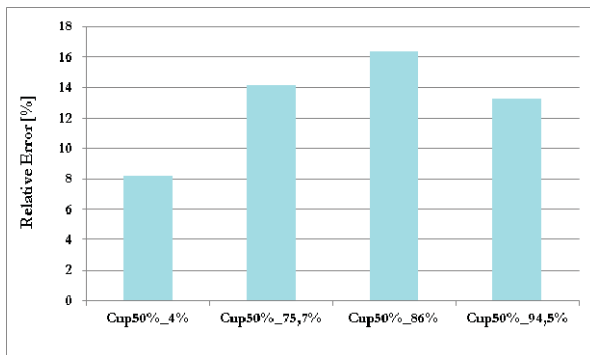


Figure 2.23. Relative error estimation with not taking into account the boundary and air layers resistances correction

The relative error of the vapor permeability due to the no-correction of vapor resistance is given in Figure 2.23. It is estimated by the formula $[(\delta_{p,corr} - \delta_p)/\delta_p] \times 100$. The histogram shows that the measurement error can be up to 17%. This error percentage may be higher when considering highly porous materials, which is the case of wood fibrous insulation.

2.5.2. Moisture diffusion coefficient

In order to assess moisture transfer in construction materials, physical modeling of phenomena is required and accurate evaluation of their input parameters is a major concern [TRA 12].

In the field of civil engineering, the prediction of water transport through the porous medium is often realized using diffusion equation where the water content is chosen as the transfer potential [BAR 07a, GAR 02, LIN 06].

The most important parameter in the diffusion equation is the moisture diffusion coefficient. This is the coefficient of proportionality between the flux of a species and the concentration gradient of that species for a given thermodynamic state.

2.5.2.1. Moisture flow mechanisms

Traditionally, the moisture flow in porous materials is regarded as a combination of vapor diffusion, with the vapor content as driving potential, and liquid flow with the pore water pressure as potential.

The transport of water vapor in a medium is by diffusion under a concentration gradient. The vapor flux density is expressed by the phenomenological relation called Fick's law defined by the equation:

$$j_v = -D_v \nabla u_v \quad [2.42]$$

where D_v is the vapor diffusion coefficient which takes into account the three types of diffusion defined in part.

The transport of liquid water is made either by capillarity or by Stokes' flow. It can be expressed by the modified Darcy's law. The density of liquid water flux is expressed as follows:

$$j_m = -\rho_l \frac{k_p}{\mu} \nabla p_l \quad [2.43]$$

where p_l is the pore water pressure, k_p is the permeability and μ is the viscosity.

Measure data is lacking for a complete description of vapor and liquid flow since it cannot be easily separated in an experiment, and a simple description of the total moisture flow j_m can be used [NIL 06, BEL 06]. Since the liquid pressure can be linked to the water vapor content through the Kelvin's law, one alternative is to use the moisture content u as a single potential for liquid moisture flow as long as the temperature remains constant or at least is independent of position, i.e. no temperature gradient is present.

$$j_m = j_v + j_l = -D_v \nabla u_v - \rho_l \frac{k_p}{\mu} \nabla p_l = -D_m \nabla u \quad [2.44]$$

Then the moisture transport in a porous medium can be approximated by a nonlinear diffusion equation:

$$\frac{\partial u}{\partial t} = -\nabla(-D_m(u) \nabla u) \quad [2.45]$$

where D_m is the moisture diffusion coefficient.

2.5.2.2. Method for assessment of moisture diffusion coefficient

For macroscopic modeling of moisture transfer, special attention is given to how the input parameters are determined. It strongly depends on the adopted transfer potentials and requires experimental data for the adjustment of the input parameters [TRA 12].

Two classes of experimental techniques are commonly used. The first class uses advanced techniques such as Nuclear Magnetic Resonance (NMR) [KOP 94], gamma-ray attenuation [NIE 72, KUM 94] or the microwaves reflection/transmission technique [MOU 95]. It measures the water content distribution within the material. Although these techniques are accurate, they

require expensive facilities. The second class is based on the analysis of gravimetric tests [TRA 12, BEL 06]. It is relatively simple to implement and does not involve substantial resources. Thus, it is widely used by the civil engineering community.

2.5.2.3. Moisture diffusion coefficient of high performance concretes (HPCs)

2.5.2.3.1. Detailed method

The presented method for the determination of the moisture diffusion coefficient is the gravimetric approach proposed by Belarbi *et al.* [BEL 06]. It is based on the analytical resolution of diffusion equation with the assumption that the moisture diffusion coefficient can be considered as a piecewise constant with respect to the ambient relative. In addition, the Fourier boundary condition is considered, which is more natural and covers larger situations to meet in reality. The geometry for which the diffusion equation is solved is such that the problem can be reduced to only one dimension. Thus, for each step, the transport equation can be written as:

$$\frac{\partial u}{\partial t} = D_m \frac{\partial^2 u}{\partial x^2} \quad [2.46]$$

where D_m is the isothermal moisture diffusion coefficient under isothermal conditions.

Figure 2.24 shows a schematic diagram of the considered problem. Note that the experimental setup must meet this diagram.

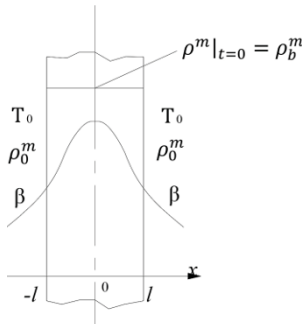


Figure 2.24. The schematic diagram of the test setup

The initial condition is:

$$u|_{t=0} = u_b \quad [2.47]$$

The boundary conditions can be defined as:

$$-D_m \frac{\partial u}{\partial x} \Big|_{x=l} = \beta(u|_{x=l} - u_0) \quad [2.48]$$

$$\frac{\partial u}{\partial x} \Big|_{x=0} = 0 \quad [2.49]$$

where β is the convective moisture transfer coefficient.

By introducing a new variable $\psi = u - u_0$, the above model can be rewritten as:

$$\frac{\partial \psi}{\partial t} = D_m \frac{\partial^2 \psi}{\partial x^2} \quad [2.50]$$

Applying the method of separate variable, we can get the analytical solution of equation [2.50]:

$$\frac{\psi(x,t)}{\psi_b} = \sum_{n=1}^{\infty} \frac{4 \sin \mu_n}{2 \mu_n + \sin(2 \mu_n)} \cos\left(\mu_n \frac{x}{l}\right) \exp\left(-\mu_n^2 \frac{D_m t}{l^2}\right) \quad [2.51]$$

where μ_n is an eigenvalue, which is the solution of the following equation:

$$\mu_n \tan \mu_n = \frac{\beta l}{D_m} \quad [2.52]$$

Expressing equation [2.52] as a function of the initial variable (u), we can get the expression of moisture content inside the medium as:

$$u(x,t) = \sum_{n=1}^{\infty} \frac{4 \sin \mu_n}{2 \mu_n + \sin(2 \mu_n)} \cos\left(\mu_n \frac{x}{l}\right) \exp\left(-\mu_n^2 \frac{D_m t}{l^2}\right) (u_b - u_0) + u_0 \quad [2.53]$$

Equations [2.52] and [2.53] have two adimensional numbers:

- Biot number: $Bi = \beta_1/D_m$ expresses the ratio between the internal and external moisture transfer resistance;
- Fourier number: $Fo = D_m t / l^2$ characterizes moisture penetration under transient conditions. For low value smaller than 0.2, the solution can be simplified by taking into consideration only the first term, which still can provide enough accurate results for most engineering applications. Thus, equation [2.53] can be simplified as:

$$u(x,t) = \frac{4\sin\mu_1}{2\mu_1 + \sin(2\mu_1)} \cos\left(\mu_1 \frac{x}{l}\right) \exp\left(-\mu_1^2 \frac{D_m t}{l^2}\right) (u_b - u_0) + u_0 \quad [2.54]$$

The amount of water per unit surface, which is transported from the medium to the ambient during the time interval $[0,t]$, can be expressed by the formula:

$$M_w = \int_{-l}^l (u_b - u(x,t)) dx \quad [2.55]$$

The total mass per unit surface of water transported during the considered stage of sorption or desorption process can be obtained by:

$$M_b - M_e = \int_{-l}^l (u_b - u(x,t)) dx \quad [2.56]$$

Then, we can get the dimensionless moisture content of the material:

$$W^+ = \frac{4\sin\mu_1}{2\mu_1 + \mu_1 \sin(2\mu_1)} \exp\left(-\mu_1^2 \frac{D_m t}{l^2}\right) \quad [2.57]$$

where:

$$W^+ = \frac{\int_{-l}^l (u - u_0) dx}{\int_{-l}^l (u_b - u_0) dx} \quad [2.58]$$

This result can be written in the following form:

$$W^+ = B \exp\left(-\frac{t}{\tau}\right) \quad [2.59]$$

with:

$$B = \frac{4 \sin^2 \mu_1}{2\mu_1^2 + \mu_1 \sin(2\mu_1)} \quad [2.60]$$

and

$$\tau = \frac{l^2}{\mu_1^2 D_m} \quad [2.61]$$

In the above equations, B represents the lag factor and τ is the characteristic time of moisture transfer during considered process. The dimensionless moisture content of the whole material can be obtained by gravimetric measurements. The values of B and τ can be identified by fitting a sorption or desorption process. Then the value of D_m is determined by solving equations [2.60] and [2.61] by some iterative methods such as the Newton's method.

2.5.2.3.2. Experimental setup

The method undertaken to assess the dimensionless moisture content as a function of time is based on a gravimetric experimental approach [TRA 12, BEL 06]. Initially, saturated samples were placed in sealed cells with $23 \pm 1^\circ\text{C}$ where the RH of ambient air was controlled using saturated salt solutions. For each following moisture stage: RH = 90.4%, 75.5%, 53.5%, 33%, 12% and 3%, a regular monitoring of mass sample in time was undertaken until obtaining the equilibrium characterized by an insignificant relative mass variation. The equilibrium is assumed if the following criterion is satisfied:

$$\frac{m(t) - m(t + 24h)}{m(t + 24h)} \leq 0.005\% \quad [2.62]$$

where $m(t)$ is the mass measured at moment t and $m(t + 24 \text{ h})$ is the measured mass 24 h later.

The sample saturation procedure consists of conserving the cylindrical specimens $11 \times 22 \text{ cm}$ underwater for at least more than 4 months. At the age of 3 months, these specimens were sawn in disks of 110 mm in diameter and $5 \pm 0.5 \text{ mm}$ in thickness. The disks were drilled of 4 mm diameter hole, allowing their fixing to scales of $\pm 0.001 \text{ g}$ accuracy for mass measurements inside the controlled RH environment. In this manner, the weighing process disturbs very little the RH inside the sealed cells during measurements.

2.5.2.3.3. Materials

The study was carried out on samples of two HPC mixtures taken directly *in situ* during the building of a highway tunnel in Paris (A1) and a viaduct in Compiègne (A2). The mixtures were manufactured by VINCI Construction. Compositions are given in Table 2.3.

Components	$A1 (\text{kg}/\text{m}^3)$	$A2 (\text{kg}/\text{m}^3)$
Cement	350 (CEM I 52.5)	355 (CEM III/A 52.5)
Additions	80 (Fly ash: SAFAMENT KWB)	0
Sand	900	880
Gravel	950	955
Water	173	186
Superplasticizer	2.8	4.3

Table 2.3. Mixture compositions of HPC A1 and A2 (Vinci Construction data)

Sampling was done on batches at the outlet side of the mixer truck after a mixing of at least 5 min at maximum speed. Samplings were carried out approximately every week for more than 1 year. Overall, 40 batches for HPC A1 (numbered from A1-1 to A1-40) and 20 batches for HPC A2 (numbered from A2-1 to A2-20) were realized. The compressive strength was measured on three cylindrical specimens of 11 cm in diameter and 22 cm in height, 28 days after their casting. Three cylindrical specimens of size $11 \times 22 \text{ cm}$ per batch were also prepared *in situ* for the experimental campaign on transfer properties. One day after mixing, the specimens were placed

underwater and then conserved in this condition for at least more than 4 months to ensure a complete hydration of cement.

2.5.2.3.4. Results

For samples from the same batch, the complete water desorption from the saturation stage to equilibrium at RH = 3% took about 1 year for the studied mixtures. Figure 2.25 shows an example of the measured mass loss in the case of samples from batch 1 from building site A1.

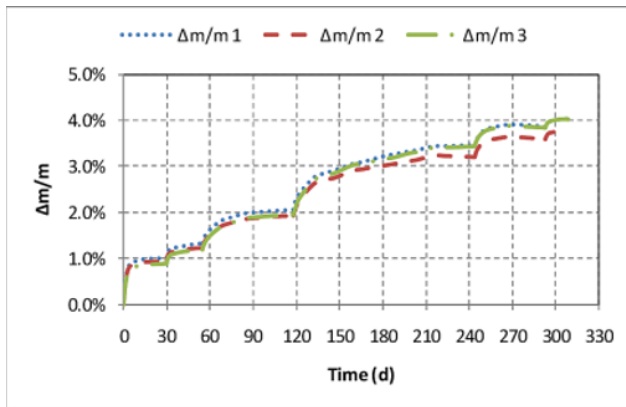


Figure 2.25. Relative mass loss for samples from the first batch of HPC A1

Transfer duration is variable according to the considered drying stage. It is about 1 month for RH = 90.4%, while it exceeds 4 months for RH = 33%. This duration depends mainly on transfer properties in the considered RH range and the moisture gradient between two stages of drying.

Moisture diffusion coefficient depends on RH (Figure 2.26). According to our procedure, we obtain five values for this parameter, i.e. the number of drying stages. The nonlinear evolution of this quantity as a function of RH is due to the nature of the transfer phenomena involved. Indeed, for low RH, the transfer is controlled by the diffusion of water vapor. In contrast, for high RH, it is controlled by the flow in the liquid phase. Between these two transfer regimes, we observe lower values for the moisture diffusion coefficient. This reflects the presence of a non-continuous phase with air entrapment, thus reducing the transfer kinetics [TRA 12].

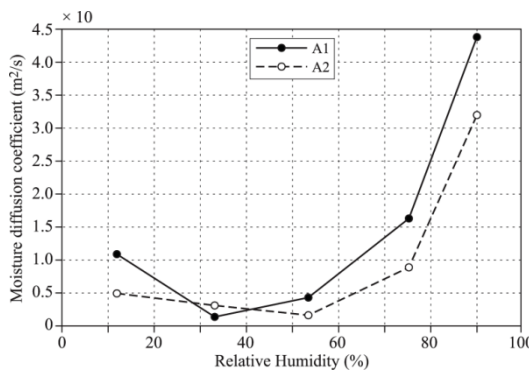


Figure 2.26. Moisture diffusion coefficient as a function of RH for HPC A1 and A2

Similarly to the water content at equilibrium, a distinction between moisture diffusion coefficients for HPC A1 and A2 can be observed, especially for the highest RH. Due to its higher porosity, HPC A2 presents a higher moisture diffusion coefficient than HPC A1.

It should be noted that the diffusion coefficients were calculated from the mass loss of disks with a small thickness (5 mm) compared to an aggregate maximum size (20 mm). Obviously, this thickness is a little representative of the material. However, the determined diffusion coefficients are of the same order of magnitude than coefficients from the literature.

Porous materials do not behave the same way in drying and wetting [CRA 96]. Figure 2.27 shows a comparison between moisture diffusion coefficients of sorption and desorption phases.

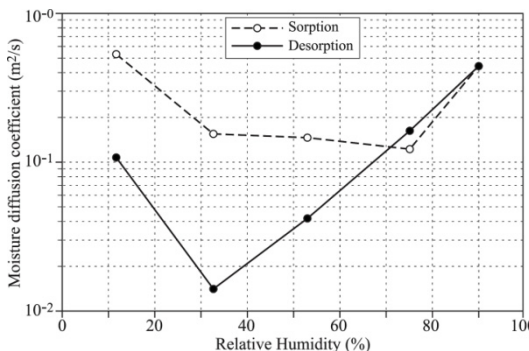


Figure 2.27. Moisture diffusion coefficient as a function of relative humidity for sorption and desorption phases for HPC A1

The bell shape of the diffusion coefficient as a function of RH is always observed. Water behaves in the same way during sorption and desorption with the same physical phenomena involved. However, we can see that the diffusion coefficient during sorption phase is lower than that in the desorption phase. We can also see that the relative difference between the wetting and drying for the same humidity increases when the RH decreases. From these two observations, we deduce that it is mainly the mass transfer controlled by the diffusion of water vapor, which would be affected. This behavior is mainly due to two reasons [TRA 10]:

- First, liquid water remains in the desorption phase in the pores, thus finest preventing the transfer of water vapor. Conversely, this water would not exist in the sorption phase.
- Second, in the performed experiment we began the test by drying and then wetting. However, the drying can modify the pore structure of the material causing the collapse of the pores of the studied cementitious material. The transfer of water vapor is then easier during the wetting.

2.5.3. Infiltration coefficient

A careful consideration of total pressure is needed to evaluate its contribution on moisture infiltration, especially with highly porous materials. In this way, a new experimental setup is undertaken with regard to different hygrothermal conditions. Moreover, the incidence of infiltration is quantified and confronted to the traditional diffusion process.

Physical model describing coupled HAM transfer within the studied materials, under adopted experimental conditions, is inspired from our theoretical work [REM 12]. The corresponding mass flow is expressed by the following relation:

$$j_v = -\delta_v \nabla \rho_v - K \nabla P - \varepsilon \delta_v \nabla T \quad [2.63]$$

In the above equation, ρ_v [kg/m^3] is the vapor content, δ_v [m^2/s] is the vapor diffusion coefficient, ε [m^2/s] is the thermogravitational coefficient represented by the ratio between D_T and δ_v , D_T [m^2/s] is the non-isothermal

moisture diffusion coefficient, K [kg/m.s.Pa] is the moisture infiltration coefficient and j_v [kg/m²s] is the mass flux.

2.5.3.1. Intrinsic and apparent infiltration coefficient

The intrinsic infiltration coefficient depends only on the porous structure of the material; it is usually done in a laminar flow by similitude to the Klinkenberg approach [KLI 41]. It depends on the fluid characteristics. The intrinsic permeability K_{int} is expressed as a function of the apparent permeability K_a and the average pressure between the two sides of the sample. Hence, the determination of intrinsic coefficient requires the implementation of measurement at different pressure levels in order to perform the calculation according to the Klinkenberg method [KLI 41].

In contrast, the apparent infiltration coefficient is estimated at equilibrium state (constant mass flow). It is a function of the mass flow, the total pressure difference and the RH gradient between the two ambiances. The calculated infiltration coefficient represents the average “apparent” infiltration of the material. For each pressure range, this coefficient is calculated according to the following equation derived from equation [2.63]:

$$K = -\frac{j_v + \delta_v \nabla \rho_v + \varepsilon \delta_v \nabla T}{\nabla P} \quad [2.64]$$

The adopted equilibrium criterion is given by the following equation:

$$\frac{j_{v(i+1)} - j_{v(i)}}{j_{v(i+1)}} \leq 0.05\% \quad [2.65]$$

where $j_{(v+1)}$ and $j_{(v)}$ are the mass flux at instant $t_{(i+1)}$ and $t_{(i)}$, respectively.

2.5.3.2. Tested materials

Three different types of hygroscopic materials are studied. It concerns wood fibrous insulation, OSB and aerated concrete whose proprieties are derived from [TRE 01]. Physical properties of OSB and wood fibrous insulation are listed in Table 2.4.

<i>Parameter</i>	<i>Unit</i>	<i>Wood fibrous insulation</i>	<i>OSB</i>
Density	$\rho(kg/m^3)$	160	601
Thermal conductivity	$\lambda(W/m.K)$	0.05	0.095
Permeability	$\delta_p(kg/msPa)$	4×10^{-11}	5×10^{-12}
Specific heat	$C_p(J/kg.K)$	2,100	1,880
Resistance to vapor diffusion	$\mu(-)$	5	40

Table 2.4. Hygrothermal and physical properties of studied materials

2.5.3.3. Experimental protocol

It should be noted that there are practically no recommended procedures by the entire scientific community devoted to the evaluation of moisture infiltration related to total air pressure difference (caused by wind or ventilation, etc.). Furthermore, these kinds of experimentations are time-consuming and expensive.

In this context, we focused on the conception of an experimental setup capable of measuring moisture infiltration for different pressure range (from 10 to 2,000 Pa), especially for extremely low values because the real conditions representative of buildings walls manipulates low pressure. This setup consists of two compartments controlled on temperature, RH, pressure and total flow rates as shown in Figure 2.28. The tested sample is placed vertically at the interface of two ambiances. A low flow control system is designed using a sensitive solenoid valve and differential pressure equipment. This system is directly related to the datalogger and is managed by a special program to regulate the pressure set point. This instrumentation permits monitoring various parameters such as mass flow rates and RH, pressure difference between the two facades of the specimen to obtain a series of “pressure/ mass flow” measurements.

The resulting mass flow and hygrothermal status within and around the material are controlled until equilibrium using temperature and RH sensors that are placed at different positions. The distance between each sensor is 10 mm.

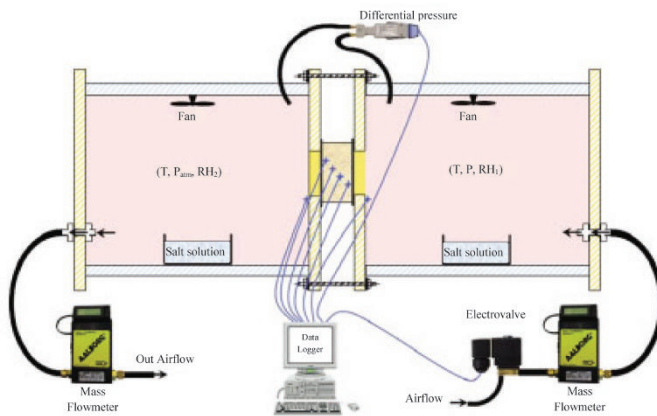


Figure 2.28. Schematic representation of the experimental bench

2.5.3.4. Case study results and discussion

Before the beginning of the moisture infiltration measurement, the specimen was subjected to different pressure stages (Figure 2.29) at a given RH (here 65% upstream and 12% downstream) between its two facades. This led us to derive a conclusion about the hygric behavior of materials according to the total pressure changes. The obtained RH distribution profiles given by sensors within aerated concrete are shown in Figure 2.30. The impact of total pressure appears clearly on the redistribution of moisture in the material after every change in pressure gradient. Here, we used high pressure range for two main reasons: better visualization of the infiltration effect and simplification of the intrinsic infiltration coefficient calculation.

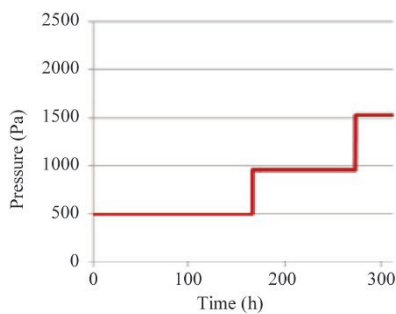


Figure 2.29. Pressure difference applied on aerated concrete

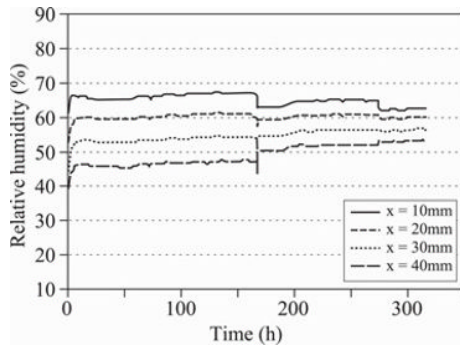


Figure 2.30. Distribution of RH of aerated concrete under the evolution of total pressure

The same experimental procedure was reapplied on wood fibrous insulation, this time for extremely low pressure gradient (Figure 2.31). The sample was placed between two ambiances of humidity: 64% downstream and 74% upstream. Moisture profile within the material was followed for each 15 min. The result is shown in Figure 2.32. The water content in the material is sensitive to these pressure excitations even with low pressure.

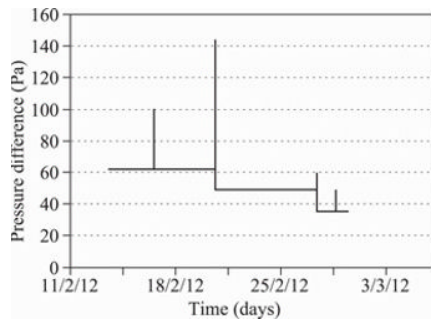


Figure 2.31. Pressure difference applied on aerated concrete

The apparent infiltration coefficients of OSB and aerated concrete are calculated (Figures 2.33 and 2.34). These figures show the existence of a linear relationship between two variables: apparent infiltration coefficient (K_a) and the inverse of the total pressure difference applied between the two sides of the sample ($1/\Delta P$). Graphically, the intrinsic infiltration coefficient corresponds to the value at the origin of these Klinkenberg's lines.

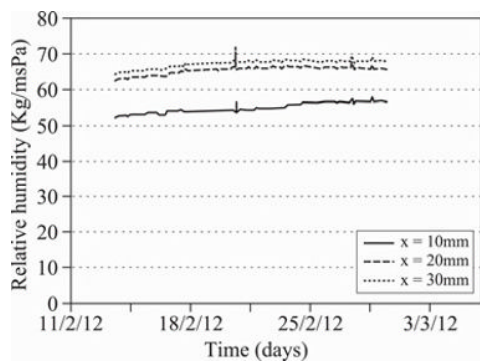


Figure 2.32. Distribution of RH of aerated concrete under the evolution of total pressure

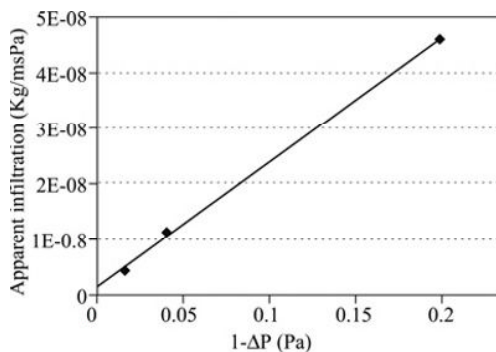


Figure 2.33. Infiltration coefficient function of total pressure for OSB

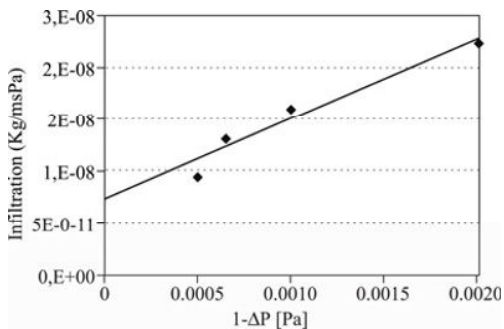


Figure 2.34. Measured infiltration coefficient function of total pressure for aerated concrete

The infiltration coefficients obtained for aerated concrete and OSB are 6.9×10^{-11} kg / m.s.Pa and 1.75×10^{-9} kg / m.s.Pa, respectively.

Contrary to an aerated concrete, OSB presents high value of infiltration. Physically, this result is justified by the macroporous structure of the specimen: OSB (50%) porosity is lower than that of aerated concrete (80%), whereby air in aerated concrete cells disfavors molecular transfer compared to the OSB. In fact, the infiltration rate decreases with the increase in the amount of free water within pores as in the case of water permeability. Thus, unsaturated zone of water becomes very thick as the passage of the water molecules becomes more difficult during the increase in total pressure. This corresponds to a decrease in the hygrometry in the material. The evolution of the RH in the pressure variation for the four humidity sensors (obtained in Figure 2.30) joined the finding described above.

Other experimental procedures to determine the infiltration coefficient are based on two main parameters: the first parameter is concerned with the total pressure at constant hydric level. The second parameter is the RH at fixed pressure level. Measurement was carried out on OSB and results are presented in Figures 2.35 and 2.36. For both cases, the means infiltration coefficients are affected by the variation of the total pressure and the RH. They are inversely proportional to the total pressure gradient in contrast to the RH parameter. This evidenced the explanation given below.

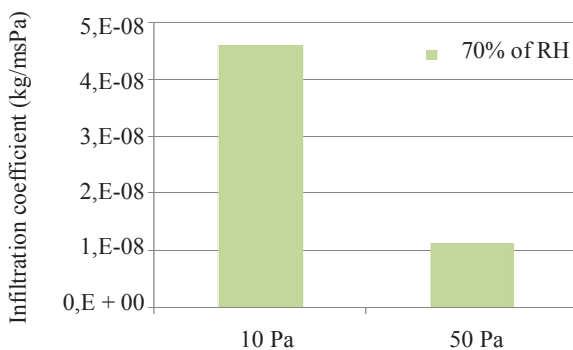


Figure 2.35. Moisture infiltration coefficient relative to total pressure obtained for OSB

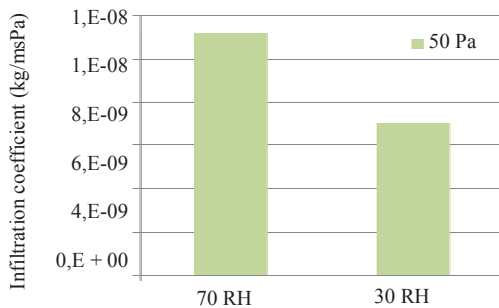


Figure 2.36. Moisture infiltration coefficient relative to RH obtained for OSB

2.5.4. Water vapor sorption–desorption isotherms

Water vapor adsorption isotherms correspond to the amount of water stored in the porous material for the whole equilibrium state corresponding to RHs between 0 and 100% at a given temperature. Its interpretation may be based on the classification originally described by [BRU 38]. It is this classification which was taken over by the International Union of Pure and Applied Chemistry (IUPAC) [SIN 85] and is reproduced in Figure 2.37.

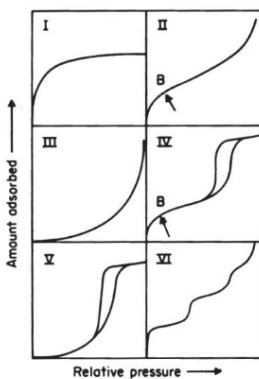


Figure 2.37. Classification of physical adsorption isotherms proposed by IUPAC

Type I is characterized by the existence of a horizontal bearing reflecting saturation of the porous material despite the increase in the partial pressure

of the adsorbable substance. It is obtained for materials having only micropores filled at a low relative pressure. The smaller the pores are, the smaller the relative pressure is.

Type II is characterized by a very gradual increase in the amount adsorbed as a function of the partial pressure of the adsorbable substance. It is obtained for macroporous materials. It describes multimolecular adsorption. Point B is often taken to indicate the stage at which monolayer coverage is complete and multilayer adsorption is about to begin.

Type IV has the same shape as the adsorption isotherm of type II for low values of partial pressure. For higher pressures, it is characterized by a saturation stage; its length considerably varies (sometimes reduced to a point of inflection). It shows a hysteresis loop, which is associated with capillary condensation taking place in mesopores.

Types III and V are not common. They differ from the adsorption isotherms of types II and IV at the lowest partial pressures. They show gradual curvature and an indistinct Point B. In such cases, the material and the adsorbate interactions are weak.

Type VI represents stepwise multilayer adsorption on surfaces energetically homogeneous. Layers are formed one by one.

It is common to observe a hysteresis of the desorption curve compared to the adsorption curve. The different forms of the hysteresis loop were mapped and classified by IUPAC [SIN 85]; this classification is presented in Figure 2.38.

Both H1 and H2 hysteresis loops appear on type IV isotherms and are representative of mesoporous materials. The H1 hysteresis loop shows parallel adsorption and desorption branches which are almost vertical. It is observed in the case of materials with a very narrow distribution of mesopores. The H2 hysteresis loop is observed in the case of materials having mesopores in intercommunication.

The two H3 and H4 hysteresis loops appear on isotherms of type II without saturation step. In these circumstances, the branch of desorption is not always reproducible and often depends on the maximum value of the amount adsorbed at the nearby relative pressures of 1. The H3 hysteresis

loop, observed for porous formed by aggregates, can be attributed to capillary condensation appearing in a non-rigid texture and is not characteristic of a defined porosity. The H4 hysteresis loop appears with microporous materials with plate-like shape in which capillary condensation may occur.

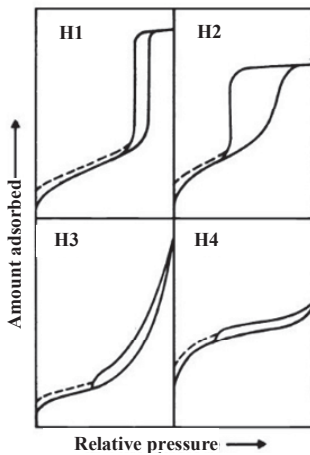


Figure 2.38. Classification-observed hysteresis loops by IUPAC [SIN 85]

The main interpretation found in the literature relies on a structural basis. The “ink bottle” shape of some pores or the interconnection of pores with different sizes allows several states of saturation with a same curvature of meniscus. During desorption, when pores are connected to finer pores, the water contained in the larger pores may get trapped by the water that saturates the smaller pores.

2.5.4.1. Methods for assessment of water vapor sorption-desorption isotherms

2.5.4.1.1. Principle

Gravimetric methods are more widely used for the characterization of hygroscopic storage and transfer in porous building materials. They are based on the monitoring of mass as a function of time for consecutive states of humidity of air surrounding the sample to characterize. Sorption/desorption tests are carried out under isothermal conditions.

For sorption, the specimen is dried until a constant mass; the specimen is placed consecutively in a series of test environments, with RH increasing in stages. For desorption, the specimen is placed consecutively in a series of test environments, with RH decreasing in stages. The moisture content is determined when equilibrium with environment for each stage is reached, i.e. when the evolution of the mass of the specimen in time does not vary. After establishing the moisture content at each RH, the sorption/desorption curve can be drawn.

The evaluation of sorption/desorption isotherms is normalized. The standard ISO 12571 [ISO 13] specifies two methods for determining hygroscopic sorption properties of porous building materials among which the reference method called desiccator method is one. In the following, we will present two methods: the reference method and a less conventional method which is the dynamic vapor sorption (DVS) method.

2.5.4.1.2. Desiccator method

It is the determination of the water content of the sample depending on the RH of the ambient air. The method consists of putting samples in hermetically sealed containers containing saturated salt solutions. For each level of RH, mass of the sample over time is monitored by regular weighing until reaching a constant mass. Thus, a point of the adsorption isotherm is obtained. The complete sorption–desorption isotherm curve is obtained by doing the same experiment for consecutive levels of humidity from 0 to 100% for sorption and 100 to 0% for desorption. The equilibrium time can vary depending on the materials tested: 1 month to about 2 years is required. The role of the saturated salt solution is to regulate naturally the air with a high accuracy for the RH inside the containers.

Name of the salt	Relative humidity (%)
Cesium fluoride	3.4
Lithium chloride	11.3
Magnesium chloride	32.8
Magnesium nitrate	52.9
Sodium chloride	75.3
Baryum chloride	90.4

Table 2.5. Relative humidity above saturated salt solutions

Table 2.5 shows a non-exhaustive list of salts used for making saturated salt solutions and the corresponding values of RH at a temperature of 25°C.

2.5.4.1.3. DVS method

This method is based on the measurement of the mass of a sample for different levels of RH of the surrounding air. To do this, we place a specimen of a few grams into a gondola connected to a balance with very high precision of the order of magnitude of micrograms; we subject it consecutively to different levels of RH and follow the evolution in time of its mass until it becomes constant for each step of the RH.

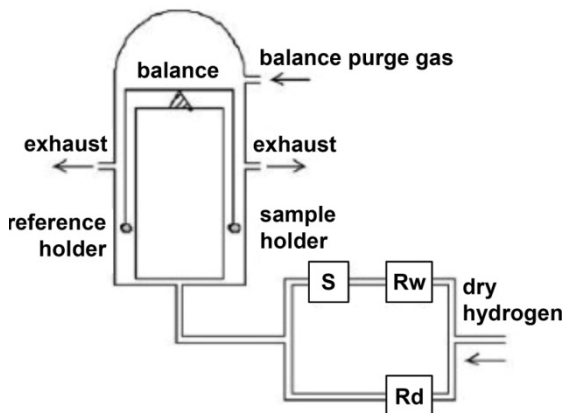


Figure 2.39. Simplified diagram of dynamic vapor sorption (DVS) [AND 08]

The RH inside the incubator is generated by enriching dry air with water vapor until target RH is reached. Figure 2.39 describes the principle of the system used. The difference with the desiccator method is the duration of the test. This device allows reducing considerably the time of the test for two major reasons: the device facilitates measurements on samples of low masses. The adsorbed mass is then even lower, and thus the time of weighing is reduced; moist air flows around the sample at a speed of 0.4 cm/s (forced convection).

2.5.4.1.4. Comparison between desiccator and DVS methods

We want to compare isothermal desorption of water vapor of concrete HPC A1 obtained using two techniques: the desiccator and the DVS

methods. Samples tested for the first technique are disks of 11 cm in diameter and 0.5 cm in thickness and having a mass of the order of 100 g. The samples tested with the second technique are grinded, and their masses are of the order of 100 mg.

According to Figure 2.40, we can see that the two methods give results in good agreement on the range of relative humidity from 0 to 53%. Beyond that, the gap increases as a function of RH; the standard deviation is then equal to 0.56%. For the variability found for this type of materials [TRA 11], this gap could be covered by the random nature of the measure. According to Arlabosse *et al.* [ARL 03], it would be linked to the apparent moisture diffusion coefficient within the porous material and the adopted equilibrium criterion. Thus, for porous materials with low diffusion coefficient, typically less than 10^{-9} m²/s, we would overestimate the moisture balance in desorption phase because it would reach an effective thermodynamic equilibrium at the surface.

This difference could also be explained by the hysteretic nature of the phenomenon of adsorption. Indeed, the equipment used for the determination of the adsorption curve by the DVS method does not go beyond 95% RH. On the other hand, the curve of desorption obtained by the desiccator method was obtained from saturation. Thus, the shape of the hysteresis is modified, and similarly the equilibrium water content.

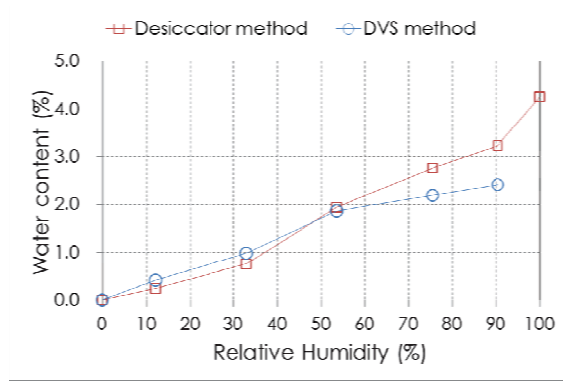


Figure 2.40. Comparison of water vapor desorption isotherms obtained by the “DVS” and the “desiccator” methods for the A1 HPC at 25°C

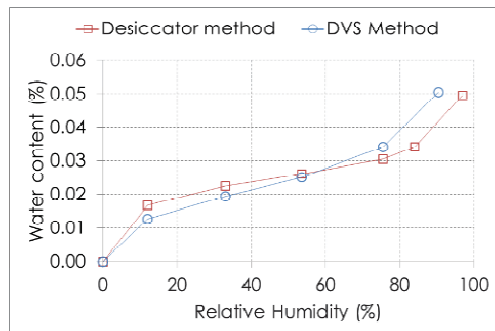


Figure 2.41. Comparison of water vapor desorption isotherms obtained by the “DVS” and the “desiccator” methods for ceramic bricks at 25°C

For ceramic bricks (Figure 2.41), we find that deviations are lower on average than for the HPC, although isotherms are compared in the desorption phase. For such a material, hysteresis phenomena are neglected.

2.5.4.1.5. Results for construction materials

Building materials differ on a number of aspects such as geometric, mechanical or even thermophysical characteristics. In this section, we present cementitious materials (ordinary and HPCs), bricks and insulation. These materials are frequently used in building as envelope or structure elements. Concretes in Tables 2.6 and 2.7 were studied, respectively, in the framework of *Durée de vie des ouvrages: Approche Prédictive Performantiel LE et probabilis Te* (APPLET) and Marine Environment Damage to Atlantic Cost Historical and transport Structures and buildings (MEDACHS) projects. Concretes in materials in Table 2.5 were tested by the Institute of Building Climatology (IBK, Dresden, Germany).

The sorption isotherm desorption is a descriptor of the microstructure. Thus, it enables us to distinguish between materials with respect to their water activity. Figure 2.42 represents the sorption–desorption isotherm of water vapor for different construction materials.

The adsorption isotherm of materials A1 and A2 belongs to type IV according to the classification of IUPAC. It belongs to type II for the other tested materials. This gives us information about the nature of the adsorption. It is multimolecular with capillary condensation for the first family of materials and multimolecular only for the second family.

For cementitious materials, there may be adsorption isotherms of several types. Concretes C15, C22, C30 and C4 are of type II because they do not contain any additions whatsoever. Conversely, the High Performance Concrete (HPC) A1 and A2 contain a Superplasticizer and fly ash. These additions modify the pore structure by increasing the proportion of the finer pores at the expense of macroporosity. This translates in the adsorption isotherm of this type of materials into the appearance of a branch where the capillary condensation at intermediate RHs occurs.

Composition and property of the material	C15	C22	C30	Unit
Porosity	15	14	10	%
Cement	275	330	380	kg/m ³
Sand	729	709	593	kg/m ³
Gravel	1,085	1,099	1,205	kg/m ³
Water	222	208	193	kg/m ³
Compressive strength	15.4	32	51	MPa

Table 2.6. Properties of concrete [MED 05]

Property of the material	Ceramic brick	Brick Joens	Calcium silicate	Aerated concrete	Unit
Bulk density	2,005	1,788	270	390	kg/m ³
Porosity	26	36	91	87	%
Dry thermal conductivity	0.5	0.87	0.069	0.095	W/(m.K)
Specific heat	840	868	1,158	1,081	J/(kg.K)

Table 2.7. Properties of building materials (IBK)

Aerated concrete, calcium silicate, brick Joens and ceramic bricks exhibit type II isotherm. This reflects a macroporous structure with a very low ratio between the hygroscopic and saturation water contents. For high RH over 98%, it is important to characterize water storage of these materials using water retention tests, and thus evaluating curves representing the water content as a function of capillary pressure.

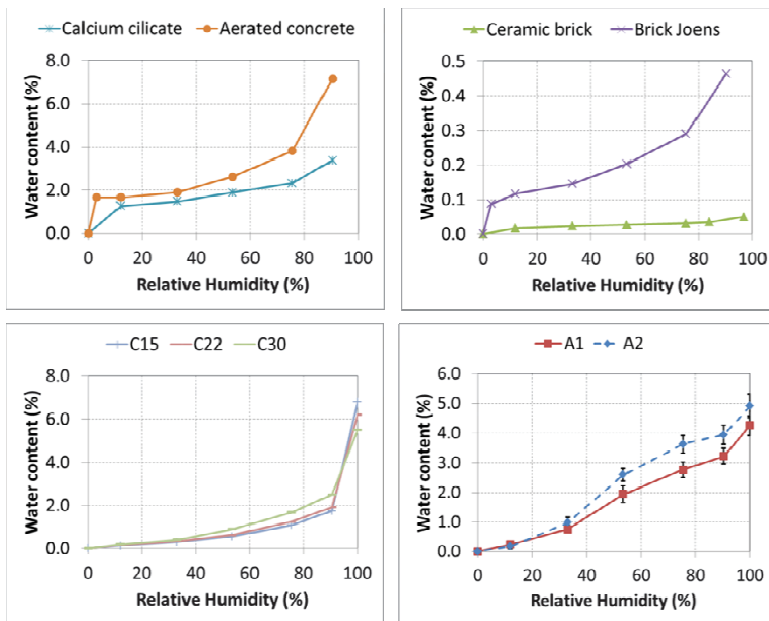


Figure 2.42. Water vapor desorption isotherms for various construction materials. For a color version of the figure, see www.iste.co.uk/ait-mokhtar/coastal.zip

2.6. Effect of statistical variability of water vapor desorption used as input data

In the field of civil engineering, prediction of water transport, i.e. the prediction of water distribution over the porous medium, requires the knowledge of the water vapor sorption/desorption isotherms. The evaluation of this property is very much time-consuming. Thus, the scientific literature is poor regarding this type of data and, in most of the cases, the characterization follows a deterministic approach on samples made in the laboratory [BAR 07, NAM 07]. The drawback of such an approach is the unawareness of the hazards due to *in situ* conditions. In fact, the material properties are generally not uniform in a structure because of the variability in the manufacture and the casting of concrete. Consequently, probabilistic models are increasingly proposed to predict the durability of reinforced concrete structures by taking into account the concrete properties variability [DEB 09, DUP 06]. However, such models require the knowledge of the distribution laws of the entry parameters.

2.6.1. Variability of water vapor desorption

To evaluate the statistical variability of the water vapor desorption isotherm (WVDI) of a concrete manufactured at a real construction site, water vapor isotherms were measured from samples of concrete taken *in situ* at different time steps of the construction of a highway tunnel in Paris, France.

Measurements included 40 batches of HPC A1 and 20 batches of HPC A2. For each batch, at least three disks were made. Overall, more than 300 specimens were tested. It should be emphasized that the isotherms measurement is time-consuming, since the determination of each curve required more than 1 year (equilibriums were reached between 1 and 3 months depending on the moisture stage).

Figure 2.43 shows the WVDI curves for HPC A1 and the average WVDI curves together with the standard deviation for each point of measurement for HPC A1 and A2. The water content was calculated on the basis of dry mass measured at 3% RH equilibrium state. We opted for such a dry mass because drying at high temperature, typically 105°C, does not only release more water but also cause also a modification of the material pore structure [THO 98]. For example, the water porosity for the HPC A1 calculated with a dry mass measured at 3% RH is equal to 10.7%, whereas it is 11.9% for a drying with 105°C. Consequently, we obtained a flattened desorption isotherm curve where the inflections were less significant.

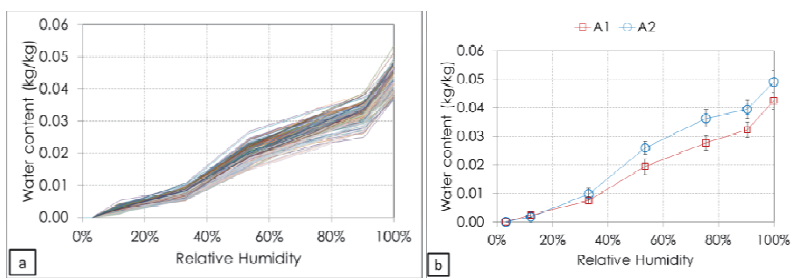


Figure 2.43. WVDI: a) curves for HPC A1 and b) mean curves for HPC A1 and A2. For a color version of the figure, see www.iste.co.uk/ait-mokhtar/coastal.zip

The WVDI obtained for both concretes belongs to type IV according to the IUPAC classification [SIN 85]. These curves have two inflections which

are often observed for such a material [BAR 07]. The desorbed amount is more or less high according to the considered RH range. Thus, desorption is multimolecular with capillary condensation on a broad interval, which shows the existence of several pore modes.

Although concrete mixtures A1 and A2 have almost the same average compressive strength (about 55 MPa), they do not have the same average desorption isotherm. For a given RH, the concrete mixture A2 has higher average water content, especially for RH above 50%. However, this result is rather consistent with the compositions because the mixture A2 has higher initial water content than the mixture A1.

Figure 2.44 shows the average water content and the standard deviation of samples from the same batch for each equilibrium state. These local data are compared with the total arithmetic mean and the standard deviation on these 20 batches. This comparison leads us to highlighting, for all the studied hydrous equilibrium states, two main observations:

- The shape of the curve expressing the water content versus the batch number is almost the same for the different studied moisture stages.
- The standard deviation per batch mainly remains lower than the total standard deviation. It is approximately 60% of the total standard deviation on average.

These observations clearly indicate that the noticed dispersion of the WVDI is not only due to the randomness of measurements results, but also due to a variability in materials properties. This variability is observed in other properties measured during the construction, such as compressive strength at 28 days.

The concrete properties may vary with time in particular because of the change in site conditions. The properties variation may also be due to operators and manufacture accuracy. Nevertheless, no clear correlation could be found between the evolution of external or concrete temperature and the evolution of the properties (strength and slump). There is also no clear correlation between the evolution during the construction of the compressive strength and the evolution of the water contents measured at equilibrium. In order to reduce the properties variation, a quality management system on a construction site is mandatory.

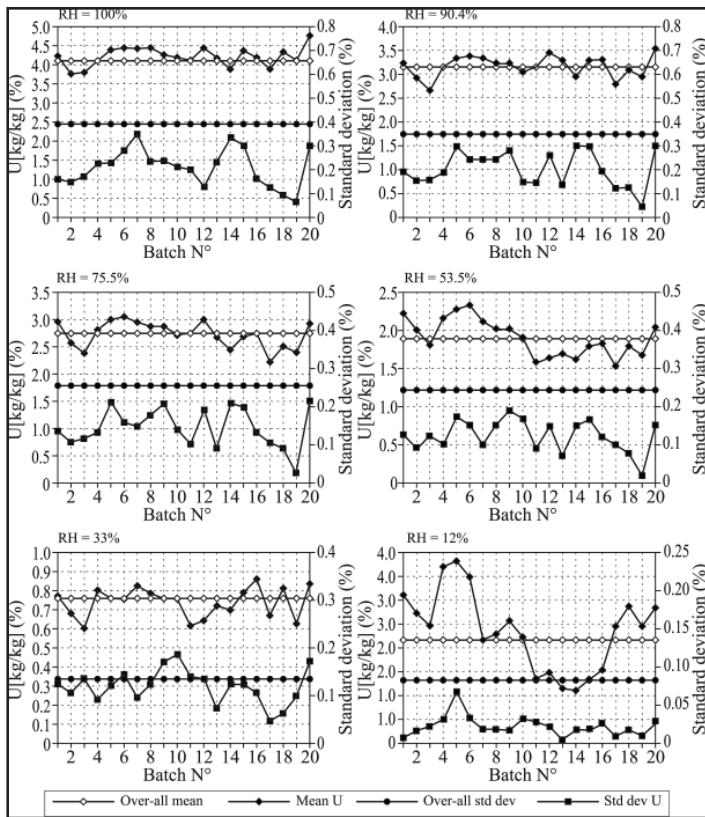


Figure 2.44. Mean water content (denoted by U) and standard deviation at the equilibrium at a given RH for the 20 batches

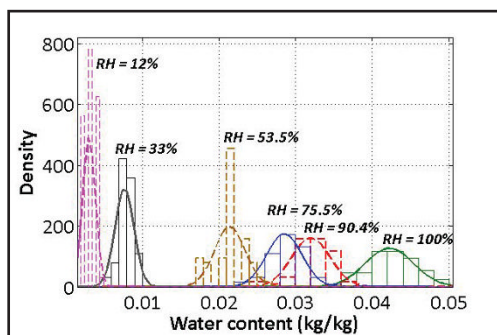


Figure 2.45. Statistical distributions of water content of HPC A1 for different moisture equilibria. For a color version of the figure, see www.iste.co.uk/ait-mokhtar/coastal.zip

Integrating the statistical variability of the sorption–desorption isotherm requires the use of probability density functions. For distribution modeling, we propose to use the Gaussian distribution because it can be easily integrated into existing mathematical models. As a reminder, Gaussian distribution has the following form:

$$f(\omega) = \frac{1}{\sigma\sqrt{2\pi}} \exp\left(-\frac{(\omega-\mu)^2}{2\sigma^2}\right) \quad [2.66]$$

where μ is the average and σ is the standard deviation.

Figure 2.45 shows the extent of water content variability for the various moisture stages studied as well as the associated probability distribution functions. The distribution function parameters and the relevance tests for the selected function are given in Table 2.6. At 95% significance level, the chi-square test is found positive [NEU 98]. Selected distribution function seems, consequently, suitable for our measurements description.

$RH (\%)$	12	33	53.5	75.5	90.4	100
$\mu (\%)$	0.2	0.8	1.9	2.8	3.2	4.3
$\sigma (\%)$	0.09	0.13	0.27	0.27	0.26	0.33
Chi-square (<i>observed value</i>)	1.031	4.764	7.588	1.509	8.073	7.521

Table 2.8. Properties of building materials (IBK)

2.6.2. Effect of statistical variability

The drying process is a complex process in which many phenomena occur (diffusion of water vapor, liquid water permeation, etc.) Our objective here is to assess the influence of its variability, presented previously, on the result of a drying computation. For the sake of simplicity, drying of concrete can be modeled by a single diffusion-type equation [2.67]:

$$\frac{\partial \omega}{\partial t} = -\nabla(-D_m(\omega)\nabla\omega) \quad [2.67]$$

where ω denotes the water content of concrete and $D_m(\omega)$ is an apparent moisture diffusion coefficient. The coefficient $D_m(\omega)$ is called “apparent” since water transport is governed by both vapor diffusion and liquid water permeation. $D_m(\omega)$ can be expressed as a function of the water content as follows [GRA 95]:

$$D_m(\omega) = \alpha \exp(\beta\omega) \quad [2.68]$$

where α and β are the constant parameters.

The external medium, where the concrete specimen is drying, can be characterized by a RH, denoted as RH. Since the diffusion problem is written in terms of water content, the boundary condition also has to be expressed in terms of water content. The WVDI $U_{eq} = f(RH)$ is used to relate the RH to the water content at the equilibrium with the external medium.

As U_{eq} denotes the water content under equilibrium conditions, the Dirichlet type is then the natural boundary condition which can be used at the interface between concrete and moisture ambiance. In such an approach of drying modeling, the variability of desorption isotherm affects only the boundary conditions.

We simulated the drying of a 10 cm width concrete wall exposed to an RH of 53.3%. An axisymmetric configuration was used: the moisture flow was thus supposed to be null in the middle of the wall.

U_0 (kg/kg)	α (m^2/s)	$\beta(-)$	$U_{eq.moy}$ (kg/kg)	$U_{eq.min}$ (kg/kg)	$U_{eq.max}$ (kg/kg)
4%	3.4×10^{-13}	84.6	1.94%	1.55%	2.34%

Table 2.9. Parameters used in the numerical simulation

Table 2.9 gives the parameters used in the numerical simulation. The parameters α and β of the moisture diffusion coefficient were identified from the average weight loss deduced from the measured ones of the 20 batches of concrete mixtures, between RH = 100% and RH = 53.3%. The initial water content U_0 is also an average value from the experimental campaign on the studied concrete.

Only the equilibrium water content U_{eq} was changed. First, simulations were performed with $U_{eq.moy}$, value of the water content at the equilibrium at $RH = 53.3\%$ determined from the average desorption isotherm curve. Two other simulations were performed for the same RH boundary condition with the maximum and minimum water content taken from measurements for the 20 batches. Dirichlet-type boundary conditions were simulated. Numerical computations were carried out using a finite element scheme with the COMSOL Multiphysics software.

For a material such as concrete, the drying kinetic is very slow. Indeed, the equilibrium is not reached even after 3 years. The impact of a varying desorption isotherm, i.e. boundary condition, is located near the boundary at 1 cm from the surface at an early drying stage. It should become higher when the equilibrium is reached (at the equilibrium, it is equal to the deviation between the different water contents $U_{eq.moy}$, $U_{eq.min}$ and $U_{eq.max}$.).

The evolution of the water content at 5 mm from the edge of the wall is shown in Figure 2.46. The deviation increases with time until the curves meet the boundary condition. Due to WVDI variability, a great discrepancy in terms of prediction is found. For example, to reach a water content equal to 2.8%, 265 days are needed using the mean desorption isotherm ($U_{eq.moy}$), while 190 days are needed for the lower isotherm ($U_{eq.min}$) and 545 days for the upper isotherm ($U_{eq.max}$).

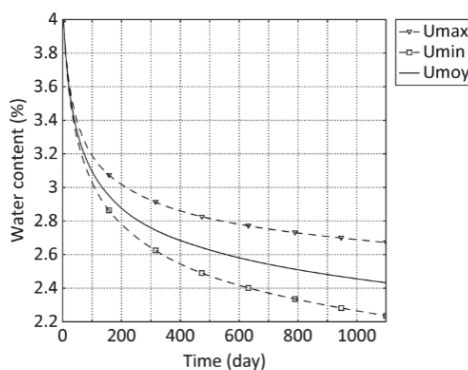


Figure 2.46. Evolution in time of the water content at 5 mm from the surface obtained for the three water contents used as boundary conditions

The variability of WVDI has a non-negligible impact on the calculated drying kinetic of the studied concrete. Moreover, the discrepancies in simulated water content profiles may have big consequences on any prediction of structure durability. Indeed, the diffusion of aggressive species, such as chloride ion, strongly depends on the water content.

2.7. Conclusion

In this chapter, a comprehensive literature review of coupled HAM transfer theory in porous building materials considering the interactions between the building envelopes and the environment was presented.

Concerning the modeling part, the coupled HAM transfers in porous materials are modeled by considering the three driving potentials: moisture content, temperature and total pressure where the role of atmospheric pressure is considered. To test the sensitivity of the hygrothermal behavior of these materials over the total pressure gradient, finite element and analytical investigation are governed. For this purpose, the presented pressure model is compared with other available works that neglect the total pressure effect. The solution of the numerical part is performed introducing the finite element method using COMSOL code. Two major cases have been regarded: the drying process (where the high temperature is addressed) and the conventional boundary conditions.

One of the difficulties in the application of this model lies in the identification of many parameters characterizing the hygrothermal properties of building materials. Therefore, a part of the presented work was devoted to the evaluation of the main properties of materials through the development of various experimental prototypes in the laboratory. For example, the water vapor permeability was evaluated using two approaches: analytical and experimental approaches. Also, an investigation on different techniques for measuring sorption isotherms desorption was discussed

Indeed, a reliable procedure for the identification of moisture infiltration on the hygrothermal behavior of three porous building materials (wood fibrous insulation, aerated concrete and OSB) was presented. For this, a new experimental setup was performed with a careful consideration of the

total pressure gradient potential from which the following points were concluded:

- The total pressure gradient has an important effect on the moisture content transport phenomena, especially with high temperature (drying process).
- The spatiotemporal evolutions of water content show qualitatively the influence of climatic conditions on the hygrothermal behavior of the building component. More precisely, this variation is about 15% in the high temperature and about 3% in the normal conditions of the envelope of building.
- The non-consideration of the total pressure can extend drying time and, subsequently, prevent the undesirable microbiological reaction due to the increase in the moisture level inside the material compared to the classical cases.

The parametric study concerned the evaluation of the incidence of total pressure and RH on moisture infiltration coefficient. This coefficient is inversely proportional to the total pressure gradient contrary to the RH parameter. It was also demonstrated that infiltration strongly depends on the type of materials. For certain materials, such as aerated concrete, having a moisture diffusion coefficient of $2.8 \times 10^{-10} \text{ m}^2 / \text{s}$ and an intrinsic infiltration coefficient of $6.9 \times 10^{-11} \text{ kg / m.s.Pa}$, the infiltration process due to the total pressure is well considered and is not negligible in comparison to the diffusion process.

Further, a sensitive analysis concerning the effect of statistical variability of water vapor sorption-desorption was investigated on two concrete types. The governed statistical analysis showed that the variability of WVDI has a significant impact on the calculated drying kinetic of the tested materials.

2.8. Bibliography

- [ABA 11] ABAHRI K., BELARBI R., TRABELSI A., "Contribution to analytical and numerical study of combined heat and moisture transfers in porous building materials", *Building and Environment*, vol. 46, pp. 1354–1360, 2011.

- [AFP 97] AFPC-AFREM, “Compte-Rendu des Journées Techniques AFPC-AFREM Durabilité des Bétons”, *Méthodes Recommandées pour la Mesure des Grandeurs Associées à la Durabilité*, pp. 121–125, 1997.
- [AND 08] ANDERBERG A., WADSO L., “Method for simultaneous determination of sorption isotherms and diffusivity of cement-based materials”, *Cement and Concrete Research*, vol. 38, pp. 89–94, 2008.
- [ANN 07] ANNEX 41, Subtask 2: experimental analysis of moisture buffering, IEA, 2007.
- [ARL 03] ARLABOSSE P., RODIER E., FERRASSE J.H. *et al.*, “Comparison between static and dynamic methods for sorption isotherm measurements”, *Drying Technology*, vol. 21, no. 3, pp. 479–497, 2003.
- [AST 05] ASTM Annual book of standards, E96, Standard test method for water vapour transmission of materials, Philadelphia, 2005.
- [AST 09] ASTM E398, Test Method for Water Vapor Transmission Rate of Sheet Materials Using Dynamic Relative Humidity Measurement, ASTM International. Available at <http://www.astm.org/Standards/E398.htm>, 2009.
- [AZE 07] AZENHA M., MAEKAWA M.K., ISHIDA T. *et al.*, “Drying induced moisture losses from mortar to the environment. Part I: experimental research”, *Materials and Structures*, vol. 40, no. 8, pp. 801–811, 2007.
- [BAR 07a] BAROUGHEL-BOUNY V., “Water vapour sorption experiments on hardened cementitious materials. Part II: essential tool for assessment of transport properties and for durability prediction”, *Cement and Concrete Research*, vol. 37, no. 3, pp. 438–454, 2007.
- [BAR 07b] BAROUGHEL-BOUNY V., “Water vapour sorption experiments on hardened cementitious materials: Part I: essential tool for analysis of hygral behaviour and its relation to pore structure”, *Cement and Concrete Research*, vol. 37, no. 3, pp. 414–437, 2007.
- [BEL 05] BELAYEV A.Y., DZHAMALOV R., KRICHETETS G.N. *et al.*, “Hysteresis effect in nutrient sorption by boggy sediments”, *Water Resources*, vol. 32, no. 2, pp. 183–191, 2005.
- [BEL 06] BELARBI R., AÏT-MOKHTAR A., QIN M. *et al.*, “Development of simplified approach to model the moisture transfer of building materials”, *Revue Européenne de Génie Civil*, vol. 10, no. 9, pp. 1033–1048, 2006.
- [BEL 08] BELARBI R., QIN M., AÏT MOKHTAR A. *et al.*, “Experimental and theoretical investigation of non-isothermal transfer in hygroscopic building materials”, *Building and Environment*, vol. 43, no. 12, pp. 2154–2162, 2008.

- [BRU 38] BRUNAUER S., EMMET P.H., TELLER E., “Adsorption of gases in multimolecular layers”, *Journal of the American Chemical Society*, vol. 60, no. 2, pp. 309–319, 1938.
- [CAR 04] CARO F., Modélisation et Simulation Numérique des Transitions de Phase Liquide Vapeur, PhD Thesis, Ecole Polytechnique de Paris, 2004.
- [CAR 99] CARMELIET J., DESCAMPS F., HOUVENAGHEL G., “A multiscale network model for simulating moisture transfer properties of porous media”, *Transport in Porous Media*, vol. 35, no. 1, pp. 67–88, 1999.
- [CHA 00] CHANG W.J., WENG C.I., “An analytical solution to coupled heat and moisture diffusion transfer in porous materials”, *International Journal of Heat and Mass Transfer*, vol. 43, no. 19, pp. 3621–3632, 2000.
- [CLA 09] CLARKE J.A., YANESKE P.P., “A rational approach to the harmonisation of the thermal properties of building materials”, *Building and Environment*, vol. 44, no. 10, pp. 2046–2055, 2009.
- [COU 01] COUSSY O., BAROUGHEL-BOUNY V., DANGLA P. *et al.*, “Evaluation de la Perméabilité à l'eau liquide des Bétons à Partir de leur Perte de Masse durant le Séchage, Numéro Spécial, Transferts dans les Bétons et Durabilité”, *Revue Française de Génie Civil*, vol. 5, nos. 2–3, pp. 269–284, 2001.
- [CRA 96] CRAUSSE P., LAURENT J.P., PERRIN B., “Porous materials hysteretic moisture characteristics: influence on water content distributions in buildings walls. Comparison of two simulation models”, *Revue Générale de Thermique*, vol. 35, no. 410, pp. 95–106, 1996.
- [DAV 10] DAVARZANI H., MARCOUX M., QUINTARD M., “Theoretical predictions of the effective thermodiffusion coefficients in porous media”, *International Journal of Heat and Mass Transfer*, vol. 53, pp. 1514–1528, 2010.
- [DE 66] DE VERIES D.A., “Thermal properties of soils”, *Physics of Plant Environment*, North Holland Publishing Co., 1966.
- [DEB 09] DEBY F., CARCASSES M., SELLIER A., “Probabilistic approach for durability design of reinforced concrete in marine environment”, *Cement and Concrete Research*, vol. 39, no. 5, pp. 466–471, 2009.
- [DEG 87] DEGIOVANNI A., MOYNE C., “Conductivité thermique de matériaux poreux humides: évaluation théorique et possibilité de mesure”, *International Journal of Heat and Mass Transfer*, vol. 10, pp. 2225–2245, 1987.
- [DEL 69] DELMON B., *Introduction à la Cinétique Hétérogène*, Institut Français du Pétrole, Collection no. 15, 1969.
- [DEL 89] DELCELIER P., Vapor transfers. CSTB298 (2322), pp. 1–18, 1989.

- [DIE 06] DIETENBERGER M.A., "Using a quasi-heat-pulse method to determine heat and moisture transfer properties for porous orthotropic wood products or cellular solid materials", *Journal of Thermal Analysis and Calorimetry*, vol. 83, pp. 97–106, 2006.
- [DUO 98] DUONG D.D., *Adsorption Analysis: Equilibria and Kinetics*, Series on Chemical Engineering, Imperial College Press, vol. 2, 1998.
- [DUP 06] DUPRAT F., SELLIER A., "Probabilistic approach to corrosion risk due to carbonation via an adaptive response surface method", *Probabilistic Engineering Mechanics*, vol. 21, no. 3, pp. 207–216, 2006.
- [EN ISO 01] European Standard ISO 12572, Building materials – Determination of water vapor transmission properties (ISO/DIS 12572:1997), March 1997.
- [ESP 06] ESPINOSA R.M., FRANKE L., "Influence of the age and drying process on pore structure and sorption isotherms of hardened cement paste", *Cement and Concrete Research*, vol. 36, no. 10, pp. 1969–1984, 2006.
- [FEM 07] FEMLAB AG, Comsol 33 Multiphysics FEM Software package, 2007.
- [FEN 04] FENGZHI L., YI L., YINGXI L. et al., "Numerical simulation of coupled heat and mass transfer in hygroscopic porous materials considering the influence of atmospheric pressure", *Fundamentals: An International Journal of Computation and Methodology*, vol. 45, no. 3, p. 249, 2004.
- [FUN 07] FUNK M., WAKILI K.G., "Driving potentials of heat and mass transport in porous building materials: A comparison between general Linear, thermodynamic and micromechanical derivation schemes". *Transport in Porous Media*, vol. 72, no. 3, pp. 273–294, 2007.
- [FUR 07] FURMANIAK S., TERZYK A.P., GAUDEN P.A., "The general mechanism of water sorption on foodstuffs – importance of the multitemperature fitting of data and the hierarchy of models", *Journal of Food Engineering*, vol. 82, no. 4, pp. 528–535, 2007.
- [GAR 02] GARBALINSKA H., "Measurement of the mass diffusivity in cement mortar: use of initial rates of water absorption", *International Journal of Heat and Mass Transfer*, vol. 45, no. 6, pp. 1353–1357, 2002.
- [GER 91] GERTIS K., "Increased insulation in building – a way to avoid the coming change in Climates?", *Bauphysiks* 13, H.5, pp. 132–137, 1991.
- [GRA 95] GRANGER L., Comportement Différé du Béton dans les Enceintes de Centrales Nucléaires. Analyse et Modélisation, PhD Thesis, Ecole Nationale des Ponts et Chaussées de Paris, 1995.
- [GRU 06] GRUNEWALD J., NICOLA A., CHAMPS-BES manual. Available at <http://beel.syr.edu/champs.htm>, 2006.

- [HEN 06] HENS H.S.L.C., “The vapor diffusion resistance and air permeance of masonry and roofing systems”, *Building and Environment*, vol. 41, no. 6, pp. 745–755, 2006.
- [ISO 13] ISO 12571, Hygrothermal performance of building materials and products – determination of hygroscopic sorption properties, 2013.
- [JAN 11] JANSSEN H., “Thermal diffusion of water vapour in porous materials: Fact or fiction”, *International Journal of Heat and Mass Transfer*, vol. 54, nos. 7–8, pp. 1548–1562, 2001
- [KLI 41] KLINKENBERG L.J., “The permeability of porous media to liquids and gases”, *American Petroleum Institute, Drilling and production Practice*, pp. 200–213, 1941.
- [KOP 94] KOPINGA K., PEL L., “One dimensional scanning of moisture in porous materials with NMR”, *Review of Scientific Instruments*, vol. 65, pp. 3673–3681, 1994.
- [KUM 94] KUMARAN M.K., Moisture diffusivity of building materials from water absorption measurements, IEA Annex XXIV Report, No. T3CA-94y0, 1994.
- [LEW 90] LEWIS R., FERGUSON W.J., “The effect of temperature and total gas pressure on the moisture content in a capillary porous body”, *International Journal for Numerical Methods in Engineering*, vol. 29, no. 02, pp. 375–369, 1990.
- [LEW 93] LEWIS R., FERGUSON W.J., “A partially nonlinear finite element analysis of heat and mass transfer in a capillary-porous body under the influence of a pressure gradient”, *Applied Mathematical Modeling*, vol. 17, no. 1, pp. 15–24, 1993.
- [LIM 07] LIMOUSIN G., GAUDET J.P., CHARLET L. *et al.*, “Sorption isotherms: a review on physical bases, modeling and measurement”, *Applied Geochemistry*, vol. 22, no. 2, pp. 249–275, 2007.
- [LIN 06] LIN M.W., BERMAN J.B., KHOSHBAKHT M. *et al.*, “Modeling of moisture migration in an FRP reinforced masonry structure”, *Building and Environment*, vol. 41, no. 5, pp. 646–656, available at <http://www.sciencedirect.com/science/article/pii/S0360132305001034>, 2006.
- [LIU 91] LIU J.Y., CHENG S., “Solutions of Luikov equations of heat and mass transfer in capillaryporous bodies”, *International Journal of Heat and Mass Transfer*, vol. 34, no. 7, pp. 1747–1754, 1991.
- [LUD 07] LUDOVIC J., PIJAUDIER-CABOT G., GHAVAMIAN S. *et al.*, “Hydraulic behaviour of a representative structural volume for containment buildings”, *Nuclear Engineering and Design*, vol. 237, nos. 12–13, pp. 1259–1274, 2007.

- [LUI 66] LUIKOV A.V., *Heat and mass transfer in capillary-porous bodies*, 1st ed., Book, Oxford: Pergamon press, 1966.
- [MAC 88] MACLEAN R.C., GALBRAITH G.H., "Interstitial condensation: applicability of conventional vapour permeability values", *Building Service Engineering Research and Technology*, vol. 9, no. 1, pp. 29–34, 1988.
- [MED 05] MEDACHS, Marine environment damage to Atlantic Coast historical and transport works or structures methods of diagnosis, repair and of maintenance, Final Report of INTERREG IIIB Atlantic Space – Project no. 197, 2005.
- [MIC 90] MICHOT L., Propriétés Physicochimiques Superficielles Du Talc et de la Chlorite, PhD Thesis, National Polytechnic Institute of Lorraine, p. 150, 1990.
- [MOJ 08] MOJTABI A., BORIES S., QUINTARD M. *et al.*, "Transferts de chaleur dans les milieux poreux-changement de phase", *Techniques de l'ingénieur*, BE8251, 2008.
- [MOU 95] MOUHASSEB H., SUHM J., GARRECHT H. *et al.*, "A new dielectric method to measure moisture in masonry", *Proceedings of Non-Destructive Testing in Civil Engineering*, pp.159–166, 1995.
- [NAM 07] NAMBIAR E.K.K., RAMAMURTHY K., "Sorption characteristics of foam concrete", *Cement and Concrete Research*, vol. 37, no. 9, pp. 1341–1347, 2007.
- [NEU 98] NEUILLY M., *La Commission d'Etablissement des Méthodes d'Analyse du Commissariat à l'Energie Atomique*, Lavoisier TEC & DOC, Paris, 1998.
- [NIE 72] NIELSEN A.F., "Gamma-ray-attenuation used for measuring the moisture content and homogeneity of porous concrete", *Building Science*, vol. 7, no. 4, pp. 257–263, 1972.
- [NIL 06] NILSSON L.O., "Modeling moisture conditions in cementitious materials – some present challenges", *2nd International Symposium on Advances in Concrete through Science and Engineering*, vol. 51, pp. 45–62, 2006.
- [PAD 98] PADFIELD T., The role of absorbent materials in moderating changes of relative humidity. PhD thesis, Technical University of Denmark, 1998.
- [PED 90] PEDERSEN C.R., Combined Heat and Moisture Transfer in Building Constructions, PhD Thesis, Report no. 214, Thermal Insulation Laboratory, Technical University of Denmark, 1990.
- [PEU 03] PEUHKURI R., Moisture Dynamics in Building Envelopes, PhD Thesis, Department of Civil Engineering, Technical University of Denmark, 2003.
- [PHI 57] PHILIP J.R., DE VERIES D.A., "Moisture movement in porous material under temperature gradients", *Transaction of American Geophysical Union*, vol. 38, no. 2, pp. 222–232, 1957.

- [QIN 08] QIN M., BELARBI R., AÏT-MOKHTAR A. *et al.*, “Nonisothermal moisture transport in hygroscopic building materials: modeling for the determination of moisture transport coefficients”, *Transport in Porous Media*, vol. 72, pp. 255–271, 2008.
- [QIN 09] QIN M., BELARBI R., AÏT-MOKHTAR A. *et al.*, “Coupled heat and moisture transfer in multi-layer building materials”, *Construction and Building Materials*, vol. 23, no. 2, pp. 967–975, 2009.
- [REM 12] REMKI B., ABAHRI K., TAHЛАITI M. *et al.*, “Hygrothermal transfer in wood drying under the atmospheric pressure gradient”, *International Journal of Thermal Sciences*, vol. 57, pp. 135–141, 2012.
- [SAN 09] SANTOS G.H., MENDES N., “Heat air and moisture transfer through hollow porous blocks”, *International Journal of Heat and Mass Transfer*, vol. 52, pp. 2390–2398, 2009.
- [SCH 05] SCHEFFLER G., PLAGGE R., “Defined drying behaviour of building materials”, *Proceedings of 7th Conference of Building Physics in Northern Countries*, 2005.
- [SIN 85] SING K.S.W., “Reporting physisorption data for gas/solid systems with special reference to the determination of surface area and porosity (recommendations 1984)”, *Pure and Applied Chemistry*, vol. 57, no. 4, pp. 603–619, 1985.
- [TAL 07] TALUKDAR P., OSANYINTOLA O.F., OLUTIMAYIN S.O. *et al.*, “An experimental data set for benchmarking 1-D, transient heat and moisture transfer models of hygroscopic building materials. Part II: experimental, numerical and analytical data”, *International Journal of Heat and Mass Transfer*, vol. 50, nos. 25–26, pp. 4915–4926, 2007.
- [THO 98] THOMAS J.J., JENNINGS H.M., ALLEN A.J., “The surface area of cement paste as measured by neutron scattering: evidence for two C-S-H morphologies”, *Cement and Concrete Research*, vol. 28, no. 6, pp. 897–905, 1998.
- [TRA 10] TRABELSI A., Études Numérique et Expérimentale des Transferts Hygrothermiques dans les Matériaux Poreux de Construction, PhD Thesis, University of La Rochelle, 2010.
- [TRA 11] TRABELSI A., BELARBI R., TURCRY P. *et al.*, “Water vapour desorption variability of in situ concrete and effects on drying simulations”, *Magazine of Concrete Research*, vol. 63, no. 5, pp. 333–342, 2011.
- [TRA 12] TRABELSI A., HAMAMI A., BELARBI R. *et al.*, “Assessment of the variability of moisture transfer properties of high performance concrete from a multi-stage drying experiment”, *European Journal of Environmental and Civil Engineering*, vol. 16, nos. 3–4, pp. 352–361, 2012.

- [TRE 01] TRECHSEL H.R., "Moisture Analysis and Condensation Control in Building Envelopes", *ASTM International*, 2001.
- [TRI 09] TRIPATHY P.P., KUMAR S., "A methodology for determination of temperature dependent mass transfer coefficients from drying kinetics: application to solar drying", *Journal of Food Engineering*, vol. 90, no. 2, pp. 212–218, 2009.
- [YOU 06] YOUNSI R., KOCAEFE D., KOCAEFE Y., "Three-dimensional simulation of heat and moisture transfer in wood", *Applied Thermal Engineering*, vol. 26, nos. 11–12, pp. 1274–1285, 2006.

Homogenization Methods for Ionic Transfers in Saturated Heterogeneous Materials

3.1. General introduction

After the presentation of the studies dealing with humidity transfer (liquid water and vapor) in porous media, particularly in cement-based materials used in building structures, this chapter deals with chloride transport mainly in these cementitious materials, as this aggressive agent is the main agent responsible for steel corrosion in reinforced concrete used in structures built in marine environment, i.e. in coastal zones.

The first studies on chloride diffusion processes in concrete carried out during the 1990s took the first and second of Fick's laws as a modeling tool in these processes [AMI 97]. The scientific community has gradually realized that these laws, originally suggested for molecular diffusion in homogeneous media, did not take into account two main features [AMI 01a, AMI 01b]:

- the heterogeneity of the cementitious materials in general and concrete in particular, wherein the mass transport is limited to the liquid phase of the cement paste, namely the part of the water-filled porosity;
- the ionic character of the mass transport in the case of chlorides involves electrical charges interactions between different ions involved in the transport

and in the solid–liquid interface, where the pore walls are electrically charged. This phenomenon is known as an electrical double layer (EDL). Moreover, in laboratory studies, given the slowness of transfer kinetics in porous cementitious materials, diffusion process is accelerated by the application of external electrical field. This electrical field generates another electrical field, called induced electrical field, within the material at molecular scale, hereafter called the “Debye scale”.

This chapter is deliberately limited to the latest developments of this issue, namely the study of these ionic transfers taking into account the two aspects mentioned above: medium heterogeneity and electrochemical interactions between ions and between solid–liquid interfaces within the microstructure of the material.

Thus, after the presentation of the two main homogenization techniques used in the framework of these studies, we use a periodic homogenization technique as a tool for a multiscale homogenization of ionic transfer in cementitious materials. The first homogenization procedure of the Nernst–Planck–Poisson (NPP) system is performed from the nanoscale (Debye length scale) to the microscale (capillary porosity scale), accounting for the EDL effects. The second homogenization step is performed from the microscale to the material scale. For the second homogenization step, the scale being much larger than the Debye length, the EDL effects are not involved in the ionic transfer and only the complexity of the microstructure geometry has an influence on the material diffusivity.

In a second step, a parametric study of the influence of the EDL effects on the homogenized transfer properties is discussed.

Finally, in order to validate the multiscale homogenization procedure, the homogenized diffusion coefficients (resulting from the two successive homogenization steps) are compared to the experimental results obtained by the electrodiffusion test for two cement paste samples. The two main scales of the cementitious material are taken into account through a modeling of the microstructure having the same porosity as the real cementitious material.

3.2. Different techniques of homogenization

Accounting for the large volume of cementitious materials usually used in concrete structures, the calculus of transfer properties accounting for all the heterogeneities at the microscopic scale is not conceivable. Therefore, cementitious materials need to be modeled as continuum media with equivalent macroscopic transfer properties. The accurate determination of these macroscopic transfer properties is possible using homogenization techniques, and accounting for the complex microstructure of the cementitious material and for the multi-physics couplings involved at the different scales must be considered¹; in particular, EDL effects² involved at the Debye length scale³. In the literature, numerous contributions exist which use homogenization techniques based on different theoretical frameworks (periodic homogenization, volume averaging method, random or nonlinear homogenization, etc.). However, the only contributions taking into account EDL effects in the ionic transfer of cementitious materials which are based on averaging method are simplifying assumptions [SAM 07]. Let us also cite other works using the periodic homogenization method leading to macroscopic models describing the electro-chemo-hydromechanical phenomenon in clays [MOY 02, MOY 06a]. In this section, we will focus mainly on homogenization via volume averaging and on periodic homogenization method.

3.2.1. Homogenization via volume averaging

Homogenization via volume averaging was initially developed by Whitaker [WHI 77, WHI 85] for thermal transfers in porous media. Then, it was extended to mass transfers and, more recently, to poroelasticity for saturated or partially saturated porous media⁴ [AHM 01, AHM 96, AMA 06, QUI 97, QUI 88, QUI 93b, QUI 93a, QUI 94, QUI 96, SAM 07, WOO 04].

Let us now focus on the main definitions and procedure of homogenization via volume averaging. For a better understanding, we will

¹ We recall that cementitious materials are strongly heterogeneous with numerous heterogeneities at different scales.

² Electrocapillary adsorption phenomena.

³ (Of the order of the nanometer for cementitious materials considered).

⁴ Using, in particular, Hill's lemma and different approximation schemes.

consider here a scalar variable⁵ θ in a two-phase medium. For what concerns us, let us consider a saturated cementitious material Ω made up of a solid phase Ω_s and a liquid phase Ω_f . The homogenization via volume averaging consists of averaging on the whole domain $\Omega = \Omega_s \cup \Omega_f$ the physical variables and the equilibrium (or mass transfer) equations, defined locally at any point M of the porous media. To do this, we define the classical averaging operator $\langle \cdot \rangle$ associated with the fluid phase Ω_f :

$$\langle \theta \rangle = \frac{1}{|\Omega|} \int_{\Omega_f} \theta d\Omega_f \quad [3.1]$$

where $|\Omega|$ denotes the volume of the whole domain Ω . The intrinsic average on the liquid phase $\langle \cdot \rangle_f$ may also be introduced:

$$\langle \theta \rangle_f = \frac{1}{|\Omega_f|} \int_{\Omega_f} \theta d\Omega_f \quad [3.2]$$

We have the classical relation between the two averaging operators:

$$\langle \bar{\theta} \rangle = \varepsilon_p \langle \theta \rangle_f \quad [3.3]$$

where $\varepsilon_p = \frac{|\Omega_f|}{|\Omega|}$ denotes the porosity of the material.

An important point concerns the variations of the mean value $\langle \theta \rangle$ versus the radius r of the sphere delimiting the volume $|\Omega|$ (Figure 3.1).

We may distinguish mainly two areas with very different behaviors:

- the area $r \in [\delta, r_0]$ where the average of θ presents fluctuations due to the fast variations of θ at the microscopic scale (pore scale);
- the area $r \in [r_0, \infty[$ where the average of θ may either stabilize or be affected by the transfer process itself.

When r is close to r_0 , the fluctuations at both scales (macroscopic and microscopic) do not affect the average value of θ . The domain whose radius is

⁵ The definitions remain valid for vector or tensor variables.

close to r_0 is classically called the representative elementary volume (REV). The characteristic length r_0 of the REV must satisfy the condition:

$$\delta \ll r_0 \ll L \quad [3.4]$$

which is a homogeneity condition of the problem. Once this condition of separation of scales is satisfied, the homogenization via volume averaging relies on the decomposition of the physical variable θ as:

$$\theta = \langle \theta \rangle + \hat{\theta} \quad [3.5]$$

where $\langle \theta \rangle$ denotes the average value of θ and $\hat{\theta}$ the associated fluctuations. The fluctuations $\hat{\theta}$ are generally linked to the mean value $\langle \theta \rangle_f$ through a linear localization relation [WHI 77, WHI 85]:

$$\hat{\theta} = a \cdot \text{grad} \langle \theta \rangle_f \quad [3.6]$$

where a is a vector depending on the liquid–solid interface Γ_{sf} of the REV. To obtain the search homogenized model, the explicit expression of a must be specified, which generally requires to make some supplementary (physical) assumptions on the problem.

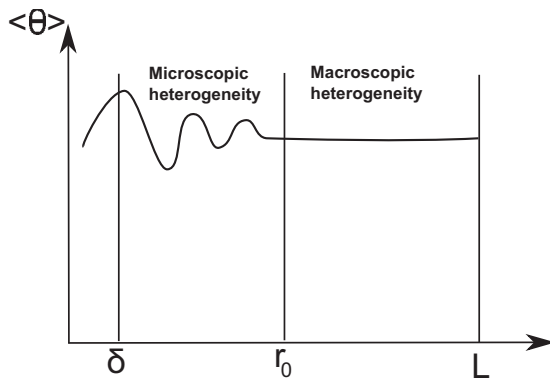


Figure 3.1. Variation of the mean value of θ versus the radius r of the sphere characterizing the integration volume. δ , r_0 and L denote, respectively, the pore scale, the REV scale and the material scale

On the other hand, as soon as the problem to be homogenized is nonlinear, another difficulty appears. Indeed, when nonlinear terms of the form $\langle \theta \lambda \rangle$ must

be calculated, for any phase functions θ and λ , the mean value of the product is given by:

$$\langle \theta \lambda \rangle = \langle \theta \rangle \langle \lambda \rangle + \langle \widehat{\theta} \widehat{\lambda} \rangle \quad [3.7]$$

As the fluctuation term $\langle \widehat{\theta} \widehat{\lambda} \rangle$ is, in general, unknown, it is neglected in the homogenization procedure [3.7]. This approximation is very questionable and may lead to incorrect results.

3.2.2. Periodic homogenization method

The second class of homogenization method that will be presented here is the periodic homogenization method [BEN 78, KEL 77, SAN 80]. Although there are many similarities with the homogenization via volume averaging, the mathematical framework and methodology are different [DAV 13]. First, the periodic homogenization method relies on the assumption that the microstructure is constituted of a periodic of an elementary cell. For the elementary cell to be representative of the microstructure and consistent with an homogenization procedure, it must contain a sufficient large number of heterogeneities. Thus, the characteristic length l of the elementary cell must be smaller than the macroscopic length L and larger than the characteristic length of heterogeneities δ . Thus, we have the following condition:

$$\delta \ll l \ll L$$

which is similar to that introduced in [3.4] with homogenization via volume averaging. In the case of a medium with periodic microstructure, the elementary cell represents a kind of REV [AUR 09] and the separation of scales requires that:

$$\varepsilon = \frac{l}{L} \ll 1 \quad [3.8]$$

where ε denotes the perturbation parameter or the scale separation parameter.

Let us now focus more in details on the mathematical formulation of the periodic homogenization procedure. Let $y = (y_1, y_2, y_3)$ be the microscopic variable (fast variable), $x = (x_1, x_2, x_3)$ be the macroscopic variable (slow

variable) and θ be some physical variable. Due to the separation of scale, θ is *a priori* a function of the two spacial variables y and x assumed to be independent:

$$\theta = \theta(x, y), \quad y = x/\varepsilon$$

In the framework of the periodic homogenization [AUR 09, BEN 78, KEL 77, SAN 80], the variables involved and their derivation are assumed to be y -periodic. The average $\langle \theta \rangle$ of the variable θ over the periodic elementary cell is represented in Figure 3.2 as a function of x . The fluctuations of variable θ around its average $\langle \theta \rangle$ are periodic of period ε corresponding to the size of the elementary cell.

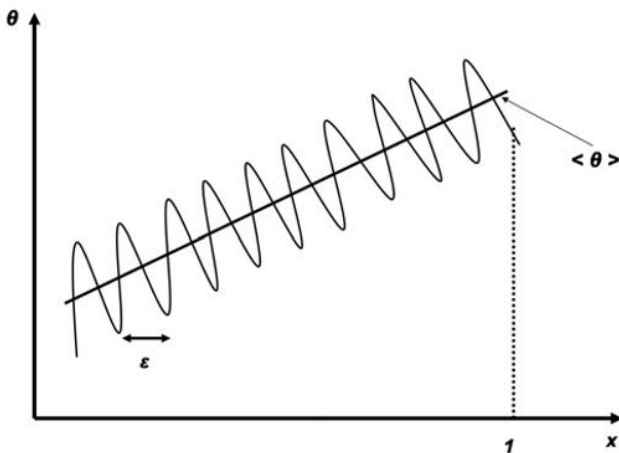


Figure 3.2. Macroscopic and local variation of θ

The periodic homogenization method is based on the asymptotic expansion [AUR 09, BEN 78, KEL 77, SAN 80] of the physical unknowns of the problem, which are assumed to admit a formal expansion with respect to ε :

$$\theta = \theta^0(x, y) + \varepsilon \theta^1(x, y) + \varepsilon^2 \theta^2(x, y) + \dots \quad [3.9]$$

where θ^i is y -periodic for all i . It is important to note that when $\varepsilon \rightarrow 0$, the size of the elementary cell tends to zero and we search to characterize the

leading term θ^0 of expansion [3.9], the solution of the homogenized problem at the macroscopic scale.

Replacing the asymptotic expansion [3.9] of unknowns in the microscopic equations governing the problem and equating to zero the factors of successive powers of ε , we obtain a chain of coupled problems. The resolution of these coupled problems leads to search the macroscopic homogenized problem whose θ^0 is a solution. More details are presented in the following sections.

3.3. Periodic homogenization of ionic transfers accounting for electrical double layer

Let us consider that the material studied occupies the domain S^* of the three-dimensional (3D) space \mathbb{R}^3 , whose characteristic length is denoted by L (Figure 3.3(a)). The macroscopic domain S^* is limited by the boundary ∂S^* . A current point of the macroscopic domain S^* will be denoted as $x^* = (x_1^*, x_2^*, x_3^*)$. The microstructure of the considered material is assumed to be periodic and is constituted of the repetition of the elementary cell $\Omega^* = \Omega_s^* \cup \Omega_f^*$, which is composed of a solid phase Ω_s^* and a fluid phase Ω_f^* (Figure 3.3(b)). The nanostructure is composed of the repetition of another periodic elementary cell $\Omega^* = \Omega_s^* \cup \Omega_f^*$, where the solid and fluid phases are denoted as Ω_s^* and Ω_f^* , respectively (Figure 3.3(c)). The boundary of the domain Ω^* (respectively, Ω^*) is denoted as Γ^* (respectively, Γ^*). It is composed of the solid–fluid interface Γ_{sf}^* (respectively, Γ_{sf}^*) between the solid and the fluid phases and of the fluid–fluid interface Γ_{ff}^* (respectively, Γ_{ff}^*) separating two neighboring elementary cells at the microscale (respectively, at the nanoscale). A current point of the domain Ω^* at the microscale (respectively, Ω^* at the nanoscale) will be denoted as $y^* = (y_1^*, y_2^*, y_3^*)$ (respectively, $z^* = (z_1^*, z_2^*, z_3^*)$). δ and l denote, respectively, the characteristic lengths at the nanoscale and the microscale. In the following, we will index by a star (*) all dimensional variables. The variables without a star will be dimensionless. Moreover, grad^* , div^* and δ^* will denote, respectively, the 3D gradient, divergence and Laplacian with respect to the dimensional variables.

First, we assume that the characteristic length at the nanoscale δ (respectively, the characteristic length at the microscale l) is very small with

respect to the microscale characteristic length l (respectively, with respect to the macroscale characteristic length L). This represents the conditions of homogenizability from the nanoscale to the microscale (or from the microscale to the macroscale). We then define the perturbation parameters $\tilde{\varepsilon}$ and ε , which satisfy:

$$\tilde{\varepsilon} = \frac{\delta}{l} \ll 1, \quad \varepsilon = \frac{l}{L} \ll 1$$

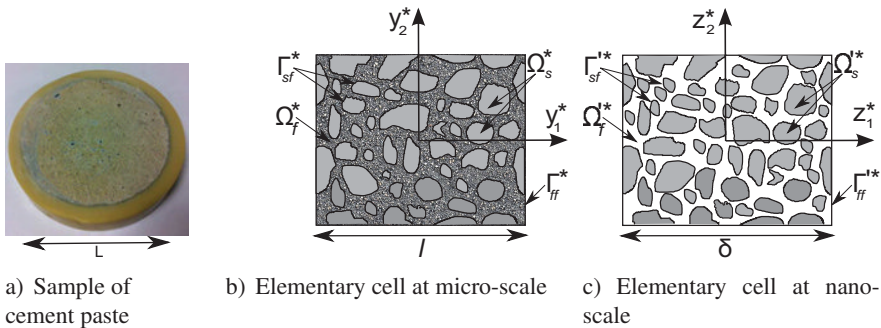


Figure 3.3. Modeling of the different scales of the material with periodic elementary cells

Classically, in saturated porous media, the ionic transfer is described by Nernst–Planck (NP) equations coupled with Poisson’s equation. However, to take into account the EDL, we will consider separately concentrations c_+^* of cations and c_-^* of anions. This decomposition naturally allows us to express the electrochemical imbalance caused by the presence of positive and negative species at the solid interfaces. Far from the solid–fluid interface near which the EDL occurs, i.e. outside the diffuse layer, we will have electroneutrality of the pore solution:

$$F(z_+ c_+^* - z_- c_-^*) = \rho_+^* - \rho_-^* = 0 \quad [3.10]$$

where z_\pm and c_\pm denote the valence and the concentration. Moreover, to take explicitly into account the EDL phenomenon, we will consider the following decomposition of the total electric potential Ψ^* involved in the NP equations as follows [MOY 02, SAS 82, SAS 81]:

$$\Psi^* = \varphi^* + \psi_b^* \quad [3.11]$$

The bulk potential ψ_b^* is defined outside the diffuse layer where the electroneutrality condition is satisfied (far from the solid–fluid interface). The potential φ^* , induced by the EDL, is called classically EDL potential. The EDL potential φ^* decreases progressively from its maximal value (in absolute value) at the solid–fluid interface to its minimal value in the bulk of the pore solution. Cation and anion concentrations strongly depend on the EDL potential according to Boltzmann's law, which is a result of the assumed thermodynamic equilibrium between the bulk solution and the EDL⁶ [DOR 95, MOY 02, MOY 06a]. We have:

$$c_{\pm}^* = C_b^* \exp(\mp \frac{|z_{\pm}|F}{RT} \varphi^*) \quad [3.12]$$

where C_b^* is the bulk concentration where the electroneutrality condition is satisfied. Without EDL, $\varphi^* = 0$, and therefore cation and anion concentrations are equal:

$$c_+^* = c_-^* = C_b^*.$$

Although the validity of Poisson–Boltzmann model and decomposition [3.12] at the nanometer scale is discussed in the literature [VAN 92, NAD 04], we consider here that it is valid.

Rewriting the classical NP equations with new variables φ^* , ψ_b^* and c_{\pm}^* , we obtain in fluid phase Ω_f^* [BOU 12a, DOR 95, GAG 14a, GAG 14b, MOY 02, MOY 06a, SAS 82, SAS 81]:

$$\frac{\partial c_{\pm}^*}{\partial t^*} - \operatorname{div}^* \left(D_{\pm}^* (\operatorname{grad}^* c_{\pm}^* \pm \frac{F}{RT} z_{\pm} c_{\pm}^* \operatorname{grad}^* (\psi_b^* + \varphi^*)) \right) = 0 \text{ in } \Omega_f^* \quad [3.13]$$

$$D_{\pm}^* \left(\operatorname{grad}^* c_{\pm}^* \pm \frac{F}{RT} z_{\pm} c_{\pm}^* \operatorname{grad}^* (\psi_b^* + \varphi^*) \right) . n = 0 \text{ on } \Gamma_{sf}^* \quad [3.14]$$

where c_{\pm}^* , D_{\pm}^* and z_{\pm} denote, respectively, the concentration, diffusion coefficient and valence of cations and anions in Ω_f^* . F and R are, respectively, the Faraday and ideal gas constants, and T is the temperature of the fluid assumed to be constant. Finally, n denotes the external unit normal

⁶ The demonstration of expression [3.12] can be found, for instance, in [MOY 06a].

to Ω_s^* . Equation [3.13] must be completed with Poisson's equation characterizing the electrical potential, which is as follows accounting for [3.11]:

$$\varepsilon_v \Delta^*(\psi_b^* + \varphi^*) = -(\rho_+^* - \rho_-^*) \quad \text{in } \Omega_f^* \quad [3.15]$$

$$\varepsilon_v \operatorname{grad}^*(\psi_b^* + \varphi^*) \cdot n = \sigma^* \quad \text{on } \Gamma_{sf}^* \quad [3.16]$$

where $\varepsilon_v = \varepsilon_0 \varepsilon_f$ denotes the dielectric constant of the fluid phase and ρ_+^* and ρ_-^* are, respectively, the volume electrical charge density of cations and anions in the fluid phase. Electrical surface charge density σ^* is assumed to be constant in the sequel.

Now, let us establish the natural compatibility condition associated with Poisson's equation. Integrating [3.15] upon the fluid domain, we obtain:

$$\int_{\Omega_f} (\varepsilon_v \Delta^*(\psi_b^* + \varphi^*)) d\Omega^* = \int_{\Omega_f} -(\rho_+^* - \rho_-^*) d\Omega^*$$

By applying the divergence theorem and using boundary conditions [3.16], we obtain:

$$\int_{\Omega_f} -(\rho_+^* - \rho_-^*) d\Omega^* = \int_{\Gamma_{sf}} \sigma^* d\Gamma_{sf}^* \quad [3.17]$$

Relation [3.17] represents the global electrical equilibrium in the fluid phase.

Finally, using Boltzmann's law [3.12] for concentrations, the volume electrical charge density ρ^* may be written as a function of the EDL potential φ^* :

$$\rho_+^* - \rho_-^* = -2F|z_\pm|c_b^* \sinh\left(\frac{F|z_\pm|}{RT}\varphi^*\right)$$

Therefore, Poisson's equation [3.15] may be rewritten as:

$$\varepsilon_v \Delta^*(\psi_b^* + \varphi^*) = 2F|z_\pm|C_b^* \sinh\left(\frac{F|z_\pm|}{RT}\varphi^*\right) \quad \text{in } \Omega_f^* \quad [3.18]$$

Equation [3.18] is often called the Poisson–Boltzmann equation. The associated boundary conditions [3.16] remain unchanged:

$$\varepsilon_v \operatorname{grad}^*(\psi_b^* + \varphi^*) \cdot n = \sigma^* \quad \text{on } \Gamma_{sf}^* \quad [3.19]$$

We discuss in the following the outlines of periodic homogenization procedure of the ionic transfer in multiscale saturated porous medium accounting for EDL effects.

3.3.1. Dimensional analysis of equations

The dimensional analysis presented here is similar to that performed in [AUR 81, AUR 91, BOU 12a, BOU 13a, BOU 13b, BOU 12b, HAM 03, MIL 01, MIL 97]. Let us define dimensionless variables as the ratio of dimensional ones (with a star) to reference data (with index r):

$$\begin{aligned} t &= \frac{t^*}{t_r}, \quad y = \frac{y^*}{l}, \quad z = \frac{z^*}{\delta}, \quad D_{\pm} = \frac{D_{\pm}^*}{D_r}, \quad c_{\pm} = \frac{c_{\pm}^*}{c_r}, \quad C_b = \frac{C_b^*}{c_r}, \\ \psi_b &= \frac{\psi_b^*}{\psi_r}, \quad \varphi = \frac{\varphi^*}{\varphi_r}, \quad \sigma = \frac{\sigma^*}{\sigma_r} \end{aligned} \quad [3.20]$$

The characteristic length of the nanoscale δ is used to normalize the spatial differential operators. Replacing the dimensionless variables defined in [3.20] in Nernst–Planck–Poisson–Boltzmann (NPPB) systems [3.13]–[3.14] and [3.18]–[3.19], we obtain the following dimensionless equations:

$$\tau \frac{\partial c_{\pm}}{\partial t} - \operatorname{div} \left(D_{\pm} (\operatorname{grad} c_{\pm} \pm z_{\pm} c_{\pm} \operatorname{grad}(\mathcal{R}^{\psi} \psi_b + \mathcal{R}^{\varphi} \varphi)) \right) = 0 \quad \text{in } \Omega_f \quad [3.21]$$

$$D_{\pm} \left(\operatorname{grad} c_{\pm} \pm z_{\pm} c_{\pm} \operatorname{grad}(\mathcal{R}^{\psi} \psi_b + \mathcal{R}^{\varphi} \varphi) \right) \cdot n = 0 \quad \text{on } \Gamma_{sf} \quad [3.22]$$

$$\mathcal{A}^{\psi} \Delta \psi_b + \mathcal{A}^{\varphi} \Delta \varphi = 2c_b |z_{\pm}| \sinh(R^{\varphi} |z_{\pm}| \varphi) \quad \text{in } \Omega_f \quad [3.23]$$

$$(\mathcal{B}^{\psi} \operatorname{grad} \psi_b + \mathcal{B}^{\varphi} \operatorname{grad} \varphi) \cdot n = \sigma \quad \text{on } \Gamma_{sf} \quad [3.24]$$

where the dimensionless concentrations of cations and anions are given by:

$$c_{\pm} = C_b \exp(\mp |z_{\pm}| \mathcal{R}^{\varphi} \varphi) \quad [3.25]$$

Finally, writing the compatibility condition [3.17] in its dimensionless form, we obtain:

$$\int_{\Omega_f} (\rho_+ - \rho_-) d\Omega + \int_{\Gamma_{sf}} \sigma d\Gamma_{sf} = 0 \quad [3.26]$$

Therefore, the dimensional analysis of equations [3.13]–[3.16] enables to appear the following dimensionless numbers, characterizing the NPPB system at nanoscale including electrochemical interactions:

$$\begin{aligned} \tau &= \frac{\delta^2}{t_r D_r}, \quad \mathcal{R}^\psi = \frac{F\psi_r}{RT}, \quad \mathcal{R}^\varphi = \frac{F\varphi_r}{RT}, \quad \mathcal{A}^\psi = \frac{\varepsilon_v \psi_r}{\delta^2 F c_r}, \\ \mathcal{A}^\varphi &= \frac{\varepsilon_v \varphi_r}{\delta^2 F c_r} \mathcal{B}^\psi = \frac{\varepsilon_v \psi_r}{\delta \sigma_r}, \quad \mathcal{B}^\varphi = \frac{\varepsilon_v \varphi_r}{\delta \sigma_r} \end{aligned} \quad [3.27]$$

– τ is the ratio of the characteristic time of diffusion $\frac{\delta^2}{D_r}$ at the nanoscopic scale to the reference time of diffusion t_r at the microscopic scale;

– the numbers \mathcal{A}^ψ and \mathcal{A}^φ depend, respectively, on the order of magnitude of the bulk potential ψ_r (on the order of magnitude of the EDL potential φ_r , respectively);

– the dimensionless numbers \mathcal{B}^ψ and \mathcal{B}^φ involved in the dimensionless boundary condition [3.24] depend on the ratio of the potential ψ_r (respectively, φ_r) to the surface electrical charge density σ_r , multiplied by the nanoscopic characteristic length δ ;

– finally, the dimensionless numbers \mathcal{R}^ψ and \mathcal{R}^φ depend directly on φ_r and ψ_r .

3.3.2. Reduction to a one scale problem

The periodic homogenization procedure of the ionic transfers requires to relate the dimensionless numbers to the perturbation parameter $\tilde{\varepsilon}$. For the EDL to be involved at the main order in the homogenized model, the size of the elementary cell δ must be of the same order of magnitude as the Debye length

l_D , characteristic length of the EDL. Hence, we must consider here that⁷ $\delta = \mathcal{O}(l_D)$. Let us note that the condition $\mathcal{A}^\varphi = \mathcal{R}^\varphi$ implies that:

$$\delta = \sqrt{\frac{RT}{z^2 F^2 c_r}} = \sqrt{2} l_D$$

where the Debye length is classically given by $l_D = \sqrt{\frac{RT}{2z^2 F^2 c_r}}$.

As in cementitious materials, the Debye length is of order 10^{-9} m, which is reasonable to consider that $\delta = 10^{-8}$ m, in order for the elementary cell to contain several times the characteristic length of heterogeneities. Thus, the homogenization procedure will be performed from the nanoscale δ to the microscale l . Note that l may be evaluated from mercury intrusion porosimetry, as in [BOU 13a, BOU 13b, BOU 12a, BOU 12b, MIL 08]. It leads to the value $l = 10 \mu\text{m}$. Consequently, the perturbation parameter $\tilde{\varepsilon} = \frac{\delta}{l}$ considered here is $\tilde{\varepsilon} = 10^{-3}$. With this value of $\tilde{\varepsilon}$, the homogenization from Debye length should lead to a homogenized model characterizing the ionic transfers at the capillary porosity scale of cement pastes, accounting for the electrocapillary effects at the solid–fluid interfaces. In this chapter, we are interested in the degradation of constructions in extreme conditions as marine environment. When the ionic transfer occurs under natural conditions (without an applied external electrical field), the characteristic time t_r is of several months for cement paste. Moreover, in the absence of external electrical field, the induced EDL potential is of the same order of the bulk potential (a few millivolts [CHA 98]). Thus, we will consider here that $\Psi_r = \psi_r = \varphi_r$.

Even if it is difficult to measure experimentally the value of the surface density charge σ_r in cementitious materials, this important parameter may be estimated indirectly from the value of the zeta potential. As the latter that may be measured experimentally is of the order of a few millivolts in the case of cementitious pastes [HOC 12], we will consider that $\sigma_r = 0.02 C/m^2$. This allows us to recover the same order of magnitude of the EDL potential at the solid–fluid interface.

⁷ The notation \mathcal{O} means “is of the same order of magnitude”.

Moreover, the reference concentration may be chosen of same order as the concentration of chlorides used in the electrodiffusion tests⁸ performed in laboratory [AÏT 04, AMI 01b, BOU 13b]. Therefore, we will consider here that the reference concentration is $c_r = 500 \text{ mol}/\text{m}^3$. Finally, the constants involved in the equations are given by $D_r = 10^{-9} \text{ m}^2/\text{s}$, $\varepsilon_v = 7.08810^{-10} \text{ F}/\text{m}$, $F = 9.65 \cdot 10^4 \text{ C/mol}$, $R = 8.3143 \text{ J/mol.K}$ and $T = 298 \text{ K}$ (the temperature is assumed to be constant).

Accordingly, in the case of an ionic transfer under natural conditions, the orders of magnitude of the dimensionless numbers characterizing the ionic transfer to be considered stand:

$$\begin{aligned}\tau &= \mathcal{O}(\tilde{\varepsilon}^2), & \mathcal{A}^\psi &= \mathcal{O}(1), & \mathcal{A}^\varphi &= \mathcal{O}(1), & \mathcal{R}^\psi &= \mathcal{O}(1) \\ \mathcal{R}^\varphi &= \mathcal{O}(1), & \mathcal{B}^\varphi &= \mathcal{O}(1), & \mathcal{B}^\psi &= \mathcal{O}(1)\end{aligned}\quad [3.28]$$

We search the unknowns of the problem (C_b, ψ_b, φ) as functions depending on the variables y, z and the time t , which are considered as separate variables. This is due to the separation of scale condition ($\tilde{\varepsilon} \ll 1$). Moreover, (C_b, ψ_b, φ) are assumed to allow a formal expansion with respect to the perturbation parameter $\tilde{\varepsilon}$:

$$C_b(y, z, t) = C_b^0(y, z, t) + \tilde{\varepsilon} C_b^1(y, z, t) + \tilde{\varepsilon}^2 C_b^2(y, z, t) + \dots \quad [3.29]$$

$$\psi_b(y, z, t) = \psi_b^0(y, z, t) + \tilde{\varepsilon} \psi_b^1(y, z, t) + \tilde{\varepsilon}^2 \psi_b^2(y, z, t) + \dots \quad [3.30]$$

$$\varphi(y, z, t) = \varphi^0(y, z, t) + \tilde{\varepsilon} \varphi^1(y, z, t) + \tilde{\varepsilon}^2 \varphi^2(y, z, t) + \dots \quad [3.31]$$

Note that owing to the separation of scale, the operators of derivative such as gradient, divergence and Laplacian operators are transformed into:

$$grad = \nabla_z + \tilde{\varepsilon} \nabla_y; \quad div = div_z + \tilde{\varepsilon} div_y; \quad \Delta = \Delta_z + 2\tilde{\varepsilon} \frac{\partial^2}{\partial y \partial z} + \tilde{\varepsilon}^2 \Delta_y \quad [3.32]$$

⁸ The concentration of chlorides used is estimated from the chlorides concentration in seawater.

3.3.3. Homogenized microscopic diffusion-migration model with EDL

Replacing the dimensionless numbers with their order of magnitude [3.28] in NPPB system [3.21]–[3.24], we obtain the following problem depending on the perturbation parameter $\tilde{\varepsilon}$:

$$\tilde{\varepsilon}^2 \frac{\partial c_{\pm}}{\partial t} - \operatorname{div}(D_{\pm}(\operatorname{grad}c_{\pm} \pm |z_{\pm}|c_{\pm}\operatorname{grad}(\psi_b + \varphi))) = 0 \quad \text{in } \Omega_f \quad [3.33]$$

$$D_{\pm}(\operatorname{grad}c_{\pm} \pm |z_{\pm}|c_{\pm}\operatorname{grad}(\psi_b + \varphi)) \cdot n = 0 \quad \text{on } \Gamma_{sf} \quad [3.34]$$

$$\Delta(\psi_b + \varphi) = 2C_b|z_{\pm}| \sinh(|z_{\pm}|\varphi) \quad \text{in } \Omega_f \quad [3.35]$$

$$\operatorname{grad}(\psi_b + \varphi)n = \sigma \quad \text{on } \Gamma_{sf} \quad [3.36]$$

where the concentrations of cations and anions are given by Boltzmann's law:

$$c_{\pm} = C_b \exp(\mp|z_{\pm}|\varphi). \quad [3.37]$$

Replacing expansions [3.29]–[3.31] and the derivative operators [3.32] in the dimensionless equations [3.33]–[3.36], we obtain different coupled problems $\mathcal{P}_0, \mathcal{P}_1, \dots$ corresponding, respectively, to the cancellation of the factors of $\tilde{\varepsilon}^0, \tilde{\varepsilon}^1, \dots$

Next, we present the result of the periodic homogenization procedure applied to ionic transfer in cementitious materials. This procedure is first conducted from the nanoscale to the microscale by taking into account the EDL phenomenon in the ionic transfer equations (see [BOU 12b] for more details). The following result is directly given in its dimensional form.

RESULT 3.1.– For natural ionic diffusion, the orders of magnitude of the dimensionless numbers characterizing the ionic transfer are $\tau = \mathcal{O}(\tilde{\varepsilon}^2)$, $\mathcal{A}^{\psi} = \mathcal{O}(1)$, $\mathcal{A}^{\varphi} = \mathcal{O}(1)$, $\mathcal{R}^{\psi} = \mathcal{O}(1)$, $\mathcal{R}^{\varphi} = \mathcal{O}(1)$, $\mathcal{B}^{\varphi} = \mathcal{O}(1)$ and $\mathcal{B}^{\psi} = \mathcal{O}(1)$. The unknowns C_b^* , ψ_b^* and φ^* are the solutions of the dimensional homogenized diffusion-migration model at the intermediary

homogenized scale:

$$\begin{aligned} \varepsilon_n \frac{\partial}{\partial t^*} \left(C_b^* \left\langle \exp(\mp \frac{F|z_\pm|}{RT} \varphi^*) \right\rangle \right) \\ - \operatorname{div}_y^* \left(\mathbf{D}_\pm^{*\text{hom}} \left(\frac{\partial C_b^*}{\partial y^*} \pm \frac{F|z_\pm|}{RT} C_b^* \frac{\partial \psi_b^*}{\partial y^*} \right) \right) = 0 \end{aligned} \quad [3.38]$$

where $\varepsilon_n = \frac{|\Omega_f^*|}{|\Omega^*|}$ denotes the nanoporosity of the considered porous medium and y^* the intermediary scale after a first homogenization step (from Debye to microscale length). The dimensional homogenized diffusion tensor $\mathbf{D}_\pm^{*\text{hom}}$ is given by:

$$\mathbf{D}_\pm^{*\text{hom}} = \frac{1}{|\Omega^*|} \int_{\Omega_f} \left(D_\pm^* \exp(\mp \frac{F|z_\pm|}{RT} \varphi^*) (I + \overline{\frac{\partial \chi_\pm^*}{\partial z^*}}) \right) d\Omega_f^* \quad [3.39]$$

where the vector $\chi_\pm^*(z)$ is periodic of zero average on Ω_f^* and solution of the boundary value problem:

$$\operatorname{div}_z^* \left(\mp D_\pm^* |z_\pm| \exp(\mp \frac{F|z_\pm|}{RT} \varphi^*) (I + \overline{\frac{\partial \chi_\pm^*}{\partial z^*}}) \right) = 0 \quad \text{in } \Omega_f^* \quad [3.40]$$

$$\mp D_\pm^* |z_\pm| \exp(\mp \frac{F|z_\pm|}{RT} \varphi^*) \left(I + \overline{\frac{\partial \chi_\pm^*}{\partial z^*}} \right) \cdot n = 0 \quad \text{on } \Gamma_{sf}^* \quad [3.41]$$

The EDL potential φ^* is the solution of the Poisson–Boltzmann equation:

$$\varepsilon_v \Delta_z^* \varphi^* = 2F|z_\pm| C_b^* \sinh(\frac{F|z_\pm|}{RT} \varphi^*) \quad \text{in } \Omega_f^* \quad [3.42]$$

$$\varepsilon_v \frac{\partial \varphi^*}{\partial z^*} \cdot n = \sigma^* \quad \text{on } \Gamma_{sf}^* \quad [3.43]$$

The complete proof of this result is detailed in [BOU 12b] with slightly different notations. It has been adapted to perform the double homogenization procedure developed in this chapter.

3.4. Particular case of ionic transfer without EDL

We have obtained in the previous section a homogenized diffusion-migration model at the microscale involving the EDL phenomenon. We will now perform an upscaling from the microscale to the macroscale, using the same procedure as previously, starting again from transfer equations [3.13]–[3.17] taking into account the electrocapillary interactions.

3.4.1. Dimensional analysis and scale problem

As discussed in section 3.3, we define the dimensionless variables as the ratio of the dimensional ones (with a star) to the reference data (with index r). Obviously, the reference variables must be adapted from [3.20] to take into account the new scale:

$$\begin{aligned} t &= \frac{t^*}{t_r}, \quad x = \frac{x^*}{L}, \quad y = \frac{y^*}{l}, \quad D_{\pm} = \frac{D_{\pm}^*}{D_r}, \quad c_{\pm} = \frac{c_{\pm}^*}{c_r}, \\ \psi_b &= \frac{\psi_b^*}{\psi_r}, \quad \varphi = \frac{\varphi^*}{\varphi_r}, \quad \sigma = \frac{\sigma^*}{\sigma_r} \end{aligned} \quad [3.44]$$

Using the characteristic length of the microscale l to normalize the derivative operators, the dimensionless equations obtained are similar to [3.21]–[3.24]. In a similar way, we must relate the dimensionless numbers to the new perturbation parameter $\varepsilon = \frac{l}{L}$. A new dimensional analysis of NPPB equations leads to the following dimensionless numbers, characterizing the ionic transfer at the micrometer scale l of the elementary cell:

$$\begin{aligned} \tau &= \frac{l^2}{t_r D_r}, \quad \mathcal{R}^{\psi} = \frac{F \psi_r}{RT}, \quad \mathcal{R}^{\varphi} = \frac{F \varphi_r}{RT}, \quad \mathcal{A}^{\psi} = \frac{\varepsilon_v \psi_r}{l^2 F c_r} \\ \mathcal{A}^{\varphi} &= \frac{\varepsilon_v \varphi_r}{l^2 F c_r}, \quad \mathcal{B}^{\psi} = \frac{\varepsilon_v \psi_r}{l \sigma_r}, \quad \mathcal{B}^{\varphi} = \frac{\varepsilon_v \varphi_r}{l \sigma_r} \end{aligned} \quad [3.45]$$

The order of magnitude of the dimensionless number [3.45] must be linked to ε chosen as the perturbation parameter of the problem.

First, the size l of the new elementary cell has already been fixed, based on mercury intrusion porosimetry [BOU 13a, MIL 08], in the previous homogenization procedure. Note that $l = 10 \mu\text{m}$ corresponds to the

“macroscale” in section 3.3. Accounting for the new reference scale $l = 10 \mu\text{m}$, the other reference data being unchanged, we obtain the following orders of magnitude of dimensionless numbers⁹:

$$\tau = \mathcal{O}(\varepsilon^2), \mathcal{A}^\psi = \mathcal{A}^\varphi = \mathcal{O}(\varepsilon^3), \mathcal{R}^\varphi = \mathcal{R}^\psi = \mathcal{O}(1), \mathcal{B}^\psi = \mathcal{B}^\varphi = \mathcal{O}(\varepsilon^2) [3.46]$$

3.4.2. Homogenized macroscopic diffusion-migration model

Replacing the dimensionless number by their order of magnitude [3.46] in NPPB equations [3.21]–[3.24], we obtain the new problem:

$$\varepsilon^2 \frac{\partial c_\pm}{\partial t} - \operatorname{div} (D_\pm (\operatorname{grad} c_\pm \pm |z_\pm| c_\pm \operatorname{grad}(\psi_b + \varphi))) = 0 \quad \text{in } \Omega_f [3.47]$$

$$D_\pm (\operatorname{grad} c_\pm \pm |z_\pm| c_\pm \operatorname{grad}(\psi_b + \varphi)) \cdot n = 0 \quad \text{on } \Gamma_{sf} [3.48]$$

$$\varepsilon^3 (\Delta \psi_b + \Delta \varphi) = 2C_b |z_\pm| \sinh(|z_\pm| \varphi) \quad \text{in } \Omega_f [3.49]$$

$$\varepsilon^2 (\operatorname{grad} \psi_b + \operatorname{grad} \varphi) \cdot n = \sigma \quad \text{on } \Gamma_{sf} [3.50]$$

Replacing in equations [3.47]–[3.50] the unknowns of the problem (C_b, ψ_b, φ) with a formal expansions similar to [3.29]–[3.31], performed with respect to the new perturbation parameter ε (instead of $\tilde{\varepsilon}$), we obtain again¹⁰ a chain of coupled problems $\mathcal{P}_0, \mathcal{P}_1 \dots$

At the leading order, problem \mathcal{P}_0 , resulting from the Poisson–Boltzmann equation [3.49] and the associated boundary condition [3.50], reduces to:

$$2C_b^0 |z_\pm| \sinh(|z_\pm| \varphi^0) = 0 \quad \text{in } \Omega_f [3.51]$$

$$\sigma = 0 \quad \text{on } \Gamma_{sf} [3.52]$$

Equations [3.51]–[3.52] mean that accounting for the characteristic size of the microstructure considered here (μm order), several orders larger than Debye length (nm order), EDL effects are not involved in the ionic transfer at the main order.

⁹ Under natural diffusion conditions that are considered here.

¹⁰ Note that a transformation of the derivative similar to [3.32] must be used.

Accordingly, in the following, we will start again from NPP equations without the EDL effects ($\sigma = 0$ and therefore $\varphi = 0$). As $\varphi = 0$ and $c_+ = c_- = C_b$, NPP equations are rewritten with a total potential Ψ , the decomposition [3.11] having no sense anymore.

Moreover, for the problem to be physically consistent, we will use multispecies notations (c_k , $k \in \{1, \dots, N\}$), instead of considering only cation and anion concentrations c_+ and c_- (as we have electroneutrality in solution, i.e. $c_+ = c_-$, when EDL effects are neglected).

Starting again from notations of [MIL 08, SAM 99] and accounting from the results obtain here, we have the following dimensionless transfer equations without any EDL effects in the multispecies framework (N species):

$$\tau \frac{\partial c_k}{\partial t} - \operatorname{div}(D_k \operatorname{grad} c_k + \mathcal{R} D_k z_k c_k \operatorname{grad} \Psi) = 0 \quad \text{in } \Omega_f \quad [3.53]$$

$$\mathcal{A} \Delta \Psi = -\rho \quad \text{in } \Omega_f \quad [3.54]$$

with $\rho = \sum_{k=1}^N z_k c_k$ and the associated boundary conditions:

$$D_k(\operatorname{grad} c_k + \mathcal{R} z_k c_k \operatorname{grad} \Psi).n = 0 \quad \text{on } \Gamma_{sf} \quad [3.55]$$

$$(\operatorname{grad} \Psi).n = 0 \quad \text{on } \Gamma_{sf} \quad [3.56]$$

where c_k , D_k and z_k denote the concentration, diffusion coefficient (obtained from the first homogenization procedure) and valence of ionic species k . The dimensionless numbers to be considered now reduce to:

$$\tau = \frac{l^2}{t_r D_r}, \quad \mathcal{R} = \frac{F \Psi_r}{RT}, \quad \mathcal{A} = \frac{\varepsilon_v \Psi_r}{l^2 F c_r}$$

We then have the following result whose proof is detailed in [BOU 13a, BOU 12a] and is not recalled here.

RESULT 3.2.– For dimensionless numbers such that $\tau = O(\varepsilon^2)$ $\mathcal{R} = O(1)$ and $\mathcal{A} = O(\varepsilon^2)$, the dimensional concentration c_k^* satisfies the electroneutrality assumption:

$$\rho^* = \sum_{k=1}^N F z_k c_k^* = 0 \quad [3.57]$$

Moreover, the macroscopic concentration c_k^* and potential Ψ^* at the scale of the material are solutions of the dimensional homogenized diffusion-migration model:

$$\varepsilon_m \frac{\partial c_k^*}{\partial t^*} - \operatorname{div}_x \left(\mathbf{D}_k^{*\text{hom}} \frac{\partial^* c_k^*}{\partial x^*} + \frac{F z_k}{RT} \mathbf{D}_k^{*\text{hom}} \frac{\partial^* \Psi^*}{\partial x^*} c_k^* \right) = 0 \quad [3.58]$$

where ε_m denotes the porosity of the porous medium at the microscale. The homogenized diffusion tensor $\mathbf{D}_k^{*\text{hom}}$ is given by:

$$\mathbf{D}_k^{*\text{hom}} = \frac{1}{|\Omega_f^*|} \int_{\Omega_f^*} D_k^* \left(I + \frac{\partial \chi^*}{\partial y^*} \right) d\Omega^* \quad [3.59]$$

where the vector $\chi^*(y^*)$ is periodic of zero average on Ω_f^* and solution of the boundary problem:

$$\operatorname{div}_y \left(D_k^* \left(I + \frac{\partial \chi^*}{\partial y^*} \right) \right) = 0 \quad \text{in } \Omega_f^* \quad [3.60]$$

$$D_k^* \left(I + \frac{\partial \chi^*}{\partial y^*} \right) . n = 0 \quad \text{on } \Gamma_{sf}^* \quad [3.61]$$

3.5. Simulations and parametric study of the EDL effects

In this section, we focus on the calculation of the homogenized diffusion tensor at the macroscopic scale, accounting for the multiscale nature of the cementitious material considered. This calculation will be performed in two steps. First, we compute the diffusion tensor resulting from the first homogenization procedure, performing from the nanoscale to the microscale accounting for the EDL phenomenon (result [3.1]). Second, we compute the diffusion tensor at the macroscale resulting from the second homogenization procedure performed from the microscale to the macroscale (result [3.2]). In

this second homogenization procedure, the EDL is naturally neglected. Before performing a complete multiscale computation of the homogenized diffusion tensor in section 3.6, the influence of the EDL will be highlighted for various two-dimensional (2D) and 3D elementary cells characterizing the nanostructure. In order to calculate the homogenized diffusion tensor given by [3.39], we must resolve first the Poisson–Boltzmann problem [3.42]–[3.43] to determine φ^* . In the second step, the resolution of the nonlinear problem [3.40]–[3.41] enables us to determine vector χ_{\pm}^* which is coupled to φ^* .

Let us note that the Poisson–Boltzmann problem [3.42]–[3.43] involves physical parameters considered as data of the problem. To highlight the influence of the physical parameters (σ^* , C_b^*) on the potential φ^* and the diffusion tensor $D_{\pm}^{*\text{hom}}$, a parametric study will be conducted on several 2D and 3D elementary cells representing the nanostructure.

3.5.1. Implementation in COMSOL Multiphysics software and validation

The numerical resolution of equations [3.39]–[3.43] is performed with the finite elements COMSOL Multiphysics software that is particularly well adapted to solve nonlinear coupled problems. We use the following predefined system of partial differential equations to solve the nonlinear weakly coupled problem [3.39]–[3.43]:

$$\operatorname{div}(\alpha \operatorname{grad}(u)) = \beta \quad \text{in } \Omega_f^* \quad [3.62]$$

$$\operatorname{grad}(u) \cdot n = \gamma \quad \text{on } \Gamma_{sf}^* \quad [3.63]$$

$$\operatorname{div}(\mathbf{J}) = F \quad \text{in } \Omega_f^* \quad [3.64]$$

$$\operatorname{grad}(\mathbf{J}) \cdot n = G \quad \text{on } \Gamma_{sf}^* \quad [3.65]$$

where u is a scalar variable, α , β and γ are any functions of the spatial coordinates and n is the unit external normal vector to Ω_f^* . Furthermore, \mathbf{J} denotes a flux tensor and F and G are right-hand side functions depending on the spatial coordinates. In our case, we solve equations [3.62]–[3.65] for chlorides with:

$$u = \varphi^*, \quad \alpha = \varepsilon_v, \quad \beta = 2F|z_-|C_b^* \sinh\left(\frac{F|z_-|}{RT}\varphi^*\right), \quad \gamma = \frac{\sigma^*}{\varepsilon_v}$$

$$\mathbf{J} = D_-^* |z_-| \exp\left(\frac{F|z_-|}{RT} \varphi^*\right) \left(I + \frac{\partial \chi_-^*}{\partial y^*} \right), \quad F = G = 0$$

The numerical resolution requires to use Newton–Raphson method to solve the nonlinear coupled problem. The gradient conjugate iterative solver is used to solve the linearized problem.

The numerical resolution of the partial differential equations [3.39]–[3.43] will be compared to the semi-analytical solution obtained in [MOY 06b], where an electro-chemo-mechanical coupling model of solute transport in clays is presented¹¹. The authors have solved equations [3.39]–[3.43] in the case of a semi-infinite channel in z_1^* direction as presented in Figure 3.4. The height of the channel is $2H$ and the transfer occurs in the fluid domain Ω_f^* in z_1^* direction.

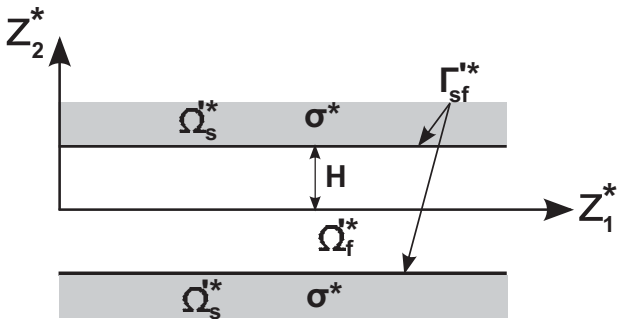


Figure 3.4. Semi-infinite channel

The parameters of the model (surface charge density and bulk concentration) are supposed to be constant. The values considered here are $\sigma^* = -0.2 \text{ C/m}^2$ and $C_b^* = 23.2 \text{ mol/m}^3$, corresponding to those used in [MOY 06b]. The half height H of the semi-infinite channel is equal to the Debye length l_D , which can be calculated from the following expression:

$$l_D = \sqrt{\frac{\varepsilon_v RT}{2z^2 F^2 C_b^*}}$$

¹¹ This model is based on NPPB equations.

The values of parameters and physical constants used in the numerical resolution are summarized in Table 3.1.

T	293 K
F	96,490 C/mol
R	8.3143 J/molK
ε_v	80×8.85410^{-12} F/m
σ	-0.2 C/m ²
C_b	23.2 mol/m ³
H/l_D	1

Table 3.1. Data of the numerical simulation

As the channel is semi-infinite in z_1^* direction, the electrical potential φ^* induced by the EDL phenomenon, solution of the Poisson–Boltzmann problem [3.42]–[3.43], depends only on z_2^* ($\varphi^* = \varphi^*(z_2^*)$). It is important to note that the surface charge density σ^* is imposed on the wall of the channel corresponding to the solid–fluid interface Γ_{sf}^* . The numerical solution computed by COMSOL Multiphysics software is presented in Figures 3.5(a) and 3.6(a). It corresponds exactly to the semi-analytical solution obtained in [MOY 06b] (Figures 3.5(b) and 3.6(b)). This enables us to validate the numerical resolution performance with COMSOL Multiphysics.

We note that the electrical potential induced by the EDL is maximum (in absolute value) on the interface Γ_{sf}^* and minimum in the center of the channel.

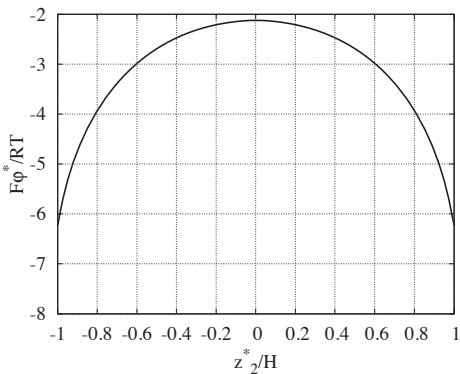
The dimensionless electrical field reaches zero at $z_2^* = 0$ and it maximum (in absolute value) at the interface Γ_{sf}^* . For $H/l_D = 1$, all the fluid domain Ω_f^* is concerned with the EDL phenomenon.

3.5.2. Bidimensional elementary cells

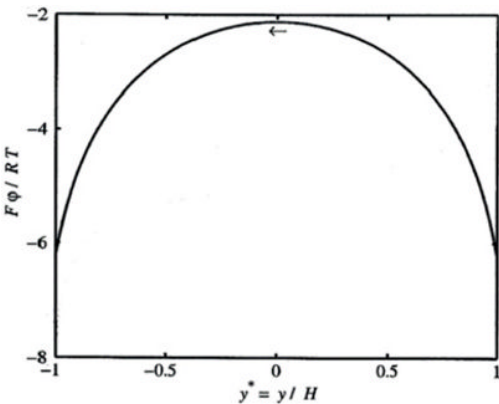
3.5.2.1. Elementary cell with circular inclusion

Let us now consider a porous media constituted of the repetition of elementary cells of size $10^{-8} \times 10^{-8}$ m composed themselves of a circular inclusion of radius R located at the center (Figure 3.7(a)). The solid phase Ω_s^* is represented by the circular inclusion and the fluid phase Ω_f^* is represented by the complementary domain. We begin with resolving the nonlinear weakly coupled problem [3.40]–[3.43] to determine φ^* and χ_-^* . After that, we

compute the homogenized diffusion tensor given by expression [3.39]. The boundary of the circular inclusion represents the solid–fluid interface Γ_{sf}^* , where the boundary conditions [3.41] and [3.43] are imposed. The external boundaries of the elementary cells correspond to the fluid–fluid interface Γ_{ff}^* on which the periodic boundary conditions are imposed.



a) Numerical solution obtained by Comsol Multiphysics.

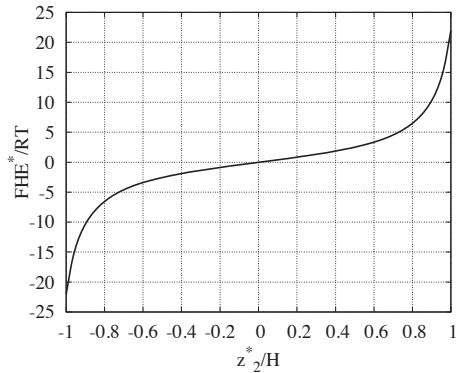


b) Solution of Moyne and Murad [MOY 06b]

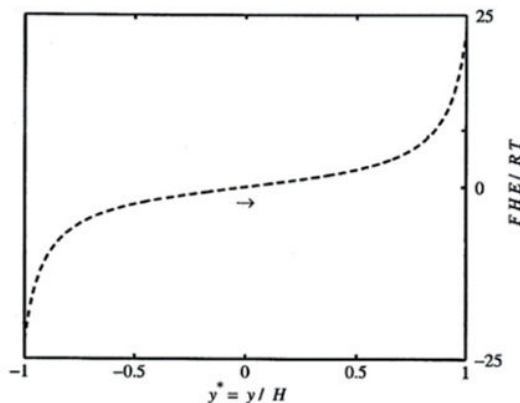
Figure 3.5. Evolution of the dimensionless electrical potential $\frac{F\varphi}{RT}$ as a function of $\frac{z_2}{H}$

Figure 3.7(b) shows the triangular finite element mesh performed for numerical resolution. For an elementary cell containing a circular inclusion of radius $R = 0.3 \cdot 10^{-8} m$, the number of triangular elements is 2,540 for

16,080 degrees of freedom. The triangular mesh is refined near the interface solid–fluid Γ_{sf}^* where the electrical field is important.



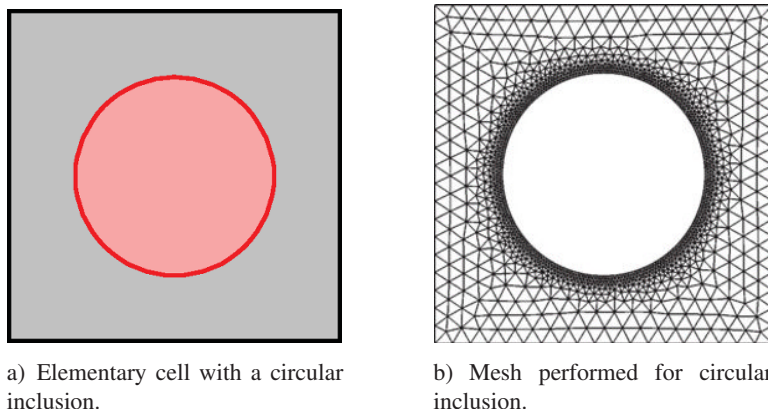
a) Numerical solution obtained by Comsol Multiphysics.



b) Solution of Moyne and Murad [MOY 06b].

Figure 3.6. Evolution of the dimensionless electrical field $\frac{FHE}{RT}$ as a function of $\frac{z_2}{H}$

We begin with studying the influence of the physical parameters (σ^* , C_b^*) on the electrical potential induced by the EDL. In a first time, the surface charge density is considered as the variable parameter and the bulk concentration is fixed to $C_b^* = 86 \text{ mol/m}^3$.



a) Elementary cell with a circular inclusion.

b) Mesh performed for circular inclusion.

Figure 3.7. Elementary cell with a circular inclusion. For a color version of the figure, see www.iste.co.uk/ait-mokhtar/coastal.zip

Figure 3.8 represents the distribution of the EDL electrical potential φ^* in mV. We note that the EDL potential reaches its maximum value (in absolute value) on the solid–fluid interface Γ_{sf}^* , where the surface charge density is required. Far from the interface Γ_{sf}^* , the electrical potential induced by the EDL decreases to its minimum value located on the fluid–fluid interface Γ_{ff}^* .

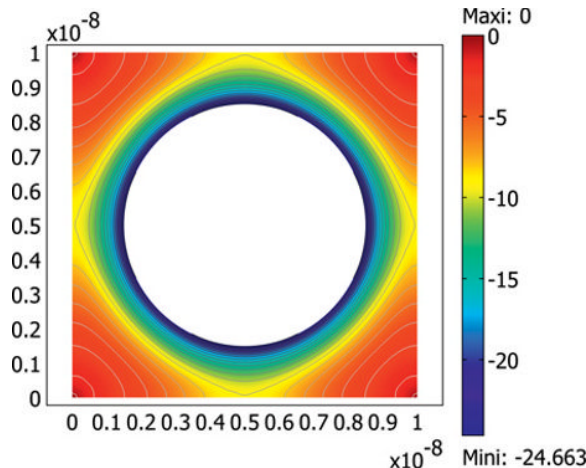
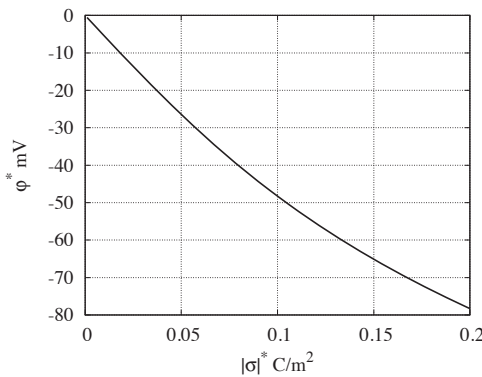


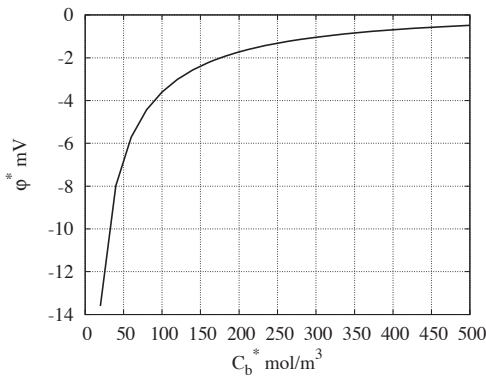
Figure 3.8. EDL potential φ mV for $|\sigma| = 0.0185 \text{ C/m}^2$, $C_b = 86 \text{ mol/m}^3$ and $\varepsilon_n = 61.5\%$. For a color version of the figure, see www.iste.co.uk/ait-mokhtar/coastal.zip

Let us consider an elementary cell of 87% of porosity. The surface charge density $|\sigma^*|$ varies in $[0 \text{ } 0.2] \text{ C/m}^2$ and the bulk concentration is fixed to $C_b^* = 500 \text{ mol/m}^3$. Figure 3.9(a) presents the variation of EDL potential in mV at any point of the interface solid–fluid Γ_{sf}^* versus the absolute value of the surface charge density $|\sigma^*|$.

We observe that the EDL potential $|\varphi^*|$ increases when $|\sigma^*|$ increases due to the more important accumulation of ions near the solid–fluid interface Γ_{sf}^* .



- a) Variation of φ^* vs $|\sigma^*|$ for $C_b = 500 \text{ mol/m}^3$.



- b) Variation of φ^* vs C_b for $|\sigma^*| = 0.011 \text{ C/m}^2$.

Figure 3.9. Variation of the EDL potential versus (σ^*, C_b)

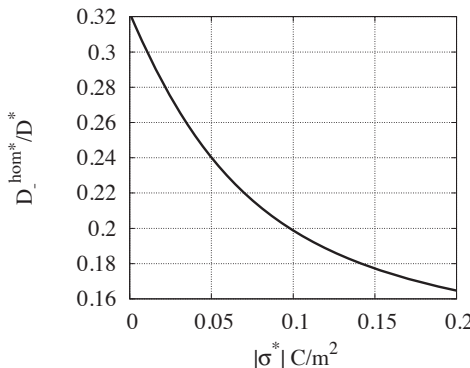


Figure 3.10. Relative homogenized diffusion coefficient versus the surface charge density for $\varepsilon_p = 49.7\%$ and $C_b = 500 \text{ mol/m}^3$

In a second time, the surface charge density is fixed to $|\sigma^*| = 0.011 \text{ C/m}^2$ and the bulk concentration is considered as the variable parameter $C_b^* \in [10 \text{ } 500] \text{ mol/m}^3$. We observe that the EDL potential increases in absolute value when C_b^* decreases. Indeed, the decrease in C_b^* leads to an increase in Debye length l_D (characteristic length of the EDL effects) and therefore to an increase in the EDL effects.

Let us now underscore the influence of the parameters (σ^*, C_b^*) on the relative homogenized diffusion coefficient D_{hom}^*/D . Figure 3.10 represents the variation of the relative homogenized diffusion coefficient D_{hom}^*/D as a function of σ^* for an elementary cell with 49.7% of porosity.

We note that the relative homogenized diffusion coefficient D_{hom}^*/D decreases when $|\sigma^*|$ increases. This result remains valid for anions because of the decreasing of the expression $\exp\left(\frac{F|z_-|}{RT}\varphi^*\right)$ involved in expression [3.39] where φ^* is negative.

For σ^* fixed, D_{hom}^*/D increases when C_b^* increases (Figure 3.11) because of the decreasing of the Debye length l_D .

Therefore, the increase in the bulk concentration leads to accelerate the ionic transfer of anions in the porous medium.

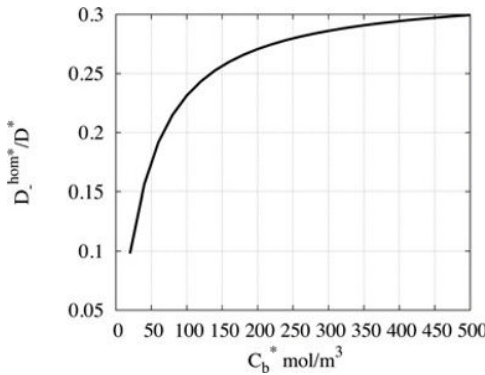


Figure 3.11. Relative homogenized diffusion coefficient versus C_b for $\varepsilon_p = 49.7\%$ and $|\sigma| = 0.011 \text{ C}/\text{m}^2$

The influence of (σ^*, C_b^*) on the relative homogenized diffusion coefficient D_{hom^*}/D for different porosities of the elementary cell is represented in Figure 3.12. To adjust the porosity ε_n , the radius of the circular inclusion varies in the interval $R \in [0.10.495] \times 10^{-8} \text{ m}$, which leads to $\varepsilon_n \in [0.23, 0.96]$. As mentioned previously, we consider C_b^* as a fixed parameter and the surface charge density varying $\sigma^* \in [0.001, 0.02] \text{ C}/\text{m}^2$.

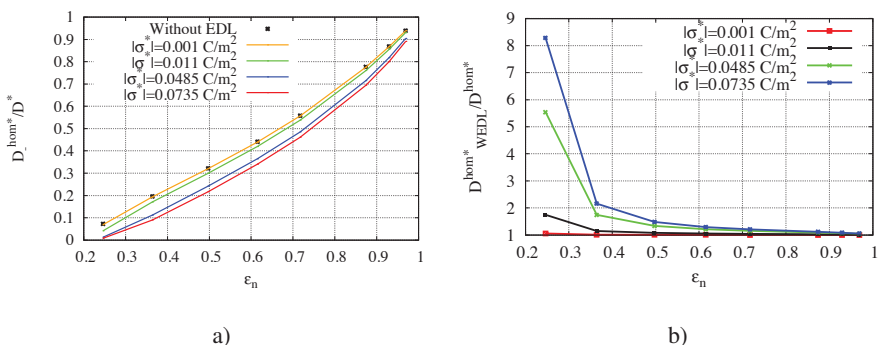


Figure 3.12. a) D_{hom^*}/D vs ε_n for $C_b = 500 \text{ mol}/\text{m}^3$ and different values of σ ; b) $D_{WEDL}^{hom^*}/D^{hom^*}$ vs ε_n for $C_b = 500 \text{ mol}/\text{m}^3$ and different values of σ . For a color version of the figure, see www.iste.co.uk/ait-mokhtar/coastal.zip

We observe that the curves corresponding to $|\sigma^*| = 10^{-3} \text{ C}/\text{m}^2$ and $\sigma^* = 0$ nearly coincide: the EDL has no influence on the relative

homogenized diffusion coefficient for very low values of σ^* . For higher values of σ^* , the relative homogenized diffusion coefficient D_{hom^*}/D^* decreases when $|\sigma^*|$ increases. This decrease is all the more important for low porosities when the solid–fluid interfaces are closer to each other.

In order to quantify more precisely this variation, we show in Figure 3.12(b) the ratio $D_{\text{WEDL}}^{\text{hom}^*}/D_{-}^{\text{hom}^*}$ versus the porosity for different values of σ^* , where $D_{\text{WEDL}}^{\text{hom}^*}$ (respectively, $D_{-}^{\text{hom}^*}$) denotes the homogenized diffusion coefficient without (respectively, with) accounting for the EDL. We observe that the influence of the EDL on the homogenized diffusion coefficient strongly depends on the porosity of the elementary cell, or equivalently on the size of the solid–fluid interface Γ_{sf}^* . For large porosities, the ratio $D_{\text{WEDL}}^{\text{hom}^*}/D_{-}^{\text{hom}^*}$ is equal to 1, whatever the value of σ^* is. In this case, the porosity is so important with respect to the size of the interface Γ_{sf}^* that the EDL has no influence on the ionic transfer. Conversely, for low porosities, the ratio $D_{\text{WEDL}}^{\text{hom}^*}/D_{-}^{\text{hom}^*}$ becomes important: the EDL slows down the transfer of anions (or accelerates the transfer of cations) in pores of small size.

Curves similar to that shown in Figures 3.12(a) and 3.12(b) would be obtained if σ^* is fixed and C_b^* varies.

3.5.2.2. More complex elementary cell

Let us consider a more complex cell geometry given in Figure 3.13(a), which is composed of a disk located at the center of the cell and of a quarter of disk of smaller radius located at each corner of the cell. This way, we have a more complex tortuosity and constrictivity of the porous network of the material.

The length of each side of the periodic cell is 10^{-8} m . The bigger disk, located at the center of the unit cell, has a radius $R = 0.45 \cdot 10^{-8} \text{ m}$. The quarters of disk have a varying radius $r \in [0.05, 0.255] \cdot 10^{-8} \text{ m}$, leading to porosities of the material $\varepsilon_n \in [0.16, 0.37]$.

As previously, we focus on the influence of the EDL on the ionic transfer parameters. The same problem [3.40]–[3.43] is solved in order to calculate the homogenized diffusion tensor D_{hom^*} given by [3.39]. First, we consider the surface charge density σ^* as a variable parameter, whereas the bulk concentration C_b^* is fixed to 500 mol/m^3 . The variation of the relative

homogenized diffusion coefficient is shown in Figure 3.14(a) according to the porosity of the elementary cell for different values of σ^* .

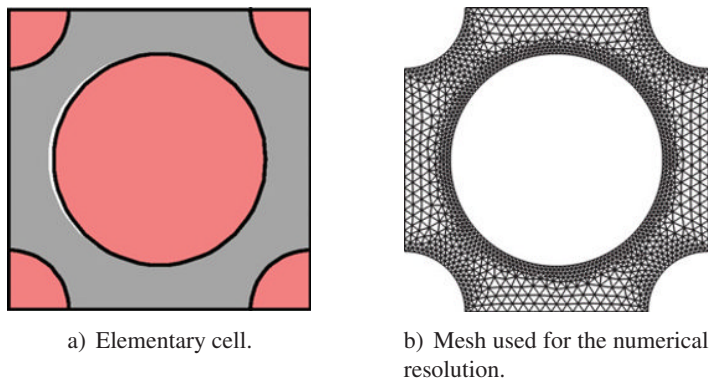


Figure 3.13. More complex elementary cell. For a color version of the figure, see www.iste.co.uk/ait-mokhtar/coastal.zip

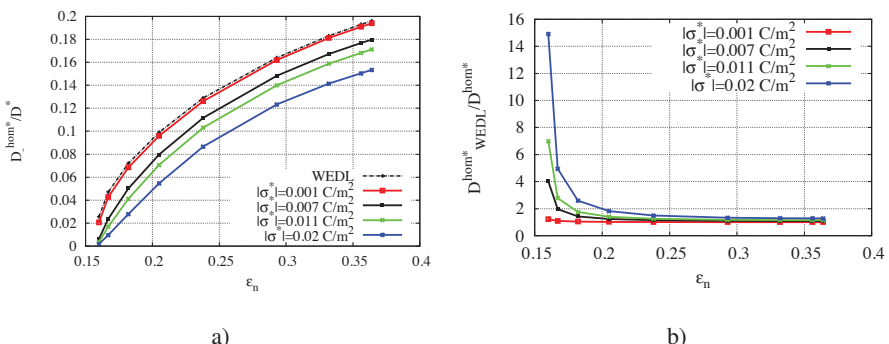


Figure 3.14. a) Relative homogenized diffusion coefficient vs ε_n for $C_b = 500 \text{ mol/m}^3$ and different values of σ^* ; b) Variation of ratio $D_{\text{WEDL}}^{\text{hom}} / D_{\text{hom}}^{\text{WEDL}}$ vs ε_n for $C_b = 500 \text{ mol/m}^3$ and different values of σ^* . For a color version of the figure, see www.iste.co.uk/ait-mokhtar/coastal.zip

We observe a similar variation of the relative homogenized diffusion coefficient with respect to the porosity as for the previous elementary cell with a circular inclusion. However, we observe a strong decrease in the relative homogenized diffusion coefficient for low porosities due to the weak distance between the central disk and the quarters of disk.

The relative homogenized diffusion coefficient decreases and attempts more lower values than in the case of a circular inclusion. This is, on the one side, due to the lower porosities attempted and, on the other side, due to the more important solid–fluid interface Γ_{sf}^* where the EDL effects occur.

The variation of ratio $D_{WEDL}^{hom*}/D_{-}^{hom*}$ versus the porosity is shown in Figure 3.14(b) by considering σ^* as a variable parameter. We remark that for porosities higher to 25%, the ratio $D_{WEDL}^{hom*}/D_{-}^{hom*}$ is closer to the 1, whatever the value of σ^* is considered; the EDL has no influence on the homogenized diffusion coefficient. In contrast, for porosities smaller than 25%, the ratio $D_{WEDL}^{hom*}/D_{-}^{hom*}$ increases with $|\sigma^*|$ and reaches high relative values. Consequently, the EDL phenomenon plays an important role for low porosities, as already mentioned for the previous cell.

However, the result obtained strongly depends on the topology of the porous network of the elementary cell considered. Indeed, given percolation problems for low porosities, overlap between inclusions leads to remove the percolation. Therefore, we will consider in the next section 3D geometries, where a 3D topology is closer to the real microstructures.

3.5.3. Three-dimensional elementary cells

3.5.3.1. Elementary cell with spherical inclusion

We consider a 3D elementary cell with a spherical inclusion shown in Figure 3.15(a). The size of the elementary cell is $10^{-8} \times 10^{-8} \times 10^{-8} \text{ m}$. The spherical inclusion is located at the center of the elementary cell and its radius is $R = 0.3 \times 10^{-8} \text{ m}$. The corresponding porosity is $\varepsilon_n = 88.7\%$. We begin with resolving the Poisson–Boltzmann problem [3.42]–[3.43]. The surface charge density σ^* is considered as a parameter varying in the interval $\sigma^* \in [10^{-3} \text{ } 0.2] \text{ C/m}^2$. The bulk concentration is fixed to $C_b^* = 500 \text{ mol/m}^3$. Tetrahedral linear elements are used to mesh the 3D elementary cells. The mesh is refined near the solid–fluid interface Γ_{sf}^* as illustrated in Figure 3.15(b). The number of tetrahedral elements is 30,810 and the number of degrees of freedom is 179,076.

The resolution of the Neumann problem [3.40]–[3.41] allows us to determine χ_-^* and then the diffusion coefficient for different values of σ^* using equation [3.39]. Boundary conditions [3.41] and [3.43] are imposed on

the spherical inclusion surface, which represents the solid–fluid interface Γ_{sf}^* . Periodic boundary conditions for φ^* and χ_-^* are imposed on the external boundaries of the elementary cell, representing the fluid–fluid interface Γ_{ff}^* .

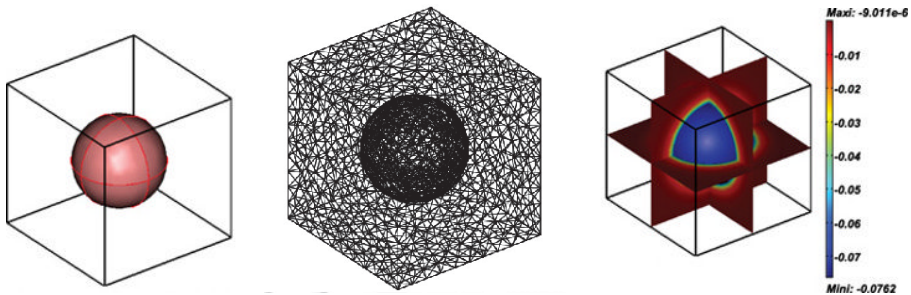


Figure 3.15. a) Elementary cell with spherical inclusion; b) Mesh of the elementary cell; c) Distribution of the electrical double-layer potential on the solid–fluid interface. For a color version of the figure, see www.iste.co.uk/ait-mokhtar/coastal.zip

Figure 3.15(c) represents the distribution of the EDL potential in the fluid phase. We note that φ^* is maximum (in absolute value) on Γ_{sf}^* where σ^* is imposed and decreases to reach its minimum value on the interface Γ_{ff}^* .

The variation of φ^* at any point¹² of the interface Γ_{sf}^* versus the absolute value of σ^* is represented in Figure 3.16(a).

The variation of the relative homogenized diffusion coefficient D_{-}^{hom*}/D^* versus $|\sigma^*|$ is represented in Figure 3.16(b). As previously, we observe that D_{-}^{hom*}/D^* decreases (for anions) with the increase in the surface charge density (in absolute value).

Figure 3.16(c) represents the influence of the bulk concentration on the variation of the induced EDL potential φ^* when σ^* is fixed. The decrease in φ^* (in absolute value) when C_b^* increases is due to the decrease in Debye length l_D . Therefore, it leads to an increase in the relative diffusion homogenized coefficient represented in Figure 3.16(d). Consequently, the increase in the bulk concentration causes an acceleration of the ionic transfer for anions as already related qualitatively in the literature [HOC 12].

12 Because of symmetry of the problem, the value of φ is identical at any point of Γ_{sf} .

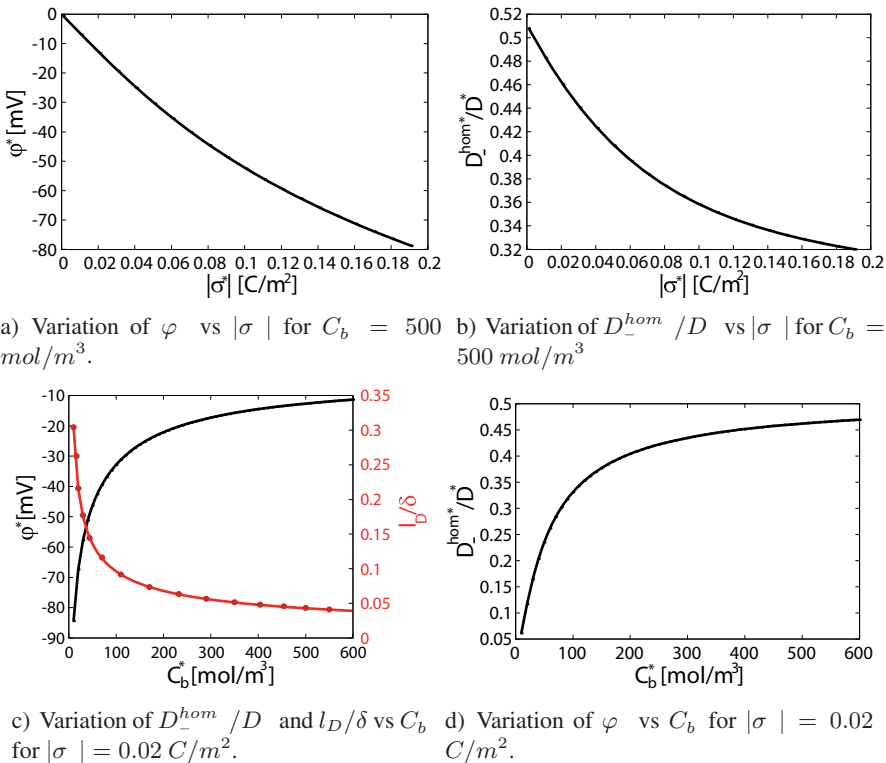


Figure 3.16. Numerical results of the parametric study for a spherical inclusion. For a color version of the figure, see
www.iste.co.uk/ait-mokhtar/coastal.zip

3.5.3.2. Elementary cell with a lower porosity

To conclude, we consider a more complex elementary cell (Figure 3.17) which is assumed to be more “representative” of the real microstructure of cementitious materials. With this elementary cell, we may attempt low porosities, close to those measured experimentally on the samples that will be used for comparison in section 3.6. This elementary cell is composed of a sphere of fixed radius located at its center, of 1/8th and 1/4th of spheres of varying radius located, respectively, at the corners and at each side of the cell. The porosity ε_n varies in the interval $\varepsilon_n \in [0.09, 0.3]$. As previously, we begin with studying the influence of the surface charge density σ^* on the homogenized diffusion coefficient $D_{\perp}^{\text{hom}*}$, C_b^* being fixed to $C_b^* = 500 \text{ mol/m}^3$. The surface charge density varies in the interval

$\sigma^* \in [0.001 \text{ } 0.2] \text{ } C/m^2$. The mesh is refined near the solid–fluid interface Γ_{sf}^* (Figure 3.17(b)). The number of tetrahedral elements is 134,743 for 933,152 degrees of freedom.

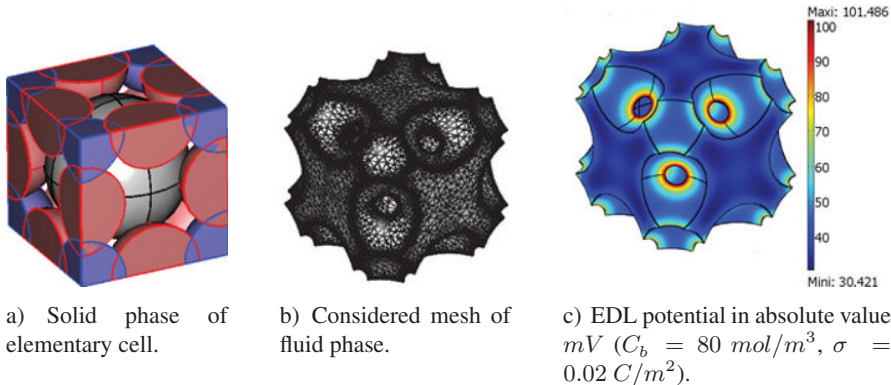


Figure 3.17. More complex elementary cell. For a color version of the figure, see www.iste.co.uk/ait-mokhtar/coastal.zip

The distribution of the EDL potential in absolute value is shown in Figure 3.17(c). As expected, $|\varphi^*|$ attempts its maximum value on the solid–fluid interface Γ_{sf}^* and decreases far from Γ_{sf}^* . For this elementary cell with a low porosity and complex microstructure, EDL effects are important.

Figure 3.18(a) represents the variations of the relative homogenized diffusion coefficient D_{-}^{hom*}/D^* versus the porosity ε_n for different values of σ^* . As expected again, D_{-}^{hom*}/D^* increases when ε_n increases and for low values of $\sigma^* = 10^{-3} \text{ } C/m^2$, the EDL effects are negligible (Figure 3.18(a)). On the contrary, when the surface charge density increases in absolute value, the relative homogenized diffusion coefficient decreases for anions and in particular for chlorides discussed here. For high porosities, the ratio $D_{-WEDL}^{hom*}/D_{-}^{hom*}$ is close to 1, and is insensitive to the variations of σ^* (the influence of the EDL is negligible). For low porosities, the ratio $D_{-WEDL}^{hom*}/D_{-}^{hom*}$ increases and becomes increasingly important when $|\sigma^*|$ increases.

Similar variations are obtained when the bulk concentration varies in the interval $C_b^* \in [10 \text{ } 600] \text{ mol}/m^3$, the surface charge density being fixed to $\sigma^* = -0.02 \text{ } C/m^2$ (see Figures 3.19(a) and 3.19(b)).

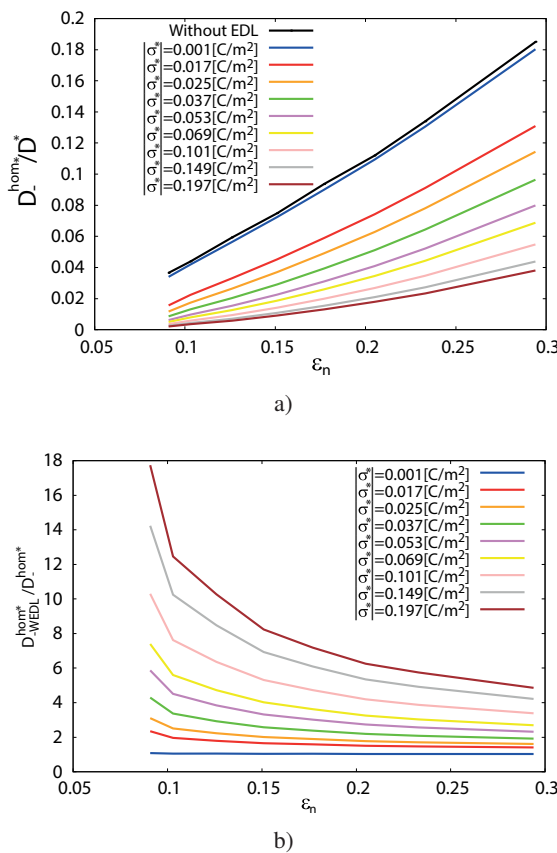


Figure 3.18. a) Variation of the relative homogenized diffusion coefficient versus porosity; b) Variation of the ratio $D_{WEDL}^{hom^*}/D^{hom^*}$ versus porosity for different values of σ and $C_b = 500 \text{ mol/m}^3$. For a color version of the figure, see www.iste.co.uk/ait-mokhtar/coastal.zip

We observe that these variations of D_{hom^*} are all more sensitive to the variations of the physical parameters (σ^* , C_b^*) and of the porosity as the 3D microstructure is complex.

3.6. Calculations of effective chlorides diffusion coefficients using a multiscale homogenization procedure

The purpose of this section is to use the results obtained previously to calculate an effective (homogenized) macroscopic diffusion coefficient in

cementitious materials, taking into account the EDL effects and the strong heterogeneities (multiscale porosity). To do this, a multiscale homogenization procedure of the ionic transfer is carried out, first, from the Debye length scale ($\delta = 10^{-8} \text{ m}$) to the capillary porosity scale ($l = 10^{-5} \text{ m}$) and, second, from the capillary porosity scale to the scale of the material ($L = 10^{-2} \text{ m}$).

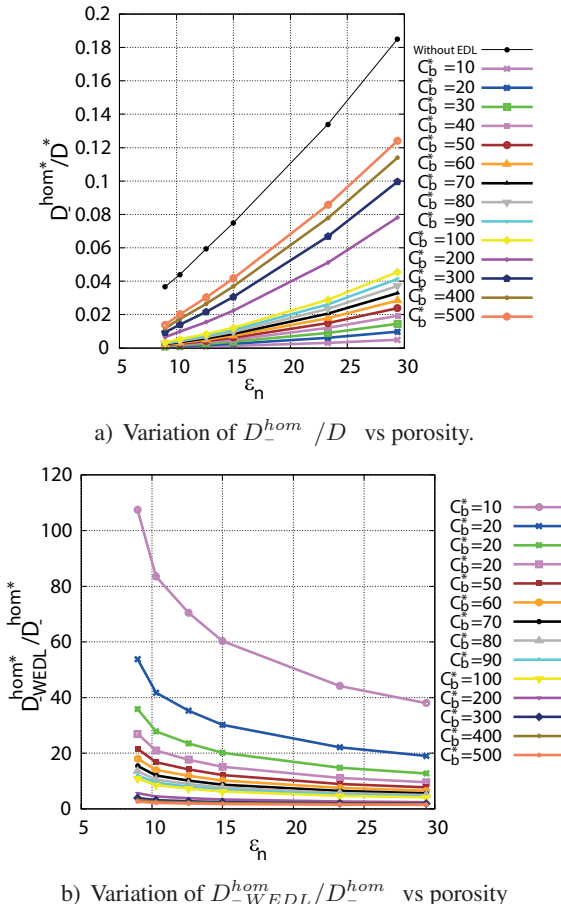


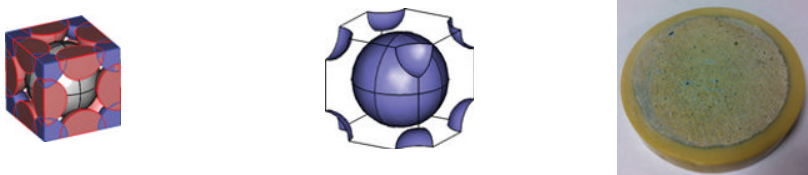
Figure 3.19. Influence of C_b (mol/m^3) on the homogenized diffusion coefficient for $\sigma = 0.02C/\text{m}^2$. For a color version of the figure, see www.iste.co.uk/ait-mokhtar/coastal.zip

In the first homogenization step, the EDL effects are taken into account, whereas they are not involved in the second homogenization step. Thus, this multiscale homogenization allows us to determine the global transfer

properties of cementitious materials taking into account the EDL effects involved at the nanoscale, and the geometrical properties of the microstructure (at the nanoscale and microscale). The results obtained will be compared to experimental measurements of electrodiffusion tests. Before performing the numerical calculation to deduce the homogenized transfer properties, it is important to note that the obtained results strongly depend on the topology of the elementary cell chosen. Even if the choice of the elementary cell is very important, it is not unique.

For the multiscale homogenization, elementary cells of Figure 3.20 are considered. We suppose that the nanostructure at the CSH scale is constituted of the repetition of the more complex 3D elementary cell considered in section 3.5.3.2 (Figure 3.20(a)). In the first procedure of homogenization, the EDL effects are taken into account according to result 3.1 of section 3.3.

On the other hand, we consider that the capillary porosity is constituted of repetition of the periodic elementary cell of Figure 3.20(b), modeling the hydrated cement grains by spherical inclusions. The EDL effects are neglected in the second homogenization procedure according to result 3.2 of section 3.4.



a) Elementary cell considered at the Debye length scale $\delta = 10 \text{ nm}$
 b) Elementary cell considered at the capillary porosity scale $l = 10 \mu \text{m}$
 c) Scale of the material $L = 1 \text{ cm}$

Figure 3.20. Modeling of the principal scales of the cement paste sample considered. For a color version of the figure, see
www.iste.co.uk/ait-mokhtar/coastal.zip

In the first homogenization procedure that will be performed, the value of C_b^* considered is the concentration of chlorides in the upstream compartment of the electrodiffusion test that will be used for experimental comparison. The value of the surface charge density σ^* is chosen in order the EDL potential (on the solid–fluid interface Γ_{sf}^*) to be of the same order of magnitude of the

zeta potential determined experimentally for cement pastes samples (between -20 mV and -10 mV according to [HOC 12]).

The total porosity of the cement material ε_p is equal to the sum of the nanoscale porosity ε_n and the microscale porosity ε_m . The choice is based on the curves of mercury intrusion porosimetry of [BOU 13b]. The results of the double homogenization procedure are presented in Table 3.2, which gives the values of the different homogenized diffusion coefficients.

ε_n	$D_{1Cl^-}^{hom}\text{ m}^2/\text{s}$	ε_m	$D_{2Cl^-}^{hom}\text{ m}^2/\text{s}$	ε_p	$D_{Cl^-}^{exp}\text{ m}^2/\text{s}$	$D_{2Cl^-}^{hom}/D_{Cl^-}^{exp}$
8 %	3.810^{-11}	10 %	6.8410^{-12}	18 %	5.9510^{-12}	1.15
12 %	8.710^{-11}	17 %	15.6610^{-12}	29 %	13.410^{-12}	1.17

Table 3.2. Comparison between the homogenized and experimental diffusion coefficients

$D_{1Cl^-}^{hom}$ and $D_{2Cl^-}^{hom}$ are the homogenized diffusion coefficients of chlorides obtained after the first and the second homogenization procedures, respectively. The second homogenized diffusion coefficient $D_{2Cl^-}^{hom}$ is compared to the experimental diffusion coefficient of chlorides $D_{Cl^-}^{exp}$ measured experimentally by electrodiffusion test [BOU 13b].

The comparison between the experimental and the homogenized diffusion coefficients is very satisfactory: the values are almost identical for the porosities of 18 and 29% considered. Therefore, taking into account the two main scales of the material porosity and the EDL effects (mainly in the first homogenization procedure) enables us to obtain values of the homogenized diffusion coefficient very close to the experimental ones. This procedure will be extended to any other microstructure, provided that elementary cells representing the heterogeneities at the nano- and microscales are given.

3.7. Bibliography

- [AHM 96] AHMADI A., QUINTARD M., “Large-scale properties for two-phase flow in random porous media”, *Journal of Hydrology*, vol. 183, nos. 1–2, pp. 69–99, 1996.
- [AHM 01] AHMADI A., AIGUEPERSE A., QUINTARD M., “Calculation of the effective properties describing active dispersion in porous media: from simple to complex unit cells”, *Advances in Water Resources*, vol. 24, nos. 3–4, pp. 423–438, 2001.

- [AÏT 04] AÏT-MOKHTAR A., AMIRI O., POUPARD O. *et al.*, “A new method for determination of chloride flux in cement-based materials from chronoamperometry”, *Cement and Concrete Composites*, vol. 26, no. 4, pp. 339–345, 2004.
- [AMA 06] AMAZIANE B., PANKRATOV L., “Homogenization of a reaction-diffusion equation with Robin interface conditions”, *Applied Mathematics Letters*, vol. 19, no. 11, pp. 1175–1179, 2006.
- [AMI 97] AMIRI O., AÏT-MOKHTAR A., SEIGNEURIN A., “A complement to the discussion of A. Xu and S. Chandra, about the paper ‘Calculation of chloride coefficient diffusion in concrete from ionic migration measurements’ by C. Andrade”, *Cement and Concrete Research*, vol. 27, no. 6, pp. 951–957, 1997.
- [AMI 01a] AMIRI O., AÏT-MOKHTAR A., DUMARGUE P. *et al.*, “Electrochemical modeling of chloride migration in cement based materials. Part I: theoretical basis at microscopic scale”, *Electrochimica Acta*, vol. 46, no. 9, pp. 1267–1275, 2001.
- [AMI 01b] AMIRI O., AÏT-MOKHTAR A., DUMARGUE P. *et al.*, “Electrochemical modeling of chlorides migration in cement based materials. Part II: experimental study—calculation of chlorides flux”, *Electrochimica Acta*, vol. 46, no. 23, pp. 3589–3597, 2001.
- [AUR 81] AURIAULT J., STRZELECKI T., “On the electro-osmotic flow in a saturated porous medium”, *International Journal of Engineering Science*, vol. 19, no. 7, pp. 915–928, 1981.
- [AUR 91] AURIAULT J., “Heterogeneous medium. Is an equivalent macroscopic description possible?”, *International Journal of Engineering Science*, vol. 29, no. 7, pp. 785–795, 1991.
- [AUR 09] AURIAULT J., BOUTIN C., GEINDREAU C., *Homogenization of Coupled Phenomena in Heterogenous Media*, ISTE, London and John Wiley & Sons, New York, 2009.
- [BEN 78] BENSOUSSAN A., LIONS J.L., PAPANICOLAOU G., *Asymptotic Analysis for Periodic Structures*, Studies in Mathematics and Its Applications, North Holland-Elsevier Science Publishers, Amsterdam, 1978.
- [BOU 12a] BOURBATACHE K., MILLET O., AÏT-MOKHTAR A. *et al.*, “Modeling the chlorides transport in cementitious materials by periodic homogenization”, *Transport in Porous Media*, vol. 94, pp. 437–459, 2012.
- [BOU 12b] BOURBATACHE K., MILLET O., AÏT-MOKHTAR A., “Ionic transfer in charged porous media. Periodic homogenization and parametric study on 2D microstructures”, *International Journal of Heat and Mass Transfer*, vol. 55, nos. 21–22, pp. 5979–5991, 2012.

- [BOU 13a] BOURBATACHE K., MILLET O., AÏT-MOKHTAR A. *et al.*, “Chloride transfer in cement-based materials. Part 1. Theoretical basis and modeling”, *International Journal for Numerical and Analytical Methods in Geomechanics*, John Wiley & Sons, Ltd, vol. 37, pp. 1614–1627, 2013.
- [BOU 13b] BOURBATACHE K., MILLET O., AÏT-MOKHTAR A. *et al.*, “Chloride transfer in cement-based materials. Part 2. Experimental study and numerical simulations”, *International Journal for Numerical and Analytical Methods in Geomechanics*, John Wiley & Sons, Ltd, vol. 37, pp. 1628–1641, 2013.
- [CHA 98] CHATTERJI S., “Colloid electrochemistry of saturated cement paste and some properties of cement based materials”, *Advanced Cement Based Materials*, vol. 7, nos. 3–4, pp. 102–108, 1998.
- [DAV 13] DAVIT Y., BELL C.G., BYRNE H.M. *et al.*, “Homogenization via formal multiscale asymptotics and volume averaging: how do the two techniques compare?”, *Advances in Water Resources*, vol. 62, pp. 178–206, 2013.
- [DOR 95] DORMIEUX L., BARBOUX P., COUSSY O. *et al.*, “A macroscopic model of swelling phenomenon of a saturated clay”, *European Journal of Mechanics – A/Solids*, vol. 14, pp. 981–1004, 1995.
- [GAG 14a] GAGNEUX G., MILLET O., “General properties of the Nernst-Planck-Poisson-Boltzmann system describing electrocapillary effects in porous media”, *Journal of Elasticity*, vol. 117, pp. 213–230, 2014.
- [GAG 14b] GAGNEUX G., MILLET O., “Homogenization of the Nernst-Planck-Poisson system by two-scale convergence”, *Journal of Elasticity*, vol. 114, no. 1, pp. 69–84, 2014.
- [HAM 03] HAMDOUNI A., MILLET O., “Classification of thin shell models deduced from the nonlinear three-dimensional elasticity. Part I: the shallow shells”, *Archives of Mechanics*, vol. 55, no. 2, pp. 135–175, 2003.
- [HOC 12] HOCINE T., AMIRI O., AÏT-MOKHTAR A. *et al.*, “Influence of cement, aggregates and chlorides on zeta potential of cement-based materials”, *Advances in Cement Research*, vol. 24, no. 11, pp. 337–348, 2012.
- [KEL 77] KELLER J.B., “Effective behaviour of heterogeneous media”, *Statistical Mechanics and Statistical Methods in Theory and Application*, in LANDMAN E.U. (ed.), pp. 631–644, Plenum, New York, 1977
- [MIL 97] MILLET O., HAMDOUNI A., CIMETIÈRE A., “Justification du modèle bidimensionnel non linéaire de plaque par développement asymptotique des équations d'équilibre”, *Comptes Rendus de l'Académie des Sciences – Series IIB – Mechanics-Physics-Chemistry-Astronomy*, vol. 324, no. 6, pp. 349–354, 1997.

- [MIL 01] MILLET O., HAMDOUNI A., CIMETIÈRE A., “A classification of thin plate models by asymptotic expansion of non-linear three-dimensional equilibrium equations”, *International Journal of Non-Linear Mechanics*, vol. 36, no. 1, pp. 165–186, 2001.
- [MIL 08] MILLET O., AÏT-MOKHTAR A., AMIRI O., “Determination of the macroscopic chloride diffusivity in cementitious porous materials by coupling periodic homogenization of Nernst-Planck equation with experimental protocol”, *International Journal of Multiphysics*, vol. 2, no. 17, pp. 129–145, 2008.
- [MOY 02] MOYNE C., MURAD M.A., “Electro-chemo-mechanical couplings in swelling clays derived from a micro/macro-homogenization procedure”, *International Journal of Solids and Structures*, vol. 39, no. 25, pp. 6159–6190, 2002.
- [MOY 06a] MOYNE C., MURAD M., “A two-scale model for coupled electro-chemo-mechanical phenomena and Onsagers reciprocity relations in expansive clays: I. Homogenization analysis”, *Transport in Porous Media*, vol. 62, no. 3, pp. 333–380, 2006.
- [MOY 06b] MOYNE C., MURAD M., “A two-scale model for coupled electro-chemo-mechanical phenomena and onsagers reciprocity relations in expansive clays: II. Computational validation”, *Transport in Porous Media*, vol. 63, no. 1, pp. 13–56, 2006.
- [NAD 04] NADLER B., SCHUSS Z., SINGER A. *et al.*, “Ionic diffusion through confined geometries: from Langevin equations to partial differential equations”, *Journal of Physics: Condensed Matter*, vol. 16, no. 22, pp. S2153–S2165, 2004.
- [QUI 88] QUINTARD M., WHITAKER S., “Two-phase flow in heterogeneous porous media: the method of large-scale averaging”, *Transport in Porous Media*, vol. 3, no. 4, pp. 357–413, 1988.
- [QUI 93a] QUINTARD M., WHITAKER S., “One- and two-equation models for transient diffusion processes in two-phase systems”, *Advance in Heat Transfer*, vol. 23, pp. 369–464, 1993.
- [QUI 93b] QUINTARD M., WHITAKER S., “Transport in ordered and disordered porous media: volume-averaged equations, closure problems, and comparison with experiment”, *Chemical Engineering Science*, vol. 48, no. 14, pp. 2537–2564, July 1993.
- [QUI 94] QUINTARD M., WHITAKER S., “Convection, dispersion, and interfacial transport of contaminants: homogeneous porous media”, *Advances in Water Resources*, vol. 17, no. 4, pp. 221–239, 1994.

- [QUI 96] QUINTARD M., WHITAKER S., “Transport in chemically and mechanically heterogeneous porous media. II: Comparison with numerical experiments for slightly compressible single-phase flow”, *Advances in Water Resources*, vol. 19, no. 1, pp. 49–60, 1996.
- [QUI 97] QUINTARD M., KAVIANY M., WHITAKER S., “Two-medium treatment of heat transfer in porous media: numerical results for effective properties”, *Advances in Water Resources*, vol. 20, nos. 2–3, pp. 77–94, 1997.
- [SAM 99] SAMSON E., MARCHAND J., BEAUDOIN J.J., “Describing ion diffusion mechanisms in cement-based materials using the homogenization technique”, *Cement and Concrete Research*, vol. 29, no. 8, pp. 1341–1345, 1999.
- [SAM 07] SAMSON E., MARCHAND J., “Modeling the transport of ions in unsaturated cement-based materials”, *Computers and Structures*, vol. 85, nos. 23–24, pp. 1740–1756, 2007.
- [SAN 80] SANCHEZ PALENCE E., “Non-Homogeneous Media and Vibration Theory,” *Lecture Notes in Physics*, Volume 129, Berlin, 1980.
- [SAS 81] SASIDHAR V., RUCKENSTEIN E., “Electrolyte osmosis through capillaries”, *Journal of Colloid and Interface Science*, vol. 82, no. 2, pp. 439–457, 1981.
- [SAS 82] SASIDHAR V., RUCKENSTEIN E., “Anomalous effects during electrolyte osmosis across charged porous membranes”, *Journal of Colloid and Interface Science*, vol. 85, no. 2, pp. 332–362, 1982.
- [VAN 92] VAN KEULEN H., SMIT J., “Analytical approximations for potential profiles in charged micropores originating from the Poisson Boltzmann equation”, *Journal of Colloid and Interface Science*, vol. 151, no. 2, pp. 546–554, 1992.
- [WHI 77] WHITAKER S., “Simultaneous Heat, Mass, and Momentum Transfer in Porous Media: A Theory of Drying,” *Advance in Heat Transfer*, vol. 13, Elsevier, pp. 119–203, 1977.
- [WHI 85] WHITAKER S., “A simple geometrical derivation of the spacial averaging theorem”, *Chemical Engineering Science*, vol. 19, pp. 50–52, 1985.
- [WOO 04] WOOD B., QUINTARD M., WHITAKER S., “Estimation of adsorption rate coefficients based on the Smoluchowski equation”, *Chemical Engineering Science*, vol. 59, no. 10, pp. 1905–1921, 2004.

Chloride Transport in Unsaturated Concrete

4.1. Introduction

The corrosion of steel in concrete structures is one of the main causes of the degradation and reduction of service life of these structures, mainly when they are exposed to marine environment or to de-icing salts. In these two situations, the corrosion of the reinforcement is due the chloride diffusion which can occur both in the saturated and unsaturated parts of the structure as shown in Figure 4.1.

In practical cases, the structures submitted to unsaturated structures are more numerous and, in this condition, the chloride ingress is accelerated due to alternation of wetting and drying cycles. For this reason, this chapter is focused on the study of the chloride transport in unsaturated conditions where the transfer of ions contained in the pore solution and the water are coupled.

After defining the position of the problem linked to chloride ingress in unsaturated porous medium, we first establish the macroscopic equation of ions transport by using the homogenization based on volume averaging method [WHI 98]. Second, the same method is used to establish the equation of water transport (convection).

In section 4.3, the parameter of coupling between chloride ingress and water transport is highlighted. Also, we discuss the difficulties linked to the determination of certain outputs of the model like diffusivity, permeability and the gas pressure (constant or not).

The last part of the chapter is focused on the simulation of chloride and water content profiles according to some experimental conditions corresponding to the *in situ* cases.

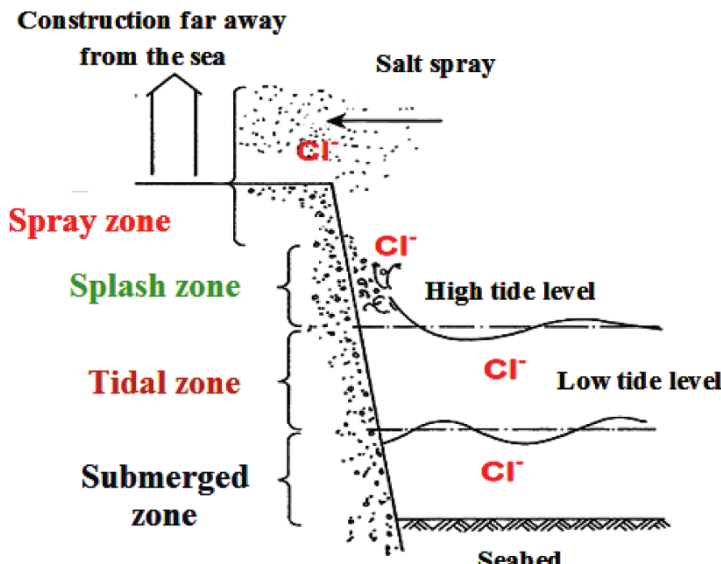


Figure 4.1. Different zones of construction exposed to chloride ingress

4.2. Chloride diffusion in unsaturated case

4.2.1. Definition of the problem

Moisture and salt can be responsible for the deterioration of buildings manufactured with concrete and mortar materials. Indeed, the water penetrates into the concrete by direct contact with liquid water or rain under a capillary pressure gradient. The liquid water transfer promotes the development of microorganisms such as bacteria and fungi. This process can

also convey aggressive media in the form of soluble salts. This, once diffused into the pores of the materials, may cause degradation of the building material. It may crystallize when the water evaporates and then cause stresses within the material crystallizations causing delamination. In addition, the presence of aggressive agents, such as chloride ions, may accelerate the corrosion of steel in concrete. This causes a structural damage. Therefore, the study of transfer of moisture and chloride is very important in order to predict the initiation of reinforcement corrosion in concrete, whatever the conditions of exposure (near the sea). In general, the diffusion in the interstitial chloride solution is relatively slow as the advection liquid phase is much faster. Therefore, the movement of water into the porous network can change the ionic flux. Indeed, in the literature some works have shown that cementitious material subject to wetting-drying cycles are less resistant to chloride penetration, a material in saturated case [NGU 07, SLE 08, FAN 98]. For any reason mentioned above (section 4.1), it is important to study the coupling between the transfer of chlorides and the moisture transfer. To do this, we will begin by developing a model describing the transfer of chlorides with related terms moisture material. The porous media considered is shown in Figure 4.2 [NGU 07].

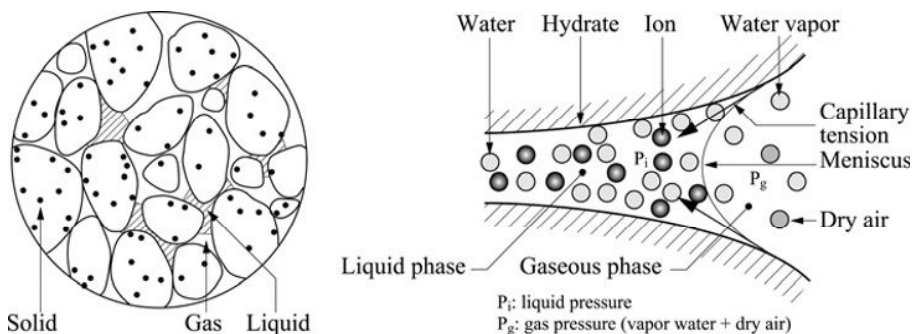


Figure 4.2. Porous media considered for studying coupling of ions and water transport

4.2.2. Theoretical aspects

In the transfer of chloride, we can distinguish two main processes based on different mechanisms. These are diffusion and advection. The diffusion

process occurs at the microscopic level while advection happens at the macroscopic scale. Indeed, the diffusion mechanism is governed by a gradient of ionic concentration; advection can transport ions by the flow of the liquid phase. The mass transport in unsaturated medium is complex, it occurs into the two processes. In fact, the transfer of salt can be divided at least into two processes based on different mechanisms. The first transfer mechanism consists of diffusion generated by a concentration gradient of ions. Ions can also be transported by advection. In this case, the velocity field of the solution which generates the advection is generally considered after a given hydrodynamic consideration, which is not fundamentally affected by the presence of chlorides. The advection of transporting the ions in the direction of flow of the solution makes a change in ionic concentration; therefore, the ion concentration gradient is modified. Thus, in these conditions, the advection and diffusion are coupled. In addition, if the pore solution contains a high concentration of salt, this may also affect the evaporation, thus the partial pressure of water vapor. This point, however, is not discussed in this study. Ions are electrically charged elements and they move at different speeds. The electrical interaction between the ions in the solution may accelerate some ions and slow down others in isothermal conditions. Globally ion diffusion will be slower. In addition, ion–ion interaction and ion–solvent interaction may also influence the ionic transfer, which is translated by chemical activity coefficient.

To describe the ion transfer, several approaches have been proposed in the literature. Most of them are based on the concept of transport potential. In this chapter, we are focused on the extended Nernst–Planck equation for the description of ion transport. For water transport, we will use Rachard's equation.

4.2.3. Ionic transport model

4.2.3.1. Assumptions

Chlorides penetrate the porous media during the liquid phase (water). They move through a movement of the whole of the liquid phase. It is therefore understandable that the movement of chlorides is intimately linked to that of the liquid phase. These chlorides are also inert with respect to the backbone of the material (solid phase). For example, chlorides react with hydrated compounds of cementitious materials. Moreover, the convection motion of the pore solution is related to hydrodynamic considerations and

trade liquid–vapor affected by the presence of solutes and multi species in the solution. In our approach, we consider both chlorides: one that is chemically bound to the solid matrix (bound chlorides), and the other that is found in the solution and that moves with the liquid phase (free chlorides). The transfer of chloride ions is considered to be a multispecies approach because it is affected by the presence of other ions present in the pore solution as mentioned by Amiri *et al.* [AMI 01] and Friedmann *et al.* [FRI 03]. The given link between the three phases of the material and between the ions themselves must make some assumptions to simplify the problem. These assumptions, some of which are considered for modeling moisture (in the next section) are as follows:

- The cementitious material is heterogeneous, composed of three phases, solid, liquid and gas (vapor and air) as shown in Figure 4.2.
- The mass transport (diffusion and convection) requires thermal equilibrium and occurs in isothermal conditions.
- The solid phase is dimensionally stable, homogeneous and isotropic.
- The liquid phase is incompressible, and is formed by water and ions in the solution. The ion transport occurs only in the liquid phase, and we neglect the transport in other phases.
- The gas phase consists of water vapor and air; this phase is assumed to be a mixture of two ideal gases. The different phases considered are shown in Figure 4.2.
- Chemical reactions between the liquid and the solid phase are solely due to chemical interactions between the chloride ions in the solution and the solid matrix.
- The phase change is possible for the water which is present in liquid and vapor forms (see the illustration shown in Figure 4.2).
- The air is considered as inert component, which is either likely to condense on the porous matrix or interact with the condensed phase.
- The flow of fluid in the porous medium is considered to be slow enough laminar.
- The electrocapillary adsorption phenomena (electrical double layer) which occur in the walls of the interstitial pore–solution interface are neglected.

4.2.3.2. Description of the ionic diffusion mechanisms in pore scale

The application of the mass conservation equation for an ionic species diffusing in the liquid [SAM 99] can be written as:

$$\frac{\partial c_{i_l}}{\partial t} + \operatorname{div}(h_{i_l}) = R_{i_l} \quad [4.1]$$

where c_{i_l} ($\frac{\text{mol}}{\text{m}^3}$) is the concentration of species i_l par m³ of the pore solution and h_{i_l} is the molar flux of species i_l phase liquid phase.

The density of molar flux of species i_l is expressed by Nernst–Planck's equation [BAR 83]:

$$h_{i_l} = -D_{i_l} \operatorname{grad}(c_{i_l}) - z_{i_l} \frac{F}{RT} c_{i_l} D_{i_l} \operatorname{grad}(\Psi_l) - D_{i_l} c_{i_l} \operatorname{grad}(\ln \gamma_{i_l}) + c_{i_l} u_l \quad [4.2]$$

where D_{i_l} (m²/s) is the diffusion coefficient of the ionic species in an infinitely dilute solution, Z_i is the charge number of the species (valence), F (C.mol⁻¹) is Faraday's constant, R (JK⁻¹.mol⁻¹) is the gas constant, T (K) is the temperature, Ψ_l is the local electrical field, γ_{i_l} is the activity coefficient of each ion i_l and u_l (m/s) is the convection velocity of the solution.

The Nernst–Planck equation contains four terms: the first term is a diffusion term described by Fick's law, and the second term is related to the convective flow velocity of the liquid phase. The two other terms which take into account electrostatic interactions and ionic activities occur between the ionic species present in the pore solution. Thus, the Nernst–Planck equation describes all physical phenomena that occur in interstitial solution.

4.2.3.3. Description of the ionic diffusion mechanisms in macroscopic scale

The study of ion transfer through the pore requires to measurement of some parameters on this scale; these measurements seem delicate and very sensitive. In order to use all of the measurable macroscopic scale of a porous medium, we use the volume average technique [WHI 98] to go from the microscopic scale to the macroscopic scale.

Using the properties related to the expression of the average gradient and divergence operator with the volume average technique [WHI 98], the average local conservation equation [4.1] is:

$$\langle \frac{\partial c_{i\alpha}}{\partial t} \rangle + \langle \text{div}(h_{i\alpha}) \rangle = \langle R_{i\alpha} \rangle \quad [4.3]$$

The spatial average of the time derivative of the molar concentration and the flux of the flow are written as:

$$\langle \frac{\partial c_{i\alpha}}{\partial t} \rangle = \frac{\partial \langle c_{i\alpha} \rangle}{\partial t} - \frac{1}{V} \int_{A\alpha\beta} c_{i\alpha} \omega_{\alpha\beta} \cdot n_{\alpha\beta} dA - \frac{1}{V} \int_{A\alpha\gamma} c_{i\alpha} \omega_{\alpha\gamma} \cdot n_{\alpha\gamma} dA \quad [4.4]$$

$$\langle \text{div}(h_{i\alpha}) \rangle = \text{div}\langle h_{i\alpha} \rangle + \frac{1}{V} \int_{A\alpha\beta} h_{i\alpha} \cdot n_{\alpha\beta} dA + \frac{1}{V} \int_{A\alpha\gamma} h_{i\alpha} \cdot n_{\alpha\gamma} dA \quad [4.5]$$

where $\omega_{\alpha\beta}$ and $\omega_{\alpha\gamma}$ are the local velocities of mass transport, respectively, on interfaces $A_{\alpha\beta}$ and $A_{\alpha\gamma}$, and $n_{\alpha\beta}$ and $n_{\alpha\gamma}$ are the normal unit vectors directed perpendicularly (from α to β) and (from α to γ), respectively.

4.2.3.3.1. Phase solid

The solid–liquid interface is subject to chemical reactions between the hydrates of cementitious matrix and ions of pore solution. This interface moves. But ω_{sl} speed due to dissolution reactions or precipitation is very low [BAR 00, SAM 00]. So, the first integral of equation [4.4] corresponding to the solid phase can be neglected. But in the long term (steady state), this simplification is questionable.

The speed at the solid–gas interface does not affect the ionic transport phenomena as in the gas phase, the diffusion of ionic species do not occur. Therefore, equation [4.4] applied to the solid phase can be written as:

$$\langle \frac{\partial c_{is}}{\partial t} \rangle = \frac{\partial \langle c_{is} \rangle}{\partial t} + \frac{\partial (\theta_s \langle c_{is} \rangle^s)}{\partial t} \quad [4.6]$$

The ionic transport occurs only in liquid phase, so the ion flux in the solid phase is zero, hence:

$$\text{div}\langle h_{is} \rangle = 0 \quad [4.7]$$

The ion flux in the gas–solid interface is zero. Thus, by replacing the two previous equations in the main equation [4.5], we obtain:

$$\frac{\partial(\theta_s \langle c_{is} \rangle^s)}{\partial t} + \frac{1}{V} \int_{A_{sl}} h_{is} \cdot n_{sl} \cdot dA = \langle R_{is} \rangle \quad [4.8]$$

The average values $\langle c_{is} \rangle^s, \langle R_{is} \rangle$ are replaced by the following notations:

$$\langle c_{is} \rangle^s = C_{i,b}; \langle R_{is} \rangle = R_{is}^{hom} \quad [4.9]$$

Replacing each term with its value in equation [4.8], the macroscopic equation of ion transport in the solid phase is:

$$\frac{\partial(\theta_s C_{i,b})}{\partial t} + \frac{1}{V} \int_{A_{sl}} h_{is} \cdot n_{sl} \cdot dA = R_{is}^{hom} \quad [4.10]$$

4.2.3.3.2. Liquid phase ω_{ls}

The solid–liquid interface is subject to chemical reactions between the cementitious material and ions contained in the interstitial solution. This interface is mobile. But the speed ω_{ls} of the reactions following dissolution or precipitation is very low [SAM 00]. In addition, the flux through the liquid–gas interface is zero, and we obtain by eliminating terms of weak magnitude in the divergence term of average flux:

$$\begin{aligned} \text{div}\langle h_{il} \rangle &= -\text{div}(\langle D_{il} \text{grad}(c_{il}) \rangle) - \text{div}\left(\langle z_i \frac{F}{RT} D_{il} c_{il} \text{grad}(\psi_l) \rangle\right) \\ &\quad - \text{div}(\langle D_{il} c_{il} \text{grad}(\ln \gamma_{il}) \rangle) + \text{div}(\langle c_{il} u_l \rangle) \end{aligned} \quad [4.11]$$

For the first two terms of equation [4.11], the molecular diffusion coefficient D_{il} is constant; thus, the average of each of the two terms is written as:

$$\begin{cases} \langle D_{il} \text{grad}(c_{il}) \rangle = D_{il} \langle \text{grad}(c_{il}) \rangle \\ \langle z_i \frac{F}{RT} D_{il} c_{il} \text{grad}(\psi_l) \rangle = z_i \frac{F}{RT} D_{il} \langle c_{il} \rangle^l \langle \text{grad}(\psi_l) \rangle \\ \langle D_{il} c_{il} \text{grad}(\ln \gamma_{il}) \rangle = D_{il} \langle c_{il} \rangle^l \langle \text{grad}(\ln \gamma_{il}) \rangle \end{cases} \quad [4.12]$$

By using some definitions dealing with the volume average technique which are detailed in [WHI 98], we can write:

$$\langle \text{grad}(c_{il}) \rangle \theta_l \text{grad} \langle c_{il} \rangle^l + \frac{1}{V} \int_{A_{ls}} \widetilde{c}_{il} \cdot n_{ls} \cdot dA + \frac{1}{V} \int_{A_{lg}} \widetilde{c}_{il} \cdot n_{lg} \cdot dA \quad [4.13]$$

where \widetilde{c}_l is the deviation of the value c_i with respect to intrinsic average $\langle c_{il} \rangle^l$.

According to Whitaker [WHI 98], the deviation of tensorial can be expressed by a linear law of type:

$$\widetilde{c}_{il} = A \cdot \text{grad} \langle c_{il} \rangle^l \quad [4.14]$$

where A is a vector which depends on the points considered on the interfaces A_{ls} and A_{lg} .

$$\frac{1}{V} \int_{A_{ls}} \widetilde{c}_{il} \cdot n_{ls} \cdot dA \frac{1}{V} \int_{A_{ls}} A \cdot \text{grad} \langle c_{il} \rangle^l \cdot n_{ls} \cdot dA = \lambda_1 \cdot \theta_l \cdot \text{grad} \langle c_{il} \rangle^l \quad [4.15]$$

$$\frac{1}{V} \int_{A_{lg}} \widetilde{c}_{il} \cdot n_{lg} \cdot dA \frac{1}{V} \int_{A_{lg}} A \cdot \text{grad} \langle c_{il} \rangle^l \cdot n_{lg} \cdot dA = \lambda_2 \cdot \theta_l \cdot \text{grad} \langle c_{il} \rangle^l \quad [4.16]$$

We define by :

$$\lambda_1 = \frac{1}{V_l} \int_{A_{ls}} A \otimes n_{ls} \cdot dA \quad [4.17]$$

$$\lambda_2 = \frac{1}{V_l} \int_{lg} A \otimes n_{lg} \cdot dA \quad [4.18]$$

$$\pi = I + \lambda_1 + \lambda_2 \quad [4.19]$$

where I is the matrix unit.

The application of equations [4.15]–[4.19] to the parameters $c_{il}\psi_l$ and γ_{il} gives us:

$$\begin{cases} \langle D_{il} \text{grad}(c_{il}) \rangle = D_{il} \cdot \theta_l \cdot \pi \cdot \text{grad} \langle c_{il} \rangle^l \\ \langle z_i \frac{F}{RT} D_{il} c_{il} \text{grad}(\psi_l) \rangle = z_i \frac{F}{RT} \cdot D_{il} \cdot \theta_l \cdot \pi \cdot \langle c_{il} \rangle^l \cdot \text{grad} \langle \psi_l \rangle^l \\ \langle D_{il} c_{il} \text{grad}(\ln \gamma_{il}) \rangle = D_{il} \cdot \pi \cdot \langle c_{il} \rangle^l \cdot \text{grad} \langle (\ln \gamma_{il}) \rangle^l \end{cases} \quad [4.20]$$

By neglecting deviation terms of the second order, the volume average of the third term in equation [4.11] is written as:

$$\langle c_{i_l}, u_l \rangle = \langle c_{i_l} \rangle^l \cdot \langle u_l \rangle + \langle \tilde{c}_{i_l}, \tilde{u}_l \rangle = \langle c_{i_l} \rangle^l \cdot \theta_l \cdot \langle u_l \rangle \quad [4.21]$$

We note:

$$D_{ei} = \pi \cdot D_{i_l} \quad [4.22]$$

where D_{ei} is the effective ion diffusion coefficient of the porous medium. It is connected to the molecular diffusion D_{i_l} coefficient by a parameter π which characterizes the geometry of the medium (porosity, tortuosity and constrictivity). As the ionic transport occurs only in the liquid phase and for simplicity, average values are replaced by the following notations:

$$C_{i,f} = \langle c_{i_l} \rangle^l; \Psi = \langle \psi \rangle^l; \ln\gamma_i = \langle (\ln\gamma_{i_l}) \rangle^l; U_l = \langle u_l \rangle; R = \langle R_{i_l} \rangle \quad [4.23]$$

By replacing each term by its value in equation [4.11], we can obtain the macroscopic equation of ion transport in the liquid phase as follows:

$$\frac{\partial(\theta_w C_{i,f})}{\partial t} - \operatorname{div} \left(D_{ei} \theta_w \operatorname{grad}(C_{i,f}) + D_{ei} \frac{z_i F}{RT} C_{i,f} \theta_w \operatorname{grad}(\Psi_l) \right) + \operatorname{div} (D_{ei} C_{i,f} \theta_w \operatorname{grad}(\ln\gamma_i) - C_{i,f} U_l) + \frac{1}{V} \int_{A_{ls}} h_{i_l} n_{ls} dA = R_{i_l}^{hom} \quad [4.24]$$

At the solid–liquid interface A_{sl} fluxes of ions are opposed; therefore, we can write:

$$h_{i_s} = -h_{i_l} \quad [4.25]$$

By summing the two macroscopic equations [4.10] and [4.24] dealing, respectively, with the solid and liquid phases, we obtain the equation of macroscopic ionic transport in the porous medium:

$$\frac{\partial(\theta_w C_{i,f})}{\partial t} + \frac{\partial(\theta_s C_{i,b})}{\partial t} - \operatorname{div} \left(D_{ei} \theta_w \operatorname{grad}(C_{i,f}) + D_{ei} \frac{z_i F}{RT} C_{i,f} \theta_w \operatorname{grad}(\Psi_l) \right) + \operatorname{div} (D_{ei} C_{i,f} \theta_w \operatorname{grad}(\ln\gamma_i) - C_{i,f} U_l) + \frac{1}{V} \int_{A_{ls}} h_{i_l} n_{ls} dA = R_{i_l}^{hom} + R_{i_s}^{hom} \quad [4.26]$$

where: $\theta_w \left(\frac{m^3 \text{solution}}{m^3 \text{total}} \right)$ and $\theta_s \left(m^3 \frac{\text{material}}{m^3 \text{total}} \right)$ are, respectively, the porosity and the compacity, $C_{i,f} \left(\frac{\text{mol}}{m^3 \text{solution}} \right)$ is the free concentration of ion i in the liquid phase, $C_{i,b} \left(\frac{\text{mol}}{m^3 \text{material}} \right)$ is the bound concentration of ion i in the solid phase solid, $D_{ei} \left(\frac{m^2}{s} \right)$ is the effective diffusion coefficient of each ion i in the liquid phase of the porous, $\Psi_l(V)$ is the electrostatic field in liquid phase due to the opposite charges of ions contained in the pore solution, γ_i is the activity coefficient of each ion i and $U_l(\text{m/s})$ is the convection velocity of liquid phase. The terms $R_{i_1}^{\text{hom}}$ and $R_{i_s}^{\text{hom}}$ are the homogeneous reactions between the ion i (chloride, for example) and others contained in the pore solution of concrete (Na^+ , K^+ and OH^-).

Equation [4.25] is the macroscopic ionic transport. This equation will be linked to those resulting from humidification and drying in order to couple the liquid and ions transport. The unknowns in this equation are θ_w and C_{if} . The input parameters of the model are the concentration of bound chlorides $C_{i,b}$, the diffusion coefficients of ions D_{ei} , the activity coefficient γ_i , ion activity, the electrostatic potential Ψ_i and the convection velocity U_l . In the following, we provide the details of the methodology used to determine these input parameters. Through equation [4.25], we show the terms reflecting the coupling between the ion transfer and moisture transfer: water content θ_w and the flow velocity of the liquid phase. These terms will be discussed below.

4.2.4. Moisture transport model

The establishment of the water transfer model is based on several assumptions. Some of them are mentioned in ionic transport section (see section 4.2.3.1). To these assumptions, we add other assumptions dealing with moisture transport:

- The phase change is possible for the water which is present in liquid and vapor form. The air is considered an inert component which is either likely to condense on the porous matrix or interact with the condensed phase.
- The flow of fluid in the porous medium is considered to be slow and laminar enough. At the pore scale, the porous medium is considered as a set

of continuous media. The application of standard methods of continuum mechanics led to locally expressing the laws of conservation of mass for each component in the different phases.

We denote by α one of the gaseous, liquid or solid phases of the cementitious material (see Figure 4.3). The equation of the transfer of moisture at the microscopic level is written in the same manner as in ion transfer:

$$\frac{\partial r_{i_\alpha}}{\partial t} + \operatorname{div}(h_{i_\alpha}) = R_{i_\alpha} \quad [4.27]$$

The local flux h_{i_α} of species i_α is expressed with respect to its local density r_{i_α} and velocity u_{i_α} :

$$h_{i_\alpha} = r_{i_\alpha} u_{i_\alpha} \quad [4.28]$$

The local flux can also be expressed according to the reference velocity of a considered phase u_α :

$$h_{i_\alpha} = r_{i_\alpha} u_{i_\alpha} = j_{i_\alpha} + r_{i_\alpha} u_\alpha \quad [4.29]$$

where j_{i_α} is the flux of diffusion of constituent i_α with the reference velocity u_α .

The term $r_{i_\alpha} u_\alpha$ is convective flux in the phase α .

The reference velocity is a combination of n barycentric velocities of each component in the phase α :

$$u_\alpha = \sum_{i_\alpha=1}^n a_{i_\alpha} u_{i_\alpha} \quad [4.30]$$

The coefficients a_{i_α} are the no-dimensional weights of the reference velocity. They should check:

$$\sum_{i_\alpha=1}^n a_{i_\alpha} = 1 \quad [4.31]$$

where n is the number of components of the same phase.

The coefficient a_{i_α} is the ratio between the density of component i and the total density of the phase α (mass fraction); it is also the ratio of the

molar concentration (mole fraction). $r_{i\alpha}$ is the local instantaneous mass density of component i_α in the phase α . The equations expressing the water transfer are written in a macroscopic scale from the microscopic scale with the homogenization method based on volume average technique mentioned above. Fluid transport in cementitious materials is summarized to the system of three macroscopic equations of three liquid components (l), water (l) vapor (v) and air (a). This system of equations, in isothermal conditions with the interface conditions, may be applied to both wetting and drying:

$$\begin{cases} \rho_w \frac{\partial \theta_w}{\partial t} + \text{div}(J_w) + \text{div}(\rho_w U_w) + m = 0 \\ \frac{\partial(\theta_g \rho_v)}{\partial t} + \text{div}(J_v) + \text{div}(\rho_v U_g) - m = 0 \\ \frac{\partial(\theta_g \rho_a)}{\partial t} + \text{div}(J_a) + \text{div}(\rho_a U_g) = 0 \end{cases} \quad [4.32]$$

The diffusive flow of liquid (water), vapor (steam) and air are:

$$\begin{cases} J_w = -D_{ads} \text{grad} \theta_{ads} \\ J_v = -D_{va} \rho_g \text{grad} \left(\frac{\rho_v}{\rho_g} \right) - D_{va} \frac{\rho_v}{\rho_g} \text{grad} \rho_g \\ J_a = -D_{va} \rho_g \text{grad} \left(\frac{\rho_a}{\rho_g} \right) - D_{va} \frac{\rho_a}{\rho_g} \text{grad} \rho_g \end{cases} \quad [4.33]$$

Flows into liquid and gas phase are governed by Darcy's law with respect to unsaturated conditions:

$$\begin{cases} U_l = -\frac{k_l k_{rl}}{\mu_l} \text{grad} p_l \\ U_g = -\frac{k_g k_{rg}}{\mu_g} \text{grad} p_g \end{cases} \quad [4.34]$$

where ρ_w is the water density, ρ_g is the gas density, ρ_a is the air density, θ_g is the gas content, θ_w is the moisture content, P_g is the gas pressure, P_l is the liquid pressure, K_g is the intrinsic gas permeability, K_l is the intrinsic water permeability, K_{rg} is the relative gas permeability, K_{rl} is the relative water permeability, μ_l is the water viscosity and μ_g is the gas viscosity.

For the complete equations expressing the moisture transport, we have to define the limit conditions governing the liquid–gas interface. As an initial approach, we can use the Clapeyron equation extended to pore solution contained salt of a_l :

$$\frac{dp_l}{\rho_l} + R_l T \frac{da}{a_l} = \frac{dp_v}{\rho_v} \quad [4.35]$$

Note that equation [4.31] can be solved using two assumptions dealing with the pressure of the gas phase, either constant or unconstant. If the pressure is assumed constant, Darcy's flux of gas phase is zero ($U_g = 0$) and the solving becomes more easy.

4.3. Summary of the model

After establishing all equations of ionic and humidity transport, it is interesting to summarize these equations.

Moisture transport:

$$\left\{ \begin{array}{l} \rho_w \frac{\partial \theta_w}{\partial t} + \text{div}(J_w) + \text{div}(\rho_w U_w) + m = 0 \\ \frac{\partial(\theta_g \rho_v)}{\partial t} + \text{div}(J_v) + \text{div}(\rho_v U_g) - m = 0 \\ \frac{\partial(\theta_g \rho_a)}{\partial t} + \text{div}(J_a) + \text{div}(\rho_a U_g) = 0 \\ J_w = -D_{ads} \text{grad} \theta_{ads} \\ J_v = -D_{va} \rho_g \text{grad} \left(\frac{\rho_v}{\rho_g} \right) - D_{va} \frac{\rho_v}{\rho_g} \text{grad} \rho_g \\ J_a = -D_{va} \rho_g \text{grad} \left(\frac{\rho_a}{\rho_g} \right) - D_{va} \frac{\rho_a}{\rho_g} \text{grad} \rho_g \\ U_l = -\frac{k_l k_{rl}}{\mu_l} \text{grad} p_l \\ U_g = -\frac{k_g k_{rg}}{\mu_g} \text{grad} p_g \end{array} \right. \quad [4.36]$$

For the relative permeability of water and gas, we used the model proposed by Van Genuchten [VAN 80] and Mualem [MUA 76]:

$$k_{rl} = \left(\frac{\theta_w}{\epsilon_0} \right)^p \left(1 - \left(1 - \left(\frac{\theta_w}{\epsilon_0} \right)^{\frac{1}{m}} \right)^m \right)^2 \quad [4.37]$$

$$k_{rl} = \left(\frac{\theta_g}{\epsilon_0} \right)^p \left(1 - \left(1 - \frac{\theta_g}{\epsilon_0} \right)^{\frac{1}{m}} \right)^{2m} \quad [4.38]$$

Ionic transport:

$$\left\{ \begin{array}{l} \frac{\partial(\theta_w C_{i,f})}{\partial t} + \frac{\partial(\theta_s C_{i,b})}{\partial t} - \operatorname{div} \left(D_{ei} \theta_w \operatorname{grad} (C_{i,f}) + D_{ei} \frac{z_i F}{RT} C_{i,f} \theta_w \operatorname{grad} (\Psi_l) \right) + \\ \quad + \operatorname{div} (D_{ei} C_{i,f} \theta_w \operatorname{grad} (\ln \gamma_i) - C_{i,f} U_l) = 0 \\ \\ i = Cl^-; OH^-; Na^+; K^+ \\ \\ grad(\Psi_l) = \frac{\sum_{i=1}^4 D_{ei} z_i \theta_w \operatorname{grad} C_{i,f} + \sum_{i=1}^4 D_{ei} z_i \theta_w \operatorname{grad} \ln \gamma_i}{\sum_{i=1}^4 D_{ei} \frac{z_i^2 F}{RT} C_{i,f} \theta_w} - \\ \quad - \frac{\sum_{i=1}^4 z_i C_{i,f} \theta_w \operatorname{grad} C_{i,f} + \sum_{i=1}^4 z_i C_{i,f} U_l}{\sum_{i=1}^4 D_{ei} \frac{z_i^2 F}{RT} C_{i,f} \theta_w} \\ \\ U_l = - \frac{k_l k_{rl}}{\mu_l} \operatorname{grad} P_l \\ \\ \ln(\gamma_i) = - \frac{A_\gamma z_i^2 \sqrt{l}}{1 + r_{\gamma i} B_\gamma \sqrt{l}} + \frac{A_\gamma z_i^2 ((-4.17 \times 10^{-15})l + 0.2) \sqrt{l}}{\sqrt{1000}} \\ \sum_{i=1}^4 z_i C_{i,f} = 0 \end{array} \right. \quad [4.39]$$

In this system of equations solved numerically, we distinguish the output parameters, constants and input parameters. These were determined experimentally or on the basis of literature data.

As the first approach, the solution activity is considered constant; therefore, we neglected its effect [TRU 00].

4.3.1. Output model

θ_w : moisture content;

p_v : water vapor pressure;

p_a : gas pressure;
 $C_{cl,f}$: free chloride concentration;
 $C_{OH,f}$: free hydroxide concentration;
 $C_{K,f}^+$: free potassium concentration;
 $C_{Na^+,f}$: free sodium concentration.

4.3.2. Constant parameters

z_i : valence of species $i z_{cl^-} = -1; z_{OH^-} = -1; z_{Na^+}; z_{K^+} = +1;$
 F : Faraday constant ($96,500 \text{ C.mol}^{-1}$);
 R : gas constant ($8,314 \text{ J.mol}^{-1}.\text{K}^{-1}$);
 T : temperature supposed constant (293 K);
 ρ_w : water density;
 R_v : gas constant for vapor water;
 R_a : gas constant for air;
 μ_w : dynamic viscosity of water;
 μ_g : dynamic viscosity of gas;
 P_{at} : atmospheric pressure;
 P_{vs} : saturated steam pressure.

4.4. Difficulties in determining some parameters of the model

The modeling of coupled ion and moisture transport was presented for a given porous medium. When we want to apply the model in the case of cement-based materials, for example, we need to have the knowledge of several input parameters that are measured experimentally. These are ionic diffusion coefficients, chloride binding capacity of concrete, intrinsic permeability to water, water relative permeability, etc. Here, we discuss the difficulties linked to the determination of these parameters.

The key parameter of the ionic diffusion is the ionic diffusion coefficient, which is very sensitive to the ionic transfer model. It can be measured experimentally by several methods. The method that is widely used is the chloride migration test through cement-based materials in steady state [AMI 01, FRI 04]. This method allows us to determine the chloride coefficient diffusion and then deduce the coefficient diffusion of other ions present in the interstitial solution. This step of deduction is based on the assumptions such as the ionic diffusion in material is proportional to the ionic diffusion in an infinitely diluted solution and that the tortuosity of material is considered as constant for all the ions. These assumptions need to be confirmed by in-depth researches. In the same field, it is also difficult to determine the diffusion coefficient in unsaturated concrete.

Another key parameter of ionic transfer is the chemical binding capacity of materials. Indeed, when the cement matrix is submitted to chloride and hydroxide ingress, a part of chloride can be absorbed and facilitate the release of hydroxide in the pore solution. Consequently, this ionic absorption capacity of material influences considerably the pH interstitial solution which plays a significant role with respect to corrosion of reinforcing steel in concrete. The measurement of ion binding capacity of concrete is often carried out on chlorides and then deduces hydroxide binding capacity of concrete. This parameter depends on the temperature and the fineness concrete specimen, and also on the conservation condition specimens (agitated or non-agitated).

Concerning the moisture transfer, we have characteristic parameters, such as the intrinsic permeability to water and water-relative permeability. In the application of Darcy's law, the intrinsic permeability of cement-based materials is theoretically independent of the fluid nature. Indeed, it depends on the microstructure of the material. However, experimental results showed a difference between the permeability of liquid and the permeability of gas. In the case of cement-based material, Bamforth [BAM 87] showed that the permeability of gas is much lower than the permeability of water. Indeed, taking into account the Klinkenberg effect (gas-slipage along the pore walls) is an interesting attempt to explain the differences between water permeability and gas permeability, but for Perraton cited by Nguyen [NGU 07], only the Klinkenberg effect does not explain these important variations. In an unsaturated media, the water permeability of material varies

on the basis of moisture content. This variation is characterized by relative permeability. Many studies, mainly conducted on soil, consist of determining the relative permeability evolution. Indeed, the relative water permeability of material varies as an increasing function of the degree of saturation. Some studies in the literature tried to calculate analytically the relative permeability, such as [MUA 76]. But there are some existing parameters to calibrate from the capillary-saturation pressure curve.

Another difficulty is linked to the determination of sorption–desorption water isotherm. Generally, the hysteresis effect is neglected because it may affect the moisture transport mainly during the drying phase.

Figure 4.3 depicts a comparison between chloride profile simulated by the model and the experimental profile obtained in tidal zone [SLE 08].

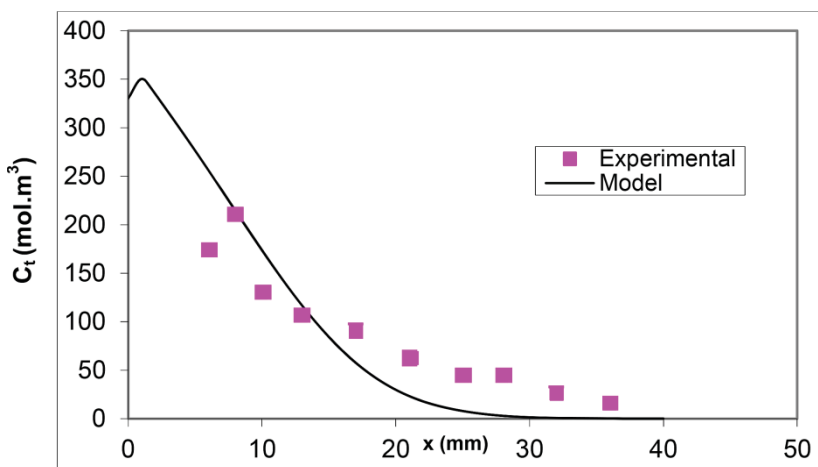


Figure 4.3. Comparison of chloride profile simulated and measured in tidal zone (laboratory test)

Overall, the model gives good results, but near the surface there are differences between the simulated and the measured values. These differences are probably due to hysteresis neglected by the model.

4.5. Numerical method description

4.5.1. Finite volume method

The model of ionic transport in the porous media can be solved numerically by several methods. Wang [WAN 05] and Perez [PER 99] used the finite element method. The finite element method is used in the work of Francy [FRA 99]. This method adapts well to nonlinear conversation law, which is the case of our study. That is the reason why the finite element method is adopted.

The transfer equations are solved by considering the assumption of one-dimensional (1D) transport. For the resolution, we discretize the calculation field into N elements, called control volume K_j . Each control volume has a center x_j where the unknown factors of the differential equations are defined (see Figure 4.4).

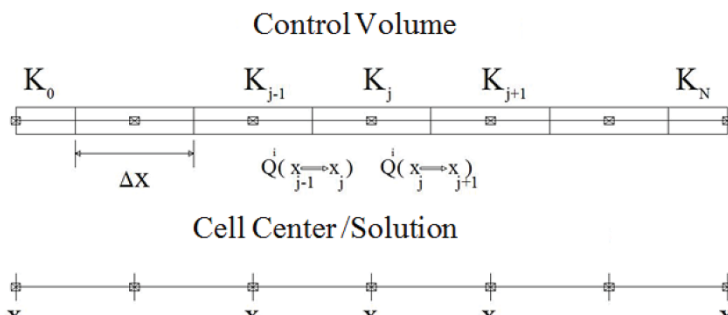


Figure 4.4. Discretization space

To simplify, we take the general case of a differential equation in continuous form. We pass to the version discretized by an Euler's approximation of the temporal derivatives and a discretization of the finite volumes for spatial derivatives. The temporal discretization is denoted by an exhibitor n and the spatial discretization is denoted by j .

The mass conservation equation is:

$$\frac{\partial(\alpha A)}{\partial t} + \operatorname{div}(Q) = 0 \quad [4.40]$$

where the flow Q is given by the following formula:

$$Q = \beta \cdot \text{grad}(B) \quad [4.41]$$

where the terms A and B are unknown factors of the problem. α, β are the two input parameters which can be constant or functions of A and B .

If we integrate equation [4.40] onto a control volume between two moments t^n and $t^{n+1} = t^n + \Delta t$, we have:

$$\int_K (\alpha(t^{n+1})A(t^{n+1}) - \alpha(t^n)A(t^n))dx + \int_{t^n}^{t^{n+1}} \int_{\partial K} Q \cdot n \, dk \, dt = 0 \quad [4.42]$$

where n is a normal vector toward the outside of control volume K and ∂K is an edge of K .

At the moment of t^n , the approximation of αA on the control volume K is given as:

$$\alpha_j^n A_j^n = \int_K \alpha(t^n)A(t^n)dx \quad [4.43]$$

The discretization in finite volume corresponds to the integration of divergent terms and to the approximation of normal derivatives on a control volume. The flow is estimated with the interface between two close elements by an average expression leading to a numerical conservative scheme.

The flux is a function of the unknown factor problem in the close meshes. If this flow is the function of the unknown factors to the step at the moment of t^n , the method is known as explicit. If it is a function of the unknown factors at the moment of t^{n+1} , the method is called implicit. The flows can be different on both sides of the control volume. Nevertheless, we chose the finite element method with conservative flow. With this method, the subjacent conservative character of the equations is exploited by choosing a common numerical flow for two close control volumes.

4.5.1.1. Implicit scheme case

$$\int_{t^n}^{t^{n+1}} \int_{\partial K} Q \cdot n \, dk \, dt = \frac{\Delta t}{\Delta x} \left[Q(x_{j-1}^{n+1} \rightarrow x_j^{n+1}) - Q(x_j^{n+1} \rightarrow x_{j+1}^{n+1}) \right] \quad [4.44]$$

Equation [4.45] is expressed as:

$$\frac{\alpha_j^{n+1} A_j^{n+1} - \alpha_j^n A_j^n}{\Delta t} = \frac{1}{\Delta x} \left[Q(x_{j-1}^{n+1} \rightarrow x_j^{n+1}) - Q(x_j^{n+1} \rightarrow x_{j+1}^{n+1}) \right] \quad [4.45]$$

with:

$$Q(x_{j-1}^{n+1} \rightarrow x_j^{n+1}) = \frac{\beta_{j-1}^{n+1} + \beta_j^{n+1}}{2} [B_{j-1}^{n+1} - B_j^{n+1}] \quad [4.46]$$

$$Q(x_j^{n+1} \rightarrow x_{j+1}^{n+1}) = \frac{\beta_j^{n+1} + \beta_{j+1}^{n+1}}{2} [B_j^{n+1} - B_{j+1}^{n+1}] \quad [4.47]$$

4.5.1.2. Semi-implicit scheme

$$\int_{t^n}^{t^{n+1}} \int_{\partial K} Q \cdot n \, dk \, dt = \frac{\Delta t}{\Delta x} \left[Q(x_{j-1}^{n+1} \rightarrow x_j^{n+1}) - Q(x_j^{n+1} \rightarrow x_{j+1}^{n+1}) \right] \quad [4.48]$$

Equation [4.49] is developed as:

$$\frac{\alpha_j^{n+1} A_j^{n+1} - \alpha_j^n A_j^n}{\Delta t} = \frac{1}{\Delta x} \left[Q(x_{j-1}^{n+1} \rightarrow x_j^{n+1}) - Q(x_j^{n+1} \rightarrow x_{j+1}^{n+1}) \right] \quad [4.49]$$

with:

$$Q(x_{j-1}^{n+1} \rightarrow x_j^{n+1}) = \frac{\beta_{j-1}^n + \beta_j^n}{2} [B_{j-1}^{n+1} - B_j^{n+1}] \quad [4.50]$$

$$Q(x_j^{n+1} \rightarrow x_{j+1}^{n+1}) = \frac{\beta_j^n + \beta_{j+1}^n}{2} [B_j^{n+1} - B_{j+1}^{n+1}] \quad [4.51]$$

4.5.1.3. Explicit scheme case

$$\int_{t^n}^{t^{n+1}} \int_{\partial K} Q \cdot n \, dk \, dt = \frac{\Delta t}{\Delta x} \begin{bmatrix} Q(x_{j-1}^n \rightarrow x_j^n) \\ -Q(x_j^n \rightarrow x_{j+1}^n) \end{bmatrix} \quad [4.52]$$

Equation [4.52] is written as:

$$\frac{a_j^{n+1} A_j^{n+1} - a_j^n A_j^n}{\Delta t} = \frac{1}{\Delta x} \begin{bmatrix} Q(x_{j-1}^n \rightarrow x_j^n) \\ -Q(x_j^n \rightarrow x_{j+1}^n) \end{bmatrix} \quad [4.53]$$

with:

$$Q(x_{j-1}^n \rightarrow x_j^n) = \frac{\beta_{j-1}^n + \beta_j^n}{2} [B_{j-1}^n - B_j^n] \quad [4.54]$$

$$Q(x_j^n \rightarrow x_{j+1}^n) = \frac{\beta_j^n + \beta_{j+1}^n}{2} [B_j^n - B_{j+1}^n] \quad [4.55]$$

4.5.1.4. Stability and convergence of numerical schemes

It is difficult to study the stability and the convergence of numerical schemes when we take into account the coupling of several nonlinear equations. Theoretically, the implicit and the semi-implicit schemes give a better stability [CRO 89]. For the explicit scheme, the transfer of one component described by the classical diffusion equation has a condition on step time, which is defined as follows:

$$\Delta t \leq \frac{(\Delta x)^2}{2\beta A^{max}} \quad [4.56]$$

In the above equation, Δt is the step time used for resolution of the equations, Δx is the spatial step size used for resolution of the equations and $\beta(A)$ is an input parameter. It is the function of variable A. Considering that equation [4.53] is a nonlinear equation, the convergence condition requires testing step time at the most disadvantageous moment which corresponds to the maximum value of $\beta(A)$. This value is denoted as $\beta(A)^{max}$.

The choice of step time is sometimes complex. If the equation makes it possible to determine step time in the case of a nonlinear equation, it is not always the case for system of coupled nonlinear equations. It is the reason why we choose a small step time, and we check at each step time for all the variables of N coupled equations the following condition [PRE 88]:

$$\frac{\max \left[\underbrace{\max \left| \frac{A_j^{n+1} - A_j^n}{A_j^0} \right|}_{\text{equa 1}}, \dots, \underbrace{\max \left| \frac{A_j^{n+1} - A_j^n}{A_j^0} \right|}_{\text{equa } i}, \dots, \underbrace{\max \left| \frac{A_j^{n+1} - A_j^n}{A_j^0} \right|}_{\text{equa } N} \right]}{\Delta E^0} \leq \frac{1}{v} \quad [4.57]$$

where ΔE^0 is the critical relative variation allowed, generally equal to 0.01; v is a coefficient related to the increment of step time, equal to 1.5.

If condition [4.57] is checked, the step time is maintained. If not, the step time is reduced by multiplying it by the left term of equation [4.57] [CRO 89].

4.5.2. Numerical simulations of chloride profiles: parametrical study

The partial differential equations [4.36] and [4.39] are solved numerically in the 1D case. The implementation of equations in one dimension is done by applying a classical linearization procedure, which consists of discretizing these equations in both time and space domains. The space and time domains are discretized by using the classical finite difference method with explicit scheme.

We have used three types of adsorption isotherms to study their influence on the chloride profile. The BET, GAB and Bradley models have been selected here to define the adsorption isotherm that relates relative humidity to water content. The equations for these isotherms are found in [QUE 89]. Empirical expressions for the parameters of these isotherms have been developed by Xi *et al.* by bets-fitting of experimental data [BAZ71] and [BAZ 72]. These parameters are the function of the temperature T, hydration age t_e and the water to cementitious ratio W/C of concrete. Figure 4.5 illustrates the three different types of adsorption isotherms used in this study. Figure 4.6 illustrates the influence of W/C on the GAB adsorption isotherm.

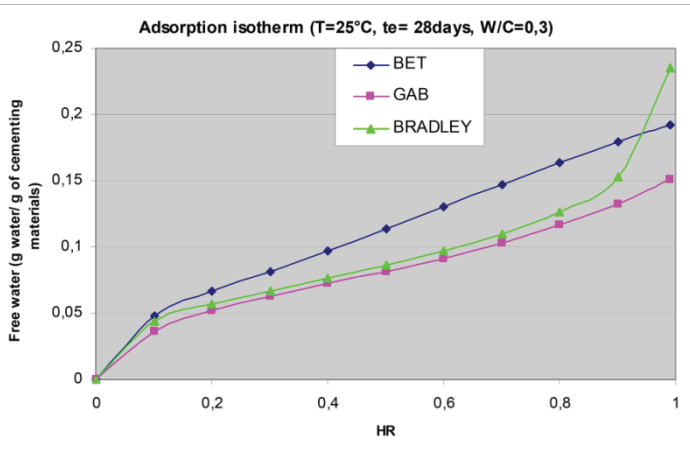


Figure 4.5. Three types of adsorption isotherm

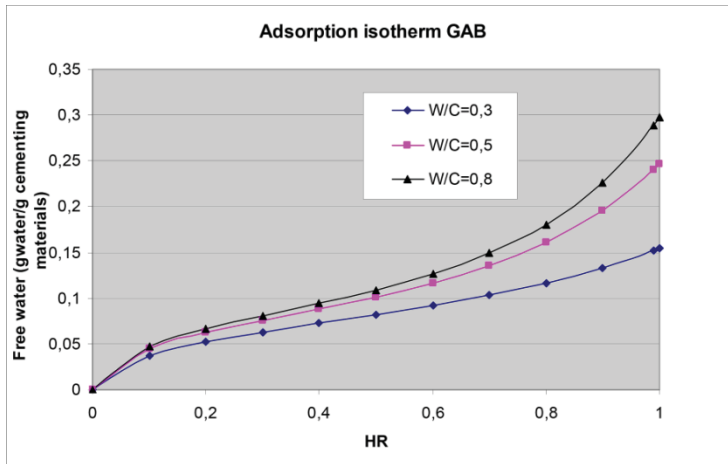


Figure 4.6. Influence of W/C (GAB isotherm). For a color version of the figure, see www.iste.co.uk/ait-mokhtar/coastal.zip

For the numerical simulations, we suppose a specimen specimen with $L = 5$ cm, decomposed in the x -direction into n equal intervals and exposed at one surface to the salt solution ($1,000 \text{ mol Cl}^-/\text{m}^3$ solution).

To solve the above equation's system, we need to have the moisture and species diffusion coefficient in ionic solution.

The moisture diffusion coefficient used in this study is obtained from [BAZ 72]. In isothermal conditions:

$$D_h = D_{h,ref} \left(0.05 + \left(\frac{0.95}{1 + \left(\frac{1-h}{1-h_c} \right)^n} \right) \right) \quad [4.58]$$

where $D_{h,ref}$ is the humidity diffusion coefficient determined at specified reference conditions, n is a parameter characterizing the spread of the drop in D_h (ranging from 6 to 16), and h_c is the humidity level at which D_h drops halfway between its maximum and minimum values taken as 0.75.

Note that the hydraulic diffusivity D_θ is obtained from humidity diffusion coefficient D_h by using the adsorption isotherm.

The ionic diffusion coefficient used in this study is taken from [BAZ 72]:

$$D_{ei} = D_{i,ref} \left(1 + \left(\frac{1-h}{1-h_c} \right) \right)^{-1}; i = \text{Cl}^-, \text{Na}^+, \text{K}^+, \text{OH}^- \quad [4.59]$$

where $D_{i,ref}$ is the ionic diffusion coefficient for $C_{i,f} = 1 \text{ g/l}$. This coefficient is obtained by Boltzmann variable analysis, from chloride profiles obtained in unsteady state diffusion tests.

An initial condition describing the moisture content, ionic concentrations at the beginning of time have to be given (Table 4.1). The boundary conditions in numerical simulation are assumed as follows: at the surface which is exposed to the external solution, the specimen is saturated and has constant ionic concentration, while on the opposite face of the specimen, the flux of water and ionic species are zero.

Chloride binding is considered in the model using the linear, Langmuir and Freundlich isotherms [PER 99].

The parameters, initial data and boundary conditions used in the simulation are given in Table 4.1. The simulations are conducted on ordinary concrete with 15% porosity.

	Water	Cl^-	OH^-	Na^+	K^+
Reference diffusion coefficients $D_{i,\text{ref}}(\text{m}^2/\text{s})$	10^{-11}	2.032×10^{-12}	5.26×10^{-12}	1.334×10^{-12}	1.957×10^{-12}
Initial value	$\theta_0 = 0.1$	$C_{\text{Clf}0} = 0 \text{ mol/m}^3$	$C_{\text{OHf}0} = 108 \text{ mol/m}^3$	$C_{\text{Naf}0} = 25 \text{ mol/m}^3$	$C_{\text{Kf}0} = 83 \text{ mol/m}^3$
Limit value at $x = 0$	$\theta = 0.15$	$C_{\text{Clf}} = 1,000 \text{ mol/m}^3$	$C_{\text{OHf}} = 108 \text{ mol/m}^3$	$C_{\text{Naf}} = 1025 \text{ mol/m}^3$	$C_{\text{Kf}} = 83 \text{ mol/m}^3$
Flux \mathbf{J}_i at $x = L$	$\mathbf{J}_{\theta l} = 0$	$\mathbf{J}_{\text{Clf}} = 0$	$\mathbf{J}_{\text{OHf}} = 0$	$\mathbf{J}_{\text{Naf}} = 0$	$\mathbf{J}_{\text{Kf}} = 0$
Porosity			0.15		
Isotherm	Linear $C_{ib} = \alpha C_{if}$		$\alpha = 0.06 \text{ m}^3 \text{ sol./m}^3 \text{ mat.}$		
	Langmuir $C_{ib} = \alpha C_{if} / (1 + \beta C_{if})$		$\alpha = 0.33 \text{ m}^3 \text{ sol./m}^3 \text{ mat.}$		
	Freundlich $C_{ib} = \alpha C_{if}^\beta$		$\beta = 0.00245 \text{ m}^3 \text{ sol/mol}$		
			$\alpha = 7.62 \text{ m}^3 \text{ sol./m}^3 \text{ mat.}$		
			$\beta = 0.36$		

Table 4.1. Data of problem

Several numerical simulations were done. The numerical model was examined by studying the influence of the different model parameters (time of exposition and initial saturation degree) and different mechanisms (ionic interactions, convection, binding and adsorption isotherm), considered in the chloride transport mechanism.

4.5.2.1. Effect of ionic interactions

Figure 4.7 shows the influence of the electrostatic interaction between the ionic species (Na^+ , OH^- and K^+) on the free chloride concentration after 6 months of exposition to saline environment. We demonstrate that the

chloride concentration without ionic interactions is weaker than the concentration obtained with ionic interactions.

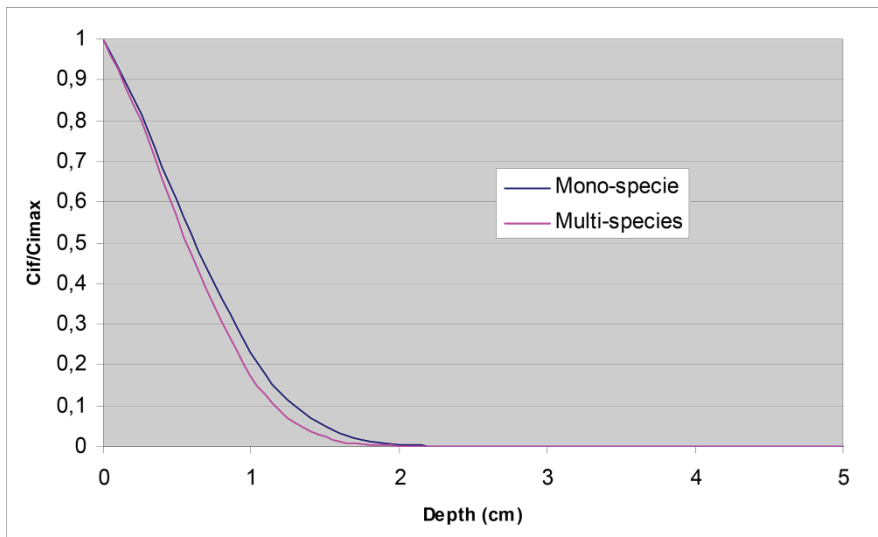


Figure 4.7. Free chloride concentration profiles (interactions effect).
For a color version of the figure, see www.iste.co.uk/ait-mokhtar/coastal.zip

This result can be explained by the effect of the electrostatic potential, which slows the fastest ions OH^- and Cl^- and accelerates the slowest ions Na^+ and K^+ .

4.5.2.2. Effect of time exposure

The effect of time on the resulting profiles is significant; thus, more chlorides are allowed to penetrate during the time mostly in the first millimeter of the specimen. Also, Figure 4.8 shows that as time increases, concentration profiles progressively become similar.

4.5.2.3. Effect of initial saturation degree

The concentration of chloride increases when the saturation degree decreases, as shown in Figure 4.9. In fact, at 100% of saturation, there is no convective movement because the mechanism of water absorption through capillarity is not possible. So, only the diffusive movement is represented,

while for $s = 66\%$ and 80% , both the diffusive and convective mechanisms occur.

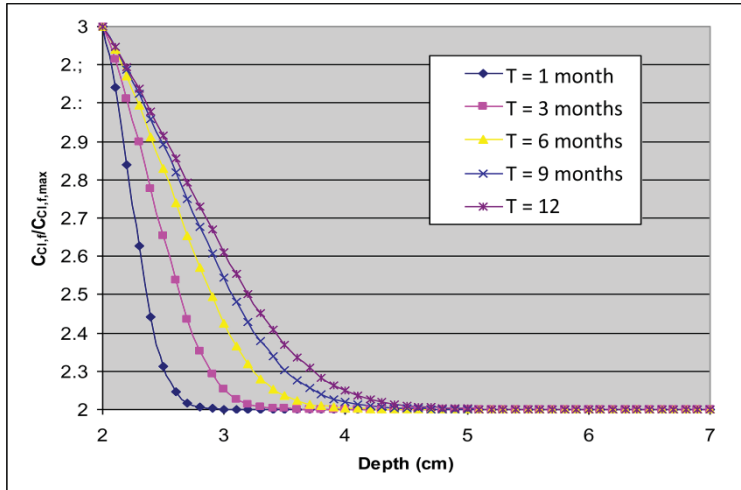


Figure 4.8. Free chloride concentration profiles (time effect). For a color version of the figure, see www.iste.co.uk/ait-mokhtar/coastal.zip

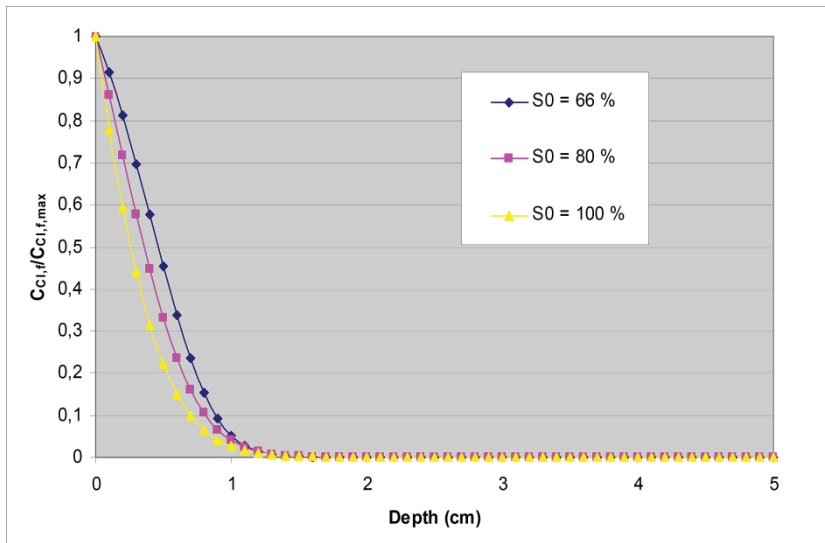


Figure 4.9. Free chloride concentration profiles (effect of initial saturation degree). For a color version of the figure, see www.iste.co.uk/ait-mokhtar/coastal.zip

4.5.2.4. Effect of the convection phenomena

Figure 4.10 shows the influence of pore solution convection mechanism due to the moisture flow in unsaturated materials. The difference is significant between the two cases; the concentration is higher when the two mechanisms (diffusion and convection) are considered after 3 months of exposition to saline environment.

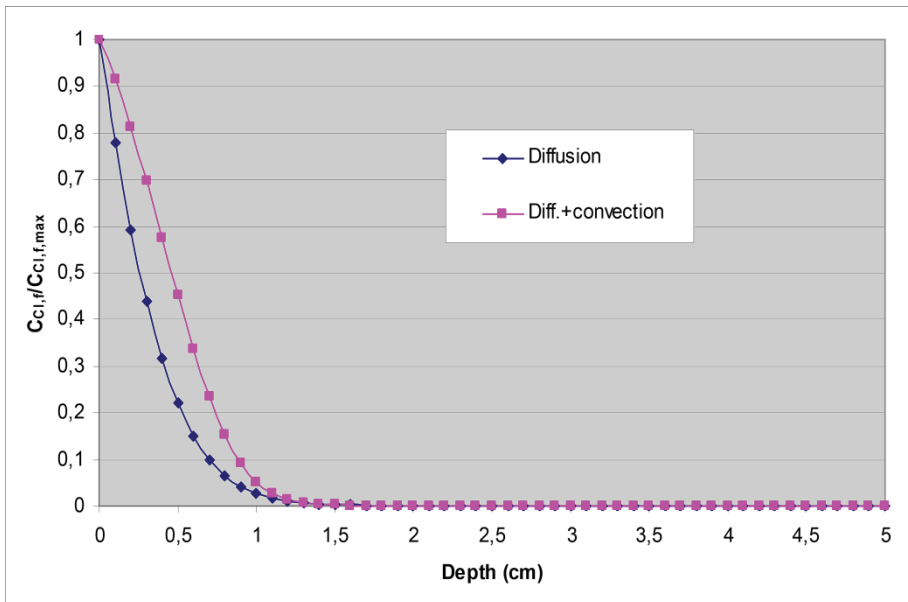


Figure 4.10. Free chloride concentration profiles (effect of convection). For a color version of the figure, see www.iste.co.uk/ait-mokhtar/coastal.zip

4.5.2.5. Effect of binding isotherm

The effect of the binding isotherm nature on the chloride concentration profiles was studied by analyzing three different cases: in the first case, binding was neglected (no isotherm); in the second case, a linear relationship between bound and free chlorides was assumed (linear isotherm); and in the third case, nonlinear binding (Langmuir and Freundlich) was taken into account. The binding constants used in this study were evaluated from the work of Perez [PER 99].

Calculation with no binding results in higher free chloride profiles. From Figure 4.11, we can conclude that the nature of the binding relationship assumed for modeling has a significant implication on the free chloride profiles.

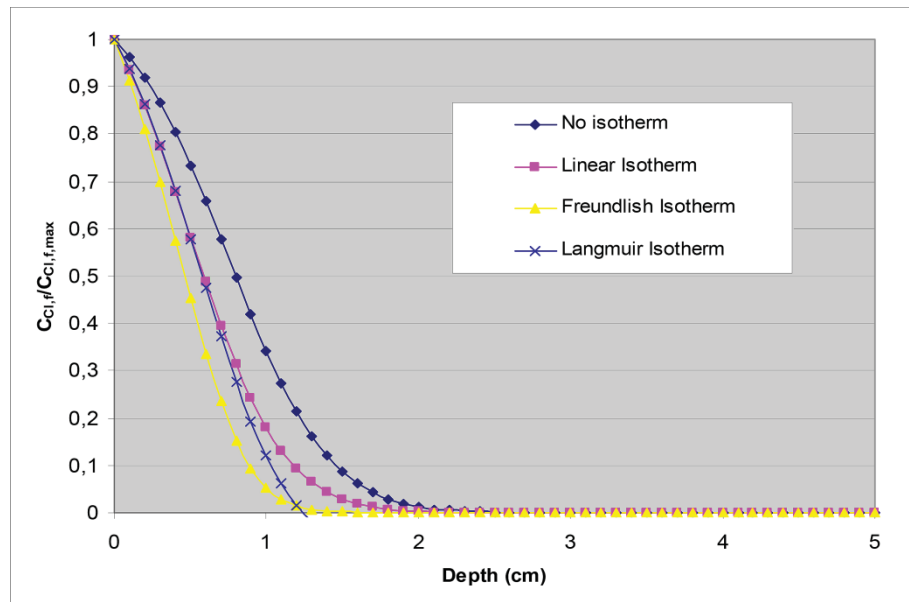


Figure 4.11. Free chloride concentration profiles (effect of chloride binding). For a color version of the figure, see www.iste.co.uk/ait-mokhtar/coastal.zip

4.5.2.6. Effect of the adsorption isotherm and W/C ratio

In this section, we discuss the influence of adsorption isotherm on the chloride profiles. A lot of works about adsorption and desorption isotherms are found in the literature. In this study, we are fascinated by the adsorption isotherm, and particularly by the following three isotherms: BET, GAB and Bradley. After one month of exposition to the saline solution, the influence of the adsorption isotherm on the chloride profile is concentrated in the first centimeter.

From Figure 4.12, particularly for BET and GAB adsorption isotherm cases, the concentration of chloride increases with the water content. For the Bradley isotherm case, the concentration of chloride is weaker than the GAB isotherm case; nevertheless, the water content is higher in the first case. This

result can be explained by the effect of higher saturation (Bradley isotherm) for the humidity between 0.9 and 1. The effect of convection gets weaker when the water content approaches saturation.

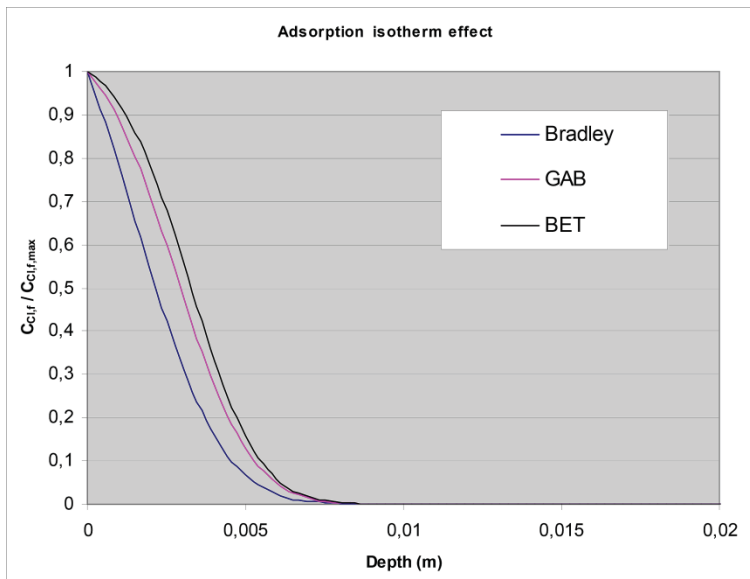


Figure 4.12. Free chloride concentration profiles (adsorption isotherm effect). For a color version of the figure, see www.iste.co.uk/ait-mokhtar/coastal.zip

The amount of chlorides penetrated into concrete decreases with the W/C ratio as shown in Figure 4.13. This result may be explained by the refined porosity produced by the reduction of the pore due to the high cement content.

4.5.2.7. Gas pressure effect

As mentioned in the previous section (section 4.5.2.6), the heaviness moisture model either depends on the gas pressure consideration constant or it does not. From mathematical point of view, in the first case, equation [4.34a] is reduced because the velocity of gas phase is zero ($U_g = 0$). In the second case, the same equation is difficult to solve.

From physical point of view, the consideration of the gas velocity means that the gas flux contributes during the drying period.

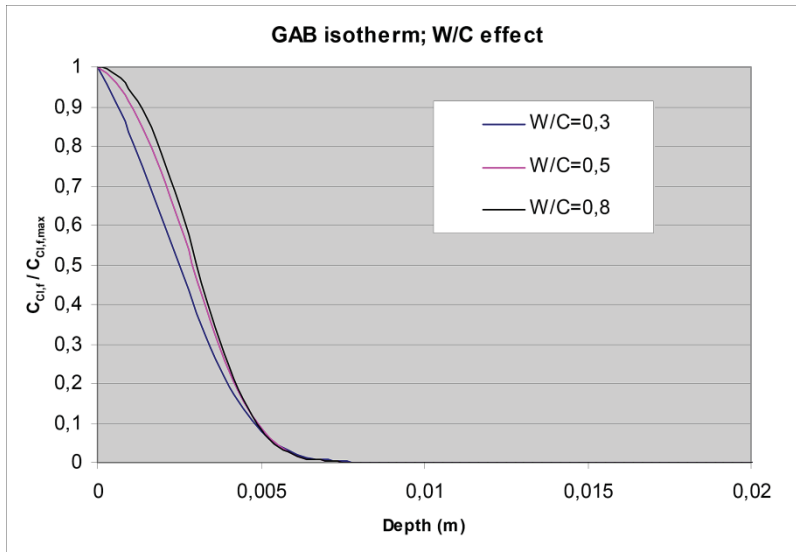


Figure 4.13. Free chloride concentration profiles (W/C ratio effect). For a color version of the figure, see www.iste.co.uk/ait-mokhtar/coastal.zip

In the literature, some authors [MAI 99] consider the gas flux, while others [NGU 07] neglect it by pointing out to the fact that during the drying a counterdiffusion of dried air is opposed to the gas flux.

We have to note that the two authors used the same equation of gas diffusivity:

$$D_v = D_{va} f_{res}(\epsilon_0, \theta_l) = \epsilon_0^{-2} (\epsilon_0 - \theta_l)^{2n+2} \quad [4.60]$$

The results obtained by one of the authors are opposite because they did not use the same value of the fitting parameter “*n*”. The effect of the parameter *n* is strong on resistivity factor $f_{res}(\epsilon_0, \theta_l)$ than on the vapor diffusivity in porous medium. Generally, weak value of *n* (*n* < 1) gives a high value of resistivity factor, and consequently the flux of water vapor is increased. For *n* > 1, the opposite occurs and we can admit the assumption of gas pressure constant.

Figure 4.14 shows an example of simulation of water profile (saturation degree) in the two cases (gas pressure constant and variable).

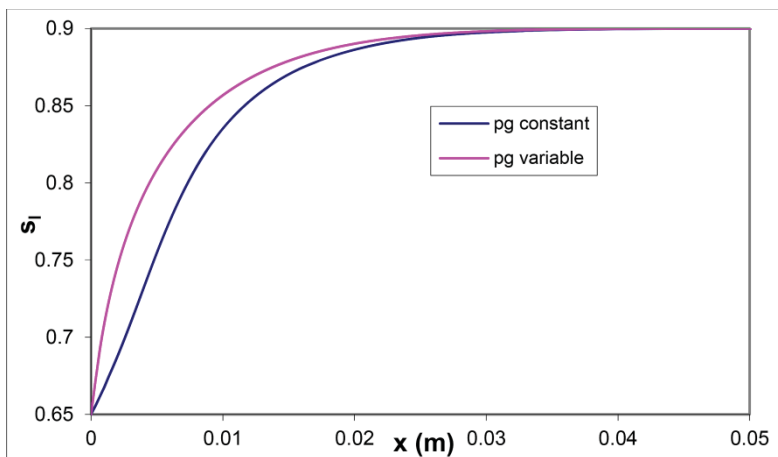


Figure 4.14. Water profile (saturation degree): effect of gas pressure

In Chapter 3, it has been shown how we can link analytically the macroscopic and microscopic diffusion coefficients of ions by using the periodic homogenization method. It will be interesting to use this method for water and gas transport. Thus, the empirical approach of Millington could be avoided.

4.6. Conclusions

In this chapter, we presented the modeling of chloride transport in unsaturated materials. This model takes into account the main mechanisms involved in unsaturated materials (diffusion, convection, ionic coupling and binding isotherm). We can draw the following conclusions:

- The influence of ionic interactions on the chloride concentration profiles was studied by supposing the presence of four ionic species in the interstitial solution. The chloride concentration considering ionic interactions is weaker than the concentration obtained without ionic interactions.
- The present study indicates the significant influence of the time exposure and the initial saturation degree on the chloride profile, mainly in unsteady state. This influence is also stronger in the first millimeter of the material.

- The numerical model illustrates that the convection by moisture transport can accelerate the chloride ingress into concrete. So, in the unsaturated case, the convection term should be considered realistically in the formulation.
- Linear and nonlinear binding isotherms have a big influence on the free chloride profiles. Calculation with no binding results in higher free chloride concentrations.
- The relative humidity, related to water content by the adsorption isotherm, affects the penetration of chloride ions into concrete. The influence of the adsorption isotherm on the chloride is varied according to the nature of the adsorption isotherm. Even though the adsorption isotherm is a function of the concrete characteristics, in particularly W/C ratio, a decrease in W/C ratio resulted in reducing the penetration of chloride.
- It is important to develop a model that takes into account the hysteresis occurring during the sorption and desorption of water.
- The consideration assumption of the gas pressure constant depends on how the empirical law of Millington is used. It will be helpful to develop an analytical law. These results could be obtained by using the periodic homogenization method presented in Chapter 3.

4.7. Bibliography

- [AMI 01] AMIRI O., AÏT-MOKHTAR A., DUMARGUE P. *et al.*, “Electrochemical modelling of chlorides migration in cement based materials. Part II: experimental study – calculation of chlorides flux”, *Electrochimica Acta*, vol. 46, no. 23, pp. 3589–3597, 2001.
- [BAM 87] BAMFORTH P., “The relationship between permeability coefficients for concrete obtained using liquid and gaz”, *Magazine of Concrete Research*, vol. 39, pp. 3–11, 1987.
- [BAR 83] BARD A.J., FAULKNER L.R., *Electrochimie*, vol. 1, Masson, 1983.
- [BAR 00] BARBARULO R., MARCHAND J., SNYDER K.A. *et al.*, “Dimensional analysis of ionic transport problems in hydrated cement systems. Part 1: theoretical considerations”, *Cement and Concrete Research*, vol. 30, pp. 1955–1960, 2000.

- [BAZ 71] BAZANT Z., NAJJAR L.J., "Drying of concrete as a nonlinear diffusion problem", *Cement and Concrete Research*, vol. 1, pp. 461–473, 1971.
- [BAZ 72] BAZANT Z., NAJJAR L.J., "Nonlinear water diffusion in unsaturated concrete", *Materials and Structures*, vol. 5, no. 25, pp. 3–20, 1972.
- [CRO 89] CROUZEIX M., MIGNOT A., *Analyse numérique des équations différentielles*, 2nd ed., Masson Edition, Paris, 1989.
- [FRA 98] FRANCY O., Modélisation de la pénétration des ions chlorures dans les mortiers partiellement saturés en eau, PhD Thesis, University of Paul Sabatier, Toulouse, 1998.
- [FRI 03] FRIEDMANN H., Modélisation multi-espèces de l'électrodiffusion instationnaire des ions chlorures dans les mortiers de ciment – Intégration de la double couche électrique, PhD Thesis, University of La Rochelle, 2003.
- [FRI 04] FRIEDMANN H., AMIRI O., AÏT-MOKHTAR A. et al., "A direct method for determining chloride diffusion coefficient by using migration test", *Cement and Concrete Research*, vol. 34, no. 11, pp. 1967–1973, 2004.
- [MAI 99] MAINGUY M., Modèles de diffusions non-linéaires en milieux poreux, applications à la dissolution et au séchage des matériaux cimentaires, PhD Thesis, Ecole Nationale de Ponts et Chaussées, Paris, 1999.
- [MIL 61] MILLINGTON R.J., QUIRK J.P., "Permeability of porous solids", *Transactions of the Faraday Society*, vol. 57, pp. 1200–1207, 1961.
- [MUA 76] MUalem Y., "A new model for predicting the hydraulic conductivity of unsaturated porous media", *Water Resources Research*, vol. 12, no. 3, pp. 513–522, 1976.
- [NGU 07] NGUYEN T.Q., Modélisation physico-chimiques de la pénétration des ions chlorures dans les matériaux cimentaires, PhD Thesis, Ecole Nationale des Ponts et Chaussées, 2007.
- [PER 99] PÉREZ B.M., Service life modeling of R.C. highway structures exposed to chlorides, PhD Thesis, University of Toronto, 1999.
- [PRE 88] PRESS W.H., FLANNERY B.P., TUEKOLSKY S.A. et al., *Numerical Recipes in C – The Art of Scientific Computing*, Cambridge University Press, Cambridge, 1988.
- [QUE 89] QUENARD D., Adsorption et transfert d'humidité dans les matériaux hygroscopiques, PhD Thesis, National Polytechnic Institute of Toulouse, 1989.
- [SAM 99] SAMSON E., MARCHAND J., BEAUDOIN J.J., "Describing ion diffusion mechanisms in cement-based materials using the homogenization technique", *Cement and Concrete Research*, vol. 29, no. 8, pp. 1341–1345, 1999.

- [SAM 00] SAMSON E., MARCHAND J., BEAUDOIN J.J., “Modeling the influence of chemical reactions on the mechanisms of ionic transport in porous materials: an overview”, *Cement and Concrete Research*, vol. 30, pp. 1895–1902, 2000.
- [SLE 08] SLEIMAN H., Etude du transport des chlorures dans les matériaux cimentaires non saturés: validation expérimentale sur bétons en situation de marnage, PhD Thesis, University of La Rochelle, 2008.
- [TRU 00] TRUC O., OLLIVIER J.P., NILSSON L.O., “Numerical simulation of multi-species transport through saturated concrete during a migration test – MsDiff code”, *Cement and Concrete Research*, vol. 30, no. 10, pp. 1581–1592, 2000.
- [VAN 80] VAN GENUCHENTEN M.T., “A closed-form equation for predicting the hydraulic conductivity of unsaturated soil”, *Soil Science Society of America*, vol. 44, pp. 892–898, 1980.
- [WHI 98] WHITAKER S., *Method of Volume Averaging*, Kluwer Academic Publishers, New York, 1998.
- [WAN 05] WANG Y., LI L., PAGE C.L., “Modelling of chloride ingress into concrete from a saline environment”, *Building and Environment*, vol. 40, pp. 1573–1582, 2005.

Construction Degradation by External Sulfate Attacks

5.1. Introduction

The action of seawater on concrete involves sulfate ions [SAN 06]. The ingress of sulfate in concrete causes chemical and physical degradations. This is known as external sulfate attacks. Sulfate ions react with hydration products, such as monosulfoaluminate, producing ettringite and gypsum. The growth of ettringite crystals due to supersaturation of sulfate generates crystallization pressure. This results in expansion and then cracking of cementitious matrix. Leaching and cracking favor the ingress of sulfate concentrated solution and accelerate the degradation [GER 00]. The increase of porosity and the propagation of cracks finally cause loss of strength and spalling of concrete cover.

The sulfate concentration in seawater is 2.8 g/L [SWE 71]. This concentration is relatively high in comparison with sulfate content of soils and groundwater. However, the combined action of sulfate ions and other chemical species in seawater is reported to generate less severe degradation than sulfate ions alone in groundwater. The concentration of chloride ions in seawater is 19 g/L. Chloride ions combine with cement phases and hydration products to form Friedel's salt, which results in a reduction in the action of sulfate ions [MEH 91]. However, damage caused by a sulfate attack influences the corrosion of steel reinforcement [DEH 07].

This chapter focuses on external sulfate attacks, i.e. the chemical action of sulfate ions and its consequences. The mechanism of degradation is complex, as sulfate attacks involve chemical, physical and mechanical parameters, and even coupling between them. Studying external sulfate attacks has favored the development of methods useful for understanding the behavior of concrete exposed to seawater. Long-term experience has provided recommendations on cement and concrete exposed to seawater and groundwater, generally given as prescriptive specifications in national standards. Some cement types have actually proved to be resistant to sulfate attacks and seawater. However, the development of new cements and concrete mixtures requires a better understanding of the mechanisms of degradation and the development of performance testing.

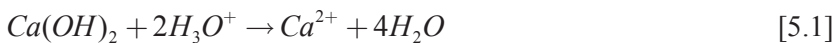
5.2. Mechanisms of degradation

5.2.1. *Chemical reactions and crystallization pressure*

In sulfate-bearing environments, such as groundwater, rivers and seawater, sulfate concentrations typically reach 0.02–3.0 g/L and a pH of 7–8 [STO 03]. The ingress of external sulfate solution modifies the chemical equilibrium between solid phases and interstitial solution in the cementitious matrix.

The cementitious matrix is mainly constituted of calcium hydroxide or portlandite $\text{Ca}(\text{OH})_2$, calcium silicate hydrate (C-S-H), and the hydration products of calcium aluminate (C_3A) and calcium aluminate ferrite (C_4AF) formed in the presence of calcium sulfate, used as set retarder by cement producers. Those are mainly alumino ferrite trisubstituted AFt ($\text{Ca}_6(\text{Al},\text{Fe})_2(\text{SO}_4)_3(\text{OH})_{12}\cdot26\text{H}_2\text{O}$ – ettringite) and alumino ferrite monosubstituted AFm ($3\text{CaO} \cdot (\text{Al},\text{Fe})_2\text{O}_3 \cdot \text{CaSO}_4 \cdot 12\text{H}_2\text{O}$ – monosulfoaluminate). The two aluminate phases are finely intermixed in the C-S-H. They are very sensitive to sulfate: monosulfoaluminate especially can easily be destabilized and transformed back to ettringite in the presence of sulfate.

The diffusion process causes leaching, i.e. the dissolution of portlandite and partial decalcification of C-S-H.



In the presence of sulfate ions, calcium sulfate ($\text{CaSO}_4 \cdot 2\text{H}_2\text{O}$ – gypsum) can form.



The increase of sulfate concentration in interstitial solution results in the formation of ettringite from monosulfoaluminate. The reaction between monosulfoaluminate and sulfate in the presence of carbonate ions CO_3^{2-} can also form thaumasite ($3\text{CaO} \cdot \text{SiO}_2 \cdot \text{SO}_4 \cdot \text{CO}_3 \cdot 15\text{H}_2\text{O}$) at low temperature [CRA 02]. The typical concentration in sulfate-rich environments is 0.2–30 mmol/L. The evolution of the phases equilibrium due to the increase of sulfate concentration in the cementitious matrix can be represented by a three-dimensional (3D) diagram (Figure 5.1).

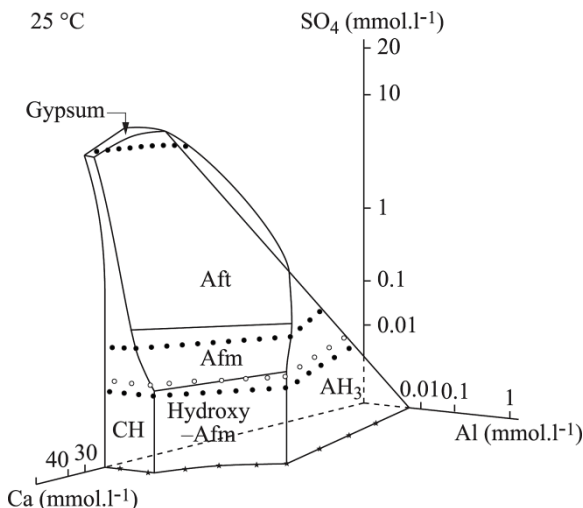


Figure 5.1. Phases equilibrium in the $\text{SO}_4\text{-Ca-Al}$ ternary system at 25°C , after Damidot and Glasser [DAM 92, DAM 93, CHA 10]

In marine environments, sulfate ions (SO_4^{2-}) are combined with chloride ions (Cl^-) [SAN 06]. Most of the studies on durability focus on sulfate attack and chloride ingress separately. Few studies deal with the combined effects of both species. Chloride ions are partially absorbed by the C-S-H and bound to monosulfoaluminate to form Friedel's salts ($\text{C}_3\text{A} \cdot \text{CaCl}_2 \cdot 10\text{H}_2\text{O}$ – hydrocalumite) [YU 01], which tends to limit the stability of ettringite [NIE 05].

Sulfate attacks can also be combined with carbonation. Carbon dioxide (CO_2) from air dissolves in pore solution and then hydrogenocarbonate reacts with calcium from portlandite and C-S-H to form calcite (CaCO_3). In the carbonated zone, in cases of sulfate attacks, monosulfoaluminate can react with sulfate ions to form ettringite or with carbonate ions to form monocarboaluminate ($3\text{CaO} \cdot (\text{Al},\text{Fe})_2\text{O}_3 \cdot \text{CaCO}_3 \cdot 11\text{--}12\text{H}_2\text{O}$). Carbonate compounds are more stable than sulfate compounds, which explain the better stability of monocarboaluminate over monosulfoaluminate in the presence of carbonate.

External sulfate attacks have been shown to cause expansion of the cement paste. Several phenomena could explain how the formation of ettringite causes expansion: increase in solid volume, topochemical reaction, swelling of ettringite considered as a colloid and crystal growth pressure. The molar volume of ettringite is $707 \text{ cm}^3/\text{mol}$, whereas the molar volume of monosulfoaluminate is $309 \text{ cm}^3/\text{mol}$; thus, there is actually an increase in solid volume. The theory that is consistent with most of the experiments and observations is the crystal growth pressure. The crystal growth theory describes the crystallization pressure produced by supersaturation and confinement [MUE 13]. Considering a crystal growth from solution in a cylindrical pore, the crystallization pressure is related to the supersaturation and the size of the pore according to Laplace's equation. Expressing the equilibrium between surface energy and crystal solubility gives equation [5.3]. Writing the equilibrium between pressure at the crystal/liquid surface and the interfacial energy γ_{cl} for a particular crystal curvature κ_{cl} gives Equation [5.4] [SCH 99, SCH 04].

$$\sigma_c = \frac{RT}{V_c} \ln \left(\frac{Q}{K} \right) \quad [5.3]$$

where: $\sigma_c = p_c - p_l$ represents the difference between the crystal and the liquid pressure, corresponding to the crystallization pressure exerted on the surrounding pore wall; R , T and V_c are, respectively, the gas constant, absolute temperature and molar volume of the crystal; Q/K is the supersaturation for a given crystal.

$$p_c - p_l = - \frac{2\gamma_{cl} \cos(\theta)}{r_p} \quad [5.4]$$

where γ_{cl} is the crystal surface energy at the crystal/liquid interface, $\kappa_{cl} = -\frac{2\cos(\theta)}{r_p}$ is the optimal curvature (crystal energy minimization) of the surface of a crystal growing inside a cylindrical pore of radius r_p with a contact angle θ .

According to the crystal growth pressure theory, the driving force for the crystallization pressure is the supersaturation of the pore solution with respect to ettringite [5.5].

$$\frac{Q}{K} = \frac{\left(a_{Ca^{2+}}\right)^6 \cdot \left(a_{Al(OH)_4^-}\right)^2 \cdot \left(a_{OH^-}\right)^4 \cdot \left(a_{SO_4^{2-}}\right)^3 \cdot \left(a_{H_2O}\right)^{26}}{K_{Ettringite}} \quad [5.5]$$

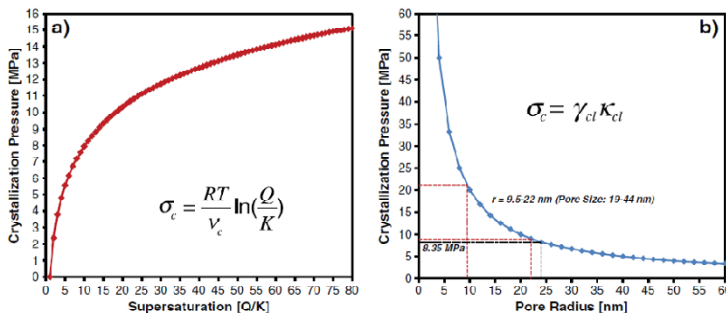


Figure 5.2. a) Dependence of crystallization pressure of ettringite on supersaturation, equation [5.3], $T = 293.15\text{ K}$, $V_c = 707\text{ cm}^3/\text{mol}$ and b) relationship between crystallization pressure and spherical pore radius according to equation [5.4]

The formation of ettringite does not necessarily result in expansion or damage. Numerous field observations actually showed no correlation between the amount of ettringite formed and expansion. Significant expansion pressure higher than tensile strength can only be exerted by ettringite, which forms in small pores within a certain size range [SCH 99, SCH 04], approximately 10–50 nm, depending on the type of cements used. The results can be understood in terms of the effect of crystal surface energy and size on supersaturation and crystal growth pressure. Yu *et al.* [YU 12, YU 13] proposed in a recent publication that penetrating sulfates first react with AFm in pockets which does not lead to stress or expansion.

On depletion of the AFm, monosulfate which is finely intermixed in the C-S-H then reacts to form expansive ettringite.

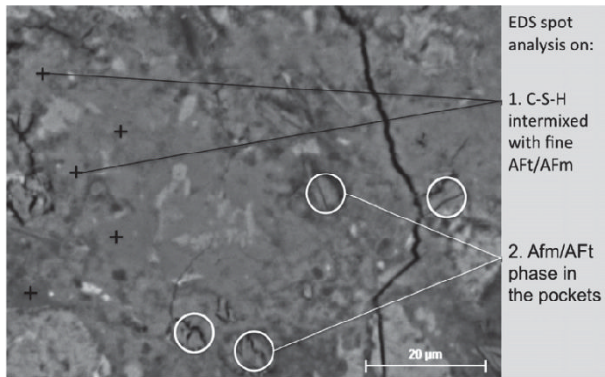


Figure 5.3. C-S-H and AFm/AfT phases in PC sample [YU 13]

5.2.2. Ingress of sulfate ions and scenario of sulfate attack

In water-saturated conditions, the leaching of cementitious matrix and the ingress of sulfate ions are due to the diffusion (Figure 5.4). Before exposure, the pore solution is saturated with respect to portlandite $\text{Ca}(\text{OH})_2$ and is characterized by high concentrations of alkali ions (Na^+ and K^+), with a pH value near 13. In seawater or groundwater, exposure conditions consist of lower calcium and alkali ion concentrations, higher sulfate concentration and lower pH.

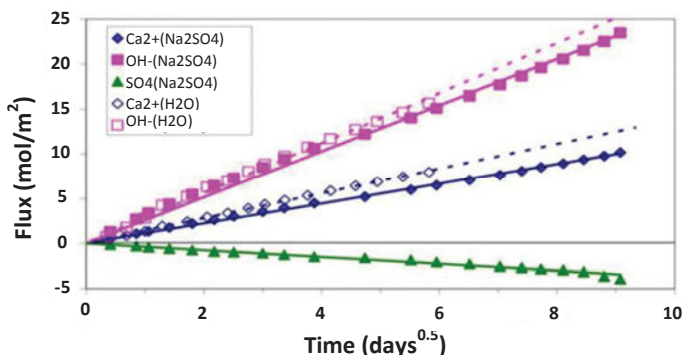


Figure 5.4. Cumulative amounts of leached ions from ordinary cement paste exposed to sodium sulfate solution ($[\text{SO}_4^{2-}] = 15 \text{ mmol/L}$) at 20°C. Adapted from [PLA 02, PLA 06]

Exposure to seawater results in gradients of calcium and alkali ions. As a consequence, alkali ions are leached, then portlandite is dissolved and calcium ions Ca^{2+} are leached. Leached calcium can also come from the decalcification of C-S-H. The ingress of sulfate ions causes the transformation of monosulfoaluminate into ettringite. Ettringite and monosulfoaluminate are not stable at pH values lower than 10–11; thus, they cannot be found in external layers where portlandite and C-S-H have been leached, and gypsum forms due to high sulfate concentrations. This scenario is confirmed by the zonation observed on damaged samples [GOL 95, CHA 10, ELH 12b] and is presented in Figure 5.5.

The main macroscopic results of external sulfate attacks of cementitious materials are expansion, softening and decohesion.

Expansion is due to the formation of ettringite in small pores. The expansion of cementitious matrix where supersaturation has been reached is restrained by unaltered material. Cracks appear when tensile stresses due to restrained expansion exceed the tensile strength of the cementitious material. As the damaged zone is generally the external layer in contact with sulfate-rich water, spalling can be observed.

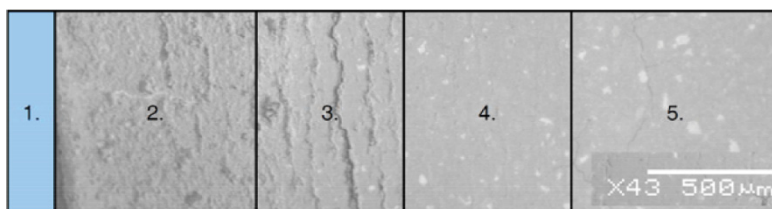


Figure 5.5. Zonation produced by sulfate attack of ordinary Portland cement paste exposed to sodium sulfate solution ($[\text{SO}_4^{2-}] = 3 \text{ g/L}$) at 20°C . SEM picture of the authors and zonation after Gollop and Taylor. 1. Sodium sulfate solution; 2. Decalcified zone and leaching; 3. Dissolution of portlandite and partial decalcification of C-S-H, precipitation of gypsum in cracks; 4. Replacement of monosulfate by ettringite; and 5. Unaltered material

The zonation and the mechanism of degradation were confirmed by microtomography observations on $2 \times 2 \times 16 \text{ cm}^3$ mortar specimens (Figure 5.6). The darker zone with higher porosity corresponds to the leaching of cement paste. In section A of the figure, cracks can be observed between the external layer and the core of the specimen. They are due to the expansion in the external layer where diffusion has first caused sulfate supersaturation and then ettringite formation. Transversal cracks observed in

section B were caused by the tensile stresses in the core generated by the crystallization pressure in the external layer. The tensile stresses exceeded the tensile strength of the material. The relative extent of leaching and cracks wherever found depends on the cement type. Ordinary Portland cement (OPC) caused higher expansion and wider cracks than sulfate-resisting cement (SRC). External sulfate attacks on mortar made of SRC caused expansion and internal cracking of the samples but the damaged layer was mainly affected by leaching and an increase in porosity.

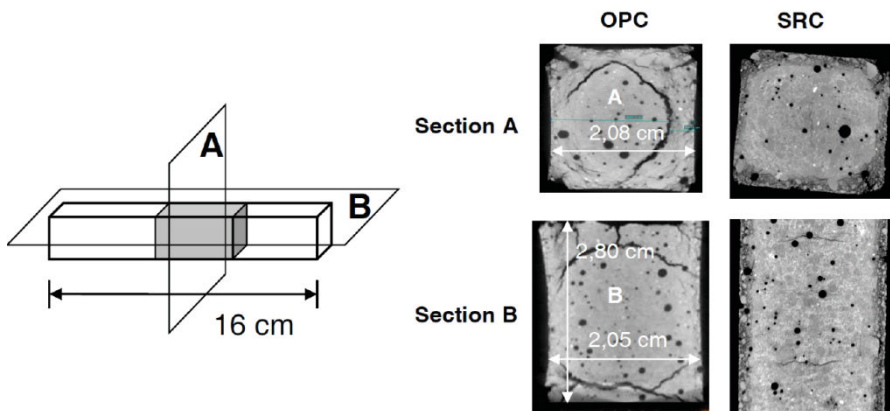


Figure 5.6. Microtomography pictures of degraded samples. Left: retained sections for microtomography observations. Right: OPC mortar, $W/C = 0.45$, $C_3A = 11.4$, $C_4AF = 5.4$; SRC mortar, $W/C = 0.45$, $C_3A = 2.2$, $C_4AF = 13.8$

These experimental results confirmed that sulfate attack does not only cause expansion but also cause softening and decohesion. The formation of gypsum and ettringite requires a source of calcium. Calcium can be provided by the leaching of portlandite and C-S-H. C-S-H is the main hydration product of cement and it provides cementitious materials with cohesion. The decalcification of C-S-H causes a softening of cement matrix and a decrease in strength.

Decohesion mainly occurs when thaumasite formation is observed. Thaumasite is formed from a sulfate source in the presence of carbonate and drawing silicon from the C-S-H; the consumption of the silica of the C-S-H can lead to a loss of its binding properties. There is no evidence that ettringite is theoretically required as a precursor to thaumasite formation, but thermodynamically as sulfate concentration increases, ettringite forms first

[SCH 07]. Ettringite and thaumasite can also enter into partial solid solution [HOB 00].

The scenario of an external sulfate attack was confirmed at the macroscopic level by measurements of length, mass and mechanical properties (Figure 5.7). Expansion was observed before cracking by the monitoring of length (Figures 5.7(a) and (b)) and mass (Figures 5.7(c) and (d)). As the absorption of water and hydration are likely to occur during immersion, differences between measures on control specimens and specimens exposed to sulfate solution were calculated to focus on the effects of sulfate ions. They are shown in Figures 5.7(b) and (d). Relative mass decrease occurred during the period of latency, when no significant expansion occurred. The mass decrease is due to leaching. The latency period corresponds to the time necessary to saturate the pore solution with sulfate with respect to ettringite formation. The mass increase is due to expansion of mortar specimens. As the mechanism of sulfate attack is based on diffusion, its kinetics are influenced by the exposed surface/specimen volume ratio. This can be seen in Figures 5.7(c) and (d), as the fastest mass increase corresponds to the specimens with the higher surface/volume ratio.

Elastic modulus (Figures 5.7(e) and (f)) does not appear as a sensitive indicator of damage during the first stage. The modulus of sulfate specimens actually remained the same or higher than the modulus of control specimens even when significant expansion and damage could be observed. Lee *et al.* [LEE 05] and Sahmaran *et al.* [SAH 07] have also shown the positive effect of sulfate attack on mechanical properties, before they finally decrease. The decrease of the elastic modulus became significant after about 120 days (Figures 5.7(e) and (f)), but mass variation appeared earlier (Figure 5.7(c)); so this would be a better indicator for a performance test.

The bulk porosity can be considered as a macroscopic indicator of damage caused by an external sulfate attack (Figure 5.8). First, the specimens were water saturated under vacuum then they were dried until constant mass to deduce the porous volume. The intermediate stage was defined as the end of the latency period, when the expansion starts increasing. No change could be shown between the initial and the intermediate stages. The latency period actually corresponds to a stage of competition between leaching of portlandite and C-S-H, and the sulfate ion ingress and reaction with the hydration products resulting in a loss of mass and an increase in porosity. The porosity increase at the final stage was

significant. This can be attributed to expansion of the cementitious matrix, and opening of microcracks and macrocracks, as shown by microtomography observations (Figure 5.6).

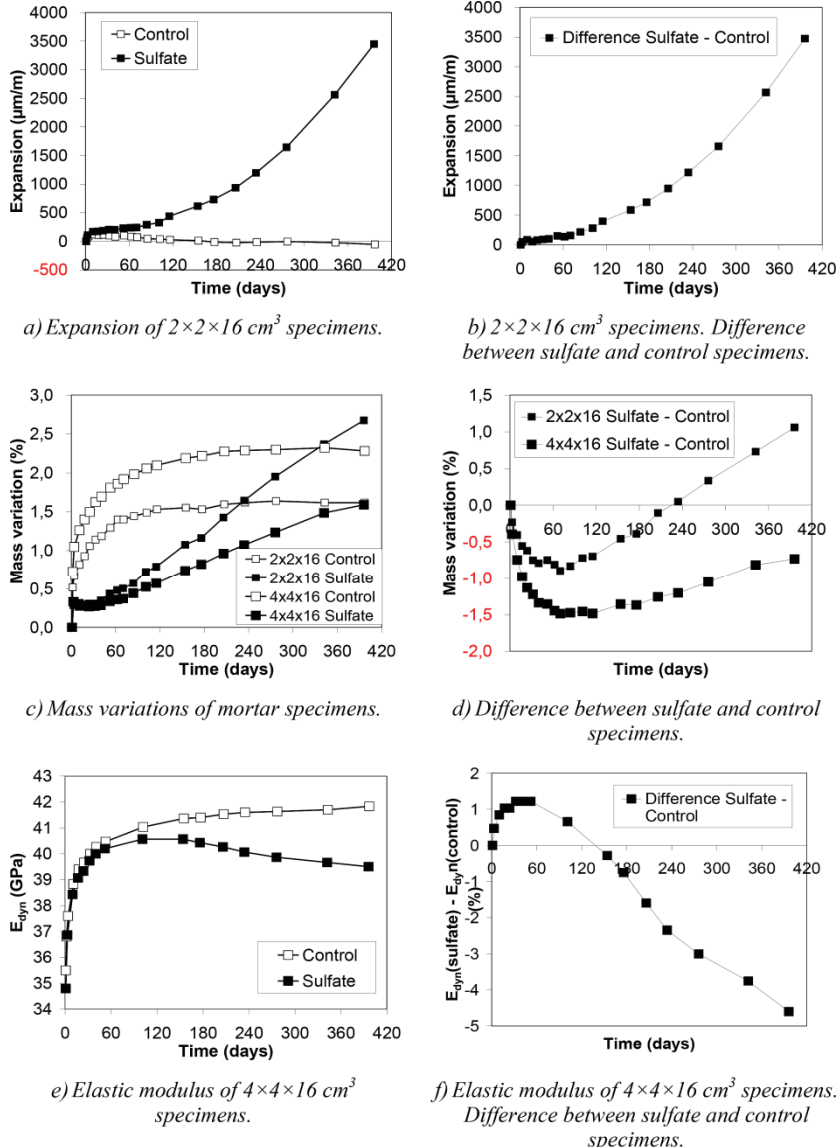


Figure 5.7. Monitoring of length, mass and elastic modulus of mortar specimens. $W/C = 0.50$, $C_3A = 7.6$, $C_4AF = 9.4$

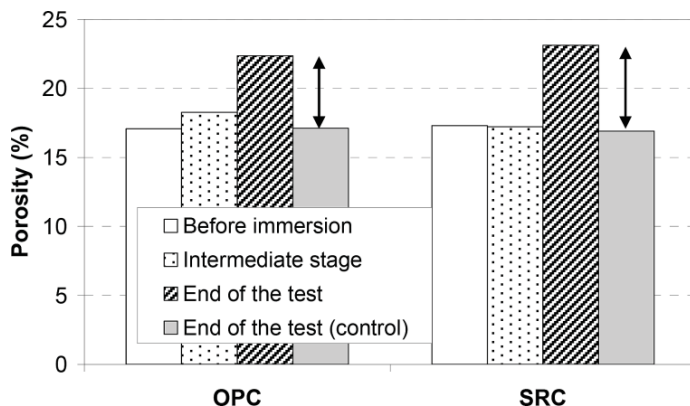


Figure 5.8. Porosity of mortar specimens exposed to external sulfate attacks ($[SO_4^{2-}] = 3g/L$) at $20^\circ C$ and control specimens

The porosity increase during expansion confirms that the theory based on the increase of solid volume cannot solely explain the expansion caused by sulfate attack. First, the ingress of sulfate ions is accompanied by leaching of the main hydrates, which results in a decrease of solid volume. Second, expansion is actually at micro scale. If the generated stresses exceed the tensile stress of a cement-based material, cracks develop.

5.2.3. Influence of exposure conditions

Sulfate concentration, counter ions, temperature and water saturation are often constant and well known in laboratory testing, although they actually vary in field conditions. Conversely, pH is generally constant in outdoor exposure conditions but not systematically controlled in laboratory test procedures. As a result, it is necessary to know the influence of these parameters in order to understand the degradation observed in field conditions and to design representative testing.

5.2.3.1. Sulfate concentration

Sulfate concentration significantly varies in tests procedures as well as field exposure conditions. As these conditions should prevail when designing test procedures, their classification is given first (Table 5.1).

		XA1 Slightly aggressive chemical environment	XA2 Moderately aggressive chemical environment	XA3 Highly aggressive chemical environment
Chemical characteristic	Reference test method			
<i>Ground water</i>				
SO ₄ ²⁻ mg/L	EN 196-2	≥ 200 and ≤ 600	> 600 and ≤ 3000	> 3,000 and ≤ 6,000
<i>Soil</i>				
SO ₄ ²⁻ mg/kg ^a total	EN 196-2 ^b	≥ 2,000 and ≤ 3,000	> 3,000 ^c and ≤ 12,000	> 12,000 and ≤ 24,000

^aClay soils with a permeability below 10⁻⁵ m/s may be moved into a lower class.

^bThe test method prescribes the extraction of SO₄²⁻ by hydrochloric acid; alternatively, water extraction may be used, if experience is available in the place of use of the concrete.

^cThe 3,000 mg/kg limit will be reduced to 2,000 mg/kg, where there is a risk of accumulation of sulfate ions in the concrete due to drying and wetting cycles or capillary suction.

Table 5.1. Limiting values for exposure classes for sulfate attacks from natural soil and ground water, after European standard EN 206-1 [NFE 04]

The sulfate concentration of seawater is about 2,800 mg/L [SWE 71], and chemically aggressive environments refer to concentrations between 600 and 6,000 mg/L [NFE 04], or between 150 and 10,000 mg/L [ACI 05, CSA 94].

The increase in sulfate concentration up to 30 g/L has been used in laboratory testing to accelerate expansion: ASTM C1012, NF P 18-837 [AST 00, NFP 93]. It has been proved to be effective in providing significant differences in material performances (Figure 5.9). The expansion mechanism is actually based on supersaturation. An increase in external sulfate concentration results in an increase in concentration gradient, and faster diffusion, thus earlier supersaturation in the micro-pores.

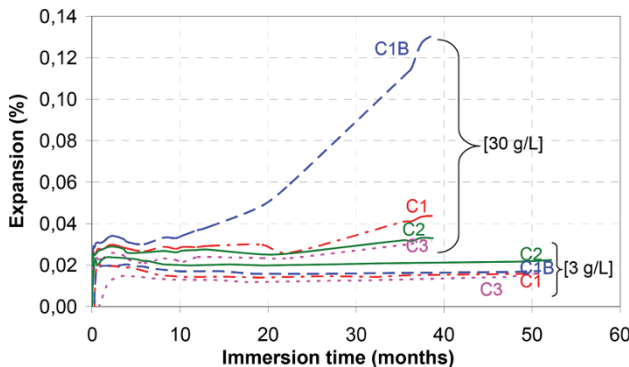


Figure 5.9. Expansion of $7 \times 7 \times 28 \text{ cm}^3$ concrete specimens

However, a 30 g/L sulfate concentration corresponds to about 10 times the concentrations found in the field; thus, such an increase in sulfate concentration is likely to modify the mechanisms of degradation. According to phases equilibrium (Figure 5.1), the limiting values given for sulfate concentrations from exposure class XA1 to XA2 actually correspond to the formation of ettringite, whereas higher concentrations correspond to the stability of gypsum. As a consequence, the highest sulfate concentrations given in test procedures (30 g/L and above) are likely to result in a different mechanism of degradation based on gypsum formation. However, gypsum can also be found at lower sulfate concentrations [ELH 12a] in the leached external layer where the pH is not high enough for the stability of ettringite, and ettringite was found in cement-based materials exposed to highly concentrated sulfate solutions. As a consequence, several studies have been carried out over the past few years to conclude on the influence of sulfate concentration on degradation mechanism.

Three concentrations have been studied: 3, 10 and 30 g/L [ELH 12b, YU 12, MUE 13]. The accelerating effect was confirmed on expansion and relative mass curves (Figures 10 and 11). The three concentrations resulted in the same stages and magnitudes on the curves. Two main stages could be identified (identified in Figures 5.10 and 5.11 with arrows on the 3 g/L curve), namely:

- the first stage corresponding to the latency period when no significant expansion can be measured with a relative mass decrease caused by leaching;

– the second stage corresponding to a mass and length increase due to expansion of damaged mortar specimens.

These results are quite similar to those obtained in other studies where these two phases were also distinguished on mortars immersed in sodium sulfate solutions at different concentrations [LEE 08, SAN 02, SAN 03]. It should be noted that these measurements were made on saturated specimens. Thus, the mass increase can be explained by the swelling of the specimens. Taking into consideration the correlation of the mass and length variations, we noticed that at the first stage leaching was the dominant phenomenon which explains this relative mass decrease. At the second stage, the formation of expansive products induced expansion and mass increase.

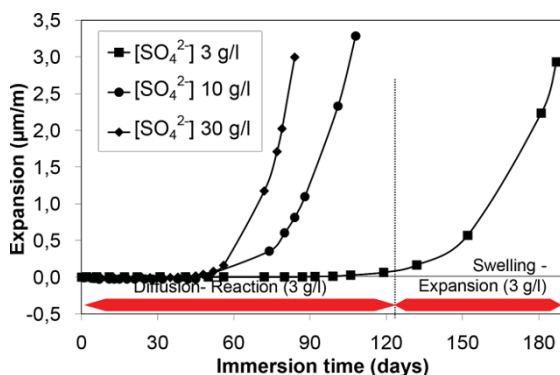


Figure 5.10. Expansion data for 3, 10 and 30 g/L of Na_2SO_4 solutions

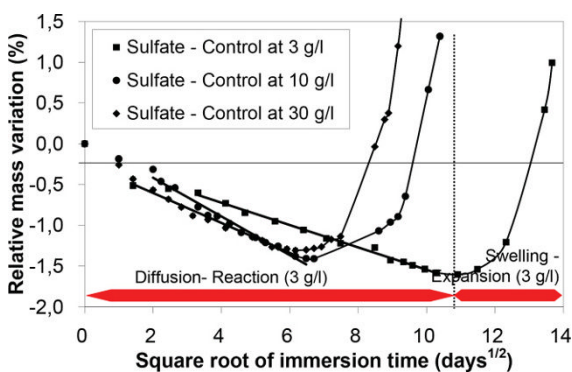


Figure 5.11. Difference of mass variation between attacked specimens and control

Figure 5.12 shows the length measurements as a function of leached ions. At early exposure time, an important quantity of calcium and hydroxides was leached but no expansion was measured. Afterward, expansion increased with a moderate rate of leached ions. Figure 5.12 also shows a common threshold required to trigger the expansion. Whatever the concentration was, the expansion began at the same level of leached ions. Since the mixtures were the same for the three tests, the calcium hydroxide content was the same at the beginning of the tests. So the time of initiation of expansion would correspond to the same amount of leached material and ingress of sulfate ions, which could be linked to a critical proportion of the cross-section of the specimens required to generate global expansion. If the same critical section results in the same expansion, this suggests that the pressures generated at different concentrations are the same. This assumption was partially confirmed by the results showed in Figure 5.13. The sulfate concentration was increased by 20 times, but the maximum crystallization pressure increased from 7.27 to 8.35 MPa [MUE 13].

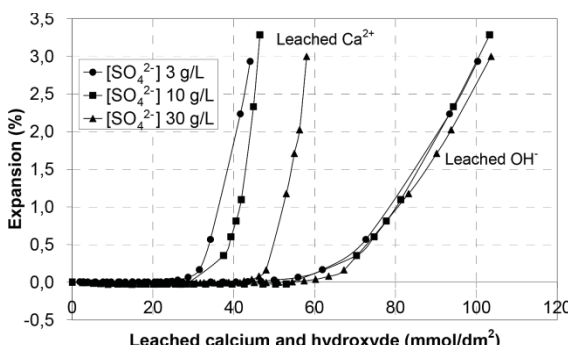


Figure 5.12. Strain vs. leached ions (calcium and hydroxide)

In order to understand the acceleration of expansion resulting from increasing sulfate concentration, the microstructure of mortar specimens exposed to the three concentrations was analyzed using scanning electron microscope (SEM) and Energy dispersive spectroscopy (EDS) (Figures 5.14 and 5.15). The three profiles did not show any significant difference in the sulfate penetration depth. The maximum sulfate content increased with an increase in external sulfate concentration, but the increase was lower than expected, and mainly due to gypsum formation in the cracks. However, these

results have several limitations. They only give the sulfate content of the solid phase and not the sulfate concentration in the pore solution. Moreover, they give the total sulfate content but not the binding mechanisms: precipitation and adsorption.

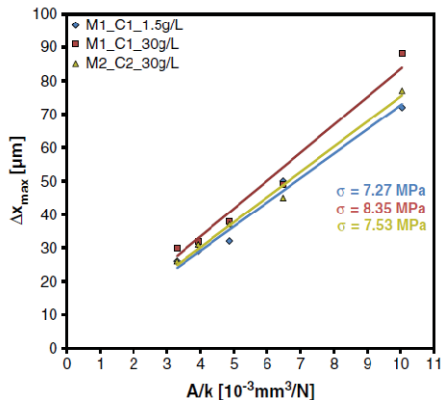


Figure 5.13. Calculation of maximum crystallization pressure for different cements and sulfate solution concentrations [MUE 13]. For a color version of the figure, see www.iste.co.uk/ait-mokhtar/coastal.zip

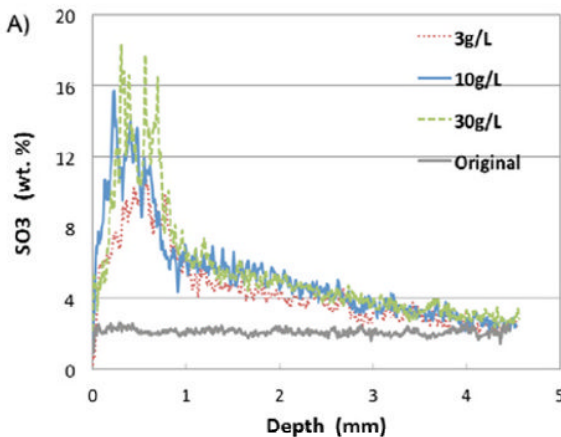


Figure 5.14. Sulfate profiles acquired by mapping methods after 120 days of exposure [YU 12]. For a color version of the figure, see www.iste.co.uk/ait-mokhtar/coastal.zip

The same experimental technique was used to assess the sulfate content in C-S-H (Figure 5.15(a)). The sulfate content of C-S-H was higher in the sample exposed to 30 g/L sulfate solution. Barbarulo *et al.* [BAR 07] assessed the quantity of sulfate bound to the C-S-H as a function of sulfate concentration. Higher sulfate concentration results in higher sulfate content of C-S-H. Ettringite precipitates when a critical sulfate concentration in the solution is reached. The SEM-EDS plots at 3 mm depth (Figure 5.15(b)) actually showed a higher sulfate content of C-S-H in the 30 g/L sample, which corresponds to the formation of ettringite crystals within the C-S-H. In the 3 g/L and 10 g/L samples, the sulfate content corresponds to monosulfoaluminate crystals mixed with C-S-H (Figure 5.3). These results help to understand the accelerating effect of high sulfate concentration. At 3 g/L and 10 g/L, the increase of sulfate concentration results in the precipitation of ettringite in the capillary pores, which buffers the increase of sulfate concentration in pore solution. At 30 g/L, the sulfate content is high enough to transform all the monosulfoaluminate in capillary pores into ettringite, and then the sulfate concentration keeps on increasing, resulting in ettringite formation in C-S-H pores. According to the crystallization pressure theory, the finer the pores, the higher the crystallization pressure is. As a result, the ettringite formation at 3 mm in the smallest pores depth would explain the higher expansion of samples exposed to 30 g/L.

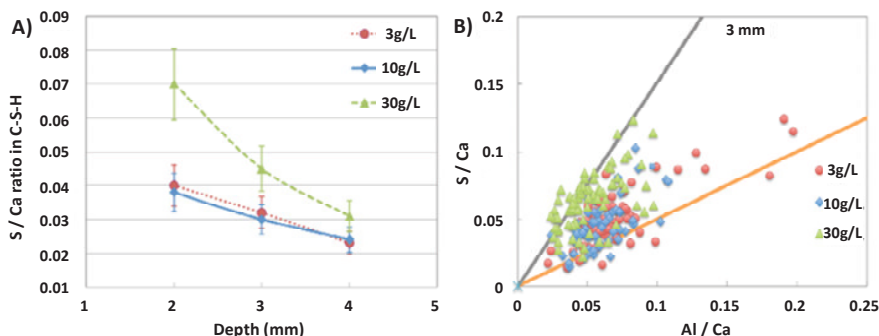


Figure 5.15. a) S/Ca atomic ratio in C-S-H at different depth. b) SEM-EDS plots of S/Ca versus Al/Ca atomic ratios from the C-S-H at 3 mm depth, for PC mortars in 3g/L, 10g/L and 30g/L Na_2SO_4 -solution [YU 12]. For a color version of the figure, see www.iste.co.uk/ait-mokhtar/coastal.zip

5.2.3.2. Counter ions and seawater

Sodium sulfate solutions are widely used in performance testing. The solubility of sodium sulfate in water is high (58 g/L) and allows us to make concentrated solutions in order to benefit from the accelerating effect previously described.

The solubility of *calcium sulfate* (2.1 g/L) is much lower than sodium sulfate [DUV 92]. The value is used as a reference to design representative tests at $[\text{SO}_4^{2-}] = 1.5 \text{ g/L}$ [PLA 06, MUE 13]. The mechanism of degradation is the same, based on leaching, ettringite formation and expansion of cementitious matrix.

Magnesium sulfate results in more severe attacks of cementitious materials, consisting of spalling, softening, loss of cohesion and significant strength decrease. The degradation is faster than in sodium or calcium sulfate [DUV 92, NEV 04]. Magnesium sulfate actually affects all the main hydration products. The dissolution of portlandite produces gypsum and magnesium hydroxide ($\text{Mg}(\text{OH})_2$ – brucite). The C-S-H is transformed into magnesium silicate hydrate without any cohesion. Ettringite has also been observed. It is noteworthy that the mechanism of degradation can occur even at low C_3A and C_4AF concentrations.

The solubility of sulfate precipitates influences each other. For instance, the solubility of calcium sulfate is higher in a sodium chloride solution. It is necessary to take into account the combined effects of ions in order to predict the performance of cementitious materials in field exposures.

Chloride ions are mainly found in the seawater. They are likely to influence sulfate attacks as Friedel's salts ($\text{C}_3\text{A} \cdot \text{CaCl}_2 \cdot 10\text{H}_2\text{O}$ – hydrocalumite) are formed [YU 01]. They tend to limit the stability of ettringite [NIE 05]; thus they theoretically mitigate the consequences of external sulfate attacks. However, combined physical effects should be taken into account, as damage resulting from external sulfate attack is likely to accelerate the ingress of chloride ions and corrosion of reinforcement. Few studies deal with the combined effects of sulfate and chloride ions.

Sodium ions do not react with hydration products but their ingress modifies the phase equilibrium and results in a decrease of the pH in a pore solution [GUI 04a]. The ingress of chloride ions in cementitious matrix causes the dissolution of monosulfoaluminate and the formation of calcium

chloroaluminate (Friedel's salt). The released sulfate ion reacts with available monosulfoaluminate to form ettringite. As a result, the ingress of chloride ions results in combined ettringite and chloroaluminate formations [GUI 04b]. The capillary porosity of cement paste exposed to sodium chloride first slightly decreases due to ettringite formation and then increases due to portlandite dissolution.

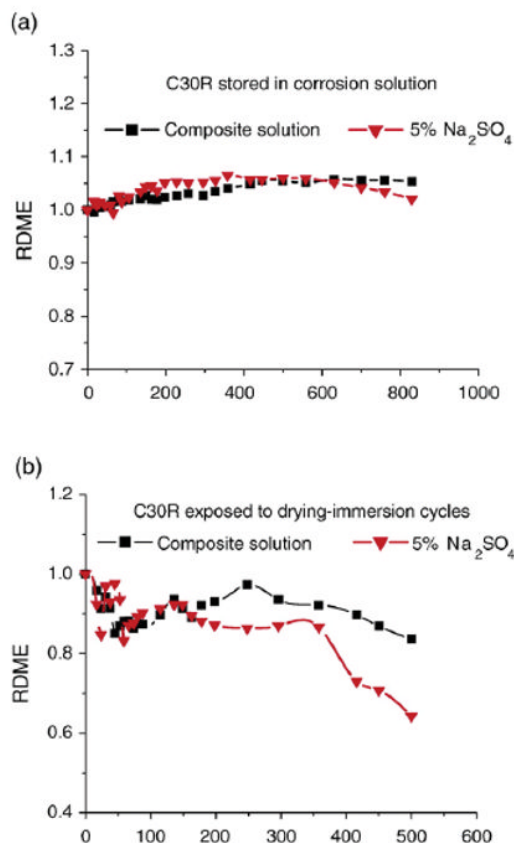


Figure 5.16. a) Relative dynamic modulus of elasticity (RDME) of concrete immersed in composite solution or 5% Na_2SO_4 solution and b) RDME of concrete exposed to drying and immersion cycles in composite solution or 5% Na_2SO_4 solution [ZUQ 07]. For a color version of the figure, see www.iste.co.uk/ait-mokhtar/coastal.zip

Experimental studies have provided data on external sulfate attacks combined with chloride ingress. Damages caused by sulfate attack have been

found to be delayed and reduced [ALA 95]. Concrete stored in chloride and sulfate solution for 12 months showed lower chloride diffusivity [FEL 91]. The chloride diffusivity of Portland cement concrete decreased, but the diffusivity of concrete with slag decreased when exposed to sulfate solution [TUM 96]. Initiation of steel corrosion in concrete exposed to chloride ions was not influenced by the addition of sulfate ions, but the corrosion rate was found to be dependent on the sulfate concentration [DEH 07]. Experimental studies done by Zuquan *et al.* [ZUQ 07] showed that the ingress of chloride ions is first reduced in sulfate solution (3.5% NaCl and 5% Na₂SO₄) but it is accelerated during the second stage.

Santhanam [SAN 06] has compared *seawater* exposure and groundwater exposure. Samples were immersed in lime water for 12 days and then stored in seawater solutions or groundwater sulfate-rich solutions. Portland cement mortar samples stored in groundwater were more damaged than samples stored in seawater. The weight loss was approximately the same but strength loss and expansion were lower in seawater. Gypsum and ettringite contents were lower in samples exposed to seawater. Chloroaluminate formation and brucite layer protected the mortar samples against sulfate attack.

5.2.3.3. Temperature

The effects of temperature on external sulfate attacks are not fully understood. However, this issue can be divided into two parts: low temperatures and high temperatures. The influence of low temperature has been investigated because it has been assumed to favor thaumasite formation [CRA 02, BLA 05, PIP 08]. Understanding the influence of high temperature is a way to understand the mechanisms of delayed ettringite formation (DEF), which causes significant damages in steam-cured concrete or in large concrete structures where the temperature exceeds 80°C at an early age due to heat released by hydration [SCR 93, BEA 91, LAW 94, DIV 98, LOT 06]. Relatively high temperatures are representative of exposure conditions of immobilization systems [HER 97, SAN 02]. This can be a way to accelerate laboratory tests [AKO 97].

Thaumasite has been reported to form at low temperatures [PIP 08]. It has actually been found in samples immersed in a sodium sulfate solution at 5°C (Figure 5.17). At 10°C, thaumasite and calcite were found, whereas at 20°C thaumasite could not be detected. Thaumasite formation resulted in lower

expansion and a decrease in strength at 5°C. Thumasite can actually be formed from C-S-H and sulfate in the presence of calcite [SCH 09].

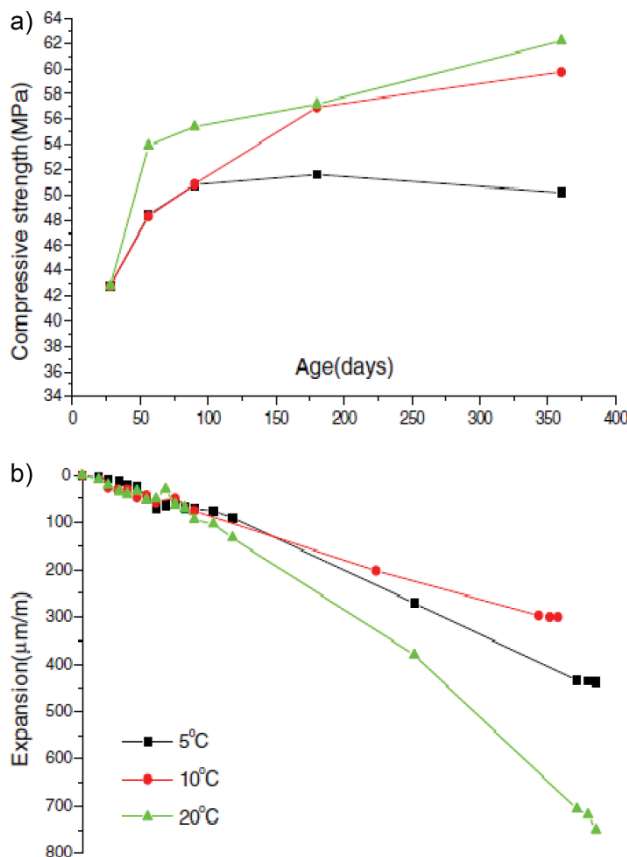


Figure 5.17. Effect of temperature of conservation in a solution of 5% Na_2SO_4 [PIP 08].
For a color version of the figure, see www.iste.co.uk/ait-mokhtar/coastal.zip

Barbarulo *et al.* [BAR 07] have studied the chemical equilibriums between C-S-H and ettringite at 20 and 85°C. The quantity of sulfate bound to the C-S-H is actually not negligible in a cement paste. It increases with sulfate concentration and temperature [DIV 98, BAR 07]. The solubility of ettringite increases with temperature, from around 0.4 mmol/L of sulfate in solution at 20°C to 5 mmol/L at 85°C. These results can help understand the mechanisms of DEF. At high temperature (e.g. during hydration or steam curing), ettringite becomes more soluble, the sulfate concentration in the

solution increases and the quantity of sulfate bound to the C-S-H increases accordingly. When the system is placed at room temperature, ettringite can precipitate, but the kinetics is quite slow.

Increasing temperature resulted in a decrease of the latency period, but the expansion rate and magnitude were not modified [SAN 02].

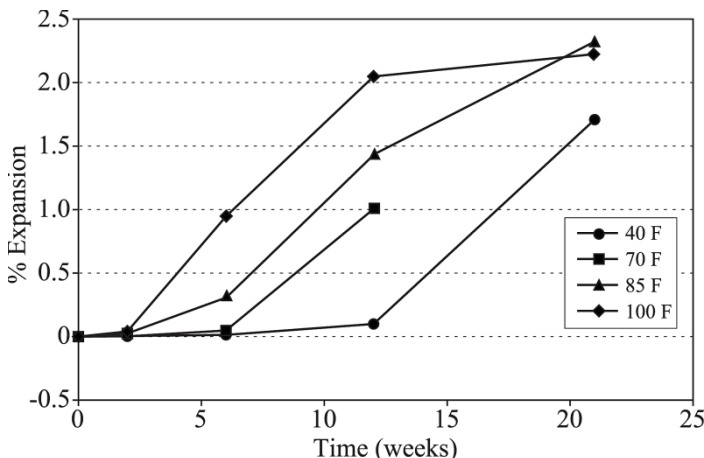


Figure 5.18. Expansion of Portland cement mortars immersed in sodium sulfate solutions at various temperatures [SAN 02]

5.2.3.4. Water saturation of concrete

The level of water in soils, rivers and seas is likely to vary; thus, the water saturation of concrete exposed to sulfate may not be constant. Wetting and drying cycles affect foundations, buried structures and concrete structures in tidal zones.

Drying of concrete allows precipitation of salts. Damages caused by the precipitation of sodium sulfate [LAF 29] are often referred to as “physical sulfate attacks” [NEV 04]. They actually do not result from chemical reactions between sulfate and cement-based materials. Sodium sulfate exists as an anhydrate called thenardite (Na_2SO_4), or as a decahydrate called mirabilite ($\text{Na}_2\text{SO}_4 \cdot 10\text{H}_2\text{O}$). Wetting and drying cycles cause repeated thenardite recrystallization and volume changes, and thus the fatigue in cement paste. Stresses sufficiently high to overcome the tensile strength of

normal porous building materials may be developed and the salt may exert a sufficient force to bring about disintegration of the material [BON 39].

In foundations and structures in tidal zones, capillary rise and evaporation are in competition. This results in an increase in the sulfate concentration in concrete. The solution may become supersaturated, and then crystal efflorescence occurs. Crystal growth below the material surface or “subflorescence” may be critical if the crystallization pressure exceeds the tensile strength of the material [SCH 04].

5.3. Influence of concrete composition and standards requirements

Laboratory tests, as well as some data from experience, demonstrate the influence of some parameters on concrete resistance to sulfates. Even though some results seem to contradict one another, a few tendencies and composition ranges can be identified where the risks are higher.

5.3.1. *Influence of binder composition*

5.3.1.1. *Cement composition*

Several studies have attempted to demonstrate the effects of the C₃A and C₃S contents of cement on the concrete sulfate resistance of concrete. Even though sulfate resistance increases when the C₃A contents reduce, the results are sometimes difficult to analyze [NEV 04]. Some sulfate degradation mechanisms do not require the presence of C₃A as a necessary condition for activation. This is the case, for example, for thaumasite formation degradation, which occurs preferentially at low temperature in the presence of carbonates: so-called sulfate-resistant cements, i.e. those that are low in C₃A, seem to be only a little effective [SAN 01, NEV 04].

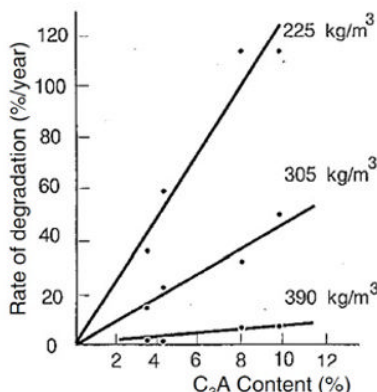
It is actually necessary to distinguish different types of sulfate attacks, since some parameters, such as the type of cation, may interact with the effect of C₃A contents. Therefore, the use of low C₃A cements can have adverse effects on the expected results, in magnesium sulfate or sulfuric acid solutions [NEV 04].

Concrete specimens were exposed to sodium sulfate [DUV 92]. For a given cement content, the rate of degradation increased linearly with C₃A

content. But the latter parameter seems to have a stronger effect, and a low C₃A content in the cement is not enough for the concrete to withstand sulfate attacks well.

The C₃A/SO₃ ratio seems to be a good indicator for resistance to seawater (which contains sulfates) [DUV 92]. The NF P 15-317 standard [NFP 95a] takes into account the C₃A content to set the maximum SO₃ content, and a ratio less than or equal to 3 for the cement guarantees a good seawater resistance.

Several studies have focused on C₃A content and W/C ratio together [NEV 04], for example the study by the US Bureau of Reclamation, which lasted for more than 40 years. They showed that the effect of the C₃A content dominates at high W/C ratios, higher than 0.40–0.45. Beyond these values, concrete permeability increases noticeably with the W/C ratio. It could be thought that when the capillary pores are connected and aggressive agents can penetrate inside the concrete, the chemical resistance of the binder makes the difference.



Concrete specimens stored in 10% Na₂SO₄ solution for 16 years. The rate of degradation was assessed from visual observations, and from strength and modulus measurements. Low cement content resulted in porous concrete and significant degradation, even at low C₃A contents.

Figure 5.19. Influence of cement content and C₃A proportion on the rate of degradation of concrete, after Duval et al. [DUV 92]

The C₃S content, and particularly the C₃S/C₂S ratio, also seems to have a noticeable effect on the sulfate resistance, even though few data are available

[SAN 01]. C_3S hydration produces more calcium hydroxide $\text{Ca}(\text{OH})_2$ than C_2S hydration does because of gypsum formation and C-S-H decomposition which may be induced. This has been observed especially in the case of magnesium sulfate attacks.

There are two main aspects of the mechanisms of degradation of cement-based materials by external sulfate attacks: leaching and ettringite formation. The leaching resistance is related to initial CaO content of cement, as portlandite is the most leachable phase. The quantity of ettringite formed depends on the aluminate content. The sum of CaO and Al_2O_3 proportions of binder has actually been found to correlate with expansion (Figure 5.20). Mineral admixtures such as fly ash and slag may be used to reduce these proportions, thus the sensitivity of concrete to sulfate attacks.

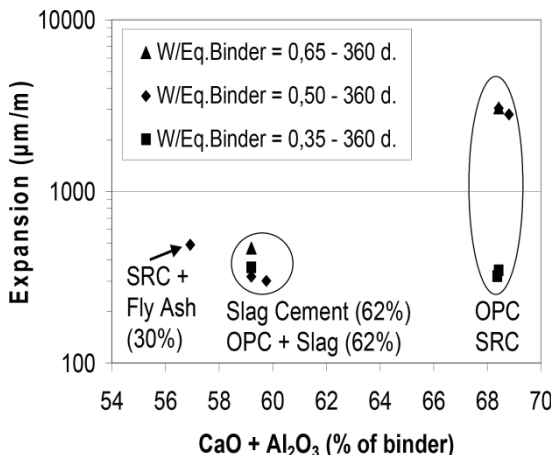


Figure 5.20. Influence of chemical composition of binder on expansion of mortars exposed to 30g/L sulfate solution

5.3.1.2. Fly ash

Fly ash often noticeably improves sulfate resistance, at least at substitution rates less than 30% (in the absence of data for rates higher than this limit) [DUV 92, NEV 04].

A study of concrete mixtures containing 15 and 30% fly ash, with constant binder equivalent, found a reduction in swelling with increasing fly ash proportions. Porosity and water absorption coefficients were close, but

the chloride ion diffusion coefficient reduced with the proportion of fly ash, regardless of the curing mode. In saturated conditions, diffusion is the principal mechanism through which aggressive ions penetrate the concrete, and fly ash seems to have a positive effect at this level.

Fly ash also acts on chemical resistance of the binder, via the pozzolanic reaction. This actually consumes the calcium hydroxide (portlandite), which would otherwise react with sulfates and initiate binder degradation (degradation via ettringite and gypsum formation).

Nevertheless, fly ash can have varied chemical and mineral composition and therefore different levels of effectiveness in increasing concrete resistance to sulfates.

5.3.1.3. Slag

The NF P 15-317 standard for PM cements and the NF P 15-319 standard for cements for structures with high sulfate content (ES) specify that the proportion of granulated blast furnace slag in CHF-CEM III cements should be higher than 60%.

Several studies have been conducted on this issue, and they demonstrated that binders with high slag content have good resistance in sulfate-rich waters, in tests when the sulfate solution concentration was higher than the threshold of the most severe exposure class (6 g/L in water and 12 g/kg in soil).

A study by Higgins [HIG 02, HIG 03] showed that the resistance of concrete which has a slag proportion of 60 or 70% in the binder is clearly better than that of Portland cement concrete, in sodium sulfate solutions, and is comparable in magnesium sulfate solutions, with concentrations of the order of 1.5% (of SO₃ by mass). It is improved with small amounts of calcium carbonate (4%).

Several explanations have been proposed for these kinds of results [DUV 92]. On the one hand, the use of slag reduces the calcium hydroxide and C₃A contents. This can explain the clear improvement in exposure to sodium sulfate, and the more mitigated results obtained in magnesium sulfate attacks. On the other hand, the addition of slag increases hydrate compactness and reduces the average pore size, which causes a reduction in transport properties.

5.3.1.4. Limestone

Taking limestone filler into account in calculating the equivalent binder content [NFE 04] is not possible in a sulfate-rich environment. The cement standards only facilitate the introduction of small amounts (less than 5%) of secondary constituents, such as calcium carbonate (the main component of limestone), in cements.

Several reasons can explain this position. Limestone fillers limit swelling, but this effect is temporary [DUV 92]. Some results are contradictory and the effect seems to depend on other parameters: the cation and cement types, for example. In any case, these constituents include carbonate ions, which can lead to thaumasite formation if the temperature and humidity conditions are favorable [IRA 03]. This study focused on the effect of limestone additions, at substitution rates of 10 and 20%, on the sulfate resistance of mortars immersed in sodium sulfate solution for 2 years (ASTM C 1012 test). The measurements and observations undertaken showed that binders with limestone fillers have a wide range of vulnerability to this type of attack.

5.3.1.5. Conclusion

With regard to the influence of mix-design parameters and the significance of different indicators on sulfate resistance, the sulfate type (cation) must also be included. The calcium and aluminate proportions of cement and binder influence its resistance to sulfate attacks. The effects of mineral admixtures are more complicated. Limestone fillers seem to have a detrimental effect, but this trend is reversed at low rates (around 5%) in the presence of slag. Slag has a favorable effect at proportions higher than 60% in the binder. In any case, the pozzolanic reaction seems to have unfortunate effects on magnesium sulfate resistance.

5.3.2. Influence of concrete composition

5.3.2.1. Water/cement ratio and cement content

Concrete resistance to external sulfate attack increases when the W/C ratio decreases and the proportion of cement in the mixture increases [DUV 92, NEV 04]. When the W/C ratio decreases, the volume and connectivity of the pore network decreases. This delays the ingress of sulfate ions and leaching of the cementitious matrix [ELH 12b]. This also improves the strength of concrete, and thus the resistance to expansion.

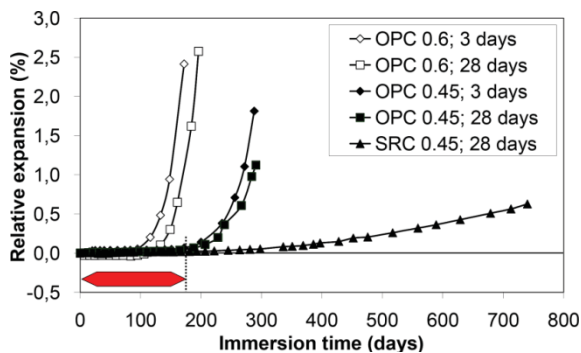


Figure 5.21. Relative expansion of mortar specimens in 3 g/L sulfate solution

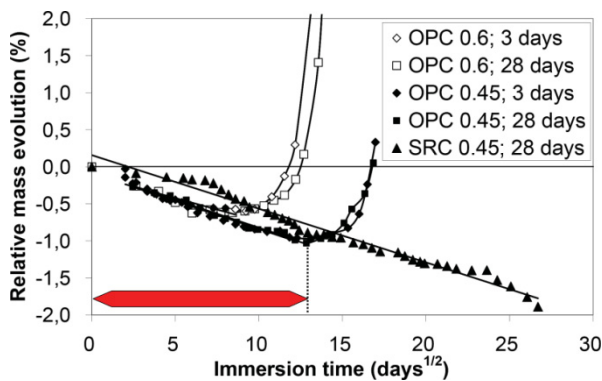


Figure 5.22. Relative mass evolution of mortar specimens in 3 g/L sulfate solution

The reduction of water-to-cement ratio from 0.6 to 0.45 actually delayed the initiation time (arrow in Figures 5.21 and 5.22), but expansion occurred. The delay can be attributed to a decrease in sulfate diffusivity of mortars (Figure 5.23). However, using OPC, the two main stages of sulfate attack could be observed on the mass evolution (Figure 5.22): leaching and expansion. At constant water-to-cement ratio, the replacement of OPC by SRC resulted in a significant change in the behavior of the mortar samples (Figures 5.22–5.24). The third stage characterized by acceleration of expansion was not observed. The loss of mass at the surface (leaching) prevailed over the macroscopic swelling, which could explain this continuous loss of mass. This was confirmed by microtomography (Figure 5.6). The expansion of mortar OPC 0.6 began after 3 months of

exposure to the sulfate solution while OPC 0.45 did not show any significant expansion before 6 months. The mortar SRC 0.45 was the last to show expansion after 8 approximately months. The slope of the expansion curves decreased, respectively, by reducing the W/C ratio and by using the SRC. These results are consistent with the standards that prescribe the use of SRC and limit the maximum W/C in an aggressive environment to 0.50 for the XA2 and 0.45 for the XA3 exposure classes (NF EN 206-1). Several material properties could explain this difference, namely the strength, the elastic modulus and the diffusion coefficient.

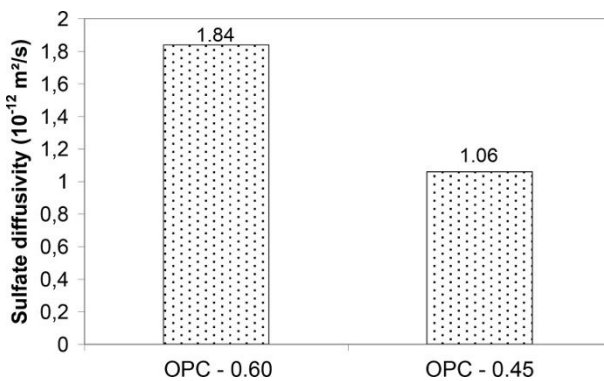


Figure 5.23. Sulfate diffusivity of two mortars

The age of the mortars at the time of immersion was not a major parameter in this test. However, the OPC 0.6 mortars exposed to sulfates after 3 days of curing were the first to show expansion followed by mortars exposed to sulfate at day 28. The difference for OPC 0.45 mortars concerning the time of immersion is not significant. The expansion of OPC 0.45 mortars exposed at day 3 began just 7 days earlier than those exposed at day 28. The difference can be explained by the degree of hydration. On the one hand, short curing actually leads to higher permeability. On the other hand, the microporosity of the cement paste is higher at early age; thus, expansive products are likely to form causing less damage than in denser microstructures.

As the three mortars were designed keeping the volume of paste constant, the initial calcium hydroxide content was higher in the OPC 0.45 and SRC 0.45 mortars. To eliminate this effect in order to explain the degradation mechanisms, the quantity of leached ions should be reported to the initial

CaO content of the binder. Equivalent damaged depths (*EDD*) may be calculated [BAD 06]. This depth is defined as the ratio between the amount of leached calcium (mol/m^2) at a time t and the theoretical initial total calcium content in the binder (mol/m^3). From the solution titration, leached calcium can be calculated and the initial CaO of the cement content is given by the producers. The *EDD* is calculated by the following equation [5.6]:

$$EDD(t) = \frac{\text{Leached calcium}(t)}{\text{Initial calcium content in binder}} \quad [5.6]$$

EDD is shown versus the square root of time in Figure 5.24. The OPC 0.6 samples showed the greatest *EDD* at early ages as they had the highest diffusion coefficient. The same conclusions could be drawn for the samples exposed at 3 days compared to those exposed at 28 days. The OPC 0.6 and OPC 0.45 curves lost the linearity. This loss of linearity correlated with the beginning of the expansion (see Figures 5.22 and 5.23). The increase in the leaching rate is actually due to the increase of diffusion as the material is damaged [GER 00] by the expansion that exceeds the tensile strain capacity of mortar. The loss of linearity is not observed on the SRC 0.45 curve. Leaching increased at a constant rate, which would mean that the diffusion coefficient was not significantly affected by sulfate attack. The leached zone reached at the end of the test is thicker for the SRC 0.45 specimens than for the OPC 0.6 and OPC 0.45 curves.

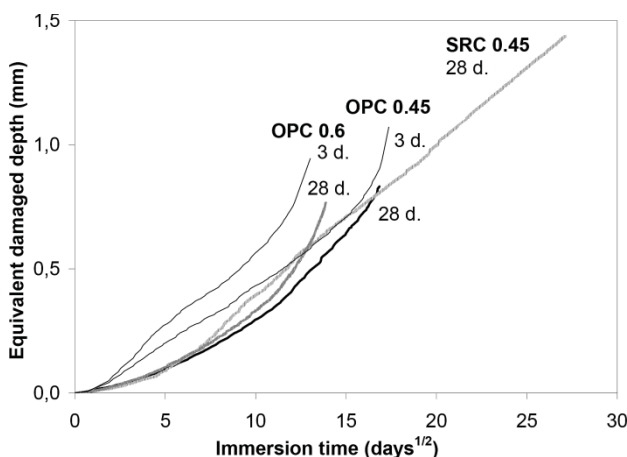


Figure 5.24. Leaching *EDD* versus square root of immersion time

Based on data from the USBR tests on concrete, Monteiro and Kurtis [MON 03] defined a potential damage Pd to predict the initiation time or saturation behavior from the composition of concrete and cement:

$$Pd = C_3 A^{1.39} C_3 S^{2.9} C_4 A F^{0.77} (w/c)^{7.80} \quad [5.7]$$

As shown in Figure 5.25, this model gives a good assessment of the behavior of mortars exposed to the same kind of test. It is difficult to find the limit of tendency to saturation behavior. For instance, M12 mortar has not shown any significant damage but saturation behavior, whereas M6 mortar has shown self-similar behavior [ROZ 09]. So slight changes in cement properties or w/b can significantly affect the performance of concrete exposed to sulfate attacks according to this test procedure.

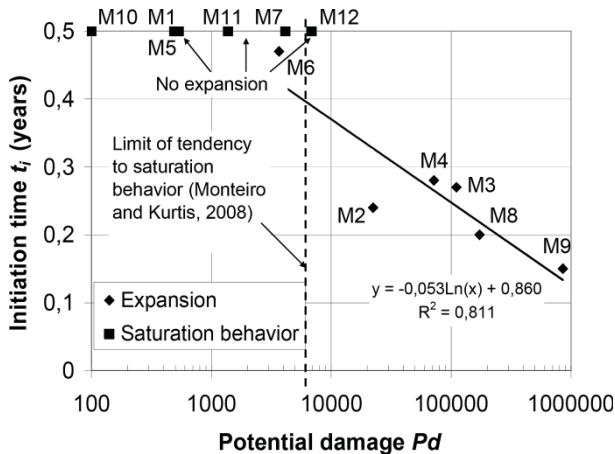


Figure 5.25. Analysis of expansion data by scaling law. Adapted from [ROZ 09]

5.3.2.2. Aggregates

Aggregates are involved at several levels in concrete sulfate resistance. Aggregate packing density and interface transition zone quality (linked to the aggregate type) are involved in the resistance to sulfate ingress.

The aggregate type is also involved at a level of chemical resistance. It has been assumed that aggregates can react with sulfate solution, since limestone aggregates contain carbonate ions. Carbonate ions are a reactant for thaumasite formation. This has actually been observed in concrete with

limestone aggregates [SAN 01]. However, other studies by the same authors showed a positive effect of limestone aggregates on concrete which contain slag. Some assumptions have been made, but the mechanism has not been clearly identified since other effects, such as calcium ion transport and the interface transition zone, can interfere. Finally, given that degradation propagates through the paste, the paste volume and conversely the aggregate volume are likely to have a significant influence.

5.3.3. Standards requirements

European standard EN 206-1 [NFE 04] classifies sulfate-rich regions as chemically aggressive environments – exposure classes XA1, XA2 and XA3. The boundaries between the three exposure classes are defined as a function of sulfate and magnesium concentration in water and sulfate concentration in soil.

In the framework of the prescriptive approach for specification of concrete, the national annex F of the European standard EN 206-1 defines composition limits that are more restrictive than for other chemical attacks with regard to mineral admixtures (A).

The upper limit for the A/(A+C) ratio is set to 0.15 when the attack comes from the presence of sulfates, instead of 0.30, for fly ash and ground slag. In any case, limestone or siliceous fillers cannot be used.

There is also a recommendation: *for class XA1, use PM cement [“seawater resisting”] and the binder composition must be such that it complies with the restrictions in NF P 15-317 [NFP 95a] and for XA2 and XA3 classes, use an ES cement [“sulfate resisting”] and the binder composition must be such that it complies with the restrictions in XP P 15-319 [NFP 95b].*

These two standards limited the amount of SO₃ and other cement phases. The NF P 15-317 standard, in particular, defined limiting values for C₃A (tricalcium aluminate) and C₃S (tricalcium silicate). The XP P 15-319 standard gave limiting values of C₃A and C₄AF contents:

$$(C_3A) \leq 5 \% \quad [5.8]$$

$$(C_4AF) + 2(C_3A) \leq 20 \% \quad [5.9]$$

5.4. Testing for sulfate resistance

Numerous tests have been designed to assess the performance of cementitious materials exposed to external sulfate attacks. The mechanisms of degradation and the field exposure conditions should be taken into account to design representative tests that help optimizing the mix-design of concrete.

5.4.1. Material and scale of the tests

Most experimental procedures consist of immersing concrete or mortar specimens in sulfate solution. This is actually representative of exposure conditions and it provides more robust procedure than wetting-drying cycles, for example [CHA 10]. The most widely used indicator of degradation is global expansion. In saturated conditions, the mechanism of degradation involves the ingress of sulfate ions into the cementitious matrix by diffusion; thus, the characteristic time of immersion tests depends on diffusivity, size and specimens. The larger the specimen, the longer the latency period or initiation time – when significant expansion can be measured. The drying radius R_0 can be introduced to represent the influence of specimen size (equation [5.10]). Shrinkage halftime is a linear function of R_0^2 [EN1 05]. The influence of the drying radius on initiation time is less prominent (Figure 5.26), which suggests that the wall effect plays a significant role. The skin of mortar specimens delayed the consequences of a sulfate attack, especially on the smallest specimens:

$$R_0 = \frac{2V}{S} \quad [5.10]$$

where V is the volume of specimen and S is the exposed surface.

Representative tests should be done on concrete. However, the representative volume of concrete results in relatively large specimens. The recommended minimum width is actually five times the maximum aggregates size. This results in relatively long initiation times (Figures 5.9 and 5.26), exceeding several years. For instance, a long-term investigation of the behavior of concrete exposed to sodium sulfate was conducted by the US Bureau of Reclamation in the 1950s. The specimens were continuously exposed to sulfate over a period of more than 40 years [NEV 04]. Studying

representative volume of mortar requires lower specimen size. For instance, a 4-mm maximum aggregate size results in a 20-mm wide specimen, and seven times lower initiation time than 70-mm wide specimen (needed to work on concrete). The ASTM C1012 standard prismatic mortar bars have a cross-section of 25 mm × 25 mm. This allows us to investigate the effect of several mix-design parameters, such as binder type and water-to-binder ratio, and to design performance-based specifications. However, shifting from mortar to concrete may have consequences on resistance to sulfate attacks that are still not totally understood.

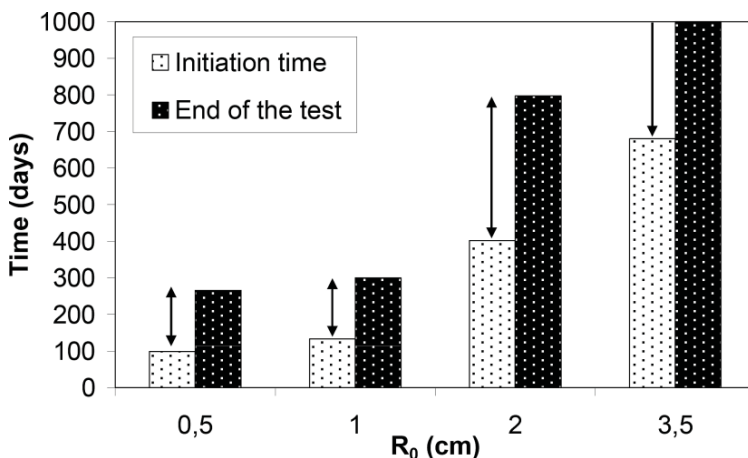


Figure 5.26. Initiation time for expansion and time end of the test.
Mortar specimens immersed in 3 g/L sodium sulfate solution

5.4.2. Acceleration of the degradation process

5.4.2.1. pH control

A continuous supply of sulfate solution, thus constant pH, can be assumed in field exposure conditions. Most of the experimental procedures recommend regular renewal of the sulfate solution [AST 00, NFP 93] to keep sulfate concentration constant, but this does not ensure constant pH. Because of leaching of alkalis and portlandite, the pH increases up to 12 or 13 within a few hours. The pH can be controlled by adding concentrated acid solution [MEH 73, MEH 75]. Keeping the pH constant accelerated the test [BRO 81], as shown by the loss of strength and the expansion rate. Comparative tests show that the time to reach significant expansion for the

uncontrolled pH condition is roughly twice as much as for the controlled pH condition [BRO 81, FER 97]. As a result, pH control results in more representative and shorter tests.

5.4.2.2. Drying and wetting

The initiation time of expansion is mainly influenced by diffusion in saturated conditions. Ingress of aggressive solution due to capillary absorption is known to be faster than diffusion [FRA 01]. This is representative of ingress of seawater in concrete in tidal and splash zones. Thus, drying and resaturation by sulfate solution has been used to accelerate external sulfate attack [MES 09, ELH 10].

The effect of drying was studied on OPC 0.6 mortar. Mortar prisms were stored in lime-saturated solution for 6 months. Then two samples were directly immersed in sodium sulfate solution ($[\text{SO}_4^{2-}] = 3 \text{ g/L}$); two other samples were stored at 20°C and 50% RH, and two samples were oven-dried at 45°C until mass stabilization. The final water saturations of the samples “6 months”, “6 months + 20°C ” and “6 months + 45°C ” were, respectively, 100%, 67% and 13%. After drying at 20 and 45°C , the mortar samples were immersed in sodium sulfate solution. The pH of sulfate solutions was controlled and the amounts of added acidic solution were monitored. The mass and length of the samples were measured each time the sulfate solution was renewed (Figures 5.27 and 5.28).

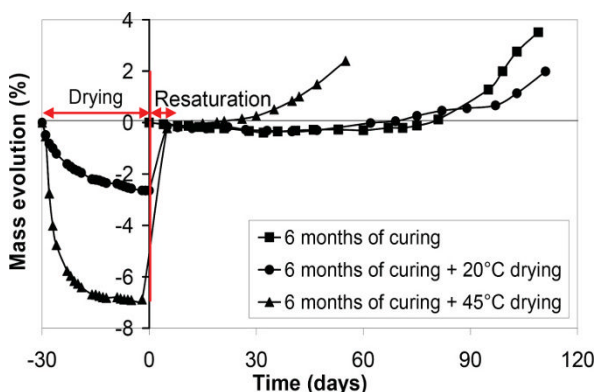


Figure 5.27. Mass change versus time for three different curings

Figure 5.27 shows the mass evolution of the specimens during the drying period in the left part of the graph. The reference time corresponds to immersion (time = 0). After the immersion in sodium sulfate solution, there was a remarkable mass increase in the dried specimens. This was due to the resaturation and not due to the sulfate attack. It was actually equal to the mass lost while drying.

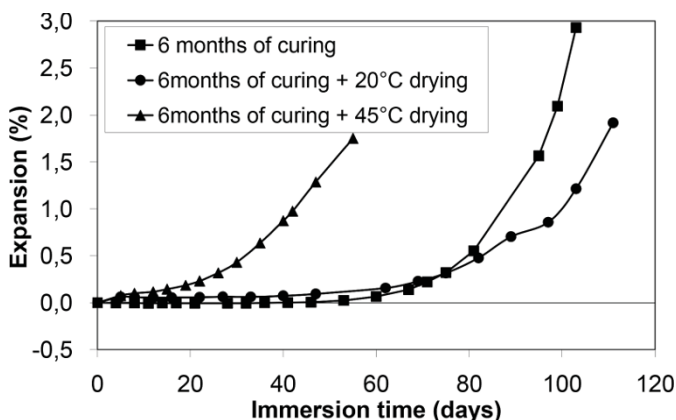


Figure 5.28. Expansion versus time for three different curing

The latency period was clearly observed for the specimens directly immersed in the sulfate solution and those dried at 20°C. It was almost unnoticeable for those dried at 45°C. The mass increase due to sulfate attack started at a very early time (less than 20 days) in the specimen dried at 45°C. These specimens were saturated by the sulfate solution that penetrates mainly by absorption into the dried specimens after immersion and that is why their response was relatively fast. The specimens directly immersed in the sulfate solution and those dried for one more month at 20°C had the same response approximately during the first two months before mass increase. The sulfate ions penetrate by diffusion into the pore solution. At the beginning of mass increase, the first ones react faster than the second ones and the degradation is more obvious. The difference between these two behaviors could be related to the pore size distribution and saturation (Figure 5.29). The ingress of sulfate ions is easier by absorption into empty capillary pores dried at 45°C than into pores dried at 20°C. Moreover, this bad response of the 45°C dried specimens could be referred to the

consecutive wetting and drying environments that can cause fatigue of the cementitious matrices and generate microcracks leading to a more permeable system [BAS 08].

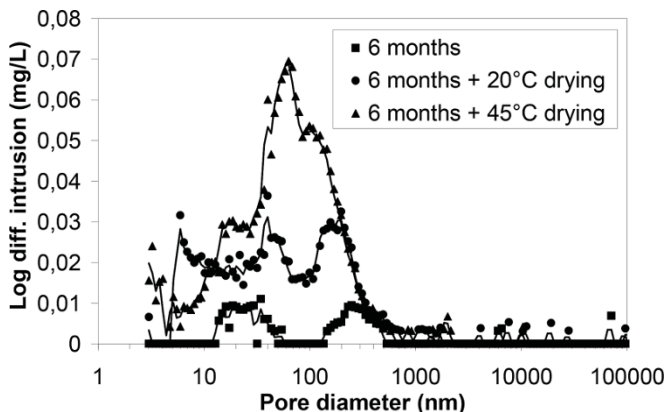


Figure 5.29. Influence of initial drying on pore sizes

The shape of the expansion curve presented in Figure 5.28 is quite similar to that of mass increase (except for the first day). Expansion was observed at the same time as mass increase. A theory has been proposed by Ping and Beaudoin [PIN 92a, PIN 92b] based on the chemical thermodynamics principles, explaining that the expansive forces are due to the crystallization pressure of ettringite. Two conditions are necessary for the occurrence of the crystallization pressure: (1) a confined place where a solid product is formed and grown, and (2) an activity product of reactants in the pore solution greater than the solubility product under atmospheric pressure.

The monitoring of added acidic solution to control the pH of sulfate solution provided the evolution of EDD (Figure 5.30). Diffusion-based degradation and leaching resulted in linear increase of EDD, as observed for “6 months” and “6 months + 20°C” specimens. The higher leaching kinetics of “6 months” samples could explain their earlier expansion. The evolution is not linear for the samples dried at 45°C because leaching was accompanied by expansion, and thus continuous increase of diffusivity.

Preliminary drying results in faster ingress of sulfate ions and significant acceleration of sulfate attack. This principle was used by Messad [MES 09]

to design accelerated test on concrete. Attention should be paid to the influence of temperature increase on the microstructure of cementitious matrix in order to avoid DEF-based mechanism [LOT 10]. However, this kind of test can be used in comparative performance-based approach [LIN 14] as it does not affect the relative performances of concrete.

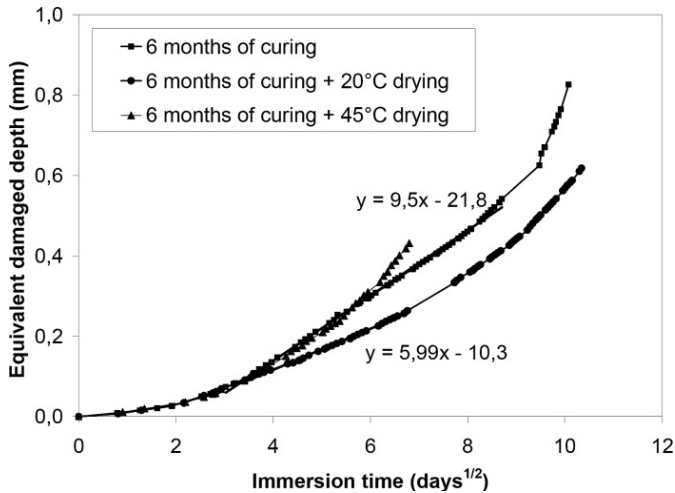


Figure 5.30. Effect of preconditioning on leaching kinetics

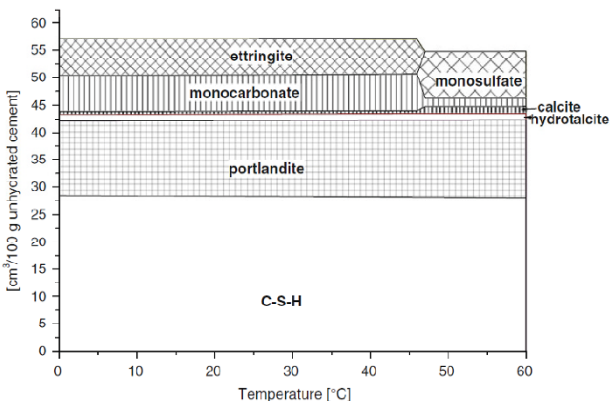


Figure 5.31. Calculated volume of solids in a hydrated cement paste as a function of temperature. Adapted from [LOT 08, LOT 10]

5.4.3. Recommendations for testing

5.4.3.1. Study of degradation mechanism

In most of the studies, two stages are identified from length measurements: the first stage is a dormant period where no or little expansion can be measured and the second stage where significant expansion occurs. More information is needed to explain the phenomena that occur during the first stage of sulfate attack. Expansion data do not provide enough information to assess the chemical reactions and understand the mechanisms causing damage.

A new experimental procedure has been designed [PLA 06, BAD 06, ELH 12a]. Tests are led at constant pH in controlled conditions. Hence, clarifications about the dormant period (first stage) during the degradation process can be made when correlating mass and length measurements with kinetics of leached calcium and hydroxide ions.

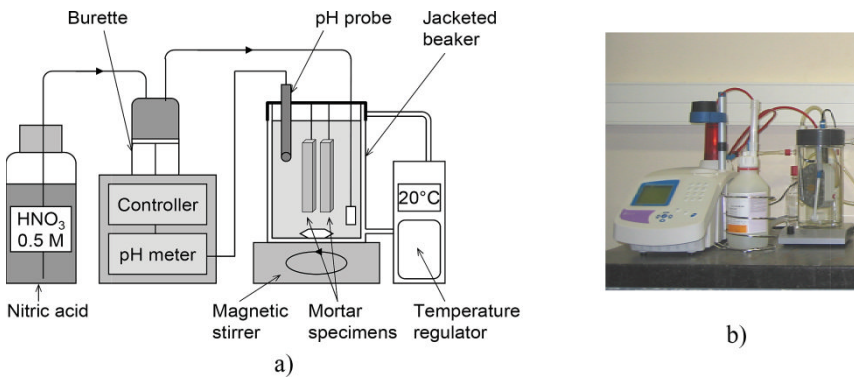


Figure 5.32. a) Schematic diagram of sulfate test, **b)** pH controller and beaker

Tests were done in controlled conditions at constant pH and temperature, 7.5 and 20°C, respectively. The pH was regulated by adding a nitric acid solution at 0.5 mol/L. The sulfate solution was renewed when the volume of added acid reached 15 mL. Hence, constant concentration of sulfates could be ensured during the test. This is meant to be representative of field conditions where concrete is exposed to continual supply of sulfate

ions. The device used for this test is presented in Figure 5.32. The mass and length are measured each time the solution is renewed. The prisms have gauge studs at both ends in order to measure the expansion with length change comparators, with an Invar cylinder as a reference length to zero the comparator. The mass of the samples is also monitored. Before each mass and length measurement, the samples are wiped to remove the water from the sample surface. The samples remain saturated with a dry surface. In parallel, the quantity of leached hydroxide ions are assessed through the added volumes of a nitric acid (HNO_3) solution and that of leached calcium by the titration of the solutions. The titration of the solution can also provide the sulfate ingress and this can be used to calibrate models.

5.4.3.2. Performance testing

The test described here is simpler, as one pH controller can be used for several concrete or mortar mixtures, and titration of the solution is not required. Concrete or mortar samples are immersed in sodium sulfate solution. The sulfate concentration is 3 g/L, and pH is controlled using 0.02 mol/L sulfuric acid solution [ROZ 09]. Solutions are renewed every month. The mass, length and elastic modulus of concrete samples are monitored. The acceleration of the test can be provided by preliminary drying [MES 09].

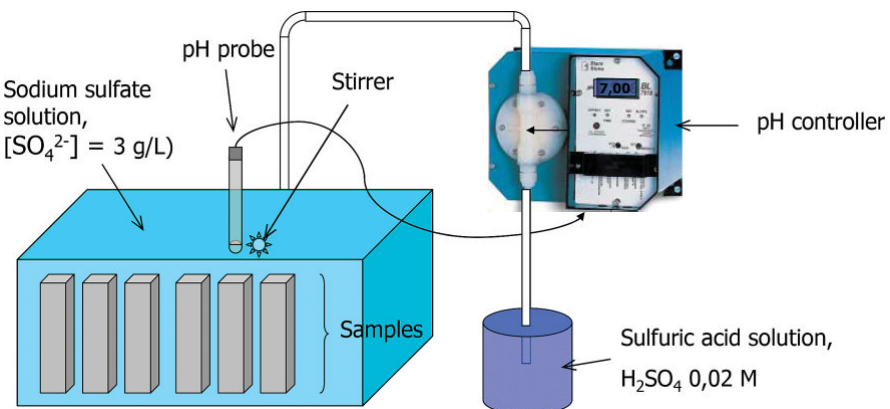


Figure 5.33. External sulfate attack with pH control

5.5. Conclusion

Sulfate-rich groundwater and seawater can be considered as chemically aggressive environments where external sulfate attacks may affect the durability of concrete. The consequences of sulfate attacks are leaching, expansion, cracking and softening of concrete. Sulfate-resisting concretes were used before the mechanism of degradation was fully understood. The behavior of existing cements and the influence of the main mix-design parameters have been widely studied; thus, available data allow us to design durable structures exposed to sulfate attacks. The development of new cementitious materials has created the need to design performance tests. The mechanisms of degradation have been studied to assess representative testing conditions and provide performance-based specifications.

The ingress of sulfate ions and leaching modify the chemical equilibrium in cementitious matrix. The increase of sulfate concentration in interstitial solution results in supersaturation and formation of ettringite from monosulfoaluminate. The formation of ettringite does not necessarily result in expansion or damage. This is supported by numerous field observations in the past in which no correlation between the amount of ettringite formed and expansion was observed. Significant expansion pressure higher than tensile strength can only be exerted by ettringite which forms in small pores within a certain size range, according to the crystallization pressure theory. Two conditions are necessary for the occurrence of the crystallization pressure: (1) a confined place where a solid product is formed and grown, and (2) an activity product of reactants in the pore solution greater than the solubility product under atmospheric pressure. These conditions can be found where the monosulfoaluminate finely intermixed in C-S-H reacts to form expansive ettringite.

As leaching and ettringite formation are main aspects of the mechanisms of degradation, external sulfate attacks can be mitigated at the chemical level by reducing the calcium and aluminates contents. Prescriptive specifications actually recommend reducing C_3A and C_4AF proportions of Portland cements, either by reducing their proportions in clinker or by using high slag proportions in blended cements. Mineral admixtures such as slag and fly ash improve sulfate resistance at chemical and physical levels. Significant proportions of these products result in lower diffusivity and leaching

sensitivity, thus better resistance to sulfate attacks. Another way to improve sulfate resistance at the physical level is to reduce water-to-cement ratio. Such concretes have shown lower diffusivity and relatively good behavior, whatever cement type was used.

Physical sulfate attacks are due to crystallization pressure caused by transformations of sodium sulfate in concrete exposed to wetting and drying cycles.

Sulfate attacks may occur in marine environments. In splash- and tidal zones, wetting and drying cycles favor physical attack. In seawater, external sulfate attacks are mitigated and delayed by the relatively high chloride content and the formation of Friedel's salt from monosulfoaluminate. However, combined effects should be taken into account, as damage resulting from external sulfate attack is likely to accelerate the ingress of chloride ions and corrosion of reinforcement.

Performance-based tests are needed to understand the behavior of new cementitious materials and develop performance-based specifications. Accelerated tests procedures are available but the laboratory conditions should be representative of field exposure. Using sulfate concentration higher than 10 g/L is not recommended because it modifies the chemical equilibrium and relative precipitations of gypsum and ettringite. Controlling the pH and periodically renewing sulfate solution results in representative and accelerated tests. The duration of the test depends on the size of specimens. Studying mortar allows us to reduce the size of the samples. Studying concrete requires another acceleration of the test, which can be preliminary drying, provided that the maximum drying temperature does not induce the DEF.

5.6. Bibliography

- [ACI 05] ACI Building Code Requirements for Structural Concrete (ACI 318-05) and Commentary (ACI 318R-05), American Concrete Institute, p. 430, 1 January 2005.
- [AKO 97] AKÖZ F., TÜRKER F., KORAL S. *et al.*, "Effects of raised temperature of sulfate solutions on the sulfate resistance of mortars with and without silica fume", *Cement and Concrete Research*, vol. 29, no. 4, pp. 537–544, April 1999.

- [ALA 95] AL-AMOUDI O.S.B., MASLEHUDDIN M., ABDUL-AL Y., "Role of chloride ions on expansion and strength reduction in plain and blended cement in sulphate environments", *Construction and Building Materials*, vol. 9, no. 1, pp. 25–33, 1995.
- [AST 00] ASTM C 1012- 95a, "Standard test method for length change of hydraulic-cement mortars exposed to a sulfate solution", *Annual Book of ASTM Standards*, vol. 04.01 cement; lime; gypsum, 2000.
- [BAD 06] BADOZ C., FRANCISCO P., ROUGEAU P., "A performance test to estimate durability of concrete products exposed to chemical attacks", *Proceedings of the 2nd International Congress of FIB*, 5–8 June 2006.
- [BAR 07] BARBARULO R., PEYCELON H., LECLERCQ S., "Chemical equilibria between C–S–H and ettringite, at 20 and 85°C", *Cement and Concrete Research*, vol. 37, pp. 1176–1181, 2007.
- [BAS 08] BASSUONI M.T., MEHDI M.L., "Durability of self consolidating concrete to different exposure regimes of sodium sulfate attack", *Materials and Structures*, vol. 42, no. 8, pp. 1039–1057, 2008.
- [BLA 05] BLANCO-VARELA M.T., AGUILERA J., MARTINEZ-RAMIREZ S., "Effect of C³A, temperature and storage medium on thaumasite formation in carbonated mortar", *Cement and Concrete Research*, vol. 36, no. 4, pp. 707–715, April 2005.
- [BON 39] BONNELL D.G.R., NOTTAGE M.E., "Studies in porous materials with special reference to building materials: I. The crystallisation of salts in porous materials", *Journal of the Society of Chemical Industry*, vol. 58, pp. 16–21, 1939.
- [BRO 81] BROWN P.W., "An evaluation of sulfate resistance of cements in a controlled environment", *Cement and Concrete Research*, vol. 11, pp. 719–727, 1981.
- [CHA 10] CHABRELIE A., Mechanisms of degradation of concrete by external sulfate ions under laboratory and field conditions, PhD Thesis, École Polytechnique Fédérale de Lausanne, 2010.
- [CRA 02] CRAMMOND N., "The occurrence of thaumasite in modern construction – a review", *Cement and Concrete Composites*, vol. 24, no. 3–4, pp. 393–402, 2002.
- [CSA 94] CSA A.23. 1-94. Concrete Materials and Methods of Concrete Construction, Rexdale (Toronto), Canada, 1994.
- [DAM 92] DAMIDOT D., GLASSER F.-P., "Thermodynamic investigation of the CaO–Al₂O₃–CaSO₄–H₂O system at 50°C and 85°C", *Cement and Concrete Research*, vol. 22, pp. 1179–1191, 1992.

- [DAM 93] DAMIDOT D., GLASSER F.-P., "Thermodynamic investigation of the CaO–Al₂O₃–CaSO₄–H₂O system at 25°C and the influence of Na₂O", *Cement and Concrete Research*, vol. 23, pp. 221–238, 1993.
- [DEH 07] DEHWAH H.A.F., "Effect of sulfate concentration and associated cation type on concrete deterioration and morphological changes in cement hydrates", *Construction and Building Materials*, vol. 21, pp. 29–39, 2007.
- [DIV 98] DIVET L., RANDRIAMBOLOLONA R., "Delayed ettringite formation: the effect of temperature and basicity on the interaction of sulphate and C–S–H phase", *Cement and Concrete Research*, vol. 28, no. 3, pp. 357–363, 1998.
- [DUV 92] DUVAL R., HORNAIN H., "La durabilité du béton vis-à-vis des eaux agressives", in BARON J., OLLIVIER J.-P. (eds), *La durabilité des bétons*, Presses de l'ENPC, 1992.
- [EN 05] EN 1992-2, Eurocode 2 – Design of concrete structures – Concrete bridges – Design and detailing rules, October 2005.
- [ELH 10] EL HACHEM R., Etude multi-critères de la dégradation des matériaux cimentaires par l'attaque sulfatique externe, PhD Thesis, Ecole Centrale de Nantes, France, 2010.
- [ELH 12a] EL HACHEM R., ROZIÈRE E., GRONDIN F. *et al.*, "New procedure to investigate external sulphate attack on cementitious materials", *Cement and Concrete Composites*, vol. 34, no. 3, pp. 357–364, 2012.
- [ELH 12b] EL HACHEM R., ROZIÈRE E., GRONDIN F. *et al.*, "Multi-criteria analysis of the mechanism of degradation of Portland cement based mortars exposed to external sulphate attack", *Cement and Concrete Research*, vol. 42, pp. 1327–1335, 2012.
- [FEL 91] FELDMAN R.F., BEAUDOIN J.J., PHILIPPOSE K.E., "Effect of cement blends on chloride and sulfate ion diffusion in concrete", *Cemento*, vol. 88, pp. 3–17, 1991.
- [FER 97] FERRARIS C.F., CLIFTON J.R., STUTZMAN P.E. *et al.*, "Mechanisms of degradation of Portland cement-based systems by sulfate attack", in SCRIVENER K.L., YOUNG J.F. (eds), *Mechanisms of Chemical Degradation of Cement-Based Systems*, E & FN Spon, London, pp. 185–192, 1997.
- [FER 05] FERRARIS C.F., STUTZMAN P., PELTZ M. *et al.*, "Developing a more rapid test to assess sulfate resistance of hydraulic cements", *Journal of Research of the National Institute of Standards and Technology*, vol. 110, pp. 529–540, 2005.
- [FRA 01] FRANÇOIS R., FRANCY O., CARÉ S. *et al.*, "Mesure du coefficient de diffusion des chlorures", *Comparaison entre régime permanent et régime transitoire*, Revue française de Génie Civil, vol. 5, nos. 2–3, pp. 309–329, 2001.

- [FU 94] FU Y., XIE P., GU P. *et al.*, "Effect of temperature on sulphate adsorption/desorption by tricalcium silicate hydrates", *Cement and Concrete Research*, vol. 24, no. 8, pp. 1428–1432, 1994.
- [GER 00] GERARD B., MARCHAND J., "Influence of cracking on the diffusion properties of cement-based materials. Part I: influence of continuous cracks on the steady-state regime", *Cement and Concrete Research*, vol. 30, no. 1, pp. 37–43, 2000.
- [GOL 95] GOLLOP R.S., TAYLOR H.F.W., "Microstructural and microanalytical studies of sulfate attack III. Sulfate-resisting Portland cement: reactions with sodium and magnesium sulfate solutions", *Cement and Concrete Research*, vol. 25, no. 7, pp. 1581–1590, 1995.
- [GUI 04a] GUILLON E., Durabilité des matériaux cimentaires - Modélisation de l'influence des équilibres physico-chimiques sur la microstructure et les propriétés mécaniques résiduelles, PhD Thesis, In French, Ecole Normale Supérieure de Cachan, P 6, 2004.
- [GUI 04b] GUILLON E., MORANVILLE M., "Physical and chemical modeling of Portland cement pastes under seawater attack", 2004.
- [HER 97] HERNANDEZ M.S., GUERRERO A., GOÑI S., *et al.*, "Effect of the temperature on the leaching performance of the cement-based immobilization systems: sulfate and chloride", *Cement and Concrete Research*, vol. 27, no. 4, pp. 515–524, April 1997.
- [HIG 02] HIGGINS D.D., CRAMMOND N.J., "Resistance of concrete containing ggbs to the thaumasite form of sulfate attack", *Proceedings of 1st International Conference on Thaumasite in Cementitious Materials*, Watford, UK, June 2002.
- [HIG 03] HIGGINS D.D., "Increased sulfate resistance of ggbs concrete in the presence of carbonate", *Cement and Concrete Composites*, vol. 25, pp. 913–919, 2003.
- [HOB 00] HOBBS D.W., TAYLOR M.G., "Nature of the thaumasite sulfate attack mechanism in field concrete", *Cement and Concrete Research*, vol. 30, no. 4, pp. 529–533, 2000.
- [IRA 03] IRASSAR E.F., BONAVETTI V.L., GONZALEZ M., "Microstructural study of sulfate attack on ordinary and limestone Portland cements at ambient temperature", *Cement and Concrete Research*, vol. 33, pp. 31–41, 2003.
- [LAF 29] LAFUMA H., "Théorie de l'expansion des liants hydrauliques", *La Revue de Matériaux de Construction et de Travaux Publics*, part 1, vol. 243, December 1929, pp. 441–444 and Part 2, vol. 244, pp. 4–8, January 1930.

- [LAW 94] LAWRENCE C.D., "Mortar expansion due to delayed ettringite formation. Effect of curing period and temperature", *Cement and Concrete Research*, vol. 25, no. 4, pp. 903–914, May 1994.
- [LEE 05] LEE S.T., MOON H.Y., SWAMY R.N., "Sulfate attack and role of silica fume in resisting strength loss", *Cement and Concrete Composites*, vol. 27, pp. 65–76, 2005.
- [LEE 08] LEE S., HOOTON R., JUNG H. *et al.*, "Effect of limestone filler on the deterioration of mortars and pastes exposed to sulphate solutions at ambient temperatures", *Cement and Concrete Research*, vol. 38, pp. 68–76, 2008.
- [LIN 14] LINGER L., ROZIERE E., CUSSIGH F. *et al.*, "Concrete equivalent performance concept for durability – an operational guide for the comparative approach", *Proceedings of The Fourth International fib Congress*, Mumbai, pp. 540–547, 14 February 2014.
- [LOT 06] LOTHENBACH B., WINNEFELD F., ALDER C. *et al.*, "Effect of temperature on the pore solution, microstructure and hydration products of Portland cement", *Cement and Concrete Research*, vol. 37, no. 4, pp. 483–491, April 2006.
- [LOT 08] LOTHENBACH B., "Thermodynamic modeling of the effect of temperature on the hydration of Portland cement", in SCHLANGEN E., DE SCHUTTER G. (eds), *Proceedings of the International RILEM Symposium on Concrete Modeling (CONMOD '08)*, 26–28 May, RILEM Publications, Delft, the Netherlands, pp. 393–400, 2008.
- [LOT 10] LOTHENBACH B., BARY B., LE BESCOL P. *et al.*, "Sulfate ingress in Portland cement", *Cement and Concrete Research*, vol. 40, pp. 1211–1225, 2010.
- [MEH 73] MEHTA P.K., "Mechanism of expansion associated with ettringite formation", *Cement and Concrete Research*, vol. 3, pp. 1–6, 1973.
- [MEH 75] MEHTA P.K., "Evaluation of sulfate-resisting cements by a new test method", *ACI Journal*, vol. 72–40, pp. 573–575, 1975.
- [MEH 91] MEHTA P.K., "Concrete in the marine environments", in BENTUR A., MINDESS S. (eds), *Modern Concrete Technology Series*, Elsevier Science Publishing, 1991.
- [MES 09] MESSAD S., Mise au point d'un essai de vieillissement accéléré de l'attaque sulfatique externe pour l'application du concept de performance équivalente dans le cadre de la norme NF EN 206-1, PhD Thesis, University of Toulouse, France, 2009.

- [MON 03] MONTEIRO P.J.M., KURTIS K.E., “Time to failure for concrete exposed to severe sulfate attack”, *Cement and Concrete Research*, vol. 33, pp. 987–993, 2003.
- [MUE 13] MUELLAUER W., BEDDOE R.E., HEINZ D., “Sulfate attack expansion mechanisms”, *Cement and Concrete Research*, vol. 52, pp. 208–215, 2013.
- [NEV 04] NEVILLE A., “The confused world of sulfate attack on concrete: review”, *Cement and Concrete Research*, vol. 34, pp. 1275–1296, 2004.
- [NFE 04] NF EN 206-1., Béton – Partie 1: Spécification, performances, production et conformité, AFNOR, French standard, from European standard EN 206 Concrete – Performance, production and conformity, 2004.
- [NFP 93] NF P 18-837, Produits de calage et/ou scellement à base de liants hydrauliques, Essai de tenue à l'eau de mer et/ou à l'eau à haute teneur en sulfates, In French, AFNOR, 1993.
- [NFP 95a] NF P 15-317, Liants hydrauliques – Ciments pour travaux à la mer, Recueil de normes françaises, Béton et constituants du béton, vol. 3, In French 4th ed., AFNOR, 1995.
- [NFP 95b] NF P 15-319, Liants hydrauliques – Ciments pour travaux en eaux à hautes teneurs en sulfates, Recueil de normes françaises, Béton et constituants du béton, vol. 3, In French 4th ed., AFNOR, 1995.
- [NIE 05] NIELSEN E.P., HERFORT D., GEIKER M.R., “Binding of chloride and alkalis in Portland cement systems”, *Cement and Concrete Research*, vol. 35, no. 1, pp. 117–123, 2005.
- [PIP 08] PIPILIKAKI P., PAPAGEORGIOU D., TEAS C. *et al.*, “The effect of temperature on thaumasite formation”, *Cement and Concrete Composites*, vol. 30, pp. 964–969, 2008.
- [PIN 92a] PING X., BEAUDOIN J.J., “Mechanism of sulfate expansion I. Thermodynamic principles of crystallization pressure”, *Cement and Concrete Research*, vol. 22, pp. 631–640, 1992.
- [PIN 92b] PING X., BEAUDOIN J.J., “Mechanism of sulfate expansion II. Validation of thermodynamic theory”, *Cement and Concrete Research*, vol. 22, pp. 845–854, 1992.
- [PLA 02] PLANEL D., Les effets couplés de la précipitation d'espèces secondaires sur le comportement mécanique et la dégradation chimique des bétons, PhD Thesis, University of Marne la Vallée, France.
- [PLA 06] PLANEL D., SERCOMBE J., LE BESCOP P. *et al.*, “Long-term performance of cement paste during combined calcium leaching-sulfate attack: kinetics and size effect”, *Cement and Concrete Research*, vol. 36, pp. 137–143, 2006.

- [ROZ 09] ROZIÈRE E., LOUKILI A., EL HACHEM R. *et al.*, “Durability of concrete exposed to leaching and external sulphate attack”, *Cement and Concrete Research*, vol. 39, pp. 1188–1198, 2009.
- [SAH 07] SAHMARAN M., KASAP O., DURU K. *et al.*, “Effects of mix composition and water–cement ratio on the sulphate resistance of blended cements”, *Cement and Concrete Composites*, vol. 29, pp. 159–167, 2007.
- [SAN 01] SANTHANAM M., COHEN M.D., OLEK J., “Sulfate attack research – whiter now?”, *Cement and Concrete Research*, vol. 31, pp. 845–851, 2001.
- [SAN 02] SANTHANAM M., COHEN M.D., OLEK J., “Mechanism of sulfate attack: a fresh look. Part 1: summary of experimental results”, *Cement and Concrete Research*, vol. 32, no. 6, 2002.
- [SAN 02] SANTHANAM M., “Modeling effect of solution concentration and temperature during sulfate attack on cement mortars”, *Cement and Concrete Research*, vol. 32, pp. 585–592, 2002.
- [SAN 03] SANTHANAM M., COHEN M.D., OLEK J., “Effects of gypsum formation on the performance of cement mortars during external sulphate attack”, *Cement and Concrete Research*, vol. 33, pp. 325–332, 2003.
- [SAN 06] SANTHANAM M., COHEN M., OLEK J., “Differentiating seawater and groundwater sulfate attack in Portland cement mortars”, *Cement and Concrete Research*, vol. 36, no. 12, pp. 2132–2137, 2006.
- [SCH 99] SCHERER G.W., “Crystallization in pores”, *Cement and Concrete Research*, vol. 29, pp. 1347–1358, 1999.
- [SCH 04] SCHERER G.W., “Stress from crystallization of salt”, *Cement and Concrete Research*, vol. 34, pp. 1613–1624, 2004.
- [SCH 07] SCHMIDT T., Sulfate attack and the role of internal carbonate on the formation of thaumasite, PhD Thesis, Ecole Polytechnique Fédérale de Lausanne, 2007.
- [SCH 09] SCHMIDT T., LOTHENBACH B., ROMER M. *et al.*, “Physical and microstructural aspects of sulfate attack on ordinary and limestone blended Portland cements”, *Cement and Concrete Research*, vol. 39, no. 12, pp. 1111–1121, 2009.
- [SCR 93] SCRIVENER K.-L., TAYLOR H.-F.-W., “Delayed ettringite formation: a microstructural and microanalytical study”, *Advances in Cement Research*, vol. 5, no. 20, pp. 139–146, 1993.
- [STO 03] STONE A., *The American Well Owner*, American Ground Water Trust, no. 3, 2003.

- [SWE 71] SWENSON E.G., “Concrete in sulphate environments”, *Canadian Building Digest*, vol. 136, 1971.
- [TUM 96] TUMIDAJSKI P.J., CHAN G.W., “Effect of sulfate and carbon dioxide on chloride diffusivity”, *Cement and Concrete Research*, vol. 26, no. 4, pp. 551–556, April 1996.
- [YU 01] YU P., KIRKPATRICK R.J., “³⁵Cl NMR relaxation study of cement hydrate suspensions”, *Cement and Concrete Research*, vol. 31, no. 10, pp. 1479–1485, 2001.
- [YU 12] YU C., SCRIVENER K., SUN W., “Comparison between expansion and microstructural changes of mortar under sulfate attack”, *Proceedings of the 2nd International Conference on Microstructural-Related Durability of Cementitious Composites*, Amsterdam, 2012.
- [YU 13] YU C., SUN W., SCRIVENER K., “Mechanism of expansion of mortars immersed in sodium sulfate solutions”, *Cement and Concrete Research*, vol. 43, pp. 105–111, 2013.
- [ZUQ 07] ZUQUAN J., WEI S., YUNSHENG Z. *et al.*, “Interaction between sulfate and chloride solution attack of concretes with and without fly ash”, *Cement and Concrete Research*, vol. 37, no. 8, pp. 1223–1232, August 2007.

@Seismicisolation

Performance-Based Design of Structures and Methodology for Performance Reliability Evaluation

6.1. Introduction

As infrastructure deteriorates over the course of its lifecycle; therefore, it is important to ensure the continued safety and serviceability of the various elements. To achieve this, it is necessary to be able to predict the point at which an infrastructural asset will deteriorate to a critical condition state. To predict this point, it is necessary to consider how this deterioration will affect the structural capacity of the asset, as well as any future increase in the applied loading, all of which have an associated level of uncertainty, hindering an accurate prediction [ANG 06]. Thus, advanced methods are required, which facilitate the consideration of all pertinent information in an analytical assessment model. There exists a hierarchy (Figure 6.1) for the levels of assessment associated with an infrastructure network [PAK 12], for which all levels are included into the decision-making tool. The most advanced level in this hierarchy is probabilistic/reliability methods.

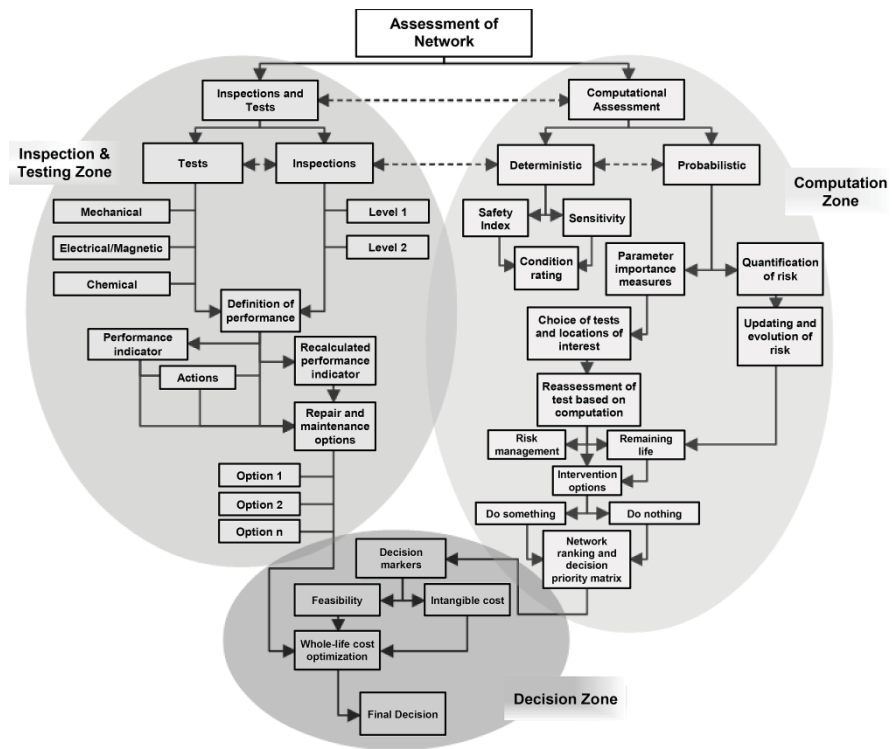


Figure 6.1. Infrastructural assessment hierarchy

Reliability is regularly related to the probability that failure will not occur; thus, it is complementary to the failure probability p_f and, consequently, this leads to the estimation of probability of structural safety over a prescribed period of time. Often, this prescribed period of time is the “design life” of a structure. The use of probabilistic methods facilitates the treatment of structures as stochastic systems rather than deterministic, a treatment which is more accurate to the actual realization of an engineering structure. Reliability methods provide for the computation of safety based on varying load models and uncertainties around the return period of extreme load events, in addition to addressing the uncertainty in the resistance capacity of a structure. Previously, widespread application of structural reliability analysis was hindered by high computational demand, but modern advances in computing technology have overcome these issues. Thus, there remains no effective restriction on the extensive implementation of the method for infrastructure assessment or design.

Probabilistic methods can sometimes be subjective in nature or may be based on an engineering judgment to a certain extent, as the input variables required for the analysis can only be modeled on the basis of the level of information available about the problem at hand. From this, the lack of information, or uncertainty in information, becomes a significant consideration in reliability analysis. Uncertainties can be defined in two ways: aleatory and epistemic. Aleatory uncertainty relates to uncertainties that are inherent to the problem and must be accounted for, whereas epistemic uncertainties are those that can be reduced or mitigated through the collection of information about the problem, and the refinement of the model used in the analysis. Consequently, it can be stated that structural reliability analysis refers more to our state of knowledge of the structure than to the actual state of the structure itself.

A brief overview of the structural reliability method is presented in the following sections, and the authors encourage those seeking a greater understanding of the method to consult the referenced bibliography for a more complete background.

6.2. Code treatment of structural reliability

6.2.1. *Formulation of structural reliability analysis*

The basic formulation of structural reliability can be expressed through a model of a single load effect variable S , resisted by a single resistance variable R , with each having its own probability density function. In the general case of engineering structures, the limit state is violated if S exceeds the value of R . This limit state can be expressed as:

$$g = R - S \quad [6.1]$$

This can also be described in different but probabilistically equivalent limit-state functions, depending on the criteria of the problem being assessed:

$$g = 1 - \frac{S}{R}, \quad g = \ln\left(\frac{R}{S}\right) \quad [6.2]$$

The probability of this violation is identical to the probability of failure p_f . This concept has its most basic form when considering a single structural

element for an ultimate or serviceability limit state, which is denoted by the limit-state function, $G(\mathbf{x})$.

$$p_f = P(R - S \leq 0) = P[G(R, S) \leq 0] = P[G(\mathbf{X}) \leq 0] \quad [6.3]$$

where P represents probability. In the case that the basic variables in the limit-state function are independent:

$$\begin{aligned} p_f &= \int_{R < S} \int f_R(r) f_S(s) dr ds \\ &= \int_0^\infty \int_0^s f_R(r) f_S(s) dr ds = \int_0^\infty F_R(s) f_S(s) ds \end{aligned} \quad [6.4]$$

where $F_R(\cdot)$ is the cumulative distribution function of R . The simplest form of structural reliability analysis can be evaluated by modeling each random variable in the problem as a normal distribution and using only the first two moments: mean μ and standard deviation σ . The reliability index β and the failure probability p_f can then be approximated as [COR 69]:

$$\beta = \frac{\mu_Z}{\sigma_Z} = \frac{\mu_R - \mu_S}{\sqrt{\sigma_R^2 + \sigma_S^2}} = -\Phi^{-1}(p_f) \quad [6.5]$$

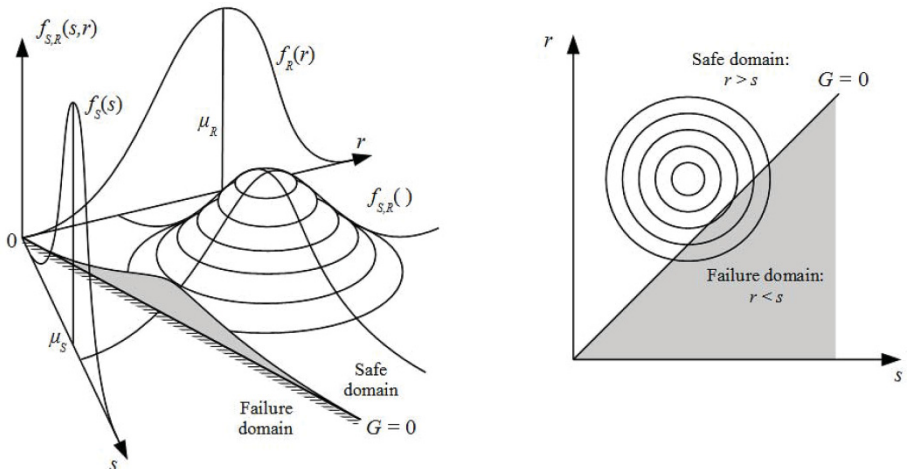


Figure 6.2. Conceptualization of the reliability problem [MEL 99]

However, the output from this method must strictly be considered nominal and is useful only when employed on a comparable basis to other analyses of the same type. Additionally, the use of this method assumes a linear limit-state function with a normal distribution. However, limit states are typically observed to be nonlinear in practice, which make it difficult to obtain the first two moments of the limit-state function.

When conducting a structural reliability analysis, four levels have been defined with increasing levels of complexity. Level I, the most basic level, is the commonly seen partial factor approach used in design codes where deterministic values are used and uncertainty is accounted for by way of partial factors. Level II methods incorporate the idea of model uncertainty by describing the input parameters as normal distributions with mean and standard deviation values. The use of this method yields a nominal failure probability useful for comparison purposes. Level III methods involve establishing the failure probability using advanced methods, such as transformations and simulations, and can be referred to as “exact” methods. Level IV methods expand on the “exact” methods by incorporating economic models in order to generate a risk analysis.

6.2.2. Incorporation of reliability analysis into normative documents

The role of normative documents, such as structural design codes, is generally to ensure a degree of harmonization of structural design, in an effort to provide minimum safety levels of structures. Having employed the use and followed the rules of a design code, the designer should have reasonable confidence in the safety and serviceability of the designed structure [MEL 99]. To this end, a design code needs to be based on advanced methods for predicting structural safety, as well as to be accessible enough to the end-user/designer. To address this issue, modern structural design codes [DNV 92, CEN 02, JCS 00] implement the concept of partial factors γ for both loads and resistance variables. The partial factor method, also called the load-resistance factor reduction (LRFD) method, is designed to be able to apply probabilistic uncertainty to deterministic design variables [ELL 96]. For the reliability method, an applied load above the mean value μ_S is said to be unfavorable, while a resistance value below the mean μ_R is also deemed unfavorable. Thus, the partial factors are applied to simulate

such an unfavorable scenario. The values for these partial factors can be determined through calibration to the limit-states equations specified in the code against the target reliabilities established to ensure that adequate safety is provided.

6.2.3. Reliability targets

The reliability target is the level for which a structure should perform at a minimum. In design, it can be used as the minimum benchmark which a structure must fulfill, thus ensuring that certain safety levels are achieved. Rather than simply be based on a pass-fail approach for all structures, the target reliability can be optimized to different scenarios where failure consequences may be considered on different levels, and where the nature of the structural failure can be predicted. Thus, target reliability indices can be seen to be situational. The specification of target reliabilities has been included in numerous design standards prepared by *Det Norske Veritas* (Table 6.1), the European Committee for Standardization (Table 6.2) and the Joint Committee on Structural Safety (Table 6.3).

Class of failure	Consequence of failure	
	Less serious	Serious
I – Redundant structure	3.09	3.71
II – Significant warning before the occurrence of failure in a non-redundant structure	3.71	4.26
III – No warning before the occurrence of failure in a non-redundant structure	4.26	4.75

Table 6.1. Target reliability for failure types and consequences [DNV 92]

A reference period refers to the period of time used as a basis for assessing stochastic actions. It should be noted that when designing a new structure or assessing an existing structure to fulfill target reliability levels, the uncertainties within the model used will affect the reliability level. Thus, the true relationship between the calculated reliability index and the target reliability index is a function of the commonality of the uncertainties and assumptions used in the establishing models.

Consequence classes	Reference period	
	1 year	50 years
<i>Low</i> consequence for loss of human life, and economic, social or environmental consequences small or negligible	4.2	3.3
<i>Medium</i> consequence for loss of human life, economic, social or environmental consequences considerable	4.7	3.8
<i>High</i> consequence for loss of human life, or economic, social or environmental consequences very great	5.2	4.3

Table 6.2. Target reliability for ultimate limit state [CEN 02]

Consequence of failure	Relative cost of safety measure		
	Large	Normal	Small
<i>Minor</i> – risk to life is small and negligible economic consequences	3.1	3.7	4.2
<i>Moderate</i> – risk to life is medium and economic consequences are considerable	3.3	4.2	4.4
<i>Large</i> – risk to life is large and economic consequences are significant	3.7	4.4	4.7

Table 6.3. Target reliability for ultimate limit state at 1 year reference period [JCS 00]

6.2.4. Consistency with deterministic and semi-deterministic methods

As mentioned previously, the target reliability can be used in order to calibrate partial factors in a design code that uses the LRFD method, or limit-state design. The typical limit-state equation used in modern design codes is as follows:

$$\phi R_n \geq \sum_{k=1}^i \gamma_k S_{km} \quad [6.6]$$

where the characteristic resistance values are typically reduced by a partial factor ϕ and the characteristic load actions are typically increased by the application of the partial factor γ . As the values of partial factors are derived from probabilistic methods in reference to target reliabilities, codes of practice which use partial factors are said to be probability-based codes or semi-deterministic/probabilistic [VRO 97]. These partial factors are derived using the following general procedure [MEL 99]:

- defining the scope of the code, based on material- or structure-type;
- selecting calibration points by dividing the design space into manageable zones, such as typical structural configurations;
- the existing design code is used to design the elements in all of the manageable zones;
- defining the limit-state functions of the new design code, in terms of the basic variables;
- assigning statistical properties to the basic variables;
- applying the structural reliability method to the defined limit-state functions;
- selecting an appropriate target reliability for each structural configuration, taking into account the consequence of the failure of the element;
- selecting a trial partial factor for each configuration (can be based on previous factors) and calculating safety index. Comparing with target reliability index;
- repeating until all configurations converge to target reliability and define partial factors.

6.3. Second moment transformation and simulation methods

In order to facilitate the broad application of the reliability method, a generalized reliability problem is required to be defined, derived from the load-resistance case presented earlier. However, in most engineering applications, R and S will not comprise single variables but will be a

function of a number of basic variables which contribute the limit-state function. All basic variables can be represented by the vector \mathbf{X} . Now, by expressing the generalized limit-state function as $G(\mathbf{X})$, the failure probability for the joint probability density function $f_{\mathbf{X}}(\mathbf{x})$ can be expressed as:

$$p_f = P[G(\mathbf{X}) \leq 0] = \int \dots \int_{G(\mathbf{X}) \leq 0} f_{\mathbf{X}}(\mathbf{x}) d\mathbf{x} \quad [6.7]$$

In most cases of evaluating the generalized failure probability, the integration of the probability density functions cannot be performed analytically, and must be approximated using appropriate methods, of which the two leading approaches are transformation methods and simulation methods. Using simulation methods, such as Monte Carlo methods, the multidimensional integral can be evaluated. Conversely, transformation methods are used when bypassing the integration is desirable, and the joint probability density function is transformed into a multinormal probability density function, which can be described by its moments. Although often seen to be competing methods, the belief held by some researchers [BJE 90] is that these methods should be seen as complementary, as one method may be more appropriate for a specific problem over another.

It is possible to evaluate the failure probability through direct integration, but only in a limited number of instances, specifically where the limit-state function is linear and all random variables are normally distributed. For this reason, it is largely considered an impractical method to solve the failure probability.

6.3.1. Problem formulation

The first-order second moment (FOSM) method was developed to linearize the nonlinear limit-state function using a Taylor series expansion about a linearization point. The location of this point is best chosen to be the design point, being the point of maximum likelihood. However, it has previously been linearized at the mean values of the random variables, giving rise to the name “mean value first-order second moment” (MVFOSM) method. Moreover, the benefit of this method is that it is easier to locate this point than that of the design point, but does not offer a good

approximation. However, linearizing the surface at the mean leads to an invariance problem, where the analysis of equivalent limit-state functions will result in a disagreement of the reliability indices. To correct this invariance problem, the first-order reliability method (FORM) was developed.

6.3.2. First-order reliability method

FORMs involve transforming non-normal random variables into comparable normal random variables that can be described using their first-order moments. This can be achieved by using methods such as the Rosenblatt [ROS 52] or the approximate Nataf transformations. However, by transforming the random variables, the limit-state function is also transformed, and is usually now represented as a nonlinear function. In order to compute the reliability index, the FORM method requires a linearization of the limit-state surface at a point that provides a better approximation than seen with the MVFOSM method. The linearization is achieved through a Taylor series expansion about a point on the limit – state surface, optimally chosen to be the design point. The prominent computational demand of FORM is through the location of the design point u^* , and methods to locate this point are discussed later on. A generalized algorithm is developed based on the location methods, which is repeated until the solution converges to a point where u^* and β stabilize in terms of value.

This method addresses the invariance problem present using the MVFOSM method by approximating the limit-state surface at a point as opposed to the mean value of the random variables. But, as can be seen, using an expansion method to linearize the limit-state surface becomes less accurate as the level of curvature of this surface increases, and as such, the use of FORM becomes less desirable in these scenarios, in comparison to the use of second-order methods.

6.3.3. Second-order reliability method

Second-order reliability method (SORM) is an extension of FORM, but without the need to linearize the limit-state surface. Instead, a hyperparabolic surface is fitted to the limit-state surface at the location of the design point.

Due to this, SORM is capable of dealing with problems of a higher degree of complexity than FORM, as the method can be extended to highly curved limit-state surfaces.

A number of methods have been proposed to evaluate the failure probability using SORM [DER 87, HOH 88, TVE 90, DER 91], but the simplest implementation of the method involved asymptotic approximations [BRE 84] and multiplied the FORM result by a correction factor:

$$p_f \approx \Phi(-\beta) \cdot \prod_{i=1}^{n-1} \frac{1}{\sqrt{1 + \beta \cdot \kappa_i}} \quad [6.8]$$

As can be seen, the correction factor is a function of the limit-state curvatures, κ_i , at the design point. Thus, the problem reduces to that of determining the curvatures of the limit-state surface.

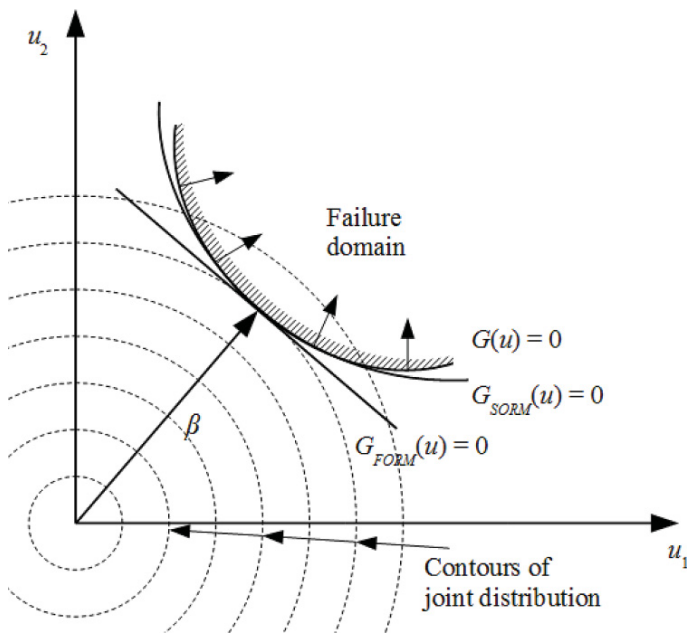


Figure 6.3. FORM linearization and SORM approximation in standard normal space

6.3.4. Monte Carlo simulation for reliability analysis

A direct method to evaluate the probability density integral for the limit-state function is through simulation methods. The use of simulation methods was proposed as an alternative to the high computational demand required for solving through direct integration, and was specifically helpful in solving nonlinear limit-state functions. Monte Carlo simulation involves artificially running a large number of experiments based on the numerical model, with the output being a function of the number of experimental failures observed. When applied to structural reliability, the failure probability is calculated as being the number of instances the limit-state function was violated during the total number of experiments run, N :

$$p_f \approx \frac{n[G(x_i) \leq 0]}{N} \quad [6.9]$$

To evaluate the accuracy of a Monte Carlo simulation, the coefficient of variance of the failure probability δ_{pf} should be checked, and it is defined as:

$$\delta_{pf} = \frac{\sigma_{pf}}{\mu_{pf}} = \sqrt{\frac{1 - p_f}{N \cdot p_f}} \quad [6.10]$$

Values of 2–5% for δ_{pf} are typically deemed to be acceptable. Knowing the acceptable levels of CoV, and having a target reliability index/failure probability, the number of samples required for an acceptable Monte Carlo simulation can be found from the following formula:

$$N = \frac{1}{\delta_{pf}^2} \left(\frac{1 - p_f}{p_f} \right) \quad [6.11]$$

It should be noted that the Monte Carlo simulation method is only a practical alternative method when the number of simulations is less than the number of integration points required for a numerical integration. Additionally, the Monte Carlo simulation can be optimized by sampling in the area of the design point. This greatly improves the efficiency of the method and is referred to as importance sampling. However, a

transformation method, such as FORM, must be conducted in order to locate the design point.

6.3.5. Computational aspects and related software

As can be seen in the formulation of the structural reliability method, there are some special cases where simplified methods can be used to evaluate the level of safety. These problems can be evaluated manually, in conjunction with probability distribution tables, or through the use of widely available spreadsheet applications.

However, due to the high level of computation required for a detailed structural reliability analysis, various software applications have been developed in order to aid the practical implementation of the method. In a study of available products [ELL 06], a number of key considerations have been outlined for the purchase of structural reliability software, namely, the need for a general-purpose application. This is to cater for a wider array of applications so as to maximize the return on investment for a company or institution. However, the consequence of employing broad, general-purpose software is the necessity for users to have a deep understanding of the theoretical framework so that the problem can be effectively modeled [PEL 06], as it is often necessary to break down and simplify the problem into a number of manageable parts. This is in contrast to more specialized software-suites that are often based on input-prompts, where only a rudimentary understanding of the theoretical principles is required to produce an accurate output.

All listed software products include the functionality to generate a reliability index using some or all of the stated computational methods; notably, FORM, SORM and Monte Carlo simulation. In addition, users can use additional advanced methods that are not discussed extensively in this chapter, namely, importance sampling and response surface, explanations of which can be found in many texts on structural reliability. When investing in a structural reliability software package, a company/institution must evaluate what additional requirements it needs or desires from the analysis, namely, the range of output (sensitivity analysis, parameter importance, etc.), probabilistic modeling (random variables, distributions, transformations, etc.) and third-party finite element compatibility.

Additional considerations when selecting appropriate products include operating system (OS) platform, computational demand and an effective graphical user interface (GUI). An attractive GUI, while seemingly a cosmetic function, can often prove crucial for a wider adoption of an unfamiliar method among the employees of companies/institutions. Thus, this is an important point that should always be factored into any decision-making tool used to evaluate potential investment in structural reliability software, and should also be kept firmly in the mind of developers of such software.

Algorithm						
	FORM/SORM	Monte Carlo Simulation	FE Compatibility	Parameter Importance	Direct Differentiation	Design Sensitivity
ANSYS		X		X	X	
CalREL	X	X	X	X		
OpenSees	X	X		X	X	
COSSAN		X	X			
NESSUS	X	X	X	X		X
PEMAS-RA/STUREL	X	X		X		X
PHIMECA	X	X	X	X		
PROBAN	X	X	X	X		
PROFES	X	X	X	X		
UNIPASS	X	X	X	X		

Table 6.4. Comparison of available software applications for reliability [PEL 06]

6.3.6. Practical implementation aspects

As the computational difficulties from the past have been rectified through the development of robust methods and commercially available software applications which implement them, there remains little reason to hinder the widespread application of the structural reliability method. Remaining difficulties include the sufficient education of engineers to be able to fully utilize the method and work with the output. However, as with any advanced numerical method and associated software application, the quality of the input data is of primary importance as small input errors can manifest in large output errors. To effectively model the input variables, the most appropriate probability distribution must be chosen, which will be discussed in the following sections.

6.4. Load and resistance modeling considering uncertainty

It is evident that the purpose of designing a new structure or inspecting an existing structure is to ensure that it is capable of performing its intended task. For engineering structures, this is typically borne by whether the structure has the capacity or resistance to sustain the applied load, in a safe manner. For new structures, this is simply accounted for in adherence to modern design codes, which have a founding in probabilistic methods. However, for existing structures, the prediction of the actual strength of the structure is often determined using imprecise methods. A condition rating is usually assigned to the structure based on the results of the assessment. For many infrastructure networks, these condition ratings are assigned based on the results of a visual inspection alone. For infrastructure managers to make maintenance decisions for a vast network, while operating under budget constraints, this is often seen as an economical approach. However, it must be noted that visual inspections cannot offer information on how a structure is likely to deteriorate over time [FRA 01], therefore, they do not make for a good decision tool when considering future intervention plans. Additionally, visual inspection cannot highlight how an internal material is performing. Thus, in order to effectively allocate future resources for areas of future need, it is necessary to make decision-based methods that make possible the accurate modeling of deterioration.

6.4.1. *Uncertainty modeling*

A benefit of using probabilistic methods in the design and assessment of engineering structures is the ability to adequately account for and model uncertainty in problem. The types of uncertainties typically associated with an engineering problem are [DNV 92]:

- physical uncertainty, which is intrinsically associated with a variable due to naturally occurring randomness in its composition. Efforts to reduce this type of uncertainty can only work to an extent, but it can never be truly eliminated;

- the uncertainty related to measurement and collection of data. This type of uncertainty is usually confined to human error and equipment error, which can be satisfactorily eliminated by calibration to a known state;

- statistical uncertainty, which can arise due to the sample size of information used in an analysis, or an insufficient number of iterations used on a convergence;

- model uncertainty, which is associated with the construction of the analytical solution. This type of uncertainty, in addition to being a function of the other types of uncertainty, is based on decisions made by the engineer, and can increase due to excessive and incorrect simplifications/assumptions made in devising the computational or physical model. Methods to account for this type of uncertainty have been developed to be integrated into the computational model [NKB 78, O'BR 14].

Another source of error in the determination of a computational model is the selection of a probability distribution for the random variables in the problem. It has been shown that curve fitting a distribution to a set of data will often allow the engineer to select a number of seemingly appropriate distributions that possess a similar form or curvature. However, the tails of these distributions are often vastly different and result in widely varying approximations of failure probability. This phenomenon has been termed as the “tail sensitivity problem”, and efforts have been made to reduce this effect by standardizing appropriate probability distributions for load and resistance random variables (Tables 6.5 and 6.6).

Variable type	Unit	Distribution	σ	CoV
Modulus of elasticity	N/mm ²	Normal	—	—
Steel strength (reinforcing steel)	N/mm ²	Lognormal	25	—
Concrete strength	N/mm ²	Lognormal	—	0.12–0.22
Area of steel	mm ²	Normal	—	—
Effective depth	Mm	Lognormal	—	0.05–0.20
Cover to reinforcement	Mm	Lognormal	—	—
Steel strength (prestressed steel)	N/mm ²	Lognormal	—	0.04
Steel strength (structural steel)	N/mm ²	Lognormal	25	0.04–0.07

Table 6.5. Material property distribution models [O'BR 14]

Variable	type	Distribution
Wind	Short-term instantaneous gust speed	Normal
	Long-term n-minute average speed	Weibull
	Extreme speed, yearly	Gumbel
Wave	Short-term instant. Surface elevation (deep water)	Normal
	Short-term heights	Rayleigh
	Wave period	Longuet-Higgins
	Long-term significant wave height	Weibull
	Long-term mean zero upcrossing or peak period	Log-normal
	Extreme height, yearly	Gumbel
Current	Long-term speed	Weibull
	Extreme, yearly	Gumbel
Forces	Hydrodynamic coefficients	Log-normal

Table 6.6. Typical probabilistic load distributions [DNV 92]

6.4.2. Need for resistance modeling

When conducting a reliability analysis, the two fundamental aspects of the limit state need to be modeled: R and S . In the explanation of the method, these were limited to single variables, but in practice each will be represented by its own equation and associated parameters. For this section, material strength is mostly considered, but the variable R can be extended to other applications including, but not limited to, flow capacity of a pipe or river, traffic capacity on a road network, soil cohesion, etc. Additionally, the variables related to the geometry of the structure are typically classified as R variables.

To accurately assess the strength of a material, the inherent variation in material properties needs to be modeled. In general, these properties tend to have variation from point to point, and an appropriate probability distribution should be used when modeling for structural reliability. Using a probability distribution allows the specification of a mean value μ and a standard deviation σ to represent the expected value of the material property and the typical range of variation. In addition to specifying the range of values, the uncertainty surrounding the expectation of these values can also be modeled. Sources for uncertainty in material strength include:

- deviation from sample used in testing;
- level of workmanship during construction;
- how the material will respond to the environment;
- the rate of deterioration for the material.

These sources of uncertainty can often be mitigated through diligent supervision and the refinement of models, and can thus be classified as epistemic, as mentioned in the previous sections. The geometry of the structure is often subject to less uncertainty than the material properties, as the built structure can be measured against what is designed for. In the design phase, uncertainty can be lowered by specifying small tolerance levels, and can be further reduced in the construction phase by competent workmanship and supervision. Due to minimal expected deviation from the mean value, the basic variables related to geometry can often be modeled as fixed or deterministic.

6.4.3. Measurement of resistance variables

In order to gather information about the safety of a structure, the material properties of the resistance material need to be tested against the values used in the design model. This quality control process can be achieved by using two distinct approaches: total testing of the material and sample testing of the material. An example of quality control is the testing of concrete specimens during the construction phase, i.e. a concrete cube/cylinder test.

For total testing, every unit produced is assessed on a pass/fail approach using a non-destructive testing method. This type of testing is analogous to an assembly line product inspection. For sample testing, a series of random samples is taken from the total population of produced units in order to establish a measure of quality, where each unit has an equal chance of being selected for inspection. With regard to structures, sampling efficiency can be improved by limiting the population to areas of interest, such as weak points, critical connections, etc.

6.4.4. Typical loading scenarios

The loads that act on structures are typically categorized into two classes: dead (permanent) and live (variable). Dead loads are those that are inherent to the geometry and composition of the structure, whereas live loading considers loads which are imposed upon the structure. Live loads can occur through human intervention (floor loading, traffic loading, etc.) or due to natural phenomena (wind loading, wave loading, etc.). In this section, wind and wave loadings have been of primary importance. More specialist references can be sought for advanced topics, such as seismic analysis.

6.5. Probabilistic assessment of limit-state violation

In the undertaking of a probabilistic assessment of limit-state violation, the methods used and the modeling of variables can provide inaccuracies when it comes to achieving comparable results. For the successful implementation of the method, the engineer needs to be aware of the limitations of some methods and the pitfalls of others.

6.5.1. Reliability index and probability of failure

For the simple case of an FOSM method, the reliability index can be seen to be equal to the number of standard deviations the mean value lies from the failure surface. It can also be seen to be the least distance from the origin to the limit-state surface in the standardized space. Thus, as the distance from the mean to the failure surface increases, so too does the reliability index, as the failure probability decreases.

The Cornell reliability index β_C is defined as a quotient of an expected value E and an uncertainty parameter D. For structural reliability applications, E can be modeled as the mean value μ of the parameter and D can be modeled as the standard deviation σ of the parameter. So, for the simple R and S scenarios, the Cornell reliability index can be defined as:

$$\beta_C = \frac{E[G]}{D[G]} = \frac{E[R] - E[S]}{\sqrt{\text{Var}[R] + \text{Var}[S]}} = \frac{\mu_R - \mu_S}{\sqrt{\sigma_R^2 + \sigma_S^2}} \quad [6.12]$$

This definition of β_C accounts only for uncorrelated basic variables. For basic variables that possess a degree of correlation, as is often seen, it is necessary to modify β_C as follows [LEM 09]

$$\beta_C = \frac{\mu_Z}{\sigma_Z} = \frac{\mu_R - \mu_S}{\sqrt{\sigma_R^2 + \sigma_S^2 - 2 \text{cov}[R, S]}} \quad [6.13]$$

where $\text{cov}[R, S]$ is the covariance matrix of the basic variables in R and S.

As the simple reliability case of R and S is a basic subtraction problem, it is not feasible to use the previous method to establish reliability indices for variables that are restricted to positive values. For such cases, the FOSM reliability index β_{RE} was developed [ROS 72] by using the logarithms of μ_Z and σ_Z in the evaluation of β . However, this is now a nonlinear limit-statefunction, and so the first two moments cannot easily be determined. As such, the limit-state surface must be linearized in order to compute β . This can be achieved by a Taylor series expansion about one of the expected

values, such as μ . This enables the limit-state function G and reliability function to be rewritten as:

$$\beta_{RE} = \frac{E[\log(R/S)]}{D[\log(R/S)]} \quad [6.14]$$

However, the limit state is now a nonlinear function, and so the first two moments cannot easily be determined. As such, the limit-state surface must be linearized in order to compute β . This can be achieved by a Taylor series expansion about one of the expected values, such as μ . This enables the limit-state function G and reliability function to be rewritten as:

$$G = \log \mu_R - \log \mu_S + \frac{R - \mu_R}{\mu_R} - \frac{S - \mu_S}{\mu_S} \quad [6.15]$$

$$\beta = \frac{\log \mu_R - \log \mu_S}{\sqrt{V_R^2 + V_S^2}} \quad [6.16]$$

In 1974, it was proposed to map the basic variables into an uncorrelated standard space, and evaluate the reliability index as the least distance from the origin of this space to the failure surface, defined by the limit-state function [HAS 74]. This gave rise to what is now considered the design point.

6.5.2. The concept of the design point

The point on the limit-state surface that satisfies the condition of being minimum distance from the origin is called the design point, and is the point of maximum likelihood for the failure domain by having the greatest probability density. This point is generally used when conducting reliability studies using FORM and SORM methods, as it is seen to be the optimum location for a linear expansion for nonlinear limit-state surfaces.

Previously, the mean point was used for the expansion point in the linearization, but using this method resulted in an invariance problem where equivalent limit states output different reliability indices.

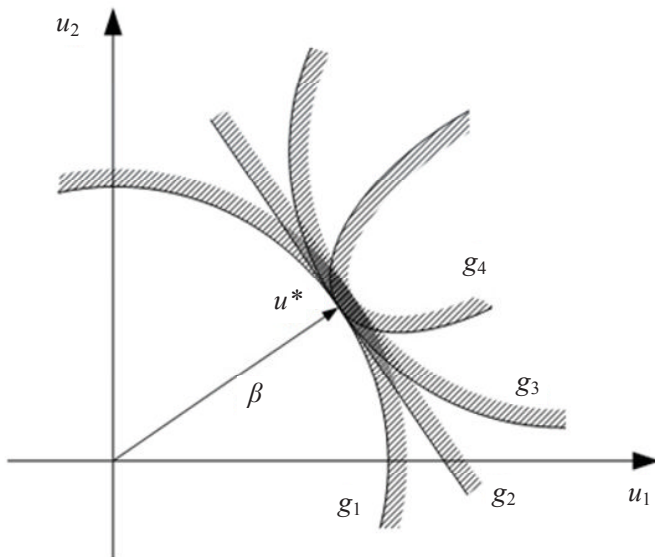


Figure 6.4. Common reliability index for differing limit states

As the design point was shown to be the optimum position for approximating the limit-state surface, a method was needed to be developed to locate this point. Many methods have been investigated to efficiently find the design point [LIU 91]: the gradient projection method, the penalty method, the augmented Lagrangian method, the sequential quadratic programming method and the Hasofer-Lind and Rackwitz-Fiessler (HL-RF) method [HAS 74, RAC 78]. The most widely used algorithm to find the design point was the iterative HL-RF method, defined by the formula:

$$u_{i+1} = \left[\frac{G(u_i)}{\|\nabla G(u_i)\|} + \alpha^T u_i \right] \alpha \quad [6.17]$$

where \$\alpha^T\$ is the transpose of \$\alpha\$, and every successive iteration, \$i+1\$, is a function of the previous iteration \$i\$. Starting from an initial expansion point, taken to be the mean value for convenience, the refined expansion point is computed using the above formula. This is repeated until the location of the design point and the reliability index stabilizes. However, this method had demonstrated a convergence problem under certain circumstances, and modifications were proposed to rectify this computation issue. The most

popular modification is by introducing a line search along a directional vector, d . This can be seen as an expansion on the gradient projection method, with the improvement that the initial checking point does not need to be located on the limit-state surface.

A significant issue with using the design point as the estimate for the reliability index, and thus failure probability, is the problem of nonlinear failure surfaces that exhibit a high degree of convexity with which it is endowed. As can be seen in Figure 6.4, four limit-state functions are presented which are of different forms but possess the same design point and reliability index. However, it is obvious that the failure probability of g_1 is much more significant than that of g_4 , which seems to have an outlying critical level as opposed to g_1 which exhibits a near constant critical level. The understanding of this pitfall is a mitigation of the negative effects that it can have on the reliability evaluation. A procedure was proposed by Ditlevsen [DIT 79a] to rectify this issue by introducing a weighting factor ψ into the normal probability density function. The use of this method is said to provide a more robust selection of the reliability index than the HL index for nonlinear failure surfaces.

6.5.3. Sensitivity studies

The parametric sensitivity is the measure of change of the reliability index due to perturbations in the basic variables [HOH 86, MAD 86]. When a parameter θ is changed in the limit-state equation, the original failure surface $g(u,\theta) = 0$ is subject to change as a function of θ . With a new failure surface $g(u,\theta + d\theta) = 0$, the design point u^* is relocated from its original position to $u^* + du^*$ (Figure 6.5). The location of the new design point can be related to the original position through the unit directional vector α and its infinitesimal orthogonal increment $d\alpha$ [BJE 89].

$$\frac{d\beta}{d\theta} = \alpha^T \frac{du^*}{d\theta} = \frac{1}{|\nabla g(u^*)|} \frac{\partial g}{\partial \theta} \quad [6.18]$$

It should be noted that a positive α -value corresponds to a load variable and a negative α -value corresponds to a resistance variable. A variable with a large α -value is considered to be stochastically important, and attention should be paid to such a variable in the design of an assessment

stage, with all efforts to reduce uncertainty surrounding the variable to be employed.

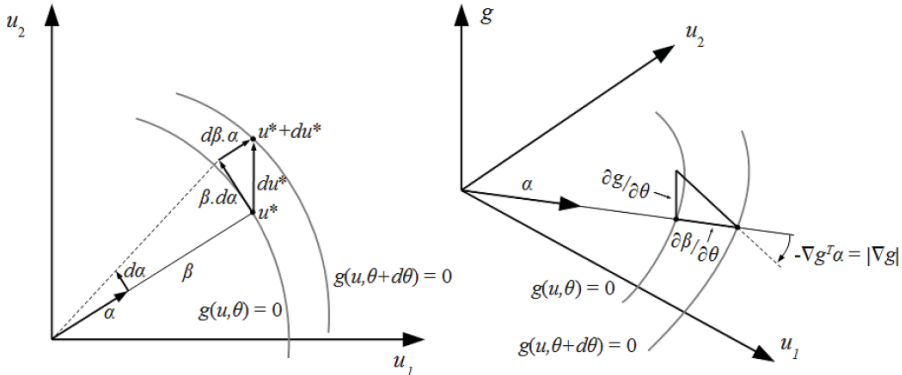


Figure 6.5. Illustration of parametric sensitivity [BJE 89]

The omission sensitivity factor γ is the measure of error for when a variable is modelled as deterministic rather than stochastic [MAD 88] and is defined as the inverse ratio between the reliability index and the corresponding value with one basic variable replaced by a deterministic value. For variables with very low omission sensitivities, it is often prudent to remodel the variable as deterministic so as to reduce the dimensionality of the space of random variables. The opposite of the omission sensitivity is the ignorance sensitivity, and it is the measure of error if a deterministic variable is treated as stochastic [DER 94].

6.5.4. Parameter importance measures

An important aspect of the output from a reliability analysis is the parameter importance measures, which highlight the model parameters that have the greatest level of influence on the level of structural safety. These measures have great practical significance as they allow for the optimization of resource allocation. This optimization can be found by prioritizing inspections to critical components in existing structures, and in the design/construction phase where a greater level of attention can be paid to the same.

6.6. Component versus system reliability

Further to the fundamentals of reliability methods outlined in the previous sections, it is possible to extend these methods to the assessment of a structural system. A structural system refers to the various limit states associated with a structure, and how they apply to the multitude of structural elements that a structure is typically constituted of. While previously the concept of structural reliability had been confined to the consideration of singular elements under a lone limit state, the ability to evaluate the safety of a structure as a whole and under multiple limit states can be undertaken by adopting a system reliability approach.

6.6.1. Network requirements

When considering system reliability events, two complementary approaches are used: the evaluation of failure modes and survival modes. For the portal frame in Figure 6.6, the failure modes are identified and represented in a fault tree, composed of events and subevents.

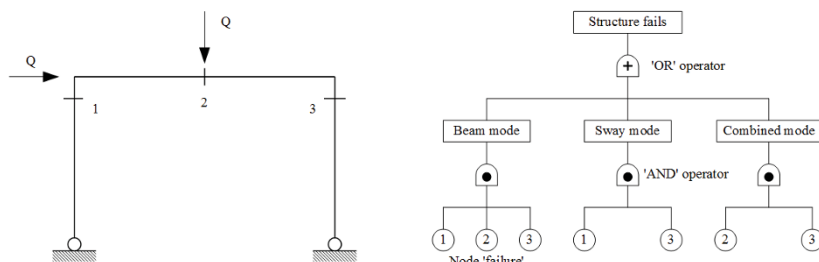


Figure 6.6. Fault tree representation [MEL 99]

The failure mode approach to this problem is to examine all the ways in which the structural system will fail, and the events required for failure to occur. A way of representing this approach is the use of an event tree or failure graph (Figure 6.7), where each branch represents a member of the frame and any complete path through the tree of graph represents a sequence of failure. The use of the failure mode approach is conceptually convenient to visualize, but can be considered a lower bound approach as a significant source of error is the overlooking of a single mode of failure. The survival mode approach, on the other hand, can be considered an upper bound

approach as it involves identifying the number of ways in which the structure will not fail. Therefore, any error in identifying a survival mode will not be considered critical. However, the difficulty of this method involves conceptualizing the number of ways in which a structure will not fail.

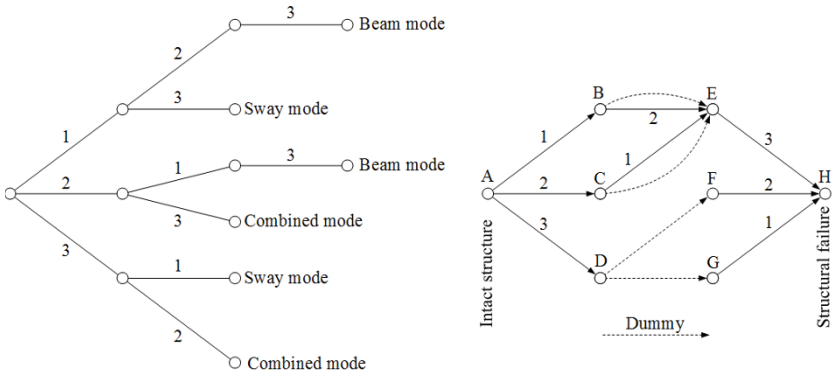


Figure 6.7. Event tree and failure graph

6.6.2. Illustration of component and system reliability

The reliability of a structural system is likely to be a function of the reliability of its members [MEL 99] due to load combinations, dependent variables, etc. Two fundamental categories are used to describe structural systems in general: series system and parallel system. The series system can most appropriately be imagined as a chain, whereby the system of the chain is deemed to have failed if only a single link undergoes failure. This is analogous to a statically determinate structure that fails when a lone element/component fails. From a statistical perspective, a series system failure is representative of the union of multiple failure events. Additionally, it is analogous to the case when a component fails upon violating a single limit state.

$$p_f = P \left[\bigcup_{k=1}^K (G_k(X) \leq 0) \right] = \int_{D \in X} \dots \int f_X(x) dx \quad [6.19]$$

where K is the number of limit states in the system and D is the failure domain in a series system. The parallel system is defined as one in which a

structural system does not fail after a single component failure, or only fails after all the limit-state functions have been violated.

$$p_f = P \left[\bigcap_{k=1}^K (G_k(X) \leq 0) \right] = \int_{D_I \in X} \dots \int f_X(x) dx \quad [6.20]$$

where D_I is the failure domain in a parallel system. This is analogous to a statically indeterminate structure, and is seen to be in the intersection of multiple failure events. However, it is unlikely that a real structure would be singly classified as one of the above systems, and therefore most structures can be classified using the hybrid definitions of a series system of parallel systems or a parallel system of series systems [DIT 96].

$$p_f = P \left[\bigcup_{m=1}^M \bigcap_{j \in c_m} (G_j(x) \leq 0) \right] \quad [6.21]$$

where M is the number of parallel sets and c_m is the number of cut sets. In order to adequately analyze a structural system, it needs to be idealized so as to be able to simply model the load, nature of the resistance and connections between the individual components.

6.6.3. Methods of estimating system reliability from component reliability

Most of the time, due to the complexity of a structural system, it is necessary to reduce the reliability problem down to a more manageable size. One of the methods of achieving this simplification is by introducing cut sets into the problem. A cut set is any combination of components whose joint failure would cause overall system failure. Once the cut sets are identified, the set which contains the minimum number of components is highlighted as being the most critical, i.e. the minimal cut set is the smallest combination of events that bring about an undesirable outcome.

As the complexity of a structural system increases, it often becomes necessary to simplify the problem into its fundamental components. A method of achieving this is to consider the state of the structural system in

terms of the states of its elements i [MAD 86]. This can be accomplished by introducing Boolean operators as state indicator variables a_i :

$$a_i = \begin{cases} 1 & \text{if element } i \text{ is functioning} \\ 0 & \text{if element } i \text{ is failing} \end{cases}, \quad i = 1, \dots, n \quad [6.22]$$

where n is the number of elements in the structure. This concept is extended to the overall structural system a_S by the inclusion of the structure function φ for the individual elements.

$$a_S = \varphi(a), \quad a = (a_1, \dots, a_n) \quad [6.23]$$

For a series system, the structure function φ_S is defined as:

$$\varphi_S(a) = \prod_{i=1}^n a_i = \min \{a_1, \dots, a_n\} \quad [6.24]$$

The product operator \prod is used to represent the “weakest link” nature of a series system. On the other hand, a parallel system requires all elements to fail; so the structure function φ_P is defined as:

$$\varphi_P(a) = 1 - \prod_{i=1}^n (1 - a_i) = \max \{a_1, \dots, a_n\} \quad [6.25]$$

Finally, the structure function for a hybrid system, or a k -out-of- n system, is defined as:

$$\varphi_K(a) = \begin{cases} 1 & \text{if } \sum_{i=1}^n a_i \geq k \\ 0 & \text{otherwise} \end{cases} \quad [6.26]$$

For this type of system, the structure is said to be in a functioning state if k out of the n elements in the system are functioning, and is associated with the previously discussed series system of parallel systems or the parallel system of series systems. A common example of such a system is a multi-strand cable.

In order to implement the above system into a complete structural system, it is often necessary to define cut sets or path sets. These sets describe the events which need to occur to constitute a functioning system or a failing system; the path set defines all the elements which need to function in order for the system to function and the cut set defines all the elements which need to fail for the system failure to occur. Each of these sets has an associated minimal set which enables them to define the overall system, using the previously introduced terminology; a parallel system of minimal series path sets and a series system of minimal parallel cut sets [MAD 86]. Therefore, it is apparent that the cut set can be seen that the cut set can be seen as a lower bound estimation of the structural condition, and the path set can be seen as an upper bound estimation of the structural condition, resulting in the expression:

$$\prod_{i=1}^C \kappa_i(a) \leq \hat{\phi}(a) \leq 1 - \prod_{j=1}^P [1 - \rho_j(a)] \quad [6.27]$$

where κ_i is the structure function for the minimal parallel cut set, ρ_j is the structure function for the minimal series path set, and C and P are the number of minimal cut sets and path sets, respectively.

6.6.4. Practical implementation aspects

Classification of brittle or ductile is crucial in the analysis of a structural system. Brittle failure is more critical as the component that experiences brittle failure is no longer capable of carrying any load. For a structural system with low statically indeterminacy, the brittle failure of a component in a parallel system often behaves as failure of a component in a series system [THO 82].

Due to the often complex nature of a full integration of the failure probability, it is often desirable to introduce bounds to the problem which define a lower and upper p_f for a structural system. The two main classifications of bounds for system analysis are first-order/simple bounds and second-order/Ditlevsen bounds [DIT 79b].

6.7. Time-dependent reliability

6.7.1. Concept of time dependence

A powerful application of the structural reliability method is the ability to perform a time-dependent reliability analysis, whereby the reliability of a structure can be predicted at a certain point in time in the future, or over a specific time interval. This is often necessary when considering a lifecycle approach to the design or assessment of structures, as the condition of a structure is likely to vary with time. Advanced applications of the method concern the evaluation of fatigue effects or the dynamic application of loads, but more fundamental topics are concerned with changes in the basic variables which govern the limit-state equations. In a typical example of the life of a structure, it is often observed that the structural resistance decreases over time due to destructive processes such as corrosion, section loss, etc., and the applied load often increases due to increased demand or unfavorable change of use. Thus, the relevant basic variables can be considered as functions of time and that the structural reliability decreases with time, typically. It should be noted that factors which improve the lifetime reliability include structural strengthening or favorable change of use.

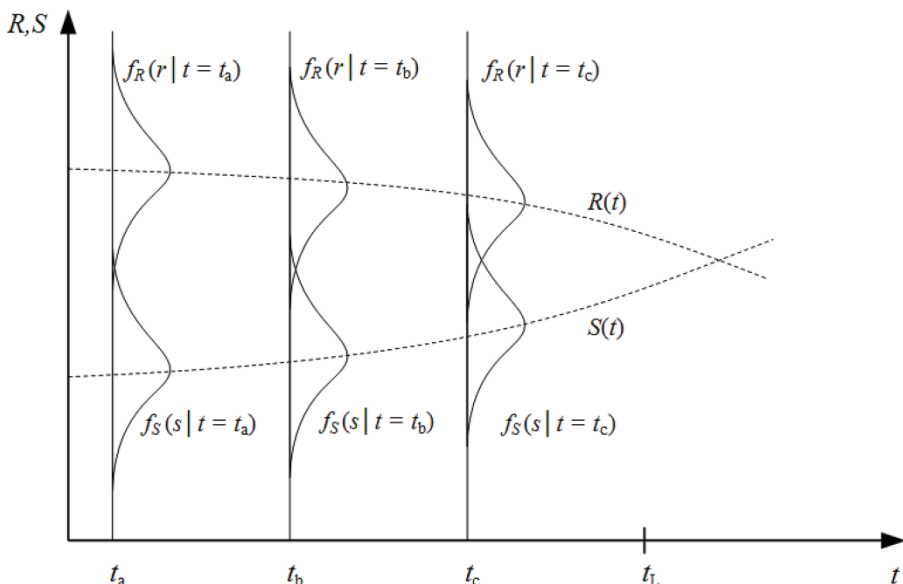


Figure 6.8. General time-dependent reliability problem

6.7.2. Handling time dependency in reliability analysis

The time-dependent reliability model extends the fundamental model previously discussed by introducing the time function t .

$$p_f(t) = P[R(t) \leq S(t)] \quad [6.28]$$

$$p_f(t) = \int_{G[X(t)] \leq 0} f_{X(t)}[x(t)] dx(t) \quad [6.29]$$

Using the above equations, the failure probability can be calculated for a specific time t or can be evaluated as the probability of failure occurring over a time period ending at t . To achieve this, integrate the above over the bounds 0 (now) to t . This time period can be defined to be the life of the structure, with the bound t_0 to t_L . It is also possible to evaluate the first instance where the load exceeds the resistance, or when $S(t)$ “crosses” $R(t)$. The evaluation of this point, known as the upcrossing point or barrier crossing point, is done using stochastic process theory, which is discussed in greater detail in specialist textbooks [MEL 99].

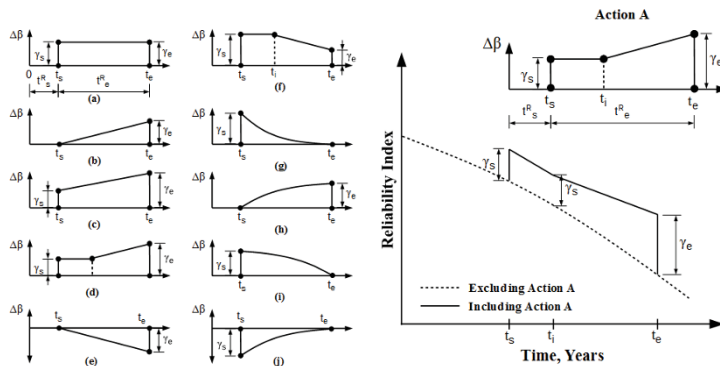


Figure 6.9. Various action-based reliability index profiles and their effect on existing reliability profiles [KON 03]

From a time-dependent reliability assessment, a reliability index profile can be created over a period of time [KON 03]. This profile plots the change in reliability index β over time due to degradation and completed intervention actions. The new profile is obtained by superimposing the profile of expected degradation or interventions onto the existing profile obtained from a time-dependent reliability assessment (Figure 6.9).

$$\beta_j(t) = \beta_{j,o}(t) + \sum_{i=1}^n \Delta\beta_{j,i}(t) \quad [6.30]$$

where $\Delta\beta_{j,i}(t)$ is the additional reliability index profile generated by the action, i , and n is the number of actions associated with the failure mode j during the lifetime. Actions associated with a value for $\Delta\beta$ greater than unity are those that positively contribute to the structural safety; examples of this include maintenance activities or physical effects, such as concrete hardening. Conversely, values for $\Delta\beta$ less than unity are those that negatively contribute to structural safety, examples of which are degradation over time or sudden effects, such as damage from an impact load. This is useful for performance-based design as it enables the evaluation of how much damage a structure can sustain at a single point in time before becoming critically unsafe.

This method can be extended to the evaluation of the structural system by combining these profiles for all components/limit states.

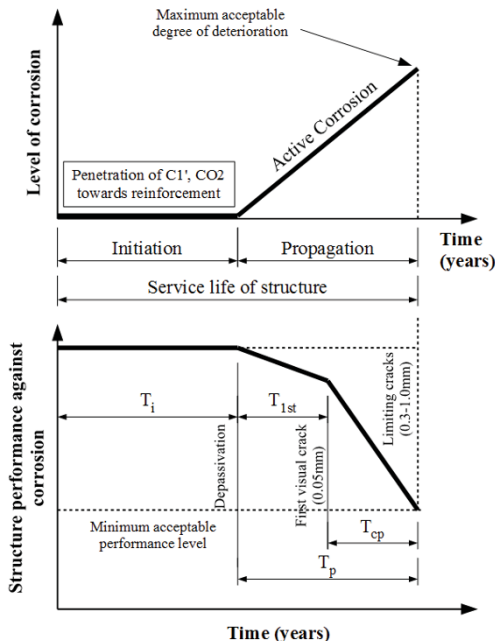


Figure 6.10. Typical process of reinforced concrete deterioration [KEN 09]

6.7.3. Time-dependent deterioration modeling

The use of time-dependent reliability assessment facilitates the prediction of future performance by including information obtained from future deterioration modeling of the structure. In this section, we will consider the chloride-induced deterioration of a reinforced concrete structure under the three main phases of deterioration: time to corrosion initiation T_i , time to crack initiation T_{1st} and time to crack propagation T_{cp} [KEN 09].

Chloride-induced corrosion is among the most widespread deterioration mechanisms for reinforced concrete structures, and its presence is typically indicated by the cracking of the concrete cover to reinforcement [O'BR 14]. This occurs due to the expansive nature of corrosion inducing a tensile stress in the concrete surrounding the reinforcing bars. The time at which corrosion will first occur, T_i , can be determined by Fick's second law of diffusion:

$$T_i = \frac{C^2}{4D_{app}} \left[\operatorname{erf}^{-1} \left(\frac{C_s - C_{cr}}{C_s} \right) \right]^{-2} \quad [6.31]$$

where D_{app} is the apparent diffusion coefficient (mm^2/year), C_s is the surface chloride concentration (% per weight of cement or concrete), C_{cr} is the critical chloride concentration (% per weight of cement or concrete) and C is the concrete cover (mm). The time (years) from this initiation of corrosion to the first instance of cracking T_{1st} can be determined from a number of numerical models, such as [EL 07]:

$$T_{1st} = \left[\frac{7117.5(D + 2\delta_o)(1 + \nu + \psi)}{i_{corr}E_{ef}} \right] \left[\frac{2Cf_{ct}}{D} + \frac{2\delta_o E_{ef}}{(1 + \nu + \psi)(D + 2\delta_o)} \right] \quad [6.32]$$

where D is the diameter of the steel rebar (mm), δ_o is the thickness of the porous zone around the steel bar which will have to be filled before the tensile stresses can be generated (mm), ψ is a factor dependent on D , C and δ_o , i_{corr} is the corrosion rate density ($\mu\text{A}/\text{cm}^2$), E_c and E_{ef} are the elastic modulus of concrete and the effective elastic modulus of concrete, respectively, ϕ_{cr} is the creep coefficient, ν is the Poisson ratio for concrete and f_{ct} is the tensile strength of the concrete. In the final phase of chloride-induced corrosion, the time (years) from the first instance of hairline cracking to maximum allowable cracking is [VU 05]:

$$T_{cp} = 0.0167 t_{corr}^{-1.1} \left[42.9 \left(\frac{wc}{C} \right)^{-0.54} + \left(\frac{w_{lim} - 0.3}{0.0062} \right)^{1.5} \right] \quad [6.33]$$

where wc is the water/cement ratio and w_{lim} is the maximum crack size. The ability to be able to determine the time in which the structure is expected to develop critical cracking enables a more accurate estimation of the future reliability of the overall structure. In addition to modeling this critical crack propagation, it is also possible to account for the expected loss of an effective reinforcement area in a time-dependent reliability model. Two models for reinforcement section loss are often considered: uniform corrosion and pitting corrosion, for which numerous methodologies exist for the calculation of section loss [AND 93, VAL 97]. As section loss increases, the structural capacity of critical structural elements is compromised and the reliability of structure is also compromised. This section loss can be modeled using the stochastic methods mentioned previously.

6.8. Conclusion

In this chapter, a performance-based approach for the design and assessment of structures was presented through the implementation of the probabilistic reliability method. The basis of the method was explained and shown to be present in modern structural design codes of practice. The rationale behind the use of this method is how it enables the stochastic modeling of variables in the limit-state design, which is more reflective of actual structural realization than the standard deterministic approach. The various reliability methods used to compute the safety classification of structures were shown, along with the evaluation of software applications which implement the method. Additionally, guidance was provided regarding which method should be chosen in response to the requirement of the structure.

The modeling of the basic variables for load and resistance was presented, and the sensitivity of the method to input parameters was highlighted, along with the potential advantageous byproducts of using the method, such as parametric sensitivity and parameter importance measures. More advanced concepts were presented on system reliability and time-dependent reliability.

It can be concluded that the reliability method is a powerful tool in the assessment of structural safety and performance, and greatly exceeds the limitations of the standard deterministic method. The practical hindrances to the widespread adoption of the method have been resolved in the development of software applications and the continued efforts to improve the robustness of the method. Furthermore, it has been shown that adoption of the method by infrastructure network managers can lead to a better framework, which can help assess the needs of the network and improve the allocation of resources.

6.9. Bibliography

- [AND 93] ANDRADE C., ALONSO C., MOLINA F.J., “Cover cracking as a function of bar corrosion. Part I: experimental test”, *Materials and Structures*, vol. 26, no. 8, pp. 453–464, 1993.
- [ANG 06] ANG A.H.-S., TANG W.H., *Probability Concepts in Engineering Planning and Design: Emphasis on Applications in Civil and Environmental Engineering*, 2nd ed., Wiley, 2006.
- [BJE 89] BJRAGER P., KRENK S., “Parametric sensitivity in first order reliability theory”, *Journal of Engineering Mechanics*, vol. 115, no. 7, pp. 1577–1582, 1989.
- [BJE 90] BJRAGER P., “On computation methods for structural reliability analysis”, *Structural Safety*, vol. 9, no. 2, pp. 79–96, 1990.
- [BRE 84] BREITUNG K., “Asymptotic approximations for multinormal integrals”, *Journal of Engineering Mechanics*, vol. 110, no. 3, pp. 357–366, 1984.
- [BUC 94] BUCHER C.G., SCHUËLLER G.I., “Software for reliability-based analysis”, *Structural Safety*, vol. 16, nos. 1–2, pp. 13–22, 1994.
- [CAS 14] CASTILLO E., O’CONNOR A.J., NOGAL M. *et al.*, “On the physical and probabilistic consistency of some engineering random models”, *Structural Safety*, vol. 51, pp. 1–12, 2014.
- [CEN 02] CEN, EN 1990 - Eurocode: Basis of structural design, European Committee for Standardization, Brussels, Belgium, 2002.
- [COR 69] CORNELL C.A., “A probability-based structural code”, *American Concrete Institute Journal Proceedings*, vol. 66, no. 12, pp. 974–985, 1969.
- [DER 87] DER KIUREGHIAN A., LIN H.S., HWANG S.-J., “Second-order reliability approximations”, *Journal of Engineering Mechanics*, vol. 113, no. 8, pp. 1208–1225, 1987.

- [DER 91] DER KIUREGHIAN A., DESTEFANO M., “Efficient algorithm for second-order reliability analysis”, *Journal of Engineering Mechanics*, vol. 117, no. 12, pp. 2904–2923, 1991.
- [DER 94] DER KIUREGHIAN A., ZHANG Y., LI C.C., “Inverse reliability problem”, *Journal of Engineering Mechanics*, vol. 120, no. 5, pp. 1154–1159, 1994.
- [DER 09] DER KIUREGHIAN A., DITLEVSEN O., “Aleatory or epistemic? Does it matter?”, *Structural Safety*, vol. 31, no. 2, pp. 105–112, 2009.
- [DIT 79a] DITLEVSEN O., “Generalized second moment reliability index”, *Journal of Structural Mechanics*, vol. 7, no. 4, pp. 435–451, 1979.
- [DIT 79b] DITLEVSEN O., “Narrow reliability bounds for structural systems”, *Journal of Structural Mechanics*, vol. 7, no. 4, pp. 453–472, 1979.
- [DIT 82] DITLEVSEN O., “Model uncertainty in structural reliability”, *Structural Safety*, vol. 1, no. 1, pp. 73–86, 1982.
- [DIT 86] DITLEVSEN O., BJERAGER P., “Methods of structural systems reliability”, *Structural Safety*, vol. 3, nos. 3–4, pp. 195–229, 1986.
- [DIT 96] DITLEVSEN O., MADSEN H.O., *Structural Reliability Methods*, Wiley, vol. 178, 1996.
- [DNV 92] DNV, Classification notes – no. 30.6: structural reliability analysis of marine structures, Det Norske Veritas, Norway, 1992.
- [EL 07] EL MAADDAWY T., SOUDKI K., “A model for prediction of time from corrosion initiation to corrosion cracking”, *Cement and Concrete Composites*, vol. 29, no. 3, pp. 168–175, 2007.
- [ELL 82] ELLINGWOOD B., GALAMBOS T.V., “Probability-based criteria for structural design”, *Structural Safety*, vol. 1, no. 1, pp. 15–26, 1982.
- [ELL 94] ELLINGWOOD B., “Probability-based codified design: past accomplishments and future challenges”, *Structural Safety*, vol. 13, no. 3, pp. 159–176, 1994.
- [ELL 96] ELLINGWOOD B., “Reliability-based condition assessment and LRFD for existing structures”, *Structural Safety*, vol. 18, nos. 2–3, pp. 67–80, 1996.
- [ELL 06] ELLINGWOOD B., “Structural safety special issue: general-purpose software for structural reliability analysis”, *Structural Safety*, vol. 28, nos. 1–2, pp. 1–2, 2006.
- [FRA 01] FRANGOPOL D., KONG J., GHARAIBEH E., “Reliability-based life-cycle management of highway bridges”, *Journal of Computing in Civil Engineering*, vol. 15, no. 1, pp. 27–34, 2001.

- [HAS 74] HASOFER A.M., LIND N.C., “Exact and invariant second-moment code format”, *Journal of the Engineering Mechanics Division*, vol. 100, no. 1, pp. 111–121, 1974.
- [HOH 86] HOHENBICHLER M., RACKWITZ R., “Sensitivity and importance measures in structural reliability”, *Civil Engineering Systems*, vol. 3, no. 4, pp. 203–209, 1986.
- [HOH 88] HOHENBICHLER M., RACKWITZ R., “Improvement of second-order reliability estimates by importance sampling”, *Journal of Engineering Mechanics*, vol. 114, no. 12, pp. 2195–2199, 1988.
- [JCS 00] JCSS, Probabilistic model code, part 1 – basis of design, Joint Committee on Structural Safety, Denmark, 2000.
- [KEN 09] KENSHEL O., O’CONNOR A., “Assessing chloride induced deterioration in condition and safety of concrete structures in marine environments”, *Revue Européenne de Génie Civil*, vol. 13, no. 5, pp. 593–613, 2009.
- [KON 03] KONG J., FRANGOPOL D.M., “Life-cycle reliability-based maintenance cost optimization of deteriorating structures with emphasis on bridges”, *Journal of Structural Engineering*, vol. 129, no. 6, pp. 818–828, 2003.
- [LEMAIRE 09] LEMAIRE M., *Structural Reliability*, ISTE Ltd., London and John Wiley and Sons, New York, 2009.
- [LIU 91] LIU P., DER KIUREGHIAN A., “Optimization algorithms for structural reliability”, *Structural Safety*, vol. 9, no. 3, pp. 161–177, 1991.
- [MAD 86] MADSEN H.O., KRENK S., LIND N.C., *Methods of Structural Safety*, Dover Publications, 1986.
- [MAD 88] MADSEN H.O., “Omission sensitivity factors”, *Structural Safety*, vol. 5, no. 1, pp. 35–45, 1988.
- [MEL 99] MELCHERS R.E., *Structural Reliability Analysis and Prediction*, 2nd ed., Wiley, 1999.
- [NKB 78] NKB, Guidelines for loading and safety regulations for structural design, Report No. 36, Nordic Committee for Building Structures, Copenhagen, Denmark, 1978.
- [O’BR 14] O’BRIEN E.J., KEOUGH D.L., O’CONNOR A.J., “Probabilistic assessment of bridge safety”, *Bridge Deck Analysis*, 2nd ed., CRC Press, 2014.
- [PAK 12] PAKRASHI V., O’CONNOR A., SALTA M., “Assessment and maintenance planning for infrastructure networks”, *Transportation Research Board (TRB) Annual Meeting*, 2012.

- [PEL 06] PELLISSETTI M., SCHUËLLER G., “On general purpose software in structural reliability – an overview”, *Structural Safety*, vol. 28, nos. 1–2, pp. 3–16, 2006.
- [RAC 78] RACKWITZ R., FLESSLER B., “Structural reliability under combined random load sequences”, *Computers & Structures*, vol. 9, no. 5, pp. 489–494, 1978.
- [ROS 52] ROSENBLATT M., “Remarks on a multivariate transformation”, *The Annals of Mathematical Statistics*, vol. 23, no. 3, pp. 470–472, 1952.
- [ROS 72] ROSENBLUETH E., ESTEVA L., “Reliability basis for some Mexican Codes”, *ACI Publication SP-31*, pp. 1–41, 1972.
- [RAC 78] RACKWITZ R., FLESSLER B., “Structural reliability under combined random load sequences”, *Computers & Structures*, vol. 9, no. 5, pp. 489–494, 1978.
- [THO 82] THOFT-CHRISTENSEN P., BAKER M.J., *Structural Reliability Theory and Its Applications*, Springer, 1982.
- [TVE 88] TVEDT L., “Second order reliability by an exact integral”, in THOFT-CHRISTENSEN P. (ed.), *Reliability and Optimization of Structural Systems'88*, Springer, London, pp. 377–380, 1988.
- [TVE 90] TVEDT L., “Distribution of quadratic forms in normal space, applications to structural reliability”, *Journal of Engineering Mechanics*, vol. 116, no. 6, pp. 1183–1197, 1990.
- [VAL 97] VAL D.V., MELCHERS R.E., “Reliability of deteriorating RC slab bridges”, *Journal of Structural Engineering*, vol. 123, no. 12, pp. 1638–1644, 1997.
- [VRO 97] VROUWENVELDER T., “The JCSS probabilistic model code”, *Structural Safety*, vol. 19, no. 3, pp. 245–251, 1997.
- [VU 05] VU K.A.T., STEWART M.G., “Predicting the likelihood and extent of reinforced concrete corrosion-induced cracking”, *Journal of Structural Engineering*, vol. 131, no. 11, pp. 1681–1689, 2005.
- [WEN 01] WEN Y., “Reliability and performance-based design”, *Structural Safety*, vol. 23, no. 4, pp. 407–428, 2001.
- [ZHA 99] ZHAO Y., ONO T., “A general procedure for first/second-order reliability method (FORM/SORM)”, *Structural Safety*, vol. 21, no. 2, pp. 95–112, 1999.

Coastal Protection Degradation Scenarios

This chapter is dedicated to the systems of protection against marine floods and, more particularly, it concerns earth fill or mixed dikes which constitute the major part of these protections. After a reminder of the structure and functions of dikes, the main failure modes are described and illustrated through feedback on recent experiences. This chapter is widely based on the synthesis of a French workgroup on dikes set up by the Ministry of Ecology [POU 15].

7.1. Functions and types of coastal dikes

A coastal dike is a linear structure that rises above the surrounding ground and that belongs to a protection system that protects against flooding by the sea or the ocean. Along with other protection structures, it protects floodable areas against submersion. Its main protective function is ensured by the system taken as a whole. Natural elements can also be used in the protection system (mounds, marshes, sand dunes, rocky outcrops, etc.). A flood protection dike can sometimes be incorporated in a more global coastal development program (navigation, tourism, etc.)

In principle, the dimensions of a dike are consistent with the entire protection project for a location. These dimensions are determined by specific studies. Regarding most historic structures, it is difficult to know for which event they have been dimensioned; generally, constructions have been designed to resist the most considerable known phenomena (sea levels and

Chapter written by Daniel POULAIN and Rémy TOURMENT.

wave heights) with a given safety “margin”. If a change occurs to the system’s environment (frequency of storms, landslide, rise of sea level, etc.), it may be necessary to modify the level of protection provided by the system.

To fulfill its function within the system, the dike can act in two different ways:

- it can prevent the passage of water by holding it outside the protected area (the main function of a flood protection dike);
- it can limit the volumes and/or flow rates of overflows and overtopping.

According to the environment in which it is located, a coastal dike can be:

- alternatively dry and under load (mainly in the presence of tides);
- mostly dry and under load only during episodes of large high tides and/or storms;
- permanently in water (wholly or partially).

Generally, coastal dikes in France are hydraulic structures of low height (<6 m) on natural ground and of great length (several kilometers or more).

7.1.1. Main types of dikes

Most dikes are earth fill structures (ranging from silt to sand, and sometimes even gravel). Their composition can be explained mainly by the history of their construction and geographic position.

Furthermore, different types of fill can be used to play the role of a dike, without them being initially intended for this purpose. This is the case of certain road fills (two functions) and railway fills, as well as of the ramparts used to protect towns. In these cases, it is difficult to identify an owner or manager. Their design, monitoring and maintenance are not always suitable. On the contrary, many structures initially designed as dikes are used as platforms for roads and railways. In both cases, it is important to ensure that these superposed uses are compatible with each other.

The sketches in this section do not constitute models of the design of dikes, but illustrations of various types of dikes with examples of different components; in particular the dimensions are not realistic. The real dikes are constituted by all or part of the elements represented on these sketches. These sketches are adapted from [ILH 13].

7.1.1.1. *Historical fill*

“Homogeneous due to its heterogeneity”.

These structures have often been built in steps over several periods as a function of protection needs. The more steps there are in the construction of a dike, the more complex its structure. Their complex construction is often synonymous with considerable heterogeneity within the same section. This heterogeneity makes an analysis of the dike's safety level difficult given the multitude of possible scenarios leading to failure and given the considerable uncertainties regarding the mechanisms involved.

It is often difficult to qualify one's structures and identify their weak zones. However, it is the junctions, when they can be identified, which usually constitute the weak points. The transitions between layers with sometimes slightly heterogeneous materials that have been unevenly compacted and having incompatible grain sizes can favor the harmful internal concentration flow of water.

For such structures, it is necessary to have available good quality archives as they facilitate their characterization and regular diagnostics.

7.1.1.2. *Homogeneous fill*

Homogeneous earth fill dikes are made up of compacted fill (or fill consolidated over time). The core of the fill is composed of a homogeneous soil generally found on site (clay or silt) that is sufficiently impermeable to prevent infiltrations. The covering layer ensures mechanical protection and acts as a filter by preventing the removal of fine material from inside the dike. In this case, the functions of imperviousness and stability are ensured by the same component (the core).

The materials used in the same dike system can vary considerably, though in a single section, the fill is generally homogeneous without zoning and specific internal drainage systems. The geotechnical characterization of

such materials can be difficult and requires precautions. Since old dikes were built without the use of heavy excavation and compacting machines, the fill is sometimes loosely compacted without specific anchoring in the foundation. In addition, in some cases, the latter has not undergone any specific sealing.

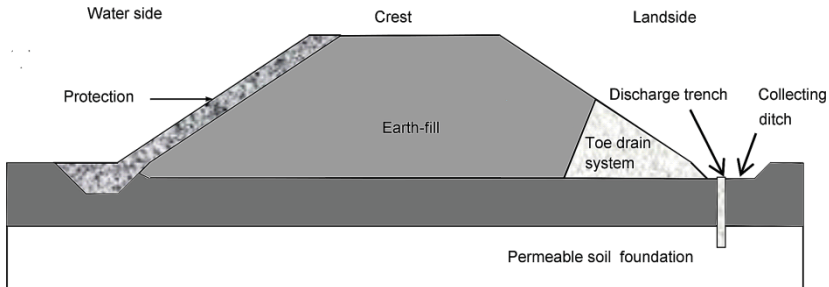


Figure 7.1. Homogeneous dike on impermeable foundation

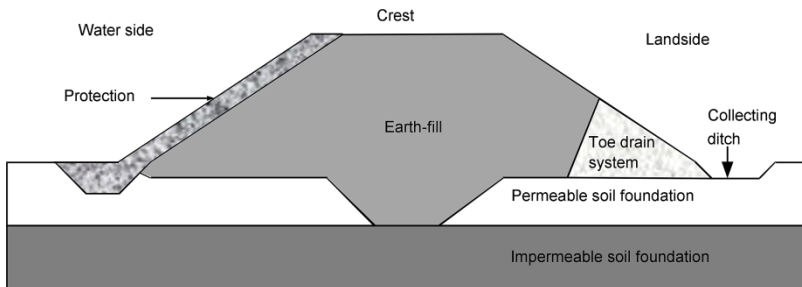


Figure 7.2. Homogeneous dike on impermeable foundation

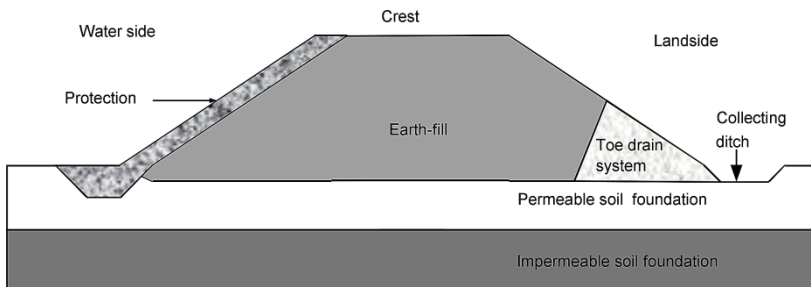


Figure 7.3. Homogeneous dike on permeable foundation without cutoff wall

Sometimes, dikes can be found with more permeable homogeneous fill material (sand). This case is common on coasts on which the dike is located on an old remodeled ridge of dunes and where a stone or concrete revetment (or rock fill) not only ensures mechanical protection but also seals the structure, preventing the removal of material from inside the dike.

7.1.1.3. Zoned fill

7.1.1.3.1. Original zoned fill

The most recent dikes (over the last 20 years) often demand designs similar to those used for earth dams. In this case, the materials are zoned with the separation of sealing and drainage functions. Sealing is often ensured by a core of silty or clayey material located at the center or the water side of the dike. When this material cannot be found on the site, substitute materials may be used as a diaphragm wall or the superposition of layers of asphalt concrete or asphalt. The core of the dike in coarser material ensures only the stability of the structure. Filter layers are installed to avoid the erosion of the core materials. If necessary, the transition between two zones with different grain sizes is ensured by a transition layer filter. Not only is the core of the structure impervious, a cutoff wall, an impervious blanket or a grout curtain can provide a watertight junction with the underlying layers if decided necessary.

The zones surrounding the impervious core are composed of random compacted fill. They ensure the structure's resistance and stability.

This type of dike is found when non-porous materials are rare or lacking on the site. In parallel, the materials with poorer hydraulic characteristics available on the site can be used to ensure the function of stability.

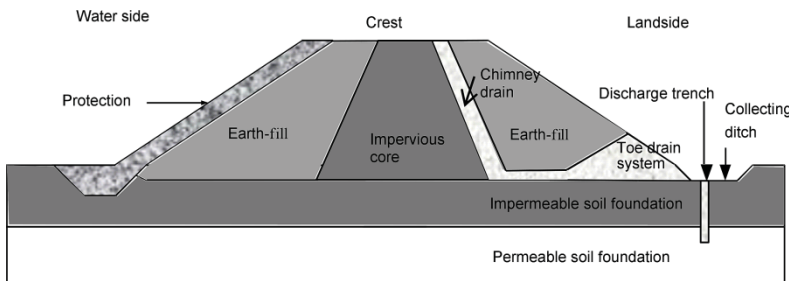


Figure 7.4. Zoned fill on impermeable foundation

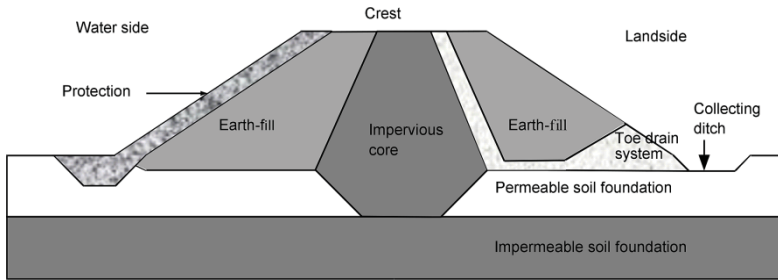


Figure 7.5. Zoned fill on permeable foundation

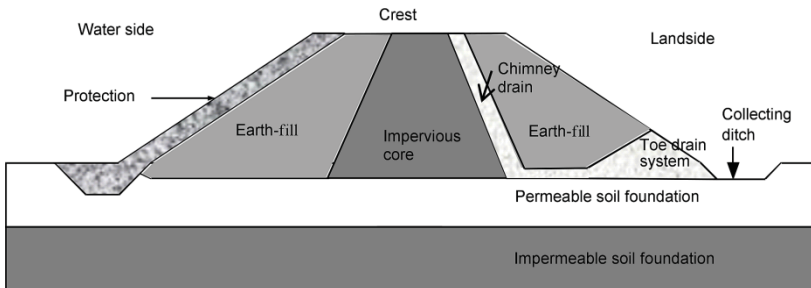


Figure 7.6. Zoned fill on permeable foundation without cutoff wall

Specific points of zoned dikes must be taken into account. The joint between the dike's components is an important item as it represents a discontinuity in the material's surface, making it necessary to take transitions between granulometries into account using a filtration law criterion. The vertical continuity of sealing can be ensured until the foundations if necessary. Furthermore, since the structure is sealed, the pressure gradients exerted on the structure under load are high. In this case of sealed zoned dikes on pervious soil, under-pressure liable to destabilize the structure must be controlled by drain-sealing systems.

7.1.1.3.2. Zone fill following reinforcement or raising

Dikes are often reinforced in successive stages. Structures may have been reinforced to improve their stability and/or the level of protection. The level of protection provided by a dike can also be modified during its history. The crest of a dike can be raised by reinforcement heightening. Thus, a large number of structures become zoned by successive reinforcement works:

– Reinforcement of porous fill, protected area side: the reinforcement of a dike on the landward side improves the stability of its slope. A filter can be installed to overcome internal erosion. This type of reinforcement is sometimes chosen to repair mechanisms liable to destabilize the structure. Also, reinforcement of the protected zone side by a berm “lengthens” the hydraulic path inside the structure and acts as a filter preventing the removal of fines.

– Impervious fill reinforcement, seaward side: a dike can be reinforced on its seaward side to improve the stability of the sealed slope, or to raise a dike without intervention on the landward side (urban pressure), or simply to improve its water resistance.

– Raised fill: it is necessary to distinguish this notion of reinforcement to correct a geotechnical stability problem of heightening so that the structure fulfills its function of hydraulic protection (higher level of protection). A dike can be raised in different ways:

- on the landward side: the dike is raised by increasing its section via the protected face;

- on the side facing the sea: the dike is raised by increasing its section via the face on the water side;

- on the crest: (i) by adding an elevation, (ii) by raising the crest and reducing its width (same slopes), (iii) by raising the crest and by raising the slopes on either side (not recommended but frequent) or (iv) by adding materials on either side to raise the crest while conserving the slopes.

7.1.1.4. Composite structure

Composite structures combine a geotechnical component (materials taken from the soil that respond “flexibly” to stresses) and a structural component (responding most of the time to stresses by rigid, brittle or semi-rigid behavior).

7.1.1.4.1. Retaining wall (frequently on the water side)

The so-called “classical” dikes whose stability is ensured by fill or core cover a large surface area. In the case of limited areas, rigid structures make it possible to reach almost vertical slopes. This makes it possible to use far less space in comparison to self-supporting structures. The stability of the structure is ensured by gravity walls (masonry or concrete) or anchored walls

(sheet pile, anchor rods, etc.). These retaining structures are mostly found on the seaward side where they ensure the structure's stability, its watertightness and/or its protection.

Rigid structures are usually quite impervious. Therefore, they must be combined with a weep hole system to balance water levels in order to avoid pressure differentials liable to destabilize the structure.

These walls with steep slopes facing the sea are reinforced on the landward side by earth fill or coarse material on which roads, for example, are often built. Modern techniques use concrete instead of masonry though the latter is sometimes used in places to give an esthetic aspect to the walls. Locally, gabion and sheet pile structures can be found. These are used to protect the seaside walls of an earth fill dike.

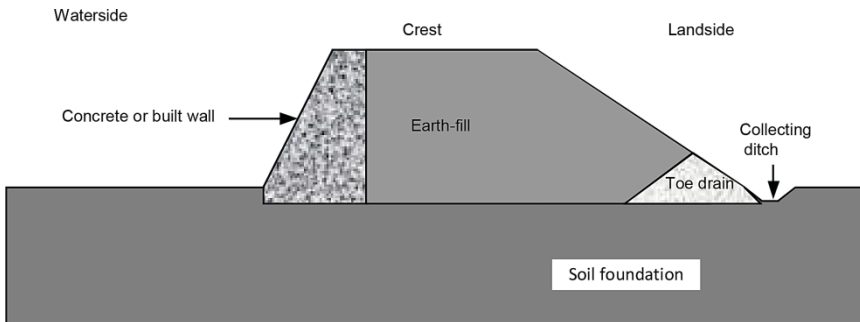


Figure 7.7. Composite structure with massive retaining wall on waterside

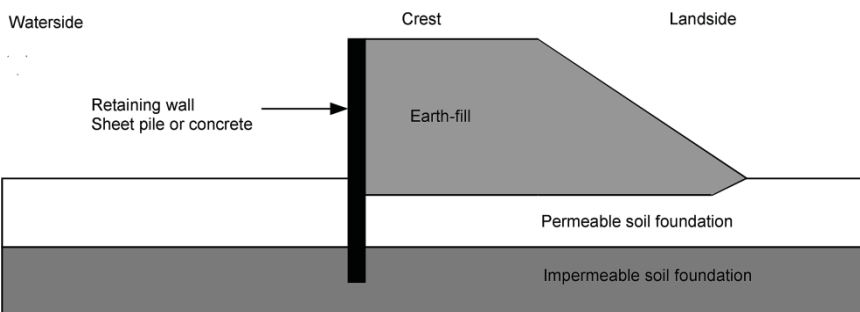


Figure 7.8. Composite structure with thin retaining wall on waterside

7.1.1.4.2. Composite structure including rigid elements on the crest and in the core of the dike

Dike crowned with a structure (possibly removable)

These are composed of a lower part whose design is similar to that of a rubble-mound breakwater crowned with a vertical structure (wall or caisson). The objective of increasing security relating to overflows and overtopping has sometimes led to raising the crests of dikes using narrow elevations, for example, a masonry crown wall placed on the crest, generally on the seaside.

Regarding coastal structures, the lower part can cause storm surges that lessen the mechanical impact on the upper part of the structure by dissipating energy. The surface area on the ground is reduced by combining the lower “sloping” part with the upper vertical part. These structures are found very frequently for structures subjected to surges where overtopping by a series of waves is limited by a vertical crown wall. In certain cases, the crest of the slope is leveled to a height close to that of low tides and is crowned by a wall of sometimes considerable height.

These composite dikes function at low tide like normal rubble-mound breakwaters. When the level of the seawater is higher, they function like vertical dikes, with the waves breaking on the lower structure. These structures are generally found on coasts with high tidal ranges, in areas where the morphology of the coast and the seabed reduce their exposure to swell.

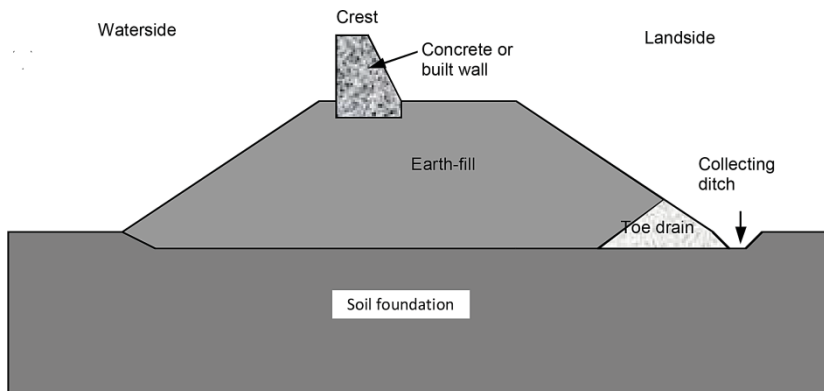


Figure 7.9. Massive concrete or built wall on the crest of earth fill

These structures can also be built when the use of a rubble-mound breakwater has too many disadvantages, because the volume of materials required for construction is too great, or because the surface area at the foot of the dike does not match the requirements of the area to be protected, or if the weight of the structure on the foundation soil is too heavy. Similarly, composite dikes are built when it is not possible to construct a vertical dike (problem of stability under the effect of waves).

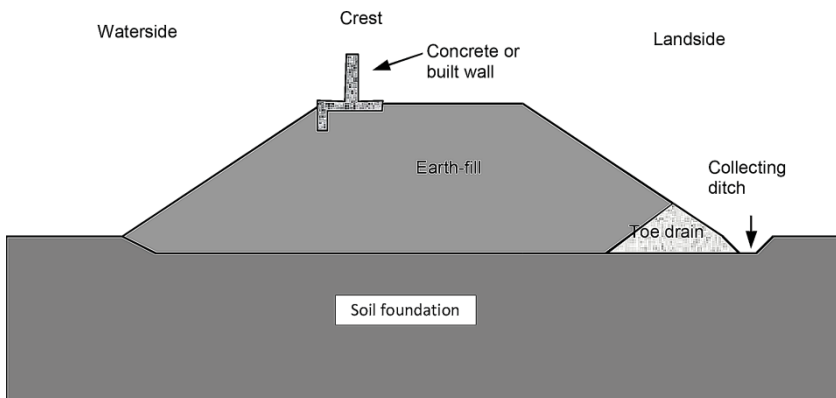


Figure 7.10. Concrete wall on the crest of earth fill

Dike with an internal curtain wall

Certain dikes whose imperviousness has deteriorated through time are “repaired” by the inclusion of a curtain wall (sheet pile cutoff or grout curtain walls).

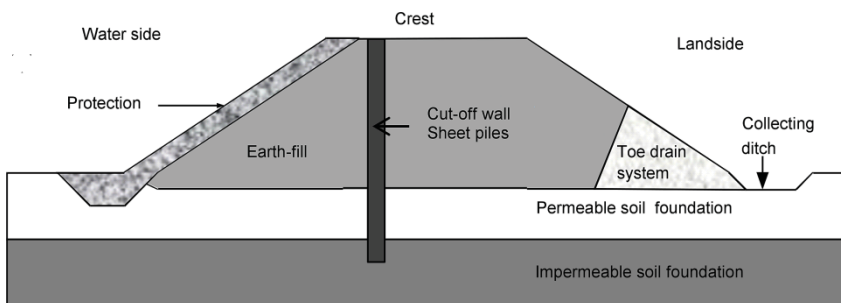


Figure 7.11. Impermeable wall in a homogeneous earth fill

7.1.2. Functional analysis of the protection system

Performing a functional analysis enables us to understand and formulate a synthetic description of the functioning of the dike system studied. It provides a formal and exhaustive representation of the functional links inside and outside the system. We propose implementing the Application to Company Techniques (APTE) method [BRE 00] which has already been used and adapted successfully for civil engineering systems.

The functional analysis approach comprises three phases: the definition of the system, the external functional analysis and the internal functional analysis. The system is therefore analyzed at different spatial scales called granularities:

- granularity 1: the entire dike system and its environment (for the external functional analysis);
- granularity 2: the subsystem of dikes composing the dike system. These are defined by their hydraulic functions (for the internal functional analysis);
- granularity 3: the structural components of the different sections of dikes are defined by their geotechnical and structural functions which can be mechanical or internal hydraulics (for the internal functional analysis).

7.1.2.1. Definition of the system concerned by the functional analysis

The first step of the functional analysis consists of defining the system that we like to study. The first step is to clearly define the dike system (its limits, the structures composing it, the context of its construction and its initial objectives). The functions of a dike system are directly linked to the conditions of the environment in which it is built. Therefore, in what follows we attempt to define the adjacent environment of the dike system by identifying the external media which interface with it.

7.1.2.1.1. Definition of the dike system

The dike system is the system that is the object of the functional analysis. A dike system is essentially defined by the installation and type of structures composing it. It can also be defined by a civil engineering manager as the structures they manage directly (this meaning does not conform to the regulations that emphasize the coherency of the system), or by the study

manager, as a number of structures and other elements ensuring the protection of a protected area.

A dike system is composed of a main line of defense, which corresponds to a line of reference protection structures from the standpoint of the manager and which generally constitutes the limit between the protected area and the marine environment. Analyzing the configuration of the main line of defense in relation to the sea and the protected area makes it possible to identify the nature of the dike system concerned.

The dike system can also comprise secondary structures and natural elements, generally fill, which make up ramifications of the main line of defense (mostly in the form of casiers). They are generally located in the protected area, but can in some cases be located on the river side in relation to the main line of defense (old layout of dikes; structure for indirect protection: groynes, river bank protection, beach replenishment, etc.). Only the secondary structures presenting the potential for breaching and/or playing a proven role of protection or providing continuity in the protection should be considered. They belong to the protection system when they involve considerable differences in the flood propagation scenarios for the protected area whether they are breached or not, or whether the longevity of the protection depends indirectly on their integrity. The structural elements not integrated in the dike system must constitute elements of its external environment of the protected area or the river.

We can also consider a protection system including, apart from the dike system itself, indirect protection structures and devices on the water side (e.g. groynes, breakwaters, beaches, etc.) and water management structures in the protected area (secondary dikes, pumping stations, sewage networks, etc.), as well as structures whose breaching or failure could have an impact on the stresses exerted on the dikes. What is important is that these elements are included in the analysis without taking a dogmatic position that links them to the dike system, the water environment or the environment of the protected area.

7.1.2.1.2. Definition of external environments

The external environments to be considered are those locally in interaction with the dike system subjected to the functional analysis. Two main types of external environment can be distinguished for the dike system:

(1) the external environment of the protected area and (2) the external environment(s) of the sea or estuary. Their association with the dike system forms the diked area (Figures 7.12–7.13).

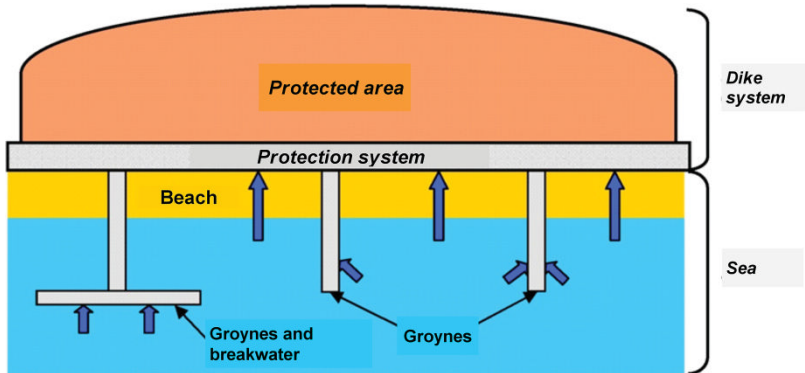


Figure 7.12. The three components of a coastal protection system: dike system, protected area and sea

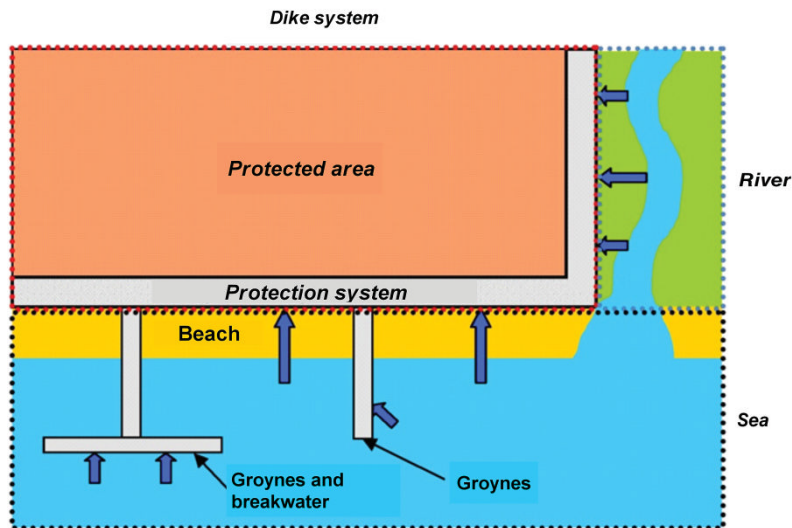


Figure 7.13. The three components of a mixed protection system: dike system, protected area and sea or estuary

Other external environments with non-negligible impacts on the dike system and the protection area can be considered, notably external environments: underground (karst, cracking, tectonic evolution, earthquake, etc.) and atmospheric. At this point, emphasis is given to the boundaries between the different external environments identified. They must be clearly defined and explained. Their establishment is a direct result of the choices made by the study manager.

7.1.2.2. External and internal functional analyses of the protection system

7.1.2.2.1. External function analysis

Performed at granularity 1, it identifies, describes and analyzes the interactions existing between the dike system and the different characteristics of its environment and determines the main and technical functions of the dike system. An external river environment is analyzed more in terms of potential impact on the dike system. The external environment of the protected area is analyzed essentially in terms of the hydraulic consequences due to a failure of the protection system. Furthermore, the conceptual model developed in the European FloodSite project (Source Pathway Receptor) results in the same analysis.

The main function of the coastal dike system

Knowledge of the dike system's configuration and its interactions with its environment make it possible to identify its main function. Seen generically, the main function of a coastal dike system is to protect the protected area against submersion by the sea. It can take the form of several protection subfunctions that depend on the type of dike system considered and that are identified by examining the interactions between the external environments, via or through the dike system.

An example is the prevention of massive inflows of water in the protected area (i.e. without, however, completely preventing spray or projections due to waves, insofar as these quantities can be managed by the sewage and drainage systems of the protected area). Other main functions associated with protection are possible, such as combating coastal erosion.

It is possible to distinguish the roles of a structure, which result from the objectives of the owner and its functions, which, whether desired or not, can be observed or deduced during the functional analysis.

The technical functions of the dike system

The technical functions of the dike system are those that ensure the performance of the main function of the system studied and those that enable its monitoring and maintenance. Therefore, these functions guarantee the system's longevity and the accomplishment of its hydraulic objectives, by resisting the stresses imposed by the external environment. These objectives are notably functions of resistance to the external stresses identified during the analysis of the external environment: sufficient watertightness, stability, resistance to external erosion phenomena, resistance to impacts, etc.

7.1.2.2.2. Internal functional analysis of the dike system

The internal functional analysis focuses on describing and analyzing the intrinsic functioning of the dike system through the different elements composing it. It is broken down into two steps: the analysis of the hydraulic functions of the dike subsystems and the analysis of the geotechnical and structural functions of the dike's components.

Analysis of the hydraulic functions of dike subsystems

This initial analysis makes it possible to identify the hydraulic role fulfilled by the different parts of a line of dikes in order to ensure the main function of the dike system. This work is performed at a granularity of 2 and leads to breaking down the dike system into homogeneous subsystems with respect to their hydraulic functions:

The hydraulic functions of dike subsystems

Dike subsystems are either linear (a section of dike, a section of dike resisting overflows, a passage where a cofferdam can be installed and a section corresponding to the boundary of the protected area open to natural ground), or punctual and included in the linear subsystems (emptying and drying structures, etc.). They can provide one or more hydraulic functions specific to their linear or punctual nature. Table 7.1 provides a possible typology of the different generic hydraulic functions that can be associated with dike subsystems. This list is not intended to be exhaustive and can be completed to fit the dike system considered. Table 7.2 gives an example of a combination of hydraulic functions for the main types of subsystems that can compose a dike system.

No	Hydraulic function	Characterization of the function	Sub-system parameters	Type of Sub-system
1	Prevent the entry of water into the protected area or the compartment located at the back of the section, up to its crest	- crest level of the section (flood; water level)	- level of the section crest - level of the natural ground - length	Section
2	Control floods in the protected area or the compartment located at the back of the section, after the crest level has been passed	- crest level of the section (flood; water level)	- level of the section crest - level of the natural ground - length	Section
3	Reduce the flood discharge downstream of the section	- crest level of the section (flood)	- level of the section crest	Section
4	Enable the release of floodwater, from the protected area towards a river or sea, after the crest of the section has passed	- crest level of the section (water level; flood)	- level of the section crest - length	Section
5	Withstand overflow	- safety level according to resistance to overflow		Section
6	Not withstand overflow and be erodible by the overflow up to a given point of resistance	- point of resistance level (flood; water level)	- level of the point of resistance - level of the natural ground	Section
7	Not withstand overflow and be erodible by the overflow up to below the foundation of the section			Section
8	Prevent the entry of water into the protected area or the compartment located at the back of the section, up to a fixed crest level, designed to be increased temporarily to a given peak level	- fixed crest level (flood; water level) - removable crest level (flood; water level)	- level of the fixed crest - level of the removable crest - level of the natural ground - length	Section/ localized

9	Subdivide the territory hydraulically and influence the water propagation in the protected area (other main function possible, example: road)	- crest level of the section(water level) - function of the section (highway, railway, road, etc.)	- level of the section crest - level of the natural ground - length	Section
10	Enable a localized water flow, from one side to the other of a linear dike subsystem	- opening size (Q_{max}) - working level (flood; water level) according to direction of flow	- geometry - level of the section crest - level of the natural ground	Localized
11	Control the localized flow of water (flow, direction, working level)	- control of working level (flood; water level) - control of direction of flow - control of flow	- type of installation - working conditions	Localized
12	Control the hydraulic load on the section	- efficiency of the installation (depending on backfill and hydraulic conditions)	- geometry - max flow - flow responsible for hydraulic load of backfill	Localized

Table 7.1. Example of the typology of the generic hydraulic functions of dike subsystems (source: Irstea – formulation of methodology in progress)

Breaking up into dike subsystems

This initial internal functional analysis leads to the breakdown of the dike system into dike subsystems. In addition to the type of functions associated with the subsystems, this breakdown is also based on their characterization. A dike subsystem must therefore be homogeneous regarding its function and characterization:

- 1) The characterization of the crest levels of the subsystems of linear dikes in comparison to stress levels

Identifying the crest heights of the subsystems of linear dikes enables us to characterize their hydraulic functions. For primary structures, the crest

level corresponds to the height beyond which, in the absence of breaches, a section no longer prevents the massive flow of water into the protected area. In the case of the functional analysis of new structures, the crest level is a design objective; thus, the information is known to the owner. In the case of the functional analysis of existing structures, the effective crest level must be either verified or determined.

2) The technical characteristics of punctual dike subsystems

Each punctual dike subsystem is defined by technical characteristics that describe its mode of functioning (Q_{\max} , level of functioning, flow direction, controlled parameters, functioning conditions, etc.). These characteristics must be identified for each punctual dike subsystem of the line of dikes. The level of functioning corresponds to the height of the water from which a flow is possible in a given direction. In the case of a new structure, it is known. In the case of an existing structure, it can be determined by applying the method used to determine the crest level.

Analysis of the geotechnical and structural functions of dike components

This analysis is performed with a granularity of 3, that is to say that of the structural components composing the different sections of the dikes and identified during the structural analysis of the dike system. The aim of this analysis is to identify and characterize the geotechnical functions ensured by these geotechnical components in the different types of dike cross-sections found in the dike system. This leads to a breakdown of the line of dikes into geotechnically homogeneous sections.

The functions of dike geotechnical components

The longevity of a given section of dike and the performance of its hydraulic functions is directly dependent on the performance of the geotechnical functions that these components must ensure in a generic way. These geotechnical functions can be characterized by the different thresholds that describe their functional state (Table 7.2).

No.	Geotechnical function family	Characterization of the function (degradation thresholds and loss of function)	Component parameters
1	Mechanical stability of the whole (affects the mechanical stability of the section)	– geometric integrity	– geometry – geomechanical properties
2	Watertightness (limits the flows to other components)	– permeability coefficient (m/s)	– granulometry/mechanical properties – thickness
3	Drainage (captures flows within the section and removes them)	– drainage flow capacity	– permeability coefficient (m/s) – geometry
4	No drive off of interface particles (prevents the migration of particles at the interface of granular components)	– state with respect to the conditions of particles not being driven off	– granulometries of the interfaced components – filtration opening (geotextiles) or porosity (granular) – thickness
5	Auto-filtration (prevents the migration of particles within a granular component)	– continuity of the granulometry	– granulometry
6	Resistance to external erosion (water, other substances)	– classification of the mechanical or geomechanical resistance according to the thickness	– mechanical or geomechanical properties – thickness
7	Resistance to intrusive external aggressions (burrowing animals, roots, etc.)	– mechanical resistance and objective of protection	– mechanical properties – mesh (geotextiles, grating, geogrid)
8	Flow (letting water pass through)	– state with respect to flow conditions	– permeability coefficient (m/s) (granular) or permittivity (s ⁻¹) (geotextiles) – thickness

Table 7.2. Example of the families of geotechnical and structural functions of dike components and their characterization
(source: Irstea – formulation of methodology in progress)

The structural components of dikes

The structural analysis of the dike system enables us to identify the different cross-sections of the geotechnical components composing it. According to the cross-section of the dike concerned, each geotechnical component fulfills one or more geotechnical functions belonging to different families of functions.

Geotechnical components	Possible associated geotechnical functions
Earthfill	1. General mechanical stability 2. Watertightness 5. Autofiltration
Impermeability element (dike, foundation)	2. Watertightness 1. General mechanical stability
Drain element (dike, foundation)	3. Drainage
Filtration element (Interfaces : drain system, watertightness)	4. Filtration 8. discharge
Protection element (slope, crest, foundation)	6. Resistance to external erosion 7. Resistance to penetration from external
Wall or other gravity structure	1. General mechanical stability 2. Watertightness
Foundation	1. General mechanical stability 2. Watertightness 5. Autofiltration

Table 7.3. *The main types of geotechnical dike component and their associated functions (Irstea – formulation of methodology in progress)*

Likewise, the functions of the same family can be found in different components of the same dike cross-section, but with different applications. For example, a section can comprise a filtration device at the interface with a drainage device as well as a filtration device at the interface of a sealing device. These are two filtration functions, but with different applications and characteristics.

7.1.2.3. Main components of a system of dikes and their hydraulic and structural functions

According to the type and environment concerned, a dike is composed of the following elements associated with the corresponding functions.

7.1.2.3.1. The foundation or supporting soil

This element is not a component of the dike itself, rather it belongs to the dike's environment. However, it plays a major functional role and must be treated with attention. The main function of the foundation is to support the dike. Thus, it is decisive for protection against geotechnical destabilization mechanisms (sliding, compaction, punching, deep circular failures, etc.). The foundation is also subject to the circulation of water and internal erosion phenomena. Managing flows and pressures is decisive, on the one hand, to avoid excessive flows leading to internal erosion, and, on the other hand, to avoid under-pressure beneath the dike leading to translational sliding. Classically, for hydraulic structures made up of fill, the foundation is considered as a part of the structure, as opposed to a building.

7.1.2.3.2. The core

The main function of the core is to ensure the stability of the dike. It is composed of the largest volumes of materials. These materials are often extracted immediately adjacent to the site (clay, silt, sand, gravel, etc.), while stone or concrete are used for rigid structures. The geotechnical and hydraulic properties of these materials have a considerable influence on the choice of type of structure and its shape. In some cases, when the materials used are relatively impervious, the dike core also ensures the sealing function. In addition, cohesive materials (clays, silts) are less permeable and less sensitive to internal erosion than granular materials (sands). In the former case, the design will be simple with a dike core made up of clay fill that will be stable, impervious and not very vulnerable to erosion (thus simple to protect). On the contrary, clay materials are sensitive to water content during construction, loading and unloading the structure and seasonal cycles (sensitivity to prolonged droughts). In the case of coarse granular materials, sufficient sealing (to both retain water and not trigger internal erosion) can only be ensured by "extending" hydraulic paths (reduction of gradients). Furthermore, sandy materials are more sensitive to different forms of erosion and require additional protection.

7.1.2.3.3. The upstream impervious core or membrane

Contrary to the dike core, an impervious core or membrane may or may not be present depending on the type of dike considered. It ensures the sealing function. It is composed of compacted clay, silt, concrete or other material of low porosity. When present, according to the conditions of the

site, the core can be anchored and/or extended by a membrane down to the layer of impervious soil (if the dike lies on a porous layer). However, the watertightness of the foundation is not necessarily the objective sought (contrary to dams). Nonetheless, it is vital to control underground flows and the absence of their harmful effects. The use of an impervious core is, in fact, rare for dikes (since this use is more frequent for earth and rock fill dams). On the other hand, in the case of heterogeneous material, it is necessary to place the least pervious material facing the water.

A very common practice in the Netherlands and Germany (especially for coastal dams with relatively gentle slopes) is to place an external layer of clay to ensure watertightness and protect against the external erosion of dikes whose cores are composed of sand.

7.1.2.3.4. Protections (mechanical)

Whatever the case considered, a dike is never only hydraulic fill left bare. It is protected against the harmful action of external agents. The protections can be more or less resistant (ranging from grass to covering with concrete). The structure is generally subjected to the action of atmospheric, environmental (burrowing fauna, flora, etc.) and anthropic (quads, motocross, horse riding, etc.) agents, in addition to the cations in water which are described further on according to the part of the structure concerned.

Seaward side

A dike can be permanently or exceptionally subjected to the actions of water (static and above all dynamic). Waves and currents cause stresses on the structure (the following section focuses on stresses). Protection can be ensured by a revetment (by loose or bound rock fill, dry or jointed stone, concrete, gabions, or by geotextile bags, etc.) or more rarely by plantations of adapted species. The roughness and porosity of the seaward protection considerably influences the loss of energy and overtopping by waves. Protection providing considerable roughness and/or porosity dissipates more energy and reduces the volumes overtopping the dike. However, this energy dissipation is synonymous with greater stress on the protection. The shape and notably the slope of the seaward side and the characteristics of the foreshore influence the hydraulic stresses on the structure (height, waves, etc.).

Regarding coastal dikes, the revetment forms the first line of defense against the mechanical action of the waves and thus protects the underlayers. Indeed, it is the block of the revetment that will dissipate most of the energy contained in the waves, before it comes into contact with the underlayers.

External protections are most commonly built using:

- natural rock fill;
- massive artificial blocks made up of concrete;
- blocks of dressed stone.

In addition, in the case of non-aggressive sea surges and for structures with gentle slopes:

- concrete slabs;
- rock fill gabions;
- rock fill bound by bituminous materials;
- geotextile bags filled with sand (attention must be given to anti-ultraviolet (UV) protection); etc.

Crest

The crest of the structure also plays a protective role. It is subjected to the action of atmospheric agents (rain). It can be subjected to stress by currents in the case of overflows and by waves in the case of overtopping. The crest of the dike generally ensures another function: that of a road used for monitoring and maintenance, or for denser traffic. It is often subjected to other uses not involved in the flood protection function (roadway, leisure area, etc.).

Landward side

The slope on the landward side is subject to stress only exceptionally and intensively by strong currents in the case of overflows and overtopping. The types of protection chosen are as different and various as on the seaward side. Well-maintained grass covering can resist erosion by sometimes considerable volumes of overtopping and overflows. The protection on the landward side (slope + protected area) is a decisive element when a dike is subjected to possible overflows and overtopping.

7.1.2.3.5. Filters

Dike degradation phenomena often occur slowly by the progressive migration of fines: internal erosion mechanism. As their name implies, filters act to filter the materials. Their role is to avoid the removal of this (generally fine) material to maintain the watertightness and structural integrity of the structure. The filters are placed between the elements composing a zoned dike in contact with other elements of very different grain sizes. Geotextiles are increasingly used as filters.

7.1.2.3.6. Drains

Dikes are subjected to the action of water. Its presence in the structure can trigger phenomena of under-pressure, expansion-retraction and geotechnical destabilization. Draining the structure permits controlling these internal phenomena. The drainage function is ensured by several elements. Drainage layers are sometimes used (drains, layers allowing water to circulate, drainage layers, etc.) combined with other systems (drainage trench, pumping, etc.). When speaking about these systems, the terms internal or deep drainage are used. Also, in the case of stone structures, the circulation of water is favored by weep holes to avoid unbalanced hydraulic loads. In this case, the terms external or superficial drainage are used.

7.1.2.3.7. Toe protections and cutoff walls

Installed on certain structures, the toe protection water side contributes to the stability and protection of the dike. It ensures the junction between the structure and its environment. In the case of a rock fill covering, it stabilizes the latter. In the zones most exposed to scouring, cutoff walls are sometimes built. They are usually composed of jointed wood piles or steel sheet piles. These prevent scouring phenomena at the foot of the structures. In addition, systems are sometimes used at the foot of the structure to extend sealing in depth (using sheet piles, impervious blankets, etc.). This is sometimes done to increase the length of the hydraulic passage (and thus increase dissipation).

On the landward side, the toe protection contributes to stability and to channeling and draining the water.

7.1.2.3.8. Berms

Initially, a berm can be an element of the dike or can be added to it by replenishment to reinforce it. On the seaward side, the role of the berm can

be to protect (reinforcement following an external erosion mechanism), stabilize (by offsetting deep or superficial rotational sliding) and provide sealing (by increasing the length of the hydraulic path).

On the landward side, a berm can fulfill the roles of providing stability, filtration and drainage. The berm on the protected side, possibly extended by a blanket, can also be used to control internal erosion phenomena occurring in the support soil and/or under-pressure in the foundation (sand boil).

7.1.2.3.9. Crown walls (breakwaters and heightening)

Dikes, especially coastal dikes, can comprise crown structures. The crown wall protects the dike by reducing overtopping by waves. In some cases, it can also be used to retain water. It often takes the form of a stone parapet wall designed to dissipate or reflect the energy of the waves. The crown wall is anchored to the dike to resist sliding and collapse caused by the force of the impact of the waves and/or water level. Many old structures have elevations that increase the protection height of the dike. These structures are present when the height of the crest of the structure is increased without widening the dike. These structures also play the role of parapet (to prevent persons and vehicles from falling).

7.2. Stress of coastal dikes

It is important to know at the beginning the stresses that can be exerted on a dike in order to dimension it and control it afterward (diagnostics, hazard studies, etc.). These stresses (or actions of the external environment) are of different natures:

- hydraulic stresses (external);
- direct mechanical stresses caused by external factors that cannot be generalized from one system to another (earthquakes, localized subsidence of the foundation, karstic environments, surrounding ground rising above the structure, anthropic actions including the circulation of vehicles, accidental actions, overloads, etc.);
- stresses caused by evolutions of the morphology of the marine environment, causing changes in the environment adjacent to the dike (foreshore or foundation) can lead to the occurrence of degradation and breaching mechanisms and scenarios.

7.2.1. Hydraulic stresses

Hydraulic stresses caused by the sea comprise different components that must be characterized case by case. These components (or their significant parameters) are:

- the hydrostatic level including its consequences on internal flows and possible overflows;
- the variations of this hydrostatic level during an event (mainly velocities of rises and falls) including their consequences in internal flows and interstitial pressures;
- a dynamic component with direct mechanical effects (e.g. wave impacts) on the structure or effects that can result through time in overtopping and under-pressure; the significant parameters are in particular wave height, propagation speed and period (wavelength);
- a velocity component in the longitudinal direction of the structure;
- sediment transport.

Precise knowledge of all these components of hydraulic stresses is required to make an accurate evaluation of the reliability of an existing structure or to dimension a projected structure.

These marine hydraulic stresses generally represent the main hydraulic actions that the dike must resist, although in certain situations it is advisable to add stresses liable to originate from the protected area such as those caused by drainage ditches and/or secondary streams at the foot of the dike, with current and rising tide velocities as well as the wave heights specific to each structure.

7.2.1.1. Characterization of heights and levels in a coastal environment

Regarding coastal and estuarine dikes, it is necessary to not only take into account the level of the sea close to the structure but also surges, and rough seas and clapotis. These two parameters are involved in evaluating both the protection provided by the structure and its security.

For example, a dike can prevent floods by submersion for an average sea height lower than its crest height. However, concomitant waves can cause floods by overtopping. There are different types of overtopping. They can be

projections generated by waves breaking on the structure, in particular vertical ones. Waves can also rise up a breast wall until they overtop it. And when the average level of the sea is high but remains below the crest of the structure, the action of the waves can overtop the dike massively and continuously.

Furthermore, swells are a decisive parameter for assessing safety, especially for coastal dikes. When the sea is deep close to the structure, there is no or hardly any dissipation; thus, large waves are generated and the stresses involved cannot be compared to those of static levels. These stresses are applicable both in front of the structure and behind it in the case of overtopping.

Logically, the further assessment of the protection and safety of a coastal dike for a given return period requires taking into account pairs of parameters (sea level – sea state). A single pair is insufficient due to the, at least partial, independence of the phenomena. In general, the response can only be given by performing a statistical study of these pairs, provided that data covering long enough periods are available.

The stresses applied to coastal and estuarine dikes depend on the sea level and the swell, wind waves and clapotis (see definition below) and interactions with the structure and the coast.

For this whole section, if the readers would like to know more about this subject, they should refer to part 4 of the rock fill guide [CET 09]. This guide can be consulted free of charge in read-only mode on the CETMEF website.

7.2.1.1.1. Sea level

The sea level comprises different components.

- *The height of the astronomical tide*

The height of the astronomical tide mainly depends on the position of the Moon and the Sun. This height can be predicted because the movements of the Moon and the Sun are well known. The astronomical tide is not very pronounced in the Mediterranean though its amplitude is high in France along the coasts of the North Sea, the Channel and the Atlantic. The tidal range can reach more than 15 m in the bay of Mont Saint Michel.

Predictions of tides in certain French ports can be accessed freely at www.shom.fr through the *Service Hydrographique et Océanographique de la Marine* (SHOM). They are limited to the year in progress, though it is possible to calculate past heights. Other information is also available, such as the heights of high tide and low tide for astronomical tides of maximum and minimum amplitude. The predictions for the current and following years are accessible in tide charts or with the SHOMAR software. Lastly, longer term predictions require the use of a specific software application or making an order to the SHOM.

Height predictions for Metropolitan France are defined in reference to a chart datum which is close to the level of the lowest tides (it may sometimes vary by several decimeters). The calculation of the heights of the astronomical tide in the IGN 69 reference system can be done in the ports where a link exists between the two reference systems. This information is available both on the site and in the SHOM tide charts.

If we want to evaluate the heights of the astronomical tide somewhere other than in the reference ports, the only method accessible to date is interpolation. However, it does not always provide acceptable results especially in areas where the coast is not rectilinear. In this case, it is necessary to carry out a measurement campaign. Care is necessary when using plans of old structures since the link between the two reference systems may have changed over time.

For further information on astronomic tides, the reader can consult [BER 07].

– Increments of meteorological origin

The actual tide is often very different from the predicted tide. The difference in height between the actual tide and the astronomical tide is called the increment or decrement. The increment is therefore not the maximum level reached by the sea.

Meteorological phenomena, namely wind and atmospheric pressure, can generate long waves in the region of several hundred kilometers. They are the source of increments of variable height according to the configuration of the coast and with durations lasting from an hour to a day.

The increments measured in the ports of Metropolitan France can reach 2 m and more, but they do necessarily occur during a high water large tide. The exceptional nature of the sea level reached at La Rochelle during Cyclone Xynthia was not due to the maximum height of the increment (1.50 m, although increments of 2 m had already been observed), but to the fact that its maximum occurred at a high tide with a very rough sea.

Combined with the astronomical tides, increments can considerably modify the sea height. A publication of the SHOM and the Centre d'Études Techniques Maritimes Et Fluvial (CETMEF) permits evaluating the resulting extreme sea levels for the Channel and the Atlantic. Bearing the title "Statistics of extreme sea levels in the Channel and the Atlantic", this document provides, in the IGN69 reference system, the predictable levels along the entire coast for different return periods. These levels do not take into account the additional height due to swells, seiches or the elevation of the sea level due to climatic change (see below).

– Increased sea level due to swells

This component of sea level is called wave setup and develops close to the coast. Its main origin is wave surges caused by upwelling. It can be seen, for example, between sand bars and the coast and on the beach among other places. Its height can exceed 10% of that of the swell of the open sea. It does not belong to the components subject to precise measurement by the permanent tide gauges of the SHOM, as these are mainly located in deep water ports and are generally sheltered from swells. It is also not taken into account in the publication "Statistics of extreme sea levels in the Channel and the Atlantic" mentioned in the previous section.

Other sea-level increase phenomena exist, notably due to the reflection of waves on a reflective coast, and in front of weirs and coastal structures (increased height of clapotis).

– Seiches

These are oscillations lasting from a few minutes to several tens of minutes. One of their causes is resonance due to coastal geometry. For example, the reflections between the island of Groix and the continent generate seiches that reach 1.50 m at Port Tudy. They are not taken into account in the publication "Statistics of extreme sea levels in the Channel and the Atlantic".

– Tsunamis

These take the form of one or several solitary waves generated by rapid movements of the seabed, or the collapse of cliffs. Ranging from modest to considerable heights, these waves propagate very quickly and over long distances then swell with the upwelling of water from lower depths, in particular when they reach the coast. Not all tsunamis have the same magnitude as those which have occurred in the Far East over the last few years. Tsunamis of lesser height occur, notably in the Mediterranean, which reach a height of approximately 2 m in the Western part, with a return period of 50 years.

– Rising sea levels due to climatic warming

The increase in the sea level is an important phenomenon on the geological scale. It is estimated that the sea is 120–130 m lower than it was 18,000 years ago. The speed of the rise is currently more modest though the sea level rose by about 20 cm in the 20th Century and this rise is currently accelerating, explained by the increase in greenhouse gas in the atmosphere. In its fourth report issued in 2007, the GIEC predicted an elevation from 20 to 60 cm by 2,100. However, many experts and workgroups consider this estimation to be too low since glaciers are melting at a rate faster than that predicted.

To know the relative elevation of the sea in relation to the Earth along coastlines, which is the only elevation of interest for dikes, it is necessary to incorporate the variations of altitude of the terrestrial base. In Norway, for example, the relative sea level today is decreasing since the upheaval of the land is faster than the rise in the sea level. On the contrary, in the Pacific atolls, the relative level is far higher than the elevation of the sea level alone, due to their subsidence.

French regulation (circular of 27 July 2011 on taking into account the risk of submersion by the sea in the Coastal Risk Prevention plans) takes as a hypothesis a rise in the sea level of 60 cm by 2,100 in metropolitan area.

7.2.1.1.2. Swells, wind seas and clapotis

Generation

Waves are generated by the wind. Initially, they appear to be disordered and cambered. This is what can be seen on the coast when a depression is

close to the continent. What can be seen in this case is a “wind sea” or “clapotis” if the wind is blowing over several kilometers. When the waves are generated on the high sea (several hundred or thousand kilometers from the coast), their movement is organized, forming almost regular, rounded waves. These are called “swells”. A “sea state” describes a number of waves whether for a swell, wind sea or clapotis, or their combination (cross swells, swell and wind sea, etc.).

A sea state can be described statistically by distribution spectra of the period, height, waves and their directional spread. The sea state depends on the force of the wind, the period for which it blows and the length of the body of water it affects.

Propagation

As the waves move toward the coast and upwelling occurs, they are modified by shoaling and refraction. In practice, these phenomena occur when the depth becomes less than half the length of the wave calculated for infinite depth.

Shoaling is the modification of wave height due to the slope of the seabed. First, the height decreases progressively by approximately 10%, and then increases at shallow depths. This increase depends on the duration of the swell. At a depth of 2 m, it is in the region of 5% for a wind sea wave with a period of 5 s, whereas it exceeds 50% for ocean swells with a period of more than 13 s.

Refraction modifies the height and direction of wave propagation. The direction of the waves tends to align with the steepest slope of the bed. This phenomenon enables us to explain the concentration of waves at headlands and their dissipation in bays. Refractions also occur in the presence of currents.

Independently of upwelling, diffraction phenomena can occur in the form of the lateral spreading of waves in areas where they are less high. This phenomenon occurs in particular around rocks, islets, islands, peninsulars, port dikes, etc. Waves are also reflected by obstacles like shoals, any emerging form, the coast and structures. A clapotis whose height is twice the height of the incident wave is generated in front of obstacles (twice as high against a perfectly reflective obstacle). The clapotis is accompanied by an increase in the average level of the body of water. Finally, waves break when

they become too arched (waves whose slopes can no longer support their crests).

Calculation codes are used to model swell propagation. They accurately reproduce the effects of shoaling and refraction. On the contrary, they do not take into account reflection. Some codes model breaking but the effect of diffraction does not often provide satisfactory results. In particular, they are limited in the presence of islets and above all groups of islets. It may then be useful to perform measurements *in situ*.

Precautions are required in order to build a reliable model. The area covered by the model must stretch, if possible, to depths greater than half the wavelength in the open sea. The sea states must also be evaluated at these depths. It is also necessary to collect bathymetric data for the whole area covered by the model. Propagations must be included by varying the direction, the period and the height of sea states and sea level in tidal seas.

Sea states adjacent to the dike

Waves can break as they approach the structure. For beaches with gentle slopes, it can be considered that breaking occurs when the height of the wave is about the same as the depth of the water. For steeper slopes, breaking will occur later. Thus, it depends on the slope and the duration of the waves. The depth in front of the structure will therefore limit the height of the waves reaching it. The altitude of the shallow bed and the foreshore for tidal seas is therefore an essential parameter for evaluating sea states next to the structure. Great care is required when the bed in front of the structure is composed of loose sediment or soft erodible rock, since any lowering will lead to increased wave height.

The average sea level in front of the structure increases due to the increment of the break (see above).

Lastly, the reflection occurring on the dike leads to the formation of clapotis, which leads to increased agitation in front of the structure, with a rise in the average sea level.

The subject is so complex that the numerical modeling of all these physical phenomena is almost impractical for reasonable prices at present. However, physical tests have been performed for standard configurations.

They have led to the clarification of professional practices in certain areas. For example, a remark can be made on the stability of the blocks covering a dike under the effect of waves. On the other hand, some subjects have been given less attention, such as the evaluation of the volumes of water overtopping structures at the top of beaches under the effect of waves. Despite the fact that it only gives a limited number of cases, a remark should be made on recent work on the subject, especially concerning the geometry of seabeds in front of structures. [HRW 15] provides access to the conclusions of this work. It should not be forgotten that observations *in situ* and tests using physical models often remain the most accurate method.

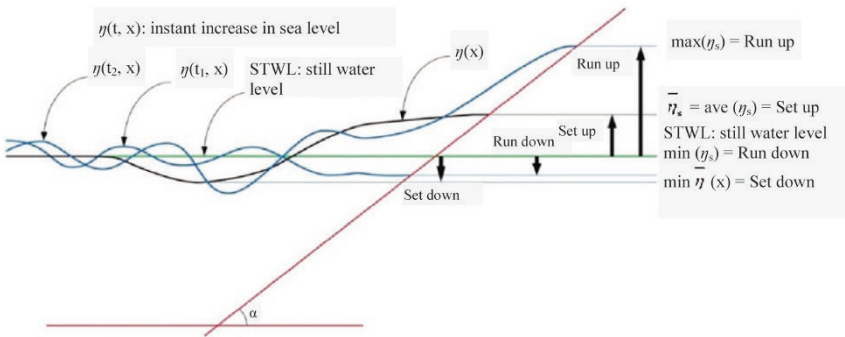


Figure 7.14. Set up and run-up (CEREMA, Wikhydro)

7.2.1.1.3. Hydraulic stresses exerted by the sea

Hydraulic stresses can often be due to currents as in the rivers. Thus, we will not focus on this subject. However, the effects of tides and swells are more specific.

The tide applies a variable hydraulic load in front of the dike. If the dike is built of earth, the effect of alternating flows must be taken into account not only for the stability of the whole structure but also for the stability of the surface. If it is composed of earth fill covered by rock fill, it is necessary to check that the fine particles do not percolate due to the effect of the water pumping through the covering. Lastly, if the fill is covered by riprap or if the dike is composed of a retaining wall, the level of the water table behind it is an essential parameter for dimensioning the screen. A pragmatic approach is

to choose a water table level behind the dike corresponding to the top of the foundation of the wall unless it is necessary to do otherwise. The efficiency of weep holes is not proven due to alternating hydraulic loads, the response time of the water table behind the dike and clogging. The entire defense must be constructed carefully to avoid the formation of cavities behind the structure due to the removal of fill material.

Swell also exerts variable hydraulic forces on the dike though the cycle is in the region of several seconds in comparison to approximately 12 h for tides in Metropolitan France. This fast variation generates specific dynamic effects such as wave overtopping and dynamic forces. These two effects strongly depend on the height of the waves at the foot of the structure (e.g. surface and volume forces are proportional to the square and cube, respectively, of the height of the swell). Since the residual height of the swell depends on the depth of the water at the foot of the structure, it is evident that the level of the foreshore is an essential parameter for evaluating both overtopping and the forces applied. In the presence of swell, the dike must be covered by a rock fill revetment or protected by a barrier, or a hybrid structure. The dimensioning of the rock fill is done according to methods clearly described in the literature. However, that of the barriers remains highly empirical, and it is often done by a quasi-static calculation of the retaining wall. The “pumping” effects due to the swell are more considerable than those of the tide. They are taken into account in the method used to dimension the rock fill. Concerning the barriers, the sealing procedures described in the previous section are applicable in the same way, though more strictly.

7.2.2. Marine geomorphology

7.2.2.1. Sediment transport

As in the rivers, sediment transport is characterized by two modes: suspension and bed load. The hydraulic stresses causing such transport are currents and swells. A specific mode of transport is the projection of materials from the high point of the foreshore due to the effect of waves, which if oblique, lead to longitudinal transport (parallel to the beach). This mode of transport is characteristic of pebble beaches.

Tides can produce currents, especially in the North Sea, the Channel and the Atlantic Ocean with respect to Metropolitan France. Their action is especially marked in estuaries and bays such as that of Mont Saint Michel. They place and maintain fine particles, particularly mud and silt, in suspension and then transport them to more sheltered areas where they are deposited. The finest particles remain in suspension a long time before being deposited. This phenomenon is particularly evident in certain estuaries with very turbid water and where it can form a sediment plug composed of very large volumes of suspended matter that move with the tide and river currents.

The passage of waves generates alternating currents on the bed and a residual component according to the direction of propagation. For the sake of brevity, alternating currents disturb the material on the bed and place it in suspension after which it is transported by residual currents. The grain sizes of the materials suspended and transported can be larger than those disturbed by the one-directional currents mentioned in the previous section, especially in exposed areas and at shallow depths. Coarse sand can thus be placed in suspension and transported during storms. Powerful currents can form close to the coast and generate considerable sediment transport (longitudinal or cross shore transport, transversal or long shore transport).

The action of swells and currents can also combine, resulting in higher volumes of transport. Bed load transport without suspension is also possible due to the action of the current, swells or both. In this case, the materials roll or jump on the seabed.

7.2.2.2. Morphology of seabeds, beaches and coastline

The morphology of seabeds, beaches and coastlines evolves especially in the presence of mobile materials such as mud, silt, sand, gravels and pebbles. The timescales of these evolutions are also very variable: during a tide, a storm, according to season and at interannual and even secular timescales. Such evolutions can be considerable. We will provide a few examples.

A pebble beach on the Normandy-Picardy coast can rise or fall by 2 m along a groyne during a storm. The foot of a dune was observed to have receded by approximately 15 m during Cyclone Xynthia. Sand and pebble beaches do not have the same shape during summer and winter. The top of the foreshore rises during summer, whereas winter storms remove material from the top of the foreshore and the foot of the dune and deposit it in the

open sea. During one winter, the pebble beach at Fécamp was lowered by 3 m.

The coastline can advance and recede over interannual and secular timescales. The dune at the island of Tudy advanced and receded several times during the 20th Century. The amplitude of these movements reaches 100 m. The altitude of beaches can also vary. The level of the sand beach at Wissant has fallen by more than 5 m in approximately 20 years and its altitude has varied by several meters more than one century.

Lastly, the shape of coasts and estuaries can be completely transformed over several centuries. Movements of several and even tens of kilometers over a few centuries have occurred.

Changes of the coast and beaches are very sensitive to long shore drift. This can be considerable and range from tens of thousands to hundreds of thousands of cubic meters a year. The interruption of this drift by building structures perpendicular to the coast, such as port dikes, can have effects several kilometers downstream and even further. At a lower scale, a groyne or breakwater can generate erosion downstream.

7.2.2.3. Stresses exerted by the sea on dikes

In the previous chapter, we focused on the morphological evolutions observed. It is necessary to understand long-term trends when situating the emplacement of a dike. If the trend is for the coastline to recede, the dike must be sufficiently in retreat from the latter, if not it must be considerably reinforced and there is a risk of it being destroyed. In the eventuality of the coastline advancing on the sea, it may be wise to wait before building a dike whose utility is not immediately proven, and implement temporary works. Heavy works are sometimes performed after a storm, whereas the results are due to the natural life of the beach and the coastline. Wherever possible, building structures on the upper beach should be avoided as the resilience of the beach is greater than that of the structure.

As for rivers, the morphological studies to be performed should be based on all available documents, maps and old and contemporary photographs. Due to the considerable sensitivity of the dimensions of a dike to changes in shallow areas, it is necessary to search for all old bathymetric surveys and topographical surveys of the foreshore.

7.2.2.4. Impact of the dike on the coast and the beach

Building a dike modifies the balance of the foreshore and shallow seabeds when they are composed of mobile or erodible materials, and especially if the site is exposed to swells. Indeed, the dike constitutes a reflective obstacle for swells; thus, they will increase at the foot of the structure and remove materials. This process is iterative, since the deepening produced leads to stronger swells that would have broken on the screen when the beach was higher, reached the structure and thus increased erosion, etc. No structure is less reflective than the beach itself; therefore, it is not possible to avoid a fall in the level of the beach following the construction of a dike. Many structures built on the Mediterranean coast have led to the disappearance of beaches. Regarding tidal seas, some beaches have become so narrow that they are no longer visible at high tide. To avoid these negative effects, the best solution is to build the dike sufficiently in retreat when possible. Mitigation solutions consist of controlling the level of the beach in front of the dike by installing groynes, breakwaters or better still, by replenishment, or by combining them.

A dike also has an impact in the presence of long shore drift, especially when a structure has been built to stabilize the beach in front of it. Long shore drift can be blocked or reduced, leading to erosion downstream of the structures and possibly to accumulation upstream (upstream and downstream in relation to the long shore drift).

7.2.3. Mechanical stresses

In addition to the hydraulic and geomorphological phenomena described previously, dikes can be subjected to mechanical stresses related to external factors specific to each structure; these can be permanent or accidental, natural or anthropic.

Accordingly, multipurpose fill structures that support roads and railway lines as well as fulfilling the role of dike must be designed by taking into account the mechanical stresses caused by the traffic travelling on them, especially factors such as overloading and vibration caused by the passage of vehicles (trucks, trains, etc.) which are important for the stability of the fill and the longevity of the sealing structures.

Regarding all dikes, stresses due to the passage of vehicles along the crest or on the berms to ensure maintenance works must be taken into account in the design phase or in reinforcement works with respect to structural stability, the minimum dimensions that must be complied with (widths of crests and berms, access ramps, etc.) and the type of surfacing which must allow the movement of vehicles in all weathers.

Certain dikes are also subject to the potential risk of impacts (vehicles, boats, falling blocks, etc.) that can affect the integrity of the structure and more generally the impervious membrane which, in this case, must be endowed with sufficient mechanical resistance. Vandalism is another element to be taken into account when designing the structure. For example, in the case of geomembrane sealing systems, mechanical protection of the latter must be installed in all spaces open to the public.

7.3. Dysfunction and failure of coastal dikes

7.3.1. Definitions

7.3.1.1. Failure, rupture and breaching

Failure can be defined as the loss of capacity of a functional unit (system or component) to fulfill a necessary function. A section or segment of a dike, having a homogeneous structure and function, is considered as failed when its situation and/or state no longer allow it to ensure the flood protection function for which it was designed. Two causes can be distinguished in the nature of this state of failure.

7.3.1.1.1. Hydraulic failure

Hydraulic failure occurs when the structure, despite its internal structural state being in conformity, is no longer capable of fulfilling its hydraulic function. It is therefore linked to the failure of the hydraulic performance of the section or segment of the dike. The reasons for this failure can be due to:

- new situations linked to modifications of environmental conditions external to the section of the dike in question: for example, modification of flows downstream or upstream due to works performed on the section after its construction;
- situations not foreseen in the design of the structure or errors in its design;

- failure or dysfunction of hydraulic systems (gates, sluices, cofferdams, spillways, etc.);
- hydraulic failure of another section or segment of the dike;
- impervious components aging.

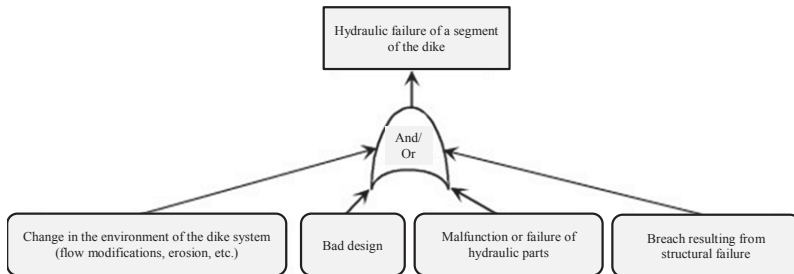


Figure 7.15. Cause of hydraulic failures of dikes (photos by R. Tourment, [ILH 13])

7.3.1.1.2. Structural failure

A structural failure (or internal failure of the system) occurs when one or more components, whose specific functions ensure the structural resistance of the section of the dike concerned, are no longer capable of fulfilling these functions and jeopardize the structural longevity of the dike. Since the longevity of the structure is no longer ensured, it is no longer possible to guarantee the flood protection function. A section or segment of dike can be in a state of structural failure before its total collapse (breach).

The failure processes of a section or segment can be slow or fast:

- Deterioration, degradation and damage processes generally occur slowly and are time-dependent. They lead to the modification of the characteristics of the structural components of a dike section or segment. This modification can result in the failure of a component characterized by a threshold beyond which its properties degrade suddenly and are no longer capable of ensuring its function or its integrity. Deterioration, degradation and damage processes therefore lead to the structural failure of the dike section or segment and can result in breaching processes, generally due to the effect of an external event or stresses (e.g. flooding or overtopping by waves).

– A breach is a catastrophic collapse resulting from a considerable loss of material from the crest or in the core of the dike, leading to a non-controlled overspill into the protected area. It corresponds to the final state of failure and characterizes the failure of the entire structure. It develops during a generally rapid process of disintegration and destruction. However, this process can be triggered by a previous initiation phase linked to the deterioration process whose duration can vary, though it can last a relatively long time. The most frequent breaching processes are linked to wave overtopping, overspill and internal erosion mechanisms affecting the structures.

It is worth noting that a structure unable to resist the stresses of an event exceeding its design specifications cannot be considered as failed.

7.3.1.2. Elementary mechanisms, scenarios and failure modes

The elementary deterioration and degradation mechanisms presented in the following section act on the individual components participating in the structure of the dike section or segment. They involve physical or chemical processes such as impacts, shearing, water flows, effect of interstitial pressures, dissolution and corrosion.

These mechanisms lead to the modification of the properties of the structural components of the dike section or segment and lead to damage in the form of cracks, seepages of water, the removal of materials, etc. However, the observable symptoms of these deteriorations, degradations and damage can be attributed to different mechanisms, whereas the same mechanism can initiate or be initiated by the deterioration of one or more components.

The sequence of deterioration, degradation and damage mechanisms in a combination or scenario of events leads to the structural failure of the components of the dike section or segment. The combination or scenario of events affecting a specific dike section or segment depends on its type, components, nature and the composition of the structures associated with it, the stresses to which it is subjected and their evolutions over time.

The term “failure mode” is generally used for failure scenarios involving several mechanisms that can succeed each other or occur at the same time; the failure mode is generally denoted by the initiating mechanism or that which is predominant in the scenario.

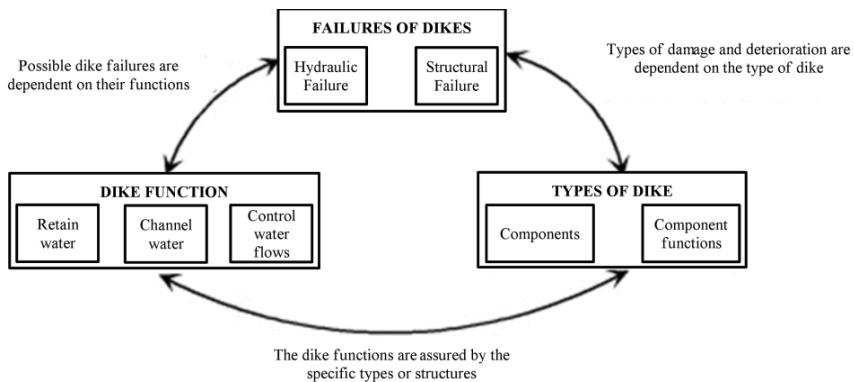


Figure 7.16. Relationships between types, functions and failures of dikes
(photos by Y. Deniaud, [ILH 13])

7.3.2. Classic process to damage and failure of embankment dikes (elementary mechanisms)¹

7.3.2.1. Embankment dikes

Individual dike deterioration, degradation and damage mechanisms can be grouped under the generic terms described below. However, it is important to bear in mind that the degradation process of a specific segment of dike combines different individual mechanisms which depend on its components, its environment and the stresses that affect it. Thus, there is a very close link between the types, functions and modes of dike damage and failure.

7.3.2.1.1. External erosion

External erosion groups all the mechanisms leading to the removal of materials under the effect of stresses exerted on the external surface of the dike. This removal of materials reduces the cross-section of the dike, the stiffening of the slopes, and finally, weakens its resistance. It leads to the occurrence of hollowing, otherwise known as scouring, in the materials.

Erosion on the landward side

The erosion of the landward side develops under the effect of interactions with the surrounding environment of the dike and the uses it provides.

1 The sketches in this section are illustrations without respect for scale, their only objective is to explain the main mechanisms of failure, they are adapted from [ILH 13].

Meteorological aggressions (rain, frost and runoff), the presence of burrowing animals, the movement of livestock, human activities and especially the passage of motor vehicles can cause considerable removals of materials and the occurrence of surface instability. Their repetition and cumulative effects that are liable to jeopardize deteriorate the structure's integrity over time. The facing onto the seaward side is subject to the same type of erosion but, generally, these factors are not critical design parameters.



Figure 7.17. Erosion landside

Erosion seaward side

In addition to the mechanisms presented above for erosion of the landward side, scouring can develop due to the effect of wave action, currents and eddies. These stresses can be exerted on the structure frontally or obliquely (waves, swells) and also longitudinally (coastal drift). Scouring undermines the bases of structures and can loosen them when it affects the supporting ground (foreshore). It can also remove the protection and then directly modify the core of the structure. The damage linked to scouring is generally linked to the morphological evolution of a section of the coast on which the structure stands. It often leads to dike instability phenomena of different scales (superficial or deep landslide affecting the structure due to the removal of toe protection material). It ends with the generalized erosion in front of the dike (lowering of the foreshore) that tends to destabilize the entire structure or increase the stresses affecting it.

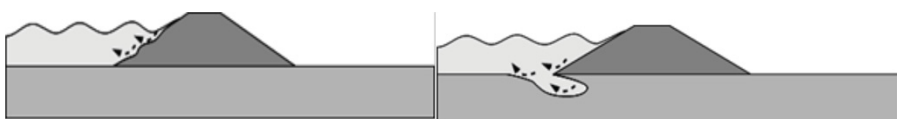


Figure 7.18. External erosion of the core and foundation of an earth fill dike (scouring) water side

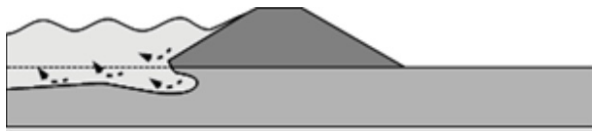


Figure 7.19. External erosion and lowering of the upstream cross-section of the dike (foreshore)

Erosion by overflows or overtopping (important specific case of that described above)

When out of control, overtopping is a major factor of external erosion and one of the most damaging. This mechanism is one of the main causes for the failure of fill dikes. Water overflowing the dike crest leads to high-velocity flows on the crest and the downstream slope of the dike (land side). This uncontrolled flow causes the backward erosion of the slope and can rapidly lead to a breach.

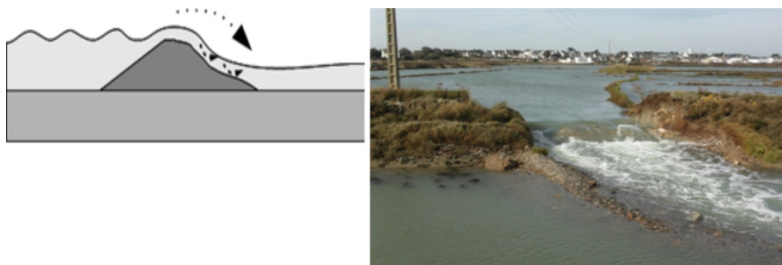


Figure 7.20. Principle of overflows and example of a breach in a structure

Coastal dikes are situated in a specific environmental context characterized by often specific cyclic stresses (swell, tides, high levels due to storms) capable of generating specific dike failure mechanisms.

The overtopping of coastal dikes by series of waves resulting from storm surges against the coast can generate considerable external erosion on the rear slopes of dikes, even before they are submerged by overflows. It can lead to the deterioration and accelerated destruction of the dike. Overtopping sometimes generates not inconsiderable volumes causing heavy floods when the storage and removal of water is not managed adequately. Furthermore, breaches can occur or be aggravated when flooded areas are emptied or simply when the tide retreats, especially in areas with high tidal ranges.



Figure 7.21. Principles of overtopping

The mechanical action of waves on the seaward sides of dikes can also lead to scouring at the toe of the dike by lowering the foreshore and through damage to the protective layers due to repeated impacts.

If water infiltrates into the core of the dike, the fluctuation of loads behind the protective layers can lead to the desegregation of the materials composing the dike by liquefaction or by the aspiration of fines outside the structure and the dislocation of the protective layers by under-pressure and piston effects; this phenomenon, which also occurs in the rivers, is generally exacerbated in coastal dikes due to the cyclic nature of the stresses involved.

Lastly, the particular chemical composition of seawater can also lead to the occurrence of specific pathologies linked to the modification of the materials composing the dike, especially its rigid masonry and stone-covered parts.

7.3.2.1.2. Internal erosion (different mechanisms)

Numerous recent research works were led to characterize this phenomenon and develop representative tests in laboratory and *in situ*; we can particularly quote the following references: bulletin 164 [CIG 13], the ERINOH project [ERI 2009] and its recommendations [DER 13] as well as the publications of [BON 11, BON 12, BON 13].

When the dike is immersed (high tide, storm), water flows through the core of fill dikes and through the foundation soil. These flows can be the starting points for the removal of materials when the hydraulic gradient reaches a threshold level known as the critical gradient of the materials composing the dike or its foundation. These phenomena are particularly sensitive to heterogeneous porosity, as the flows are concentrated in the most porous sectors, increasing the flow velocity gradients.

The term “internal erosion” therefore covers several different particle removal phenomena linked to flows inside an earth fill structure:

- Backward erosion: materials are torn away at the outlet of the flow network when the flow gradient exceeds the critical buoyancy gradient of the soil. A pipe is progressively created from downstream to upstream, amplifying the gradient and the flow velocities through time.

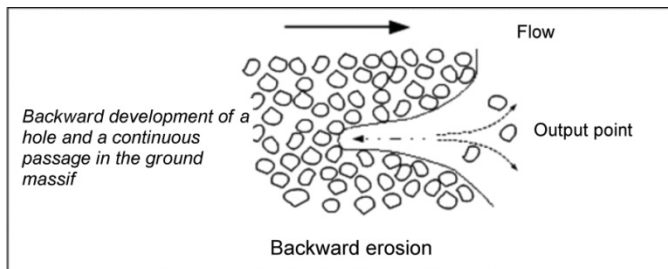


Figure 7.22a. Principle of backward erosion

- Concentrated erosion or piping: materials are removed along the sides of an open crack or interconnected cavities when the shearing stress caused by the current is higher than a critical value linked to the characteristics of the materials. This type of erosion can develop in particular along associated structures such as buried pipes and walls.

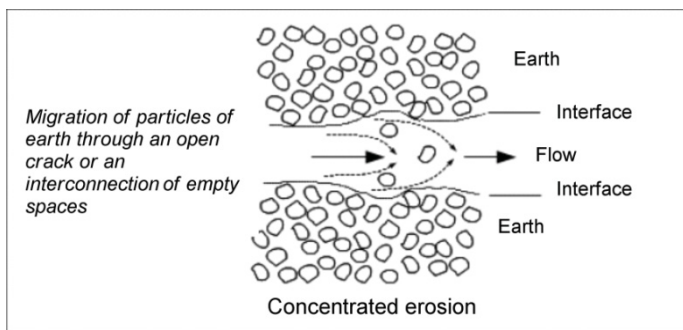


Figure 7.22b. Principle of piping

– Contact erosion: this type of erosion develops at the horizontal interface between two granular materials or between a granular material and a cracked material. The finest particles are washed away by the flow in the porous space of the layer of coarsest materials or in the cracks of the damaged material.

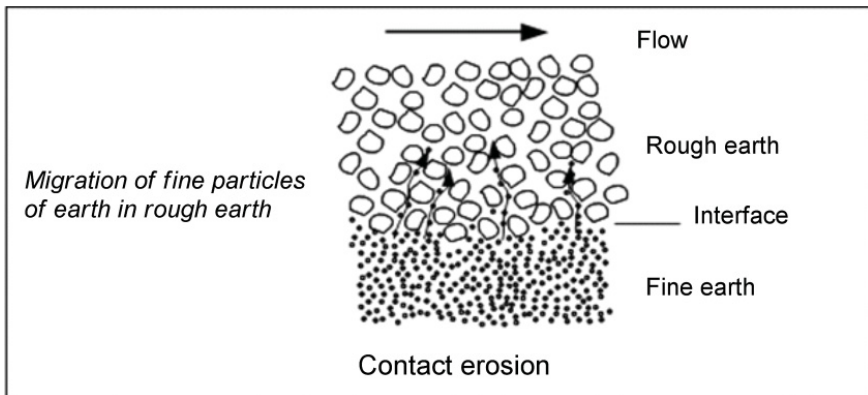


Figure 7.22c. Principle of contact erosion

– Suffusion is a phenomenon that affects certain types of unstable soil in which the smallest particles are washed through a soil skeleton composed of the coarsest materials.

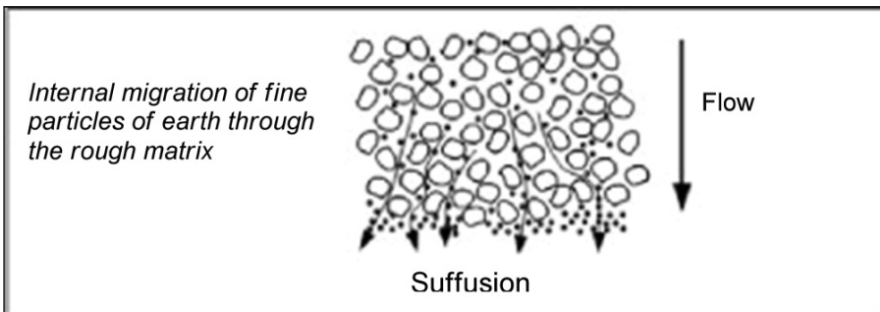
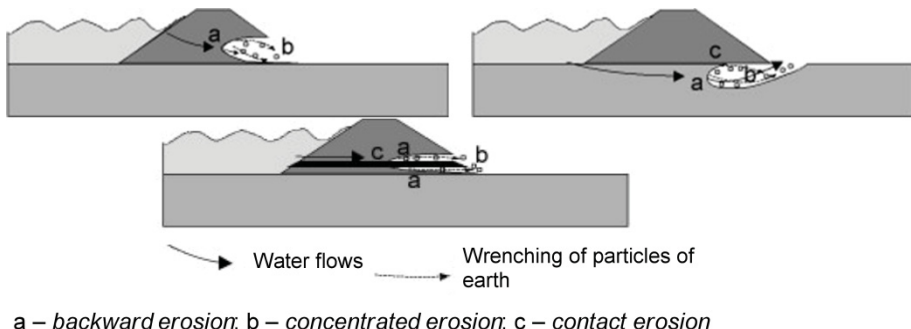


Figure 7.22d. Principle of suffusion

These different mechanisms often combine to generate erosion in the core or the soils of the foundations supporting earth fill dikes. They are preferentially localized at the interfaces with structures that cross, are supported by or which compose the dike.



a – backward erosion; b – concentrated erosion; c – contact erosion

Figure 7.23. Internal erosion of the dike core a), the foundation b) or along a structure crossing c) an earth fill dike

7.3.2.1.3. Fill and foundation instability

Normally, the stability of dike slopes must be ensured by design and sizing that conforms to the geotechnical practices governing the construction of earth fill structures. However, the evolution of stresses through time, especially during high tide periods, can lead to instabilities related to the following in particular:

- steepening of slopes due to the action of external erosion (removal of the toe protection);
- increase in hydraulic pressure inside the dike following a drainage dysfunction and/or the presence of heterogeneous layers with different hydraulic behaviors;
- increase in loads on the structure or on the foundation soil (new construction, raising, widening, etc.);
- negative changes through time of the characteristics of the dike's construction materials or foundations (soaking-drying cycle, creep, liquefaction, etc.).

The main instability mechanisms of earth fill structures are therefore:

- Superficial landslides: the mechanical characteristics of the materials located at the surface of the dike core can deteriorate due to the effect of meteoric water. Superficial landslides involving the modified materials of the dike core may occur when the shearing resistance of these materials is insufficient to maintain them in the initial geometric slope configuration of the dike.

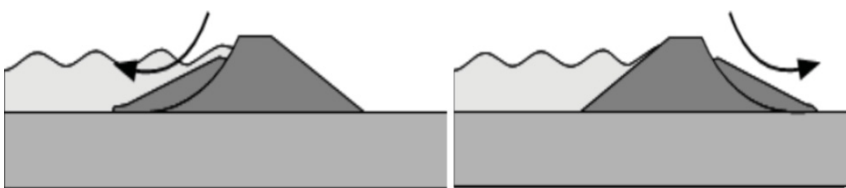


Figure 7.24. Superficial landslides affecting the core of earth fill dikes

– Rotational and translational landslides: the increase in hydraulic loads linked to a high sea level or the increase in loads linked to an elevation of the dike, a considerable modification of its cross-section or of the use of its crest, can lead to the occurrence of considerable rotational or translational landslides involving all the materials composing the dike. These phenomena may also affect the foundation soil, especially if the materials composing it have poor shearing characteristics (plastic or organic clays, peats, etc.). Rotational movements occur when the shearing resistances of the materials composing the dike core and/or certain clay horizons of the foundation soil are lower than the overlaying loads applied by the weight of the materials, the hydraulic forces and additional service loads. The translational movements of blocks are liable to occur when the shearing resistance of a soil horizon is insufficient to withstand the hydraulic forces applied on the dike core. These translational movements can also affect the core of a structure, notably when its mechanical characteristics are very stratified or it presents a singular horizontal surface (limit at which works were performed on an existing structure, the point at which the crest of a structure was raised, etc.).

– Landslides generally result in the appearance of cracks, vertical displacements at the crest of the slope and a ridge at the foot of the slope. These signs can be masked or eroded by the effects of flooding.

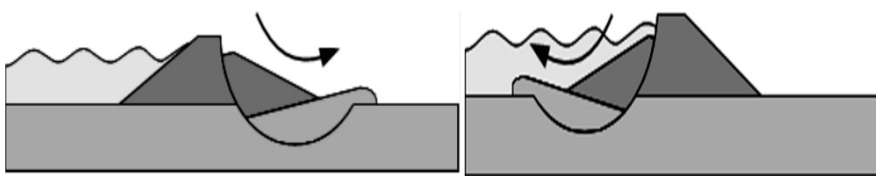


Figure 7.25. Rotational landslide affecting the core of an earth fill dike and its foundation

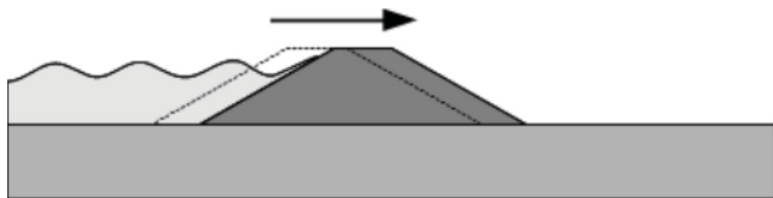


Figure 7.26. Translational landslide affecting the core of an earth fill dike

– Settlement: the occurrence of compaction may be linked to the poor compacting of the materials employed when constructing the core of the dike or to consolidation and/or creep phenomena linked to the presence of compressible levels in the foundation soils of the structure; internal erosion can also be the cause of compaction on the crest. The lowering of the topography of the crest caused by these compactations reduces the effective protective height of the dike which will then be affected more quickly by an overflow. Distortions of the longitudinal profile and cracking generated by compaction, also weakens certain components of the structure which become more porous and more sensitive to infiltration and internal erosion phenomena.

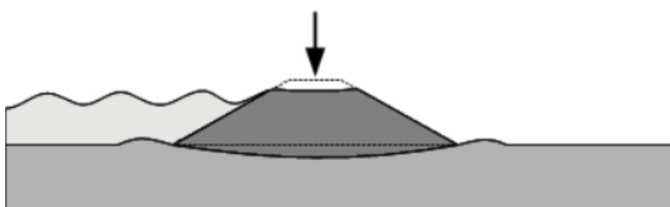


Figure 7.27. Settlement affecting the core of an earth fill dike

– Liquefaction: under certain stress conditions, notably cyclic (earthquakes, swells, etc.), the shearing characteristics of some specific materials can deteriorate rapidly. The liquefaction of certain foundation support soils under the effect of such stresses can lead to the collapse of the dike core above them, due to sapping and undermining.

– Collapse: instability due to cavities already present in the substrata of dike foundations can lead to major degradations linked to subsidences in the core of the structure. The entrainment of materials composing the structure into an underlying cavity can lead to localized subsidence or sudden collapse. These phenomena are regularly masked when rigid surface revetments are used (concrete slabs, asphalted roads, etc.).

7.3.2.2. Composite dikes

Composite dikes are fill dikes that incorporate rigid elements such as walls, retaining walls or protection consisting of stone, masonry or concrete. The classical deterioration, degradation and damage mechanisms of the structures include the following.

7.3.2.2.1. External deteriorations linked to mechanical stresses

External deteriorations are generated by mechanical actions external to the structure as follows.

External instabilities

These instabilities cover the following phenomena:

– punching: when the bearing capacity of the foundation soil is insufficient to maintain the weight of the structure, the excessive sinking of the base of the dike destabilizes it, tipping it over and destroying it. For structures on crests, the low bearing capacity of the dike core can also result in the occurrence of a superficial landslide carrying away the overlying structure;

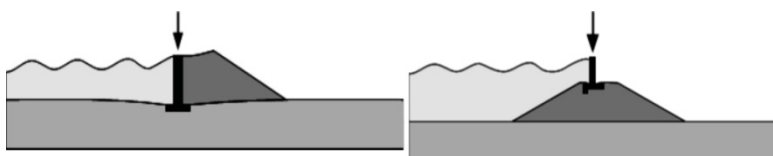


Figure 7.28. Punching of rigid structures integrated in a composite dike

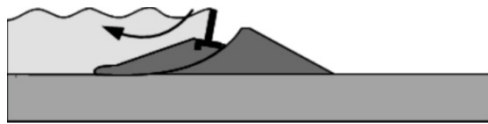


Figure 7.29. Superficial landslide affecting a structure with a crest

– landslide under the base: in the case of strong thrust forces on a retaining wall structure, its foundation can slide on its base. The resulting displacement generally leads to the destruction of a rigid structure not designed for such stresses;

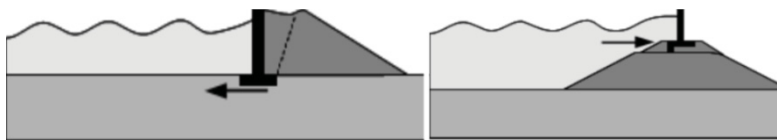


Figure 7.30. Landslide at the base of rigid structures

– overturning: excess dust upstream of a correctly founded wall or retaining wall-type structure can lead to the excessive displacement of the top of the structure. This displacement can result in the overturning or complete tipping over of the structure;



Figure 7.31. Overturning of rigid structures

– abutment fault: by design, or more generally due to scouring, an abutment fault leads to the destruction of such structures by the overturning of the retaining wall or by the loosening and sliding of the walls and stone-covered slopes;

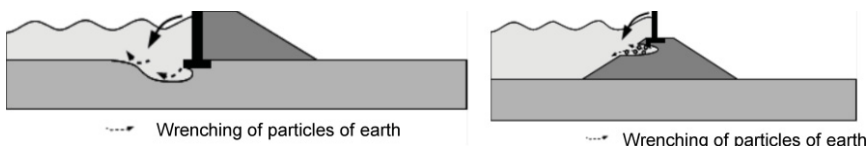


Figure 7.32. Scouring and abutment faults of composite dikes

- raising: raising of the base of rigid structures is caused by excess interstitial pressure or by abutment faults.

General instability

A structure and its supporting site form an assembly. If the site's mechanical characteristics are poor, the assembly is exposed to the risk of sliding.

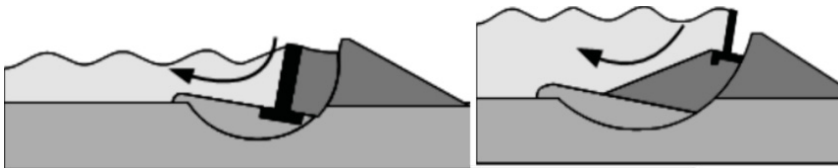


Figure 7.33. Generalized sliding affecting rigid structures

7.3.2.2.2. Internal deteriorations linked to the modification of the materials composing the dike

Internal deteriorations reduce the resistance of the structure. Above a certain threshold of internal deterioration, the resistance of the structure is no longer sufficient for it to fulfill its function, possibly resulting in its destruction. Insufficient internal resistance of the structure can result from poor initial dimensioning, but it is generally due to deterioration through time of the materials composing it (masonry, concrete and steel). Regarding this, it is worth noting that all rigid structures have a given design lifetime.

Among the internal deterioration phenomena, mention should be made of:

- wear: wear is a deterioration phenomenon that occurs to the materials over time and is linked to the friction of the environment on the structure;
- impacts: the modification of a structure by impacts has two dimensions: (i) wear generated by impacts of low magnitude but which are repeated and (ii) failure generated by a strong impact higher than the resistance of the material;
- chemical actions (solubilization, swelling, corrosion, etc.): in the presence of certain chemical substances present in the natural environment

of the structure, chemical reactions can degrade the mechanical capacities of the materials composing it;

- biological actions: root development (river dikes) and the colonization of structures by incrusting species (coastal dikes) can lead to the development of cracks and the progressive fracturing and disaggregation of the materials.

7.3.3. Case studies of the damage and failure of coastal dikes

7.3.3.1. Failure and damage due to external erosion

7.3.3.1.1. Erosion of a pebble dike



Figure 7.34. Bas-Champs dike: areas flooded following breaches in February 1990 (photos by Cerema)

7.3.3.1.2. Erosion/abrasion of a stone coastal dike

The Génie Dike at Aiguillon (French Administrative Department 85), at the site known as the Sablons in the Lay estuary, is a dike several kilometers long with a maximum height of 2.50 m, landward side, above the road that runs along its whole length. This dike, built of stone in the 19th Century, has been subject to two main types of dysfunction:

- external erosion by abrasion of the seaward side and by weathering of the crest and wall on the landward side;
- the formation of ettringite in old cement (aggravated by contact with seawater) causing swelling and therefore deformations and cracks, accelerating the action of atmospheric degradation agents.

On several occasions, the dike has been breached at sections of limited length given the rigid nature of the dike:

- filling of breaches by riprap embedded in concrete;
- the replenishment of rock fill seaward side to avoid erosion of the wall and break the energy of the waves;
- the application of shotcrete on the landward side to limit weathering and the action of atmospheric agents on the degraded stone.



Figure 7.35. The Génie Dike: abrasion of stone, seaward side (the cement joints project outward) and weathering of the crest (photos by Irstea)



Figure 7.36. The Génie Dike: shotcrete road side (broken in places due to the swelling of the masonry) and repair of a breach by rock fill embedded in concrete, seaward side (photos by Irstea)

It is worth noting that the abrasion speeds of stone vary as a function of the materials composing the dike and also of the force of the swell (level of stress exerted on the dike) and the nature of the foreshore. Abrasion speeds for concrete of 1 cm a year have been observed in certain situations. Figure 7.37 shows the dike at Pors Kaïg on the Ile de Sein where abrasion by pebbles stripped away the concrete from its steel reinforcement in certain places.



Figure 7.37. The Pors Kaïg dike: example of abrasion of concrete by pebbles (photos by Cerema)

7.3.3.1.3. Erosion of the abutment of a dike made up of stone and an earth fill dike with a stone revetment

The erosion of concrete and stone on the seaward side can occur on the wall as described previously, but the toe of the slope (link between the dike and its foundations) often remains the point most vulnerable to erosion phenomena (though not systematically), notably during the lowering of the height of the natural land, seaward and river side. If these types of erosion are not stopped by appropriate renovation, hollows may form under the masonry in the case of rigid dikes and the loss of part of the material in the case of fill protected by a rigid revetment. There are many examples of this type of erosion.

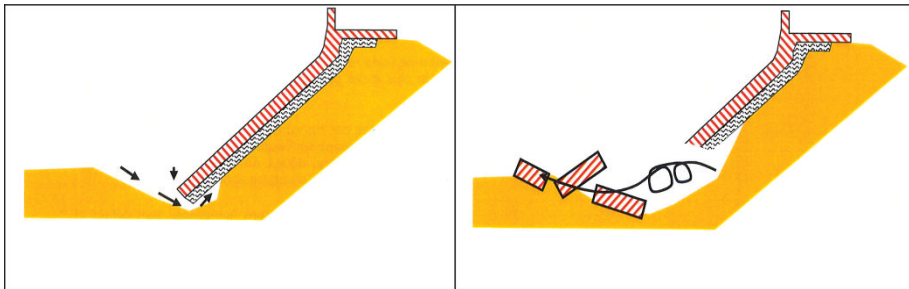


Figure 7.38. Diagram of erosion at the toe of the slope leading to failure [BRL 06]

The Erromardie Dike (Figure 7.39(a)) at Saint Jean de Luz (Pyrénées atlantiques) is a low stone structure which, in particular, protects a camp site. The lowering of the foreshore has led to the erosion of the toe of the structure to the point of undermining its foundations.

The west dike of Saint Clément les Baleines (Figure 7.39(b)) on the Ile de Ré is also subject to erosion by abrasion of the stone composing the wall and of the foot of the wall, linked to the lowering of the foreshore. Regular reinforcement of the most degraded zones must be performed at the toe and on the wall (in this case, concrete revetment).



Figure 7.39. a) Undermining of the Erromardie Dike (mainly sandy foreshore). b) Saint Clément les Baleines Dike: abrasion of the riprap and lowering of the limestone outcrop requiring a coating on the wall and replenishing at the toe of the slope (photos by Cerema and Ifremer)

7.3.3.1.4. Erosion by overflows and overtopping (Figure 7.40)

During the storm Xynthia, fill dikes with rigid protection (concrete or stone) seaward side were subject to failures following overflows (generalized or by series of waves) which led to the erosion of the wall, land side and to the successive formation of cavities under the rigid structure seaward side, then to the collapse of this structure and thus to breaches whose width was limited only by the resistance of the protection because the often sandy fill was washed away very rapidly (Figure 7.40).

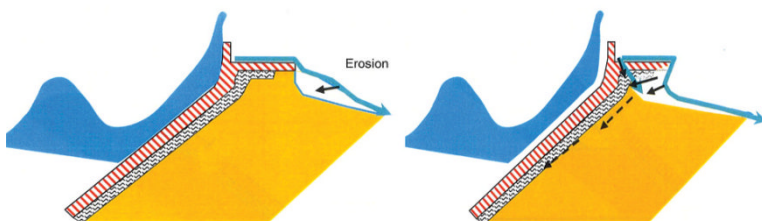


Figure 7.40. Diagram of erosion and failure as a result of overtopping [BRL 06]

Two examples are given below:

– The Bouin Dike (French Administrative Department 85) is composed of earth-fill-protected seaward side by concrete slabs and is crowned by a parapet wall (*a priori* a simple breakwater); the water overflowing this parapet led to the erosion of the cohesive fill until cavities were formed under the slabs which then subsided (Figure 7.41); at certain points, the phenomenon was severe enough to cause the collapse of the concrete slabs, leading the opening of breaches.



Figure 7.41. The Bouin Dike: erosion of the fill by overflows (photograph taken landward side) until the occurrence of cavities under the slabs which subsided (photograph taken seaward side) (photos by Irstea)

– The west dike of Saint Clément les Baleines (Ile de Ré) is a sand fill dike equipped at its seaward side with a stone revetment topped at its crest with a parapet wall acting as a breakwater (*a priori* not designed to contain a permanent level of water). The crest is protected by a concrete slab. The overflow led to the erosion of the sand composing the dike, with the formation of cavities under the slab on the crest which subsided (Figure 7.42(a)), after which the phenomenon continued under the protection until its collapse at certain points resulting in the formation of a breach (Figure 7.42(b)).



Figure 7.42. The West dike of Saint Clément les Baleines: collapse of the crest slab a) which continued with the collapse of the stone protection of the slope until the formation of a breach b) – courtesy DDTM 17

7.3.3.1.5. Erosion by localized overflow (low points corresponding to passages)

Failures of earth fill dikes following a localized overflow at a low point caused by anthropic erosion due to frequent passages are not anecdotal. For example, the ridge of dunes west of Faute Sur Mer is not a dike in the strict sense but it forms a natural element composing the system protecting residential areas. This ridge of dunes several tens of meters wide is crossed by pedestrians who walk to the beach, creating a low point by erosion and the removal of sand (Figure 7.43(a)). During Cyclone Xynthia, this ridge of dunes was subject to two failures including one opposite the village at the place where the main access to the beach is situated. A pedestrian path and networks (notably electric), probably to supply several light commercial constructions for summer use, were located at this low point which is where the failure occurred (Figure 7.43(b)) and where the initial overflows were concentrated. The presence of a trench with less compact soil and the

possibility of preferential flows along the networks could have been aggravating factors in the formation of the breach.



Figure 7.43. Ridge of dunes of Faute sur mer: a) pedestrian path forming a low point on the dune and b) breach in the dune during Cyclone Xynthia, next to the pedestrian path, the electric cables and a pipe (photos by Irstea)

7.3.3.2. Failure due to internal erosion and under-pressure

7.3.3.2.1. Entrainment of fine particles of earth fill through the slope protection

Previously, we saw that overflows on the landward side can lead to the removal of the material supporting the protection by entrainment to the landward side, and thus form cavities under the rigid structure on the crest and under the revetment seaward side. The formation of voids under the protection can also occur due to internal erosion by the entrainment of particles through the protection system whose filtration function either does not exist or has failed. The formation of cavities under the protection seaward or river side can lead to sudden failures in the case of rigid revetments.

The process of entrainment of fine particles toward the “water” side occurs when the flood level of the river or the tide, in the case of coastal dikes, subsides. At this moment, the piezometric level is higher in the fill if it was saturated when the water was rising after which the direction of the flow reverses so that the flow goes from the fill to the river or the sea. This phenomenon is particularly important for coastal dikes where tide cycles involve the repetition of this phenomenon, as illustrated by the two following examples:

– The dike of Nouveau, a part of the dikes west of Saint Clément les Baleines (Île de Ré), is a sand fill dike whose covering seaward side is protected by masonry. The average state of these walls subject to considerable stress (Figure 7.44) will permit the circulation of sea water in the core of the sand fill dike and favor the removal of sand. The core of the sand dike will lose its volume, thus creating voids between the concrete revetment and the core of the dike (Figure 7.44).



Figure 7.44. Diagram of a failure [BRL 06] as a result of a fault of the dike wall

– The protection system of Boyardville (Île d'Oléron) is composed of dikes along the channel located south of the town; a portion of these dikes is equipped with a vertical wall channel side to form a wharf for unloading boats. A fault in the sealing of the vertical wall led to the entrainment of the fine particles of the fill at this point and to the subsidence of the platform, sometimes exceeding 30 cm in places (Figure 7.45).



Figure 7.45. Subsidence of the platform behind the wharf of Boyardville (photos by Irstea)

7.4. Bibliography

- [BON 11] BONELLI S., BENAHMED N., "Piping Flow erosion in water retaining structures", *The International Journal on Hydropower and Dams*, no. 3, 2011.
- [BON 12] BONELLI S., *Erosion of Geomaterials*, ISTE Ltd, London and John Wiley & Sons, New York, 2012.
- [BON 13] BONELLI S. (ed.), *Erosion in Geomechanics Applied to Dams and Levees*, ISTE Ltd, London and John Wiley & Sons, New York, 2013.
- [BRE 00] BRETESCHE B., *La méthode APTE: Analyse de la valeur, analyse fonctionnelle*, Pétrelle éditions, 2000.
- [BRL 06] BRL INGÉNIERIE, Diagnostic des digues maçonnées de l'île de Ré, Rapport au Conseil Général de Charente maritimes, 2006
- [CET 09] CETMEF, Guide enrochements : l'utilisation des enrochements dans les ouvrages hydrauliques, version française du Rock Manual – 2^{ème} édition, available at <http://www.cetmef.developpement-durable.gouv.fr/guide-enrochement-a130.html>, 2009.
- [CIG 13] COMITÉ INTERNATIONAL DES GRANDS BARRAGES (CIGB/ICOLD), Internal erosion of existing dams, levees and dikes, and their foundations – bulletin: internal erosion processes and engineering assessment, vol. 1, no. 164, 2013.
- [DER 13] DEROO L., FRY J.J., Recommandations ERINOH (volume 3): maîtrise de l'érosion interne – 2^{ème} Colloque National sur les digues maritimes et fluviales de protection contre les submersions – Comité Français des Barrages et Réservoirs, 2013.
- [ERI 09] ERINOH, Caractérisation de l'érosion interne au laboratoire, rapport final axe 1 du projet national ANR sur l'Erosion INterne dans les Ouvrages Hydrauliques, p. 94, available at <http://erinoh.lyon.cemagref.fr/>, 2009.
- [EUR 07] EUROTOP, Wave overtopping of sea defences and related structures: assessment manual, p. 193, available at <http://www.overtopping-manual.com/eurotop.pdf>, 2007.
- [HRW 15] HR WALLINGFORD LTD., Wave Overtopping, available at: www.overtopping-manual.com, 2015.

[ILH 13] INTERNATIONAL LEVVE HANBOOK (ILH), CIRIA C731, p. 1332, available at. <http://www.leveehandbook.net/>, 2013.

[POU 15] POULAIN D., Référentiel technique digues maritimes et fluviales, Working Group of French Ministry of Ecology, published by French Ministry of Ecology, p. 176, 2015

[SIM 07] SIMON B., *La marée océanique côtière*, Institut océanographique, p. 433, 2007.

List of Authors

Kamilia ABAHRI
ENS-Cachan – CNRS LMT UMR
Cachan
France

Abdelkarim AÏT-MOKHTAR
University of La Rochelle – CNRS
LaSIE UMR
La Rochelle
France

Ouali AMIRI
University of Nantes – CNRS
GeM UMR
Saint-Nazaire
France

Rafik BELARBI
University of La Rochelle – CNRS
LaSIE UMR
La Rochelle
France

Khaled BOURBATACHE
INSA Rennes
LGCGM EA
Rennes
France

Rana EL-HACHEM
Ecole Centrale de Nantes - CNRS
GeM UMR
Nantes
France

Ameur HAMAMI
University of La Rochelle – CNRS
LaSIE UMR
La Rochelle
France

Ciarán HANLEY
University College Cork
Dynamical Systems and Risk
Laboratory
Cork
Ireland

Ahmed LOUKILI
Ecole Centrale de Nantes - CNRS
GeM UMR
Nantes
France

Olivier MILLET
University of La Rochelle – CNRS
LaSIE UMR
La Rochelle
France

Phu-Tho NGUYEN
University of Nantes – CNRS
GeM UMR
Saint-Nazaire
France

Vikram PAKRASHI
University College Cork
Dynamical Systems and Risk
Laboratory
Cork
Ireland

Daniel POULAIN
IRSTEA – Hydrology Research Unit
Aix en Provence
France

Emmanuel ROZIÈRE
Ecole Centrale de Nantes – CNRS
GeM UMR
Nantes
France

Hassan SLEIMAN
Lebanese University
Faculty of Engineering
Tripoli
Lebanon

Rémy TOURMENT
IRSTEA – Hydrology Research Unit
Aix en Provence
France

Abdelkarim TRABELSI
University of Lyon 1 – CNRS
CETHIL UMR
Villeurbanne
France

Philippe TURCRY
University of La Rochelle – CNRS
LaSIE UMR
La Rochelle
France

Index

B, C

binding isotherm, 189, 193, 194
cementitious materials, 1, 10, 13, 15,
24, 28, 99, 100, 117–119, 130, 132,
151, 154, 155, 164, 173, 203, 204,
214, 229, 237, 238
chloride, 161
profile, 178, 183, 185, 190, 193,
194
coastal dike, 285, 286, 298, 307,
309–311, 322, 327, 328, 337, 343
computation, 34, 105, 107, 138, 248,
256, 258–262, 268
constructed microstructure, 24–27,
32–34
construction materials, 1, 41, 331
crystallization pressure, 197, 198,
200, 201, 204, 211–213, 219, 233,
237, 238

D, E, F

degradation scenario, 285
diffusion coefficient, 44, 52, 55, 56,
73, 77–87, 98, 106, 109, 118, 126,
136, 145–156, 166, 168, 170, 171,
176, 177, 184, 185, 193, 222, 225,
226, 279

electrical double layer, 118, 119,
124–133, 150, 165
electrocapillary adsorption, 165
embankment, 325
failure mode, 271, 278, 285, 324
flooding, 285, 323, 332
functional analysis, 295–309

G, H, I, L

gypsum, 68, 197, 199, 203, 204, 209,
211, 214, 216, 221, 222, 238
heat transfer, 53, 54, 57, 59, 72
heterogeneous materials, 117, 287
homogenized diffusion tensor, 133,
137, 138, 141, 147
imaging techniques, 10–14, 32
ionic transport, 164–171, 175, 179
leaching, 14, 197, 198, 202–205, 207,
209, 210, 214, 221, 223, 224, 226,
230, 233, 234, 237

M, N

microstructure, 1, 3, 5, 13–34, 99,
118, 119, 122, 124, 135, 149, 151,
152, 153, 155, 156, 177, 211, 225,
234
microtomography, 11–14, 203, 204,
206, 224

moisture, 14, 41, 162, 163, 165, 171–178, 184, 185, 189, 191, 194
diffusion, 43–45
transfer, 41, 163, 171, 177
monosulfoaluminate, 197–200, 203, 213–215, 237, 238
multispecies modeling, 136
Nernst-Planck equation, 125, 128, 164, 166
NMR, 7–10, 78

P, R

periodic homogenization method, 119, 122–124, 193, 194
physical and chemical adsorption, 49
Poisson-Boltzmann system, 128
porous
construction materials, 1, 41
media, 1–3, 15, 23, 41–43, 49, 51, 52, 66, 117, 119, 120, 140, 163, 164, 179

protection system, 285, 295–309, 343, 344
reliability analysis, 248–252, 258–259, 264, 270, 276–278
risk, 42, 67, 219, 251, 314, 320, 322, 336

S, T, X

sensitivity analysis, 259
statistical variability, 101–109
submersion, 285, 298, 310, 314
sulfate attacks, 197
testing, 65, 198, 207, 208, 214, 229–236, 264, 265
thaumasite, 199, 204, 205, 216, 219, 223, 227
thermodiffusion, 51
time dependence, 276
total pressure variation, 63
X-Ray microtomography, 11–14

Other titles from



in

Civil Engineering and Geomechanics

2014

DAÏAN Jean-François

Equilibrium and Transfer in Porous Media – 3-volume series

Equilibrium States – volume 1

Transfer Laws – volume 2

Applications, Isothermal Transport, Coupled Transfers – volume 3

2013

AMZIANE Sofiane, ARNAUD Laurent

Bio-aggregate-based Building Materials: Applications to Hemp Concretes

BONELLI Stéphane

Erosion in Geomechanics Applied to Dams and Levees

CASANDJIAN Charles, CHALLAMEL Noël, LANOS Christophe,

HELLESLAND Jostein

Reinforced Concrete Beams, Columns and Frames: Mechanics and Design

GUÉGUEN Philippe

Seismic Vulnerability of Structures

HELLESLAND Jostein, CHALLAMEL Noël, CASANDJIAN Charles,
LANOS Christophe

Reinforced Concrete Beams, Columns and Frames: Section and Slender Member Analysis

LALOUI Lyesse, DI DONNA Alice

Energy Geostructures: Innovation in Underground Engineering

LEGCHENKO Anatoly

Magnetic Resonance Imaging for Groundwater

2012

BONELLI Stéphane

Erosion of Geomaterials

JACOB Bernard *et al.*

ICWIM6 – Proceedings of the International Conference on Weigh-In-Motion

OLLIVIER Jean-Pierre, TORRENTI Jean-Marc, CARCASSES Myriam

Physical Properties of Concrete and Concrete Constituents

PIJAUDIER-CABOT Gilles, PEREIRA Jean-Michel

Geomechanics in CO₂ Storage Facilities

2011

BAROTH Julien, BREYSSE Denys, SCHOEFS Franck

Construction Reliability: Safety, Variability and Sustainability

CREMONA Christian

Structural Performance: Probability-based Assessment

HICHER Pierre-Yves

Multiscales Geomechanics: From Soil to Engineering Projects

IONESCU Ioan R. *et al.*

Plasticity of Crystalline Materials: from Dislocations to Continuum

LOUKILI Ahmed

Self Compacting Concrete

MOUTON Yves

Organic Materials for Sustainable Construction

NICOT François, LAMBERT Stéphane

Rockfall Engineering

PENSÉ-LHÉRITIER Anne-Marie

Formulation

PIJAUDIER-CABOT Gilles, DUFOUR Frédéric

Damage Mechanics of Cementitious Materials and Structures

RADJAI Farhang, DUBOIS Frédéric

Discrete-element Modeling of Granular Materials

RESPLENDINO Jacques, TOULEMONDE François

Designing and Building with UHPFRC

2010

ALSHIBLI A. Khalid

Advances in Computed Tomography for Geomechanics

BUZAUD Eric, IONESCU Ioan R., VOYIADJIS Georges

Materials under Extreme Loadings / Application to Penetration and Impact

LALOUI Lyesse

Mechanics of Unsaturated Geomechanics

NOVA Roberto

Soil Mechanics

SCHREFLER Bernard, DELAGE Pierre

Environmental Geomechanics

TORRENTI Jean-Michel, REYNOUARD Jean-Marie, PIJAUDIER-CABOT Gilles

Mechanical Behavior of Concrete

2009

AURIAULT Jean-Louis, BOUTIN Claude, GEINDREAU Christian
Homogenization of Coupled Phenomena in Heterogenous Media

CAMBOU Bernard, JEAN Michel, RADJAI Fahrang
Micromechanics of Granular Materials

MAZARS Jacky, MILLARD Alain
Dynamic Behavior of Concrete and Seismic Engineering

NICOT François, WAN Richard
Micromechanics of Failure in Granular Geomechanics

2008

BETBEDER-MATIBET Jacques
Seismic Engineering

CAZACU Oana
Multiscale Modeling of Heterogenous Materials

HICHER Pierre-Yves, SHAO Jian-Fu
Soil and Rock Elastoplasticity

JACOB Bernard *et al.*
HVTT 10

JACOB Bernard *et al.*
ICWIM 5

SHAO Jian-Fu, BURLION Nicolas
GeoProc2008

2006

DESRUES Jacques *et al.*
Advances in X-ray Tomography for Geomaterials

FSTT
Microtunneling and Horizontal Drilling

MOUTON Yves

Organic Materials in Civil Engineering

2005

PIJAUDIER-CABOT Gilles *et al.*

Creep Shrinkage and Durability of Concrete and Concrete Structures

CONCREEP – 7

@Seismicisolation

This book provides a series of designs, materials, characterizations and models that will help create safer and stronger structures in coastal areas.

The authors take a look at the different materials (porous, heterogeneous, concrete, etc.), the moisture transfers in construction materials as well as the degradation caused by external attacks and put forward systems to monitor the structures or to evaluate the performance reliability as well as degradation scenarios of coastal protection systems.

Abdelkarim Aït-Mokhtar is Professor in Civil Engineering at La Rochelle University in France and the head of the Engineering Sciences laboratory (LaSIE UMR CNRS 7356). His research focuses on mass transfer in porous media, aiming applications on aggressive agent transfer within building materials for the improvement of structure durability in aggressive environments (in a marine or carbon gas environment). He is a specialist in experimental diffusion processes by the assessing of materials' microstructures, chloride and carbon gas ingress within cementitious materials, and corrosion initiation in reinforced cement-based materials using electrochemical methods.

Olivier Millet is Professor in Mechanics and Civil Engineering at La Rochelle University in France. He is a specialist of continuum mechanics, homogenization techniques, ionic transfers, and electrocapillary effects. He is also the head of the research network "Multi-Physics and Multiscale Couplings in Geo-environmental Mechanics". The topics addressed in this book constitute one of the major axes of this research network.